2008

Parametric study of a pulsed vertical jet in cross-flow

Guillaume Francois Bidan
Louisiana State University and Agricultural and Mechanical College

PARAMETRIC STUDY
OF
A PULSED VERTICAL JET IN CROSS-FLOW

A Thesis

Submitted to the Graduate Faculty of the
Louisiana State University and
Agricultural and Mechanical College
in partial fulfillment of the
requirements for the degree of
Master of Science in Mechanical Engineering

in

The Department of Mechanical Engineering

by
Guillaume F. Bidan
Ecole Nationale Supérieure d'Ingénieurs de Constructions Aéronautiques, Toulouse, France
August 2008

Acknowledgements

I would like to thank my advisor, Dr. Dimitris Nikitopoulos for his support and advice during these two years. I would also like to thank Dr. Sumanta Acharya and Dr. Keith Gonthier for being part of my advisory committee.

Because the work presented in this Thesis is part of a project conducted by a team of graduate students, I would also like to acknowledge Lem Wells who has been my lab partner during these two years and Clémentine Vézier who joined us later. I would also like to thank Pierre-Emmanuel Boulladoux and Jeremiah Oertling who worked on the project before me and gave part of the raw data presented in this Thesis, and without whom we might not have obtained funding to continue the project.

I would also like to thank my parents and family for their support in this adventure that these two years abroad represented.

Finally, I would like to thank Céline Ramet for her support, her patience, and these wonderful two years spent in Baton Rouge.

Table of Contents

Acknowledgements ..... **ii**

List of Tables ..... **vi**

List of Figures ..... **vii**

List of Equations ..... **xii**

Abstract ..... **xiii**

Chapter 1: Introduction **1**
1.1. Background 1
1.2. Film Cooling 1
1.3. Literature Survey 3
1.4. Motivations and Objectives 7

Chapter 2: Notations and Definitions **8**
2.1. Notations 8
2.2. Definitions 9
2.2.1. Blowing Ratio (BR) 9
2.2.2. Forcing Frequency (f_f) 10
2.2.3. Duty Cycle (DC) 10

Chapter 3: Experimental Apparatus **11**
3.1. Wind Tunnel 11
3.2. Jet 12
3.2.1. Jet Geometry 12
3.2.2. Jet Feeding 12
3.2.2.1. Air Supply 12
3.2.2.2. Control Valves 13
3.2.2.3. Connection 13
3.2.2.4. Reagent Injection 14
3.3. Control and Acquisition 14
3.3.1. Forcing System 14
3.3.2. Acquisition System 15
3.3.2.1. Flow-Meters 16
3.3.2.1.1. Main Flow-Meter 16
3.3.2.1.2. Seeding Flow-Meter 17
3.3.3. Traverse System 17
3.4. Measurements 17
3.4.1. Hot-wire Measurements 17
3.4.1.1. Generalities on Constant Temperature Anemometry (CTA) 17
3.4.1.2. Hot-wire System 18
3.4.1.3. Probes and Thermocouple 19
3.4.1.4. Calibration 19
3.4.1.5. Constant Temperature Anemometry Experiments 20
3.4.2. Visualizations 21
3.4.2.1. Generalities 21
3.4.2.2. Tracer 22

3.4.2.3. Tracer Seeding System 22
3.4.2.3.1. $TiCl_4$ Line 23
3.4.2.3.2. Water Line 24
3.4.2.4. Psychrometric Charts 24
3.4.2.5. Visualizations System 25
3.4.2.5.1. LASER 25
3.4.2.5.2. Camera 25
3.4.2.5.3. Optics 26
3.4.2.5.4. Synchronizer 26
3.4.2.5.5. Computer 27
3.4.2.6. Experiments 27

Chapter 4: Data Reduction 29
4.1. Constant Temperature Anemometry Measurements Processing 29
4.1.1. Calibration 29
4.1.1.1. One Component Probe Calibration 29
4.1.1.2. Two Components Probe Calibration 30
4.1.2. Experiments Data Reduction 30
4.2. Flow-Meter Measurements Processing 32
4.2.1. Instantaneous Blowing Ratio Reading 33
4.2.2. Experiments Data Reduction 33
4.3. Image Processing 34
4.3.1. Averaging 34
4.3.2. Phase Averaging 34
4.3.3. Quantification 35
4.3.3.1. X-Z Visualizations Quantification : Jet Penetration 36
4.3.3.2. X-Y Visualizations Quantification: Jet Coverage 36

Chapter 5: Results and Discussion 39
5.1. System Characterization 39
5.1.1. Wind Tunnel Characterization 39
5.1.1.1. Boundary Layer 40
5.1.2. Jet Characterization 43
5.1.2.1. Measurements without Cross-Flow 43
5.1.2.2. Measurements with Cross-Flow 45
5.2. Steady State Results 47
5.2.1. Visualizations and Constant Temperature Anemometry 48
5.2.1.1. Protocols and Actual Conditions 48
5.2.1.1.1. Visualizations 48
5.2.1.1.2. Hot-wire Measurements 49
5.2.1.2. Results 50
5.2.2. Image Quantification 71
5.2.2.1. X-Z Visualizations 71
5.2.2.2. X-Y Visualizations 73
5.3. Pulsed Cases Results 78
5.3.1. Visualizations and Constant Temperature Anemometry 79
5.3.1.1. Protocols and Actual Conditions 79
5.3.1.1.1. Visualizations 79
5.3.1.1.2. Hot-wire Measurements 82
5.3.1.2. Results 82
5.3.2. X-Z Visualizations 96

5.3.3. X-Y Visualizations 97

Chapter 6: Conclusion 109

References 111

Appendix: Pulsed Cases Visualizations and CTA Measurements 113

Vita 149

List of Tables

Table 3-1: Duty cycle values to set to obtain nominal conditions. 15

Table 5-1: Boundary layer characteristics[†]. 41

Table 5-2: Verification of boundary layer characteristics - Metrics at X/D_j = -4.75 and X/D_j = 0..... 43

Table 5-3: Blowing ratio actual values during a) X-Z visualizations, b) X-Y visualizations. 48

Table 5-4: Flow conditions for velocity profiles..... 49

Table 5-5: Flow and jet conditions during localized hot-wire measurements. 50

Table 5-6: Characteristics of the ten cases studied during the pulsed jet survey. 79

Table 5-7: Jet actual conditions during forced jet visualizations at BR_m=0.250..... 80

Table 5-8: Jet actual conditions during forced jet visualizations at BR_m=0.350..... 81

Table 5-9: Harmonics found in both type of analysis for a given frequency x. 83

Table 5-10: Wavelet analysis of upper shear layer velocity records and found frequencies. 94

List of Figures

Figure 1-1: Increase in operational temperature of turbine components. After Schulz et al, Aero. Sci. Techn.7:2003, p73-80. 2

Figure 1-2: Advance of materials and cooling technology (Royal aeronautical Society/Aerospace 1994).. 2

Figure 1-3: Internal coolant passage and film cooling arrays on a turbine blade (Nirmalan & Hylton, 1990) 3

Figure 1-4: Typical structures found in jets in cross-flow configurations (from Fric & Roshko, 1994). 4

Figure 2-1: Example of a typical flow-meter record and definition of the principal parameters..... 10

Figure 3-1: Wind tunnel schematic. 11

Figure 3-2: Coordinates system, jet and section principal parameters..... 12

Figure 3-3: Air supply schematic. 12

Figure 3-4: Control valves setup. 13

Figure 3-5: Valve control system 14

Figure 3-6: Constant Temperature Anemometry system. 20

Figure 3-7: Setup in constant temperature anemometry configuration. 21

Figure 3-8: Tracer seeding system principle. 23

Figure 3-9: Psychrometric charts of (a) $TiCl_4$ (b) H_2O in N^2 at 10 psig. 25

Figure 3-10: Visualization System detail. 26

Figure 3-11: Setup in visualizations configuration (top-view). 27

Figure 4-1: Matlab interface developed for single wire calibration purposes..... 29

Figure 4-2: Matlab interface developed for cross-wire calibration purposes..... 30

Figure 4-3: Comparison between a) wavelet analysis and b) Fourier spectrum analysis in pulsed conditions. 31

Figure 4-4: Comparison between a) wavelet analysis and b) Fourier spectrum analysis in intermittent conditions. 32

Figure 4-5: Flow-meters instantaneous reading virtual instrument. 32

Figure 4-6: Matlab interface developed for flow-meters time records conversion in a) Steady state experiments, b) Forced case experiments. 33

Figure 4-7: Calibration targets used in visualizations experiments for a) Side-view visualizations, b) Top-view visualizations. 35

Figure 5-1: Wind tunnel velocity calibration as a function of the controller frequency†. 39

Figure 5-2: Free stream power spectrum at $X/D_j=0$ for $U=1.6m.s^{-1\dagger}$. 40

Figure 5-3: Power spectrum of the boundary layer with a free stream velocity $U_\infty = 1.6m.s^{-1}$ and at four different heights of (Z/D_j=0.067, 0467, 1.067, 11.067) †. 41

Figure 5-4: Boundary layer profiles at a) $X/D_j = 0$, b) $Y/D_j = 0^{\dagger}$ 42

Figure 5-5: Verification of boundary layer characteristics – Velocity profiles at $X/D_j = -4.75$ and $X/D_j = 0$. 43

Figure 5-6 : Power spectrum from hot-wire measurements performed at the jet exit for different values of $W_j^{\dagger}$ 44

Figure 5-7: Mean velocity and RMS velocity profiles at $W_{max}/U_\infty \approx 0.5$ (a, b); $W_{max}/U_\infty \approx 1.0$ (c,d); $W_{max}/U_\infty \approx 1.5$ (e,f) without cross flow scaled with $W_{max}^{\dagger}$ 44

Figure 5-8: Vertical (w_j) and stream-wise (u_j) velocity profiles at the jet exit for different values of W_{max} with cross-flow at $U_\infty=1.6m.s^{-1\dagger}$. 46

Figure 5-9: RMS velocities (a), Skewness (b) and Kurtosis (c) of the unforced JICF†. 47

Figure 5-10: Steady State Visualizations at BR=0.150. a) (1-6) X-Z visualizations. b) (1'-6') X-Y visualizations. c) Averaged X-Z image. d) Colorized Normalized Averaged X-Z image. e) Averaged X-Y image. d) Colorized Normalized Averaged X-Y image. 51

Figure 5-11: Wavelet Analysis for hot-wire measurements at BR=0.150 for a) $X/D_j=0, Z/D_j=0$, b) $X/D_j=3.5$, $Z/D_j=0.75$ 52

Figure 5-12: Steady State Visualizations at BR=0.188. a) (1-6) X-Z visualizations. b) (1'-6') X-Y visualizations. c) Averaged X-Z image. d) Colorized Normalized Averaged X-Z image. e) Averaged X-Y image. d) Colorized Normalized Averaged X-Y image. 53

Figure 5-13: Wavelet Analysis for hot-wire measurements at BR=0.188 for a) X/Dj=0,Z/Dj=0, b) X/Dj=3.5, Z/Dj=0.75 53

Figure 5-14: Stream wise a) Velocity profile, b) Rms velocity profile, at X/Dj=3.5, for BR=0.150 and BR=0.188. 54

Figure 5-15: Steady State Visualizations at BR=0.600. a) (1-8) X-Z visualizations. b) (1'-8') X-Y visualizations. c) Averaged X-Z image. d) Colorized Normalized Averaged X-Z image. e) Averaged X-Y image. d) Colorized Normalized Averaged X-Y image. 56

Figure 5-16: Wavelet Analysis for hot-wire measurements at BR=0.600 for a) X/Dj=0,Z/Dj=0, b) X/Dj=0,Z/Dj=0.5, c) X/Dj=3.5, Z/Dj=2.0 57

Figure 5-17: Steady State Visualizations at BR=0.250. a) (1-8) X-Z visualizations. b) (1'-8') X-Y visualizations. c) Averaged X-Z image. d) Colorized Normalized Averaged X-Z image. e) Averaged X-Y image. d) Colorized Normalized Averaged X-Y image.....58

Figure 5-18: Wavelet Analysis for hot-wire measurements at BR=0.250 for a) $X/D_j=0,Z/D_j=0$, b) $X/D_j=0,Z/D_j=0.25$, c) $X/D_j=3.5$, $Z/D_j=1.25$.....59

Figure 5-19: Stream wise a) Velocity profile, b) Rms velocity profile, at X/Dj=3.5, for BR=0.250. 60

Figure 5-20: Steady State Visualizations at BR=0.300. a) (1-8) X-Z visualizations. b) (1'-8') X-Y visualizations. c) Averaged X-Z image. d) Colorized Normalized Averaged X-Z image. e) Averaged X-Y image. d) Colorized Normalized Averaged X-Y image.....61

Figure 5-21: Wavelet Analysis for hot-wire measurements at BR=0.300 for a) $X/D_j=0,Z/D_j=0$, b) $X/D_j=0,Z/D_j=0.25$, c) $X/D_j=3.5$, $Z/D_j=1.5$.....63

Figure 5-22: Steady State Visualizations at BR=0.365. a) (1-8) X-Z visualizations. b) (1'-8') X-Y visualizations. c) Averaged X-Z image. d) Colorized Normalized Averaged X-Z image. e) Averaged X-Y image. d) Colorized Normalized Averaged X-Y image.....64

Figure 5-23: Example of a horse-shoe vortex riding the flattened interface of the jet after the ring-like vortex shedding.....65

Figure 5-24:Wavelet Analysis for hot-wire measurements at BR=0.365 for a) $X/D_j=0,Z/D_j=0$, b) $X/D_j=0,Z/D_j=0.25$, c) $X/D_j=3.5$, $Z/D_j=1.5$.....65

Figure 5-25: Steady State Visualizations at BR=0.465. a) (1-8) X-Z visualizations. b) (1'-8') X-Y visualizations. c) Averaged X-Z image. d) Colorized Normalized Averaged X-Z image. e) Averaged X-Y image. d) Colorized Normalized Averaged X-Y image.....67

Figure 5-26: Wavelet Analysis for hot-wire measurements at BR=0.465 for a) X/Dj=0,Z/Dj=0, b) X/Dj=0,Z/Dj=0.25, c) X/Dj=3.5, Z/Dj=1.5 68

Figure 5-27: Stream wise a) Velocity profile, b) RMS velocity profile, at X/Dj=3.5, for BR=0.465. 68

Figure 5-28: Fundamental frequencies from wavelet analysis scaled using: a) the Strouhal number based on the cross-flow velocity, b) the Strouhal number based on the jet mean velocity, plotted as a function of the blowing ratio. 70

Figure 5-29: Recirculation region vorticity shedding at a) BR=0.300, b) BR=0.365, c) BR=0.465 70

Figure 5-30: Possible dynamics of the ring-like vortices/recirculation region vorticity shedding. 71

Figure 5-31: Imagined dynamics of the core of the ring-like vortex. 71

Figure 5-32: Jet penetration estimation for BR=0.150 to BR=0.600. 72

Figure 5-33: Jet upper limit extracted from the penetration at given streamwise locations for BR=0.150 to BR=0.600. 73

Figure 5-34: Coverage Coefficient (C_c) as a function of the blowing ratio (BR). Computation with and without horse-shoe vortex coverage. 74

Figure 5-35: Jet footprint computed as the 0.5 contour of the Normalized Intensity matrix. 75

Figure 5-36: Normalized intensity contour plots extracted from the averaged images showing the two boundaries used for span-wise average. 76

Figure 5-37: Span-wise averaged normalized intensity for a) $-2.5 < Y/D_j < 2.5$, b) $-0.9 < Y/D_j < 0.9$, as a function of X/D_j. 77

Figure 5-38: a) Normalized intensity on the jet centerline, b) Jet breakup location. 78

Figure 5-39: Ideal square waves decomposed in the frequency domain using wavelet analysis. 83

Figure 5-40: Flow-meter records decomposed in the frequency domain using wavelet analysis. 84

Figure 5-41: Value of the overshoot (BR_{os}) as a function of BR_h and relative value of BR_{os} with respect to BR_h as a function of BR_{pp}. 86

Figure 5-42: Pulsed cases Visualizations at BR_m=0.250, BR_{pp}=0.250, DC=0.25, f_f=0.5Hz - a) (1-10) X-Z visualizations. b) (1'-10') X-Y visualizations. c) Phase averaged flow-meter record. d)-f) Wavelet analysis of the hot-wire records at d) X/D_j=0, Z/D_j=0, e) X/D_j=0, Z/D_j=0.5, f) X/D_j=3.5, Z/D_j=1.25 - Case#3. 87

Figure 5-43: Pulsed cases Visualizations at BR_m=0.250, BR_{pp}=0.250, DC=0.25, f_f=1.0Hz - a) (1-10) X-Z visualizations. b) (1'-10') X-Y visualizations. c) Phase averaged flow-meter record. d)-f) Wavelet analysis of the hot-wire records at d) X/D_j=0, Z/D_j=0, e) X/D_j=0, Z/D_j=0.5, f) X/D_j=3.5, Z/D_j=1.25 - Case#3. 88

Figure 5-44: Pulsed cases Visualizations at BR_m=0.250, BR_{pp}=0.250, DC=0.25, f_f=5Hz - a) (1-49) X-Z visualizations. b) (1'-49') X-Y visualizations. c) Phase averaged flow-meter record. d)-f) Wavelet analysis of the hot-wire records at d) X/D_j=0, Z/D_j=0, e) X/D_j=0, Z/D_j=0.5, f) X/D_j=3.5, Z/D_j=1.25 - Case#3. 89

Figure 5-45: Pulsed cases Visualizations at BR_m=0.250, BR_{pp}=0.250, DC=0.25, f_f=10Hz - a) (1-49) X-Z visualizations. b) (1'-49') X-Y visualizations. c) Phase averaged flow-meter record. d)-f) Wavelet analysis of the hot-wire records at d) X/D_j=0, Z/D_j=0, e) X/D_j=0, Z/D_j=0.5, f) X/D_j=3.5, Z/D_j=1.25 – Case#3. 90

Figure 5-46: Potential mechanism of horse-shoe vortex transport associated with starting vortex/ring-like vortex 92

Figure 5-47: Velocity record at DC=50%, f_f=5.0Hz (Case#4) for a) X/D_j=0, Z/D_j=0, b) X/D_j=3.5, Z/D_j=1.25. 95

Figure 5-48: Velocity record at DC=70%, f_f=10Hz (Case#5) for a) X/D_j=0, Z/D_j=0, b) X/D_j=3.5, Z/D_j=1.25. 95

Figure 5-49: Jet penetration estimation for pulsed jet cases#1 to 10. 96

Figure 5-50: Coverage coefficient as a function of f_f and jet footprint for Case#1 to 10. 98

Figure 5-51: Coverage coefficient comparison at BR_m=0.250, BR_{pp}=0.250 for several duty cycles. 99

Figure 5-52: Coverage coefficient comparison at BR_m=0.250, BR_h=0.325 for several duty cycles and BR_{pp} 100

Figure 5-53: Coverage coefficient comparison at BR_m=0.250, BR_l=0.188 for several duty cycles and BR_{pp}..... 101

Figure 5-54: Coverage coefficient comparison at BR_m=0.350, BR_{pp}=0.250 for several duty cycles. 102

Figure 5-55: Coverage coefficient comparison at BR_m=0.350, BR_h=0.425 for several duty cycles and BR_{pp}..... 103

Figure 5-56: Coverage coefficient comparison at BR_l=0.188, DC=50% for several BR_m. 103

Figure 5-57: Coverage coefficient comparison at BR_m=0.250, DC=50% for several BR_{pp}. 104

Figure 5-58: Coverage coefficient comparison at BR_m=0.350, DC=50% for several BR_{pp}. 104

Figure 5-59: Span-wise averaged normalized intensity ($<I^N>_{spanwise}$) for $-2.5 \leq Y/D_j \leq 2.5$ and $-0.9 \leq Y/D_j \leq 0.9$. 105

List of Equations

Equation 2-1: Blowing ratio (BR) definition. 9

Equation 2-2: Relationships between BR_m, BR_l, BR_h, BR_{pp} and DC. 9

Equation 3-1: Hot-wire relationship between flow velocity and heat transfer. 18

Equation 3-2: TiCl4 reaction equations 22

Equation 3-3: $TiCl_4$ Saturation pressure law. 24

Equation 3-4: Water saturation pressure law. 24

Equation 3-5: Specific humidity ratio as a function of the nitrogen pressure and the saturation pressure. 24

Equation 4-1: Intensity normalization equation for side-view visualizations. 36

Equation 4-2: Intensity normalization equation for top-view visualizations. 36

Equation 4-3: Adiabatic efficiency definition 37

Equation 4-4: Equivalence between temperature of the wall in adiabatic experiments and tracer intensity 37

Abstract

The potential of pulsed vertical jet in cross-flow for film cooling purposes was experimentally studied and is discussed in this Thesis. A single vertical jet placed in laminar cross-flow conditions was first characterized in steady state at relatively low blowing ratios ranging from 0.150 to 0.600, using Mie scattering visualization methods and hot-wire measurements. Wavelet spectral analysis and image quantification algorithms were applied to the velocity records and averaged visualizations to obtain quantitative data on the jet characteristic frequencies, penetration and coverage. Two different regimes characterized by different structures are identified and adapted scaling variables are provided. Trends in the jet penetration and jet coverage support the transition from one regime to another.

The pulsed jet study is carried at duty cycles of 0.25, 0.50 and 0.70 and forcing frequencies of 0.5, 1.0, 5.0 and 10Hz for a total of 40 studied cases. Similar measurements and processing were applied to the forced experiments data. The presence of a starting vortex is observed in each case and an attempt to explain the dynamics of this structure is provided. The image quantification shows an overall decrease in the performance of the pulsed jet when compared to legitimate steady state cases, even though few cases exhibit a relative improvement.

Chapter 1: Introduction

1.1. Background

Jets in cross-flow (JICF), also known as transverse jets, are simple flow configurations and can be encountered in many different situations. It describes the fluidics associated with a flow exiting from a nozzle in a flowing environment. However, to the simplicity of the configuration, one may oppose the complexity of the three dimensional structures involved and their sensibility to the configuration and/or cross-flow parameters.

From the fumes of a volcano down to the micro scale features used in electronics cooling, a multitude of applications and justifications can be found to JICF studies. One of the principal domains of application concerns dispersion of pollutant emitted from a chimney. This subject is more than ever relevant because of the growing restrictions on air pollution and reinforced emissions regulations. In numerous studies chimney geometry such as exit shape, nozzle contraction, height, and even surrounding structures such as the building supporting the chimney itself are shown to have a consequent influence on the structures observed and the dispersion performance.

Another relevant application also linked to environmental concerns is fuel injection in combustion engines. Indeed, the mixing quality between fuel and air directly influences the quality of the combustion, the performance of the engine, and the composition of the exhaust gases. Jets in cross-flow are also found in the turbine of jet engines or gas turbine engines and are used for cooling purposes.

1.2. Film Cooling

Blade cooling is a major element in actual combustion engines equipped with turbine. Indeed, first stage blades and first stage vanes of turbine engines are exposed to high temperatures (generally above 1200K) required for high efficiency and performance, and constitute one of the main limitation factors for increased combustion temperature. An overshoot of more than 25°C in the operation temperature could reduce the life of a blade of about 50%. Material sciences have already allowed a net increase in combustion temperature and blade durability with the implementation of coated mono-crystal

blades made of Nickel Aluminum alloys, but cooling methods are still required to push even further the material limits.

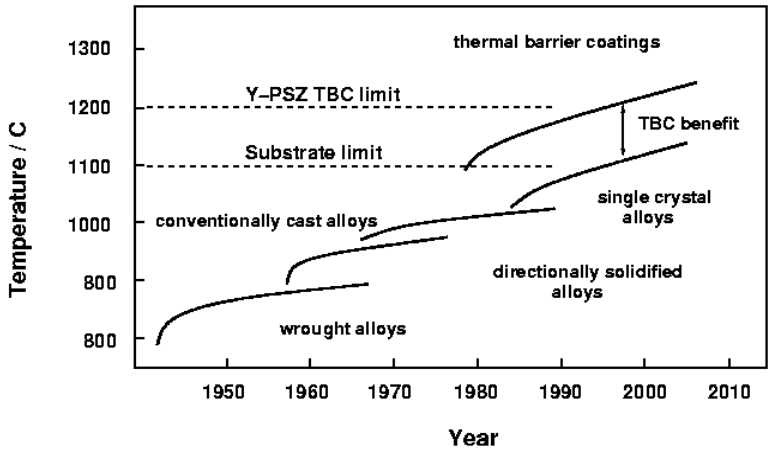

Figure 1-1: Increase in operational temperature of turbine components. After Schulz et al, Aero. Sci. Techn.7:2003, p73-80.

Internal cooling is one solution to temperature management issues. Air extracted from the compressor of the engine is circulating through a series of serpentines inside the blade to lower the overall temperature. Finally, external cooling, or film cooling constitutes the last feature of modern turbine blades in order to protect them from the hot gases environment. For this last method, part of the relatively cooler air used for internal cooling is bled through arrays of jets at the surface of the turbine blade, protecting it from the hot gases issued from the combustion chamber.

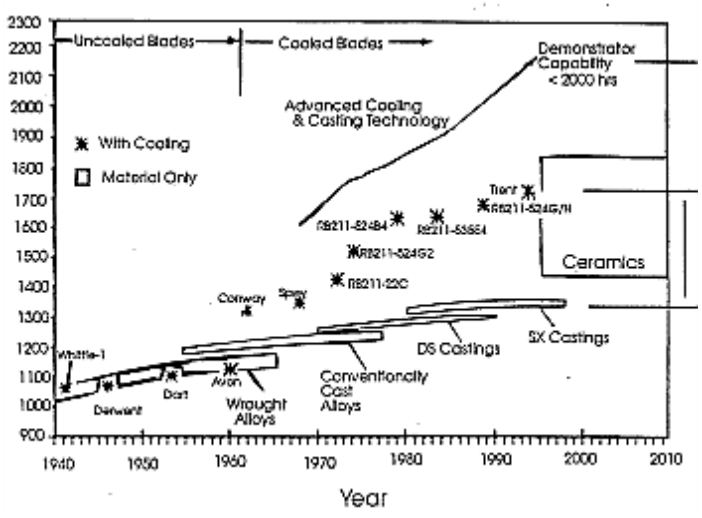

Figure 1-2: Advance of materials and cooling technology (Royal aeronautical Society/Aerospace 1994)

The efficiency of such system is judged on its ability to isolate the blade from the hot gases, and to limit heat exchange between the blade and the free stream. The consequential objectives are to increase the coverage of the jets, while decreasing their mixing behavior, two properties directly depending on the physics of Jets in Cross Flow.

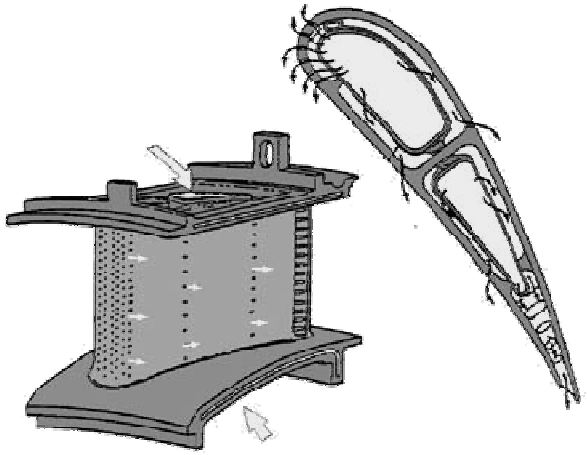

Figure 1-3: Internal coolant passage and film cooling arrays on a turbine blade (Nirmalan & Hylton, 1990)

However, the amount of coolant drawn from the high pressure compressor is a major drawback to fluid cooling techniques. It is estimated that $1/5^{th}$ to $1/3^{rd}$ of the flow from the HP compressor is used for cooling purposes, representing a proportional loss in thrust. Moreover, actual film cooling performance allows a certain turbine inlet temperature (combustion temperature) which it is important to increase in order to obtain higher efficiency. A more efficient film cooling system could allow a decreased need in coolant resulting in better efficiency and/or lower turbine inlet temperature for reduced NO_x emissions. Such a system could also lead to an increased turbine inlet temperature and thus a higher Overall Pressure Ratio. For that matter, it is important to explore more complex, and intelligent systems using actively controlled film cooling techniques.

1.3. Literature Survey

Transverse Jets structures are complex but well studied. Among these, the Counter-Rotating Vortex Pair (CRVP), identified by Kamotani & Greber in 1972 is held responsible for dramatic mixing enhancement. It is now commonly admitted that the formation of the CRVP is due to a folding of the

cylindrical shear layer, entrained by the cross flow (Karagozian 2001; New 2003). Other typical structures include horse-shoe vortex located on the windward side of the jet, shear layer vortices at the interface between jet and cross-flow, and wake vortices underneath the detached jet (Figure 1-4). Several other studies (Gopalan 2004; Lele 2006) have identified two regimes of steady jets in cross flow depending on the blowing ratio. The first one is characterized by the existence of a separation bubble directly downstream of the jet, the second is a fully detached regime with the apparition of Von Karman street vortices in the jet wake, reinforcing the CRVP strength and entraining cross flow beneath the jet. In the case of film cooling, both effects need to be limited in order to achieve higher efficiency and lower heat transfer (Figure 1-4).

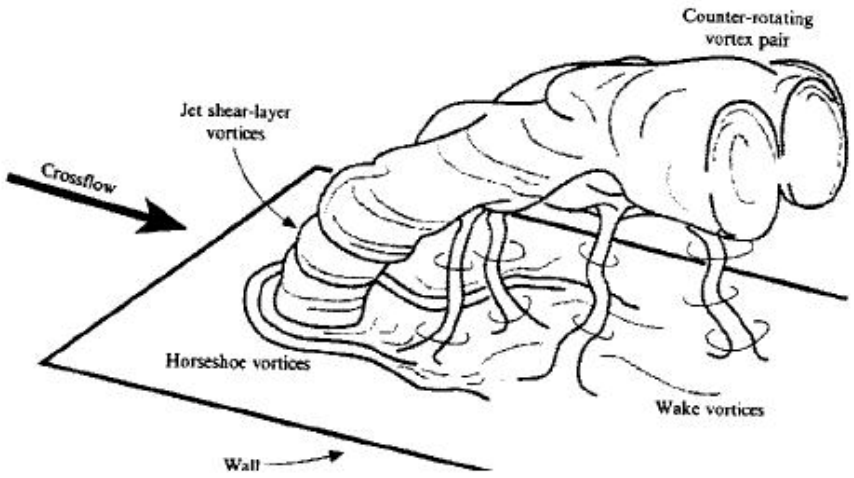

Figure 1-4: Typical structures found in jets in cross-flow configurations (from Fric & Roshko, 1994).

Passive film cooling improvements studies have been numerous, especially concerning the geometry of the jet exit. The effect of compound angle, hole geometry, shaping, tabs and aspect ratio have been extensively studied (Ekkad 2001). These geometry modifications are actually directly impacting the jet exit conditions.

Actively controlled film cooling systems could bring new perspective on the problems of steady jets by introducing beneficial dynamic structures while decreasing the coolant mass-flow necessary to obtain good performance. Moreover, they could be instantaneously adapted to be efficient at any regime of a jet engine. Recent studies have already shown the potential of pulsed jets in different domains.

Enhanced mixing has been achieved by using pulsing frequencies interacting with the natural shedding modes of the jet shear layer (Johari 1999; M'Closkey 2002), increasing the mixing rate up to twice the one of steady jets. Such enhancement is believed to come from the interactions of structures generated during the pulsing with the jet structures (CRVP) thus increasing the unsteadiness of the jet (Narayanan 2003). These studies have emphasized the importance of pulsing variables such as duty cycle, amplitude, waveform and frequency. Even though mixing enhancement purposes are completely opposed to film-cooling ones, these studies have revealed the possible alteration of the natural structures of JICF with pulsed generated vortices.

Pulsed jets have also been successfully used in several studies to reattach separated boundary layers in low Reynolds flow (Bons 2001; Bons 2002). Significant results have been obtained regarding separation of the boundary layer using 30 degree inclined jets with a 90 degree compound angle to the main flow, called Vortex Generator Jets (VGJ). Indeed, steady VGJ located upstream of the natural separation region were found to almost completely eliminate this separation and decrease integrated wake loss coefficient by 60%. However, pulsed VGJ have been able to match these results while decreasing by an order of magnitude the mass-flow needed, and even decreasing the wake loss coefficient of 40% regarding to the steady VGJ. It is believed that, regarding of where these pulsed VGJ are located; their effect is either to reenergize the boundary layer by injecting high momentum crossflow or to trigger an early transition of the boundary layer. These studies state that even very small duty cycles are efficient and attribute the improvement mechanisms to the starting vortices and their wake generated as the jet "kicks on" and "off", not to the actual high and low parts of the cycle. Moreover, it was shown that the effect of pulsed VGJ was not detrimental to higher Reynolds flows observed at other regimes of the engine.

It is not until recently that the effects of actively controlled jets in cross flow applied to film-cooling started to be addressed. In their study, Ekkad et al. (Ekkad 2006) used a single 20 deg. inclined jet with a 90 deg. compound angle, located at the leading edge of a turbine blade at blowing ratios between 0.5 and 2.0. Using a transient infrared technique (Ekkad 2004) they focused on film efficiency and heat

transfer coefficient quantifications. Several pulsed cases have been identified to be more efficient in term of coverage with slightly lower heat transfer than the corresponding steady state cases. Indeed, the effect of pulsing was shown to be promising by decreasing the lift off and increasing the spread, especially at blowing ratios above 1.0. This study also stated that the effect of duty cycle was more important compared to the pulsing frequency, and that higher effectiveness was reached for duty cycles of 25% but decreased for duty cycles below 10% due to the lack of coolant mass-flow.

More recently, Coulthard et al. (Coulthard 2007; Coulthard 2007) conducted similar experiments with a single row of 35 deg. inclined jets with no compound angle over a flat plate, for blowing ratios between 0.25 and 1.5. Their results stated that only in few high pulsing frequencies cases, the effectiveness was improved by reducing the amount of lift off regarding to the corresponding steady state case. Lower pulsing frequencies tended to have opposite effect and decrease the overall effectiveness. Concerning the heat transfer coefficient, their findings were that the pulsing of the jet was unfavorable except for few cases at high blowing ratios and high frequencies (same cases where the effectiveness was improved). The overall best effectiveness and lower heat transfer though were achieved for a steady state case at blowing ratio of 0.5 and no pulsed case showed better results.

Attention must be paid to the fact that both studies were carried with a pulsed jet seeded by an "on/off" solenoid resulting in a "flow/no-flow" type of pulsing. However, both reported that during high duty cycle tests and/or high frequency tests, the velocity of the air in the injection chamber and at the exit of the jet did not have time to reach a zero value before the next pulse. Moreover, in Coulthard et al. study the only cases where improvements were noticed were the one with this type of residual velocity. Finally, none of these two studies were able to accurately monitor the actual blowing ratio during experiments and only relied on estimated flow-rates based on single point hot-wire measurements at the jet exit.

Even though recent studies have started to address the potential of forced film cooling, by quantifying film effectiveness and heat transfer coefficient, the fluidics involved with pulsed jet in cross-flow are still unclear.

1.4. Motivations and Objectives

In the present Thesis, a single actively controlled jet in cross flow is studied in order to provide a clear understanding of the physics involved, using visualizations based on Mie scattering techniques, and hot wire measurements. Various duty cycles (25, 50, and 70%), frequencies (0.5, 1, 5 and 10Hz) and amplitudes (mean blowing ratios from 0.25 to 0.45) are considered to quantify their influence on the behavior of the jet. In opposition to the previous studies, the low part of the cycle is fixed at a non-zero value to explore the effect of residual velocities after the valve closing. It is believed that pulsing may decrease or completely eliminate the formation of CRVP responsible for enhanced mixing, increase the spread and coverage by introducing dynamic structures such as Starting Vortices, decrease or eliminate the lift off observed at high steady state blowing ratios, and decrease the amount of coolant needed by relying not only on the mass-flow injected in a passive way but on controlling the dynamics of the flow to fully exploit the amount of coolant ejected.

Chapter 2: Notations and Definitions

2.1. Notations

BR	Blowing Ratio
BR_m	Mean Blowing Ratio
BR_l	Low Blowing Ratio
BR_h	High Blowing Ratio
BR_{pp}	Peak to Peak Blowing Ratio
C_c	Coverage coefficient
D_j	Jet diameter
DC	Duty Cycle
$d^t_{x,y}$	Tracer density at point (x,y)
dP/dx	Pressure gradient along the wind tunnel test section
f_f	Forcing Frequency
H	Shape factor (δ^*/θ)
$I_{i,j}$	Image intensity
$I^N_{i,j}$	Normalized image intensity
$\langle I^N \rangle^{yl}_{spanwise}$	Span-wise averaged normalized intensity for $-y_l < Y/D_j < y_l$
Le	Lewis number ($Le = \alpha/D$)
$\dot{m}$	Mass flux
P^g_{sat}	Saturation pressure of gas 'g'
P^g_c	Critical pressure of gas 'g'
Pr	Prandtl number (α/ν)
q	Heat transfer
Re_x	Reynolds Number based on the distance *d* from the jet to the test section inlet and the cross-flow velocity ($U_\infty . d/\nu$)
Re_j	Reynolds Number based on jet diameter and mean jet velocity ($U_j . D_j/\nu$)
Sc	Schmidt number (ν/D)
St_j	Strouhal number based on the jet velocity ($f . D_j/U_j$)
St_∞	Strouhal number based on the cross-flow velocity ($f . D_j/U_\infty$)
T_c	Critical temperature
T	Temperature
TI	Turbulence Intensity ($std(U)/\bar{U}$)
u	Stream-wise velocity
U	Mean velocity
W	Vertical velocity
W_{max}	Jet maximum velocity
α	Fluid thermal diffusivity
ν	Fluid kinematic viscosity
D	Mass diffusivity
ρ	Fluid density
δ	Boundary layer thickness at 99%
δ^*	Displacement thickness ($1/U_\infty \int_0^\infty (U_\infty - U)\, dz$)
θ	Momentum thickness ($1/{U_\infty}^2 \int_0^\infty (U_\infty - U).U\, dz$)
Θ	Injection angle
ω	Specific humidity
Φ	Relative humidity
$\eta_{x,y}$	Adiabatic effectiveness at point (x,y)

Subscripts:

j	Jet
∞	Cross-flow
rms	Root mean square
Sk	Skewness
Ku	Kurtosis
exp	Actual experimental value
mean	Mean value

2.2. Definitions

2.2.1. Blowing Ratio (BR)

The blowing ratio is defined as the jet to cross-flow mass flow-rate ratio (Equation 2-1). In this study since it is a cold flow study, and since both gases used for the jet and the cross-flow are air, the density ratio is close to unity, which means that the blowing ratio is also equal to the mean velocities ratio.

$$BR = \frac{\rho_j U_j}{\rho_\infty U_\infty}$$

Equation 2-1: Blowing ratio (BR) definition.

For steady state experiments, only one blowing ratio parameter is needed. However, for pulsed jet experiments, several parameters are required to completely describe the jet cycle. The low flow of the cycle is characterized by the low blowing ratio BR_l, the high part of the cycle is described by the high blowing ratio BR_h, the difference between the these two values is the peak to peak blowing ratio BR_{pp} and the time averaged value of the blowing ratio over a cycle is the mean blowing ratio BR_m. Two equations relate these parameters together (Equation 2-2). From the five parameters BR_m, BR_l, BR_h, BR_{pp}, DC, only three can be independently fixed since we have five parameters, two equations implying three degrees of freedom. For the present study, blowing ratios between 0.150 and 0.600 were considered for the steady state experiments, and mean blowing ratios of 0.250 to 0.450 were used in forced flow experiments but only mean blowing ratios of 0.250 and 0.350 will be discussed in this document.

$$BR_{pp} = BR_h - BR_l$$

$$BR_m = DC \cdot BR_h + (1 - DC) \cdot BR_l$$

Equation 2-2: Relationships between BR_m, BR_l, BR_h, BR_{pp} and DC.

2.2.2. Forcing Frequency (f_f)

During pulsed flow experiments, one of the main parameters is the forcing frequency which is the frequency used to define the pulsing signal. According to the scaling of the experiment, forcing frequencies of 0.5, 1, 5, and 10Hz were considered for this study.

2.2.3. Duty Cycle (DC)

Since the signal used to force the flow is a square wave, it requires a last parameter to completely characterize it. This parameter is the duty cycle DC and is defined as the amount of time the square signal is at the maximum value over the cycle period. Three different values of DC are encountered in this study: DC=0.25, 0.50 and 0.70.

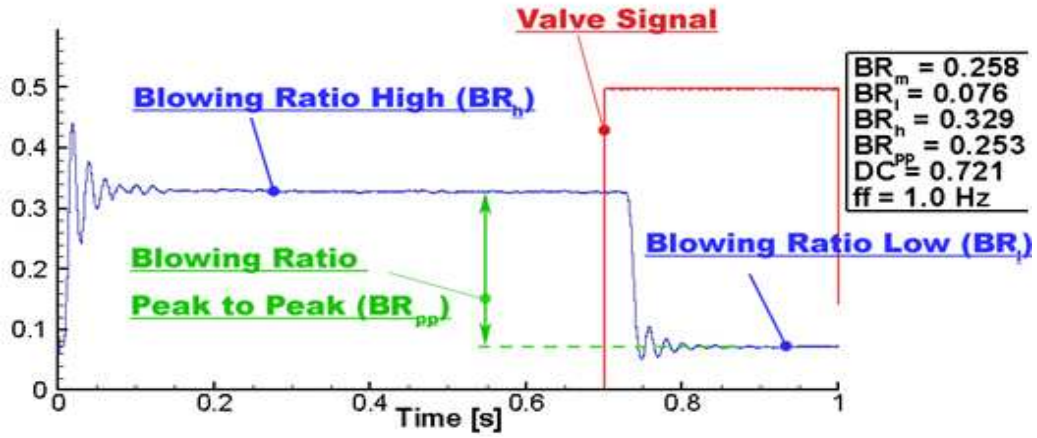

Figure 2-1: Example of a typical flow-meter record and definition of the principal parameters.

Chapter 3: Experimental Apparatus

3.1. Wind Tunnel

The experiments took place in the test section of the aerodynamic wind tunnel of Louisiana State University which schematic is presented in Figure 3-1. This open loop wind tunnel has a 10ft long test section with an inlet cross-section of 3x2 feet. The side walls of the test section are angled at 1.45 degrees with respect to the centerline in order to keep a zero pressure gradient. One of them is made of acrylic, in order to allow visualizations in the test section during experiments. A set of five conditioning screens, followed by a contraction with an area ratio of 20 is located directly upstream of the test section to provide stable inlet conditions during the experiments. The flow in the wind tunnel is powered by a fan with adjustable pitch from New Philadelphia Fan Company (Model# 45-17-1176), with 9 stator blades and 12 rotor blades, capable of 1200 rpm, allowing a range of velocities going from 0 to 30m.s^{-1} in the test section. Finally, a set of 2 removable roofs were used during the experiments. The first one is made of wood and comports small openings to perform hot-wire measurements without compromising the flow in the test section. The second roof is similar to the acrylic side wall and allows visualizations during experiments.

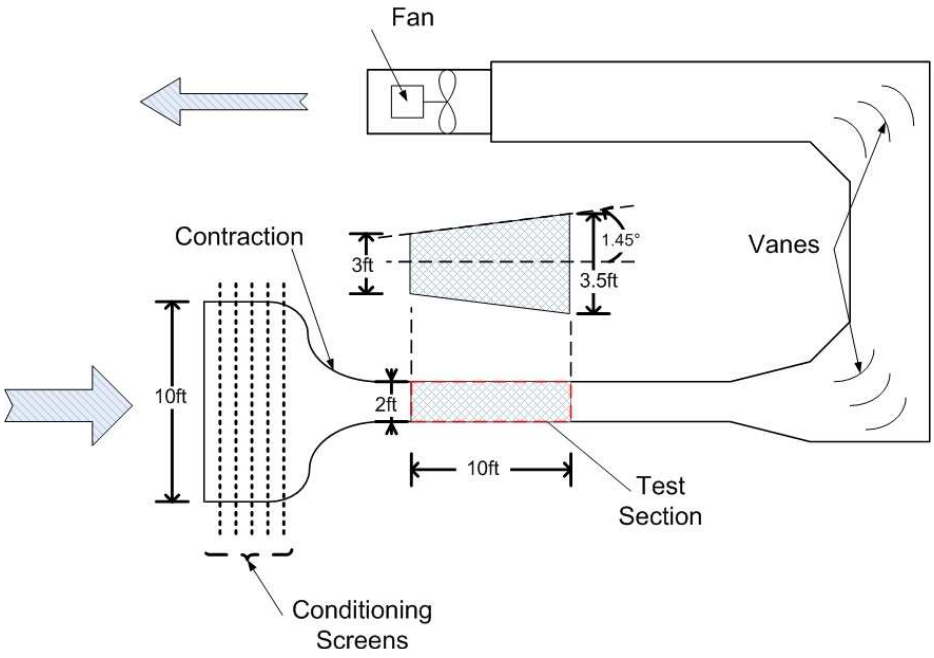

Figure 3-1: Wind tunnel schematic.

3.2. Jet

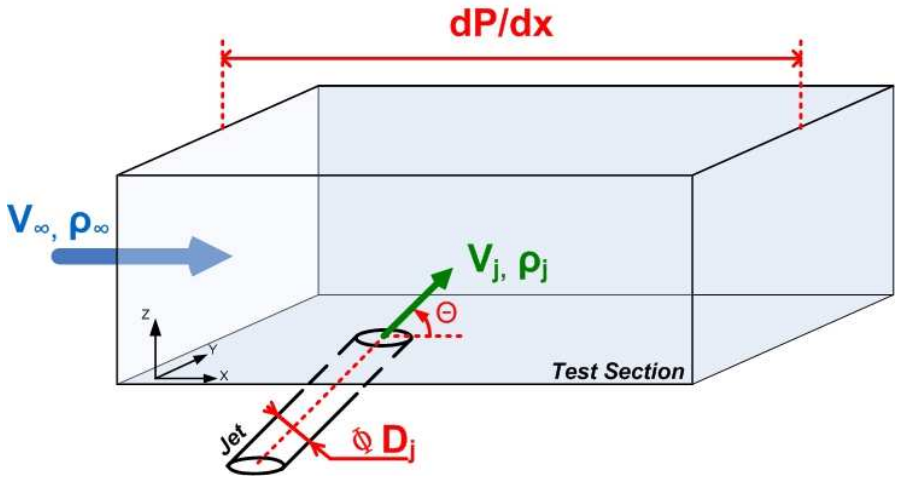

Figure 3-2: Coordinates system, jet and section principal parameters

3.2.1. Jet Geometry

The jet used during the experiments exits from a 1inch round exit located 30in. downstream of the test section and is mounted flush to the bottom wall as presented in Figure 3-2.

3.2.2. Jet Feeding

3.2.2.1. Air Supply

The air supply for the jet is provided by an industrial compressor (Atlas Copco Model GR110) with an exit pressure of 180 psig. The compressed air is dried using an inline desiccant dryer connected a high capacity reservoir feeding the experiment. For the experiment, the air from the reservoir is regulated at 20 psig using an inline bleeding regulator. The air supply system is represented in Figure 3-3.

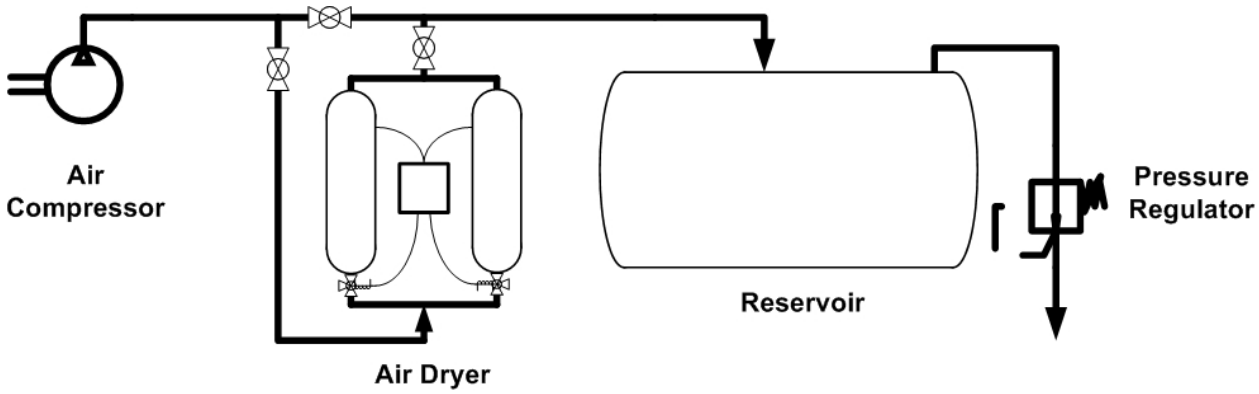

Figure 3-3: Air supply schematic.

3.2.2.2. Control Valves

The regulated air is connected via a flexible air hose to a set of three valves in order to perform pulsed experiments at variable blowing ratios (Figure 3-4). The setup is composed of two branches, one principal and one bypass, each comporting a metering valve to control the flow in the branch. The bypass also comports a solenoid valve controlled by a computer and used to pulse the flow during forced flow experiments. The main branch is used to set a desired low blowing ratio (solenoid closed), while the bypass is used to set the high blowing ratio by adding air to the main branch (solenoid open). A flow-meter, preceded by an inline filter is connected to the valve setup in order to control the experiment settings and obtain time-resolved records of the blowing ratio during experiments.

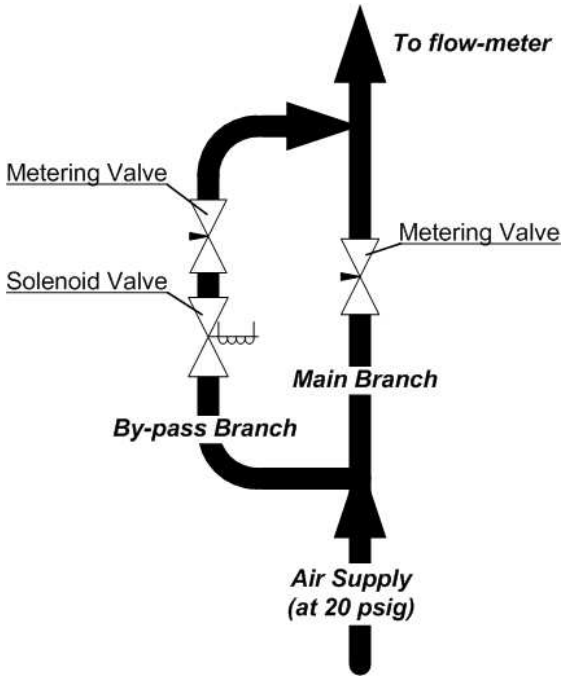

Figure 3-4: Control valves setup.

3.2.2.3. Connection

Downstream of the flow-meter, the jet is finally fed by a 12in. long and 1in. diameter stainless steel pipe attached to the bottom wall of the test section via an acrylic bloc. This acrylic bloc is supported by an external frame located underneath the wind tunnel and is inserted in the bottom wall of the test section by a 5in round opening.

3.2.2.4. Reagent Injection

In order to seed the jet with a tracer for visualizations, two reagents must be injected in the jet at different levels, but far enough from the jet exit so that the reaction can have time to take place. The first reagent to be injected is water and is supplied via a T located between the flow-meter and the 12in. stainless steel pipe. The second reagent is Titanium Tetrachloride ($TiCl_4$) and is injected in the jet by 8 holes of 1/8in. diameter located on the stainless steel pipe and supplied by a radial injection chamber placed around the tube.

3.3. Control and Acquisition

3.3.1. Forcing System

In order to pulse the jet during forced flow experiments, a three elements system is required. The first element is the previously introduced solenoid valve located on the bypass branch, allowing the jet to pass from low to high blowing ratio by being opened or closed. This valve is supplied a 17V power supply relayed at 12V. The second element is a data acquisition chassis from National Instrument (Model SC2345) loaded with the following modules:

- SCCRLY01: Relay used to control the power signal sent to the valve (valve closed at rest, open when supplied by the 12V signal).
- SCCDO01: Digital output module used to send a 0-5V copy of the valve signal to the acquisition system (detailed in the next section) and a trigger signal for visualizations in forced experiments.

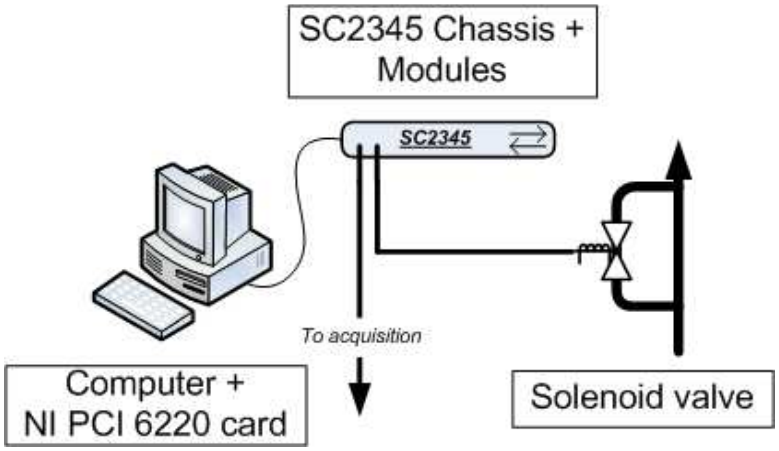

Figure 3-5: Valve control system

Finally, the third element is a computer used to control the SC2345 chassis via a data acquisition PCI card (National instrument, Model NI PCI 6220). Using National Instrument Labview Virtual Instruments, the signal sent to the solenoid is changed in order to adjust pulsing frequency and duty cycle. Even though the response time and accuracy of the modules and the PCI card are satisfying, the solenoid valve suffers of a lag time at frequencies higher than 1Hz, changing the effective value of the duty cycle at these frequencies. To prevent the results to be biased by this problem, a lower value of duty cycle has to be set instead of the actual value. These values were obtained by calibration and are summarized in Table 3-1.

Table 3-1: Duty cycle values to set to obtain nominal conditions.

	DC to set (%)			
Desired DC (%)	**f_f=0.5Hz**	**f_f=1Hz**	**f_f=5Hz**	**f_f=10Hz**
25	25	25	15	5
50	50	50	40	30
70	70	70	60	55

3.3.2. Acquisition System

To control the experiment and perform different types of measurements, several signals are acquired:

- Control/acquisition of the jet flow parameters:
    - Main flow-meter
    - Seeding flow-meter
- Control/acquisition of the pulsing parameters:
    - Solenoid valve signal
- Constant Temperature Anemometry:
    - CTA channel 1
    - CTA channel 2
    - CTA temperature probe

- Visualizations
    - Images from camera

All these signals, with exception of the camera images, are acquired using a single system composed of two elements. The first element is a SC2345 chassis from National instrument equipped with three identical acquisition modules SCCAI03. These modules are analog voltage input modules with a range of acquisition of +/- 10V, which is the reason why the SCCDO01 module had to be used in the previous chassis, in order to send a lower voltage copy of the 12V valve signal. Each module has two analog inputs allowing a total of 6 channels of acquisition. The second element of the system is a computer equipped with a National Instrument PCI acquisition card (Model PCI-MIO-16E-4) connected to the SC2345 chassis and capable of recording the 6 channels signals using a National Instrument Labview Virtual Instrument.

3.3.2.1. Flow-Meters

A set of two flow-meters are used to control the flow and the characteristics of the pulsing. The first one was previously introduced and is controlling the jet flow-rate, while the second one is located on the jet tracer seeding system to control the seeding flow-rate when visualizations are made. Because of the highly corrosive character of the reaction generating the tracer, no flow-meter can be placed after the reagent injection points to control the overall blowing ratio. Consequently, to obtain the total blowing ratio during an experiment, the flow-rates of the two flow-meters are added and the equivalent blowing ratio is computed. Finally, for consistency purposes, even during experiments not necessitating tracer, the seeding flow-rate is still maintained constant using pure nitrogen.

3.3.2.1.1. Main Flow-Meter

This flow-meter is a TSI mass flow-meter (Model 40241) based on the measurements of two hot-wires. Its response time is of the order of 4ms and has a range of operation from 0 to 200StdL/min. These characteristics allow acquisition of time-resolved flow-rate records even at forcing frequencies of 10Hz. A filter is required at the inlet of the device to protect the sensors from any particle present in the system.

3.3.2.1.2. Seeding Flow-Meter

The tracer generation uses two reagents carried as vapors by pure nitrogen and injected in the jet at different locations. In order to obtain good characteristics of the tracer, the quantity of each reagent must be controlled using a TSI mass flow-meter (Model 4140). Its response time is less than 4ms and its range of operation is from 0 to 20 StdL/min. A complete description of the tracer seeding system is given in section 3.4.2.3.

3.3.3. Traverse System

The traverse system is a 3 axis system allowing to reach precisely any point in the test section for constant temperature anemometry purposes, or above the test section for visualizations purposes. The system is composed of 2 X-axis beams on each side of the test section, one Y-axis beam mounted perpendicular to the two previous one, and one Z-axis beam perpendicularly attached on the Y-axis one. Each axis is equipped with an electric motor coupled with an endless screw allowing a flat plate to move along this axis. Three switches can also be used on each beam, two as limit switches used to set movement boundaries (for instance to prevent the traverse from bringing the probes too close to the bottom wall), the last one as a home switch used to set an axis origin. The motors are supplied by three drives connected with the 9 switches to a common indexer which is the interface between the traverse and the computer used to control the traverse. This computer, which is also the acquisition computer, is connected to the indexer via an ISA card from Compumotor (Model AT6400 AUX1) and operates the traverse using several National Instrument Labview Virtual Instruments. Because the computer used for the acquisition is able to operate the traverse, completely automated hot-wire measurements acquisition can be performed in several points of the test section, with no intervention from the operator.

3.4. Measurements

3.4.1. Hot-wire Measurements

3.4.1.1. Generalities on Constant Temperature Anemometry (CTA)

The CTA or hot-wire measurement is based on the cooling effect of a flow over a controlled heated body. In our case, the probes used are composed of one or several thin cylindrical tungsten wire

sensors of 1mm length by 5µm diameter. In this case, the heat transfer q of a normal flow past a cylinder is a function of the flow (normal) velocity U, the wire temperature and the fluid properties:

$$q = (T_{wire} - T_{flow}).A_{wire}.h \cong C_1 + C_2.U^n, n \cong 0.5 \; and \; C_1 \& \; C_2 \; constants$$

Equation 3-1: Hot-wire relationship between flow velocity and heat transfer.

These wires are part of a Wheatstone bridge, heated by an electrical current, maintaining the temperature (and the wire resistance) constant. The higher the normal flow velocity, the higher the heat transfer implies a higher current to maintain a constant temperature. The measured quantity is not the current but the voltage using the Ohm's law $V = R.I$. The advantages of hot-wire measurements are:

- High frequency response. A 5µm diameter sensor has a response time of about 10µs in a 30m.s^{-1} flow.
- High spatial resolution. This resolution is directly related to the size of the sensor, in our case 1mm.
- High operation and measurement range. The probes used in our experiments were calibrated for velocities going from 0 to 50m.s^{-1}.

The inconvenient of hot-wire measurements are:

- CTA is sensitive to flow temperature variations. A change of 1°K in temperature of the flow can lead to an error of approximately 2% in the estimated flow velocity.
- Intrusive method.
- The wire sensors are sensitive to all orthogonal components of the velocity to the wire axis, but any axial component may bias the measurements.

The first problem can be corrected by using a thermocouple to measure the actual flow temperature during the experiments and apply a corrective coefficient to the calibrated values.

3.4.1.2. Hot-wire System

The hot-wire measurement system is composed of three elements. The first element is the probe itself and its different probe-holders. The second element is the constant temperature anemometer (from

TSI model IFA 300) containing the Wheatstone bridge, all the associated electronics, and all the inputs and outputs respectively connected to the probe and the acquisition system. The third element is a computer equipped with the software corresponding to the constant temperature anemometer and connected to it via an ISA card. This software allows to control the anemometer, but also to calibrate the probes when the anemometer is connected to the calibrator (see section 2.3.5.4).

3.4.1.3. Probes and Thermocouple

As discussed above, a wire sensor can measure the value of the velocity component normal to the wire axis. Several types of probes are available from single wire probes for one component measurements, to three wires probes for 3 components measurements. Their orientation can differ from a straight probe to an L shaped probe (end flow or cross flow probes). For this study, three types of probes were used:

- Straight single component probe (TSI Model 1210).
- L-shaped single component probe (TSI Model 1212 and 1218).
- Straight two components probe (TSI Model 1241).

To correct the influence of the changes in flow temperature a thermocouple (Omega) was used to record the actual flow temperature.

3.4.1.4. Calibration

The principle of Constant Temperature Anemometry is quite simple as explained above: to an output voltage is associated a flow velocity. The aim of the calibration is to find the precise relationship between voltage and velocity for a given probe. In addition to the anemometer, the probe and the probe holder that are being calibrated, the calibration requires a pressure transducer and a calibrator (Model TSI 1129) in order to set with accuracy a flow with known velocity in which the probe is going to be placed (see Figure 3-6). The calibration results are not computed using the calibration software of the anemometer, but using a Matlab program (see section 4.1.1). For that matter, the anemometer and the calibrator are only used to determine the gain and the offset of the probe and to obtain the voltages corresponding to known values of the velocity and acquire them with the previously introduced

acquisition system. In addition, the temperature during the calibration needs to be known if the temperature correction wants to be applied during experiments. These values are then fitted using a 4th order polynomial. Finally, the result of the calibration is:

- Probe gain
- Probe offset
- Polynomial regression coefficients (U=f(V))

The calibration of the X-wire probe (two components) comports another step which consists in the acquisition of another set of voltages corresponding to yaw coefficients in order to determine the influence of the angle of the flow on the acquired voltage.

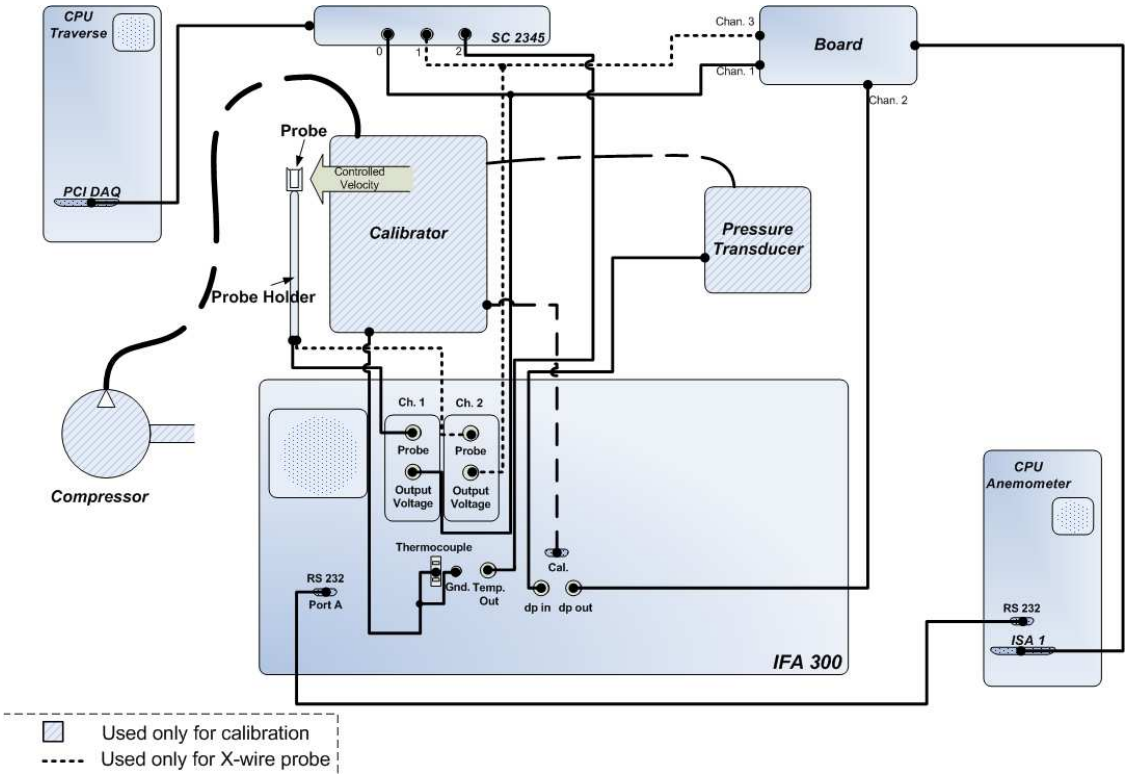

Figure 3-6: Constant Temperature Anemometry system.

3.4.1.5. Constant Temperature Anemometry Experiments

The setup for CTA experiments is composed of the three CTA elements plus the acquisition system and is presented in Figure 3-7. The probe-holder is mounted on the traverse, parallel to the z-axis, and goes through the openings of the wood roof. For long probe-holders, a stiffening rod can be added to

the traverse and envelops the probe-holder to prevent flexibility resulting in errors in location. The acquisition system, coupled with the traverse can perform manual or fully automated measurements.

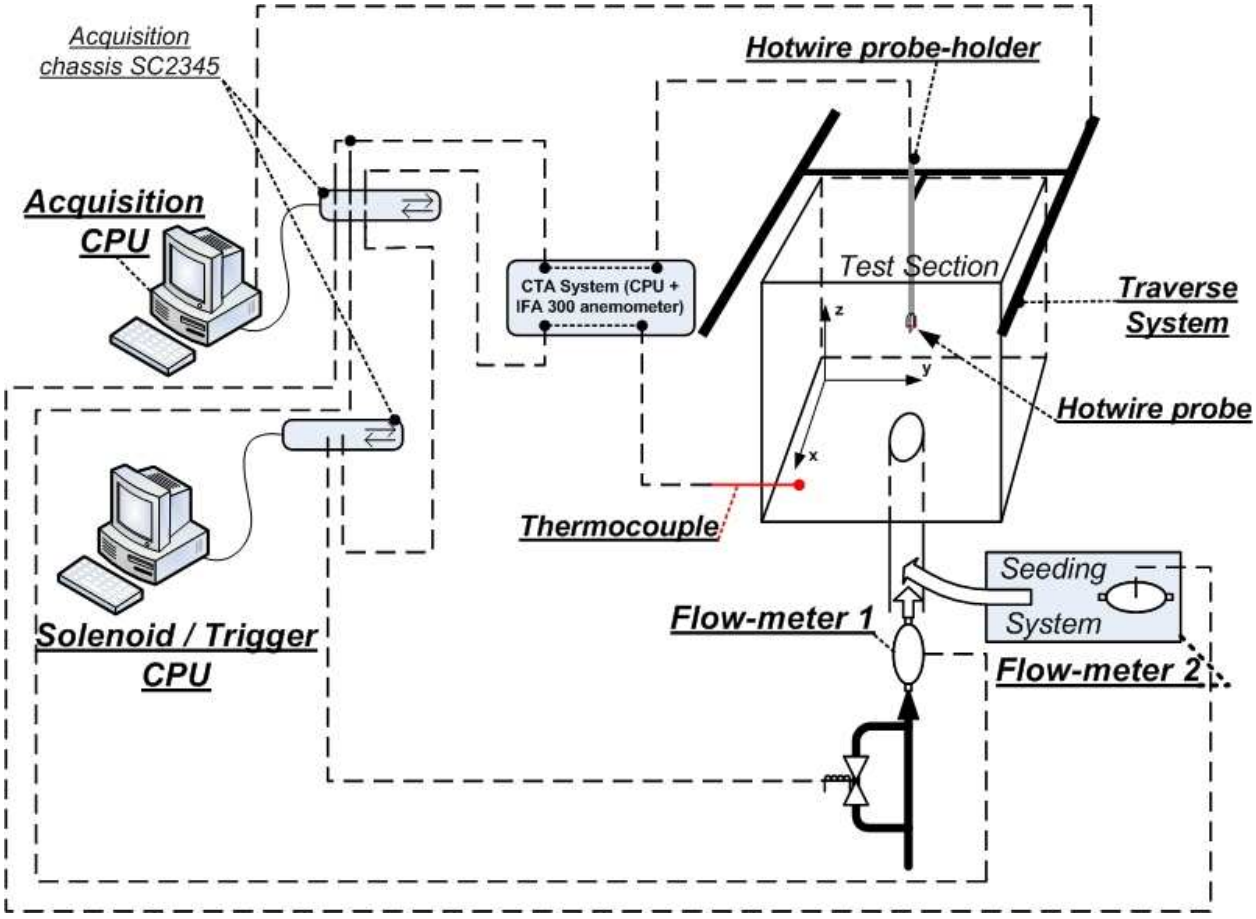

Figure 3-7: Setup in constant temperature anemometry configuration.

3.4.2. Visualizations

3.4.2.1. Generalities

To provide complimentary understanding of the jet structures and determine the interesting points to analyze with hot-wire measurements, a visualization system based on Mie scattering techniques was used. The visualizations necessitate the injection of a tracer into the jet flow in order to reveal the structures due to mixing with the cross-flow. The test section and the seeded jet are then illuminated using a LASER sheet, and images are taken using a digital camera perpendicular to the illuminated plane. The result is a “slice” of the flow corresponding to the illuminated plane. Two different visualization planes were considered for this study. The first one is the plane perpendicular to the bottom wall of the test

section and parallel to the test section centerline (X-Z visualizations), while the second one is the plane parallel to the bottom wall of the test section at $Z/D_j=1/8$ (X-Y visualizations).

3.4.2.2. Tracer

Small solid particles or small liquid droplets are both potential tracers for such purposes. These particles or droplets need to be small enough to follow the path lines of jet air particles but big enough to be illuminated by the LASER and detected by the camera sensor. The tracer used in our experiment is Titanium Dioxide (TiO_2) generated from the reaction of Titanium Tetrachloride ($TiCl_4$) and Water (H_2O) and presented in Equation 3-2. Another product of the reaction is Hydrochloric Acid which when reacting with water gives Hydronium.

$$TiCl_4 + 2\,H_2O \rightarrow TiO_2 + 4\,HCl$$

$$HCl + H_2O \rightarrow H_3O^+ + Cl^-$$

Equation 3-2: TiCl4 reaction equations

The advantage of this reaction is that the size of the resulting TiO2 particles is ideal for PIV and visualizations purposes. However, the products of the reaction are extremely toxic and/or corrosive and require protection and careful handling during experiments. Goggles, heavy duty latex gloves and respiratory masks are essential elements during handling and experiments. Because of the highly corrosive character of the reaction products, all valves, fittings and tubing on the path of $TiCl_4$ are made of stainless steel, Teflon or Viton.

3.4.2.3. Tracer Seeding System

Because of the high tendency of TiO_2 particles to clog any lines, the reaction has to happen in the jet itself which diameter and flow-rate are high enough to prevent any clogging. The reagents are both carried as vapor in pure nitrogen gas and injected in the jet flow where they finally mix and can react to form TiO_2 particles. The tracer seeding system is the device used to saturate pure nitrogen in water and $TiCl_4$ vapors and inject it in the jet flow and is presented in Figure 3-8. This system is composed of two separate lines, one for $TiCl_4$, one for water, both supplied by a single source of pure nitrogen regulated by

a pressure regulator at 10 psig. A flow-meter (seeding flow-meter) is placed at the exit of the nitrogen bottle to control the overall seeding flow-rate.

3.4.2.3.1. $TiCl_4$ Line

To obtain $TiCl_4$ saturated nitrogen, a stainless steel tube supplied with nitrogen is plunged into a glass container filled with liquid $TiCl_4$. This glass container is sealed and has only one inlet (immersed in the liquid chemical) and one outlet (outside of the liquid chemical). This way, the pure nitrogen passes through the chemical, saturates in chemical vapors and then reaches the surface. The gas contained in the container is actual nitrogen saturated with $TiCl_4$ vapor. This gas exits by the outlet and is driven by the pressure to the injection chamber feeding the injection holes. A set of two metering valves placed respectively before the inlet and after the outlet regulates the flow through the glass container, monitored by the seeding flow-meter. Finally a bypass regulated by a metering valve is located before the inlet valve and after the outlet valve, and is used during experiments not necessitating tracer to maintain similar conditions by still injecting the same amount of nitrogen into the jet flow.

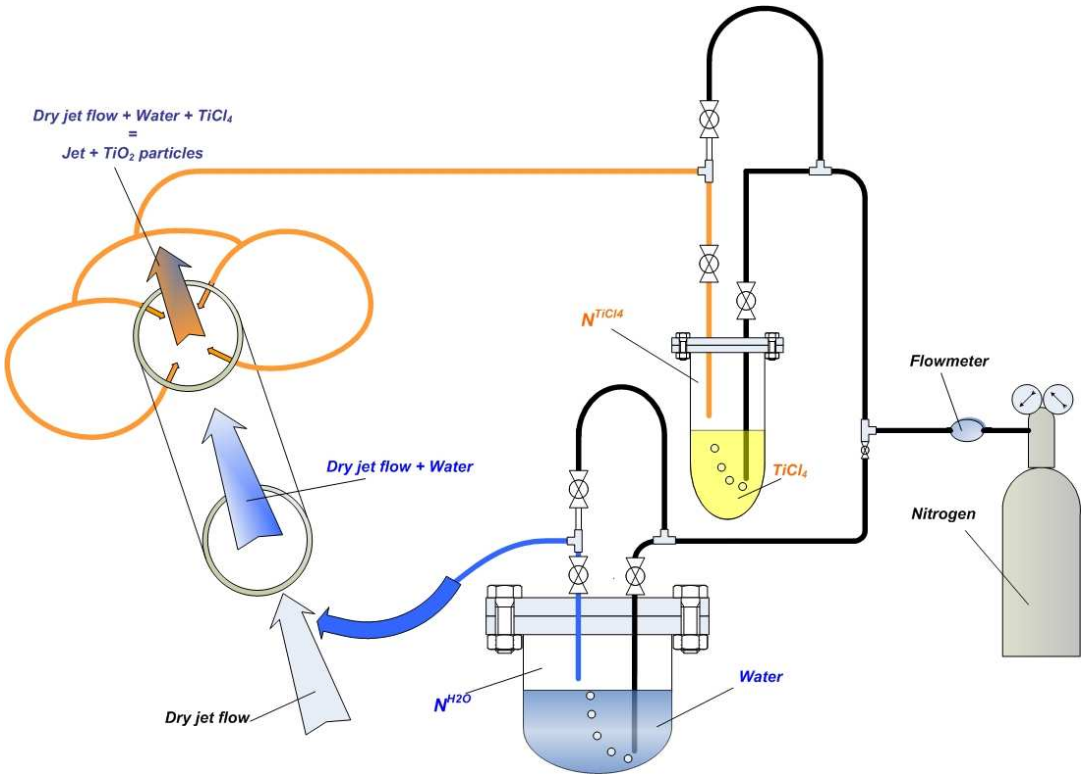

Figure 3-8: Tracer seeding system principle.

3.4.2.3.2. Water Line

The water line is similar to the $TiCl_4$ line with a comparable system of container (stainless steel container) and set of valves to control the flow. The outlet is driving water saturated nitrogen into the jet.

Using the two sets of metering valves on both lines, the flow-rate in each section can be adjusted and the ratio of water to $TiCl_4$ can be set in order to have the desired amount of each reagent and obtain a total reaction in the jet flow.

3.4.2.4. Psychrometric Charts

In order to determine the flow-rate needed in each branch of the seeding system, the psychrometric charts of saturated nitrogen in water and saturated nitrogen in $TiCl_4$ had to be computed. Even though the pressure in the two containers is not 10psig, the assumption will be made that it is the case and the charts will be computed for a pressure of 10 psig.

The saturation pressure of Titanium Tetrachloride is given by:

$$\log_{10}\left([P_{sat}]_{mmHg}\right) = 7.6443 - \frac{1947.6}{[T]_K}$$

Equation 3-3: $TiCl_4$ Saturation pressure law.

Similarly, the saturation pressure for Water is given by

$$\ln\left(\frac{[P_{sat}]_{kPa}}{[P_c]_{kPa}}\right) = (-7.859.\tau + 1.844.\tau^{1.5} - 11.786.\tau^3 + 22.680.\tau^{3.5} - 15.962.\tau^4 + 1.801.\tau^{7.5}).\frac{\mathrm{Tc}}{[\mathrm{T}]_\mathrm{K}}$$

$$\tau = 1 - \frac{[T]_K}{Tc}$$

Equation 3-4: Water saturation pressure law.

Using the law of partial pressures for a vapor *v* in a gas *g*:

$$P = P^v + P_g$$

With ω the specific humidity (or humidity ratio) and Φ the relative humidity:

$$\omega = \frac{m_v}{m_g}, \quad \phi = \frac{m_v}{m_{sat}} \Rightarrow \omega = \frac{\phi.m_{sat}}{m_g} = \frac{\phi\, P^v_{sat}.V/R^v.T}{P_g.V/R_g.T} = \frac{\phi P^v_{sat}}{P_g}\cdot\frac{R_g}{R^v}$$

Equation 3-5: Specific humidity ratio as a function of the nitrogen pressure and the saturation pressure.

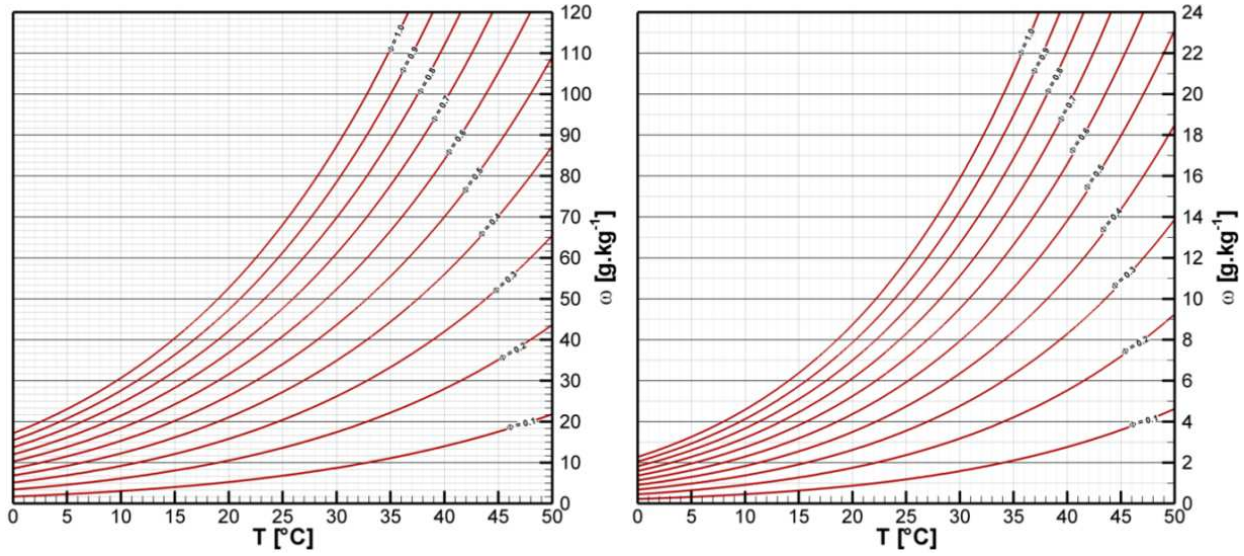

a) **b)**

Figure 3-9: Psychrometric charts of (a) $TiCl_4$ (b) H_2O in N^2 at 10 psig.

According to the computed psychrometric charts, the necessary flow rate ratio between water and $TiCl_4$ is 1.67 at 25°C.

3.4.2.5. Visualizations System

3.4.2.5.1. LASER

The LASER used for the visualizations is an Nd: YAG LASER from New Wave Research (MODEL Gemini 30 PIV). This LASER is equipped with two heads grouped in a single housing, each capable of firing at 30Hz a LASER beam with a wavelength of 532nm. The heads are supplied by an individual power supply and controlled by a separate remote controller for manual use. These controllers can adjust independently the firing rate, the firing mode and the flashlamp voltage for each head. An additional setting knob is located on the first LASER head remote control to adjust the intensity of an optical attenuator attached to the housing. The LASER can also be operated via an external triggering device, which is the mode that was selected for the current visualizations.

3.4.2.5.2. Camera

The camera used for the visualizations is a digital camera from Kodak (MEGAPLUS ES 1.0) with a 1016x1008 pixel monochromatic sensor. Its maximum acquisition rate is of 29.5Hz and the chosen export format is TIFF.

3.4.2.5.3. Optics

To provide a LASER sheet and only illuminate a plane of the flow to give “sliced” visualizations, the LASER head is equipped with a DANTEC 80X60 LASER Mount, a 80X63 Light Sheet Thickness Adjuster and a 80x61 20° Light Sheet Module.

Depending on the plane observed (X-Z or X-Y), different camera lenses were used. For side-view visualizations (X-Z plane) the camera was equipped with a Panasonic Video Lens TV 200M Lens J6x12. For top-view visualizations (X-Y plane) the camera was equipped with a Nikor 28-90mm lens preceded by a Nikon to C-mount adapter to fit on the camera.

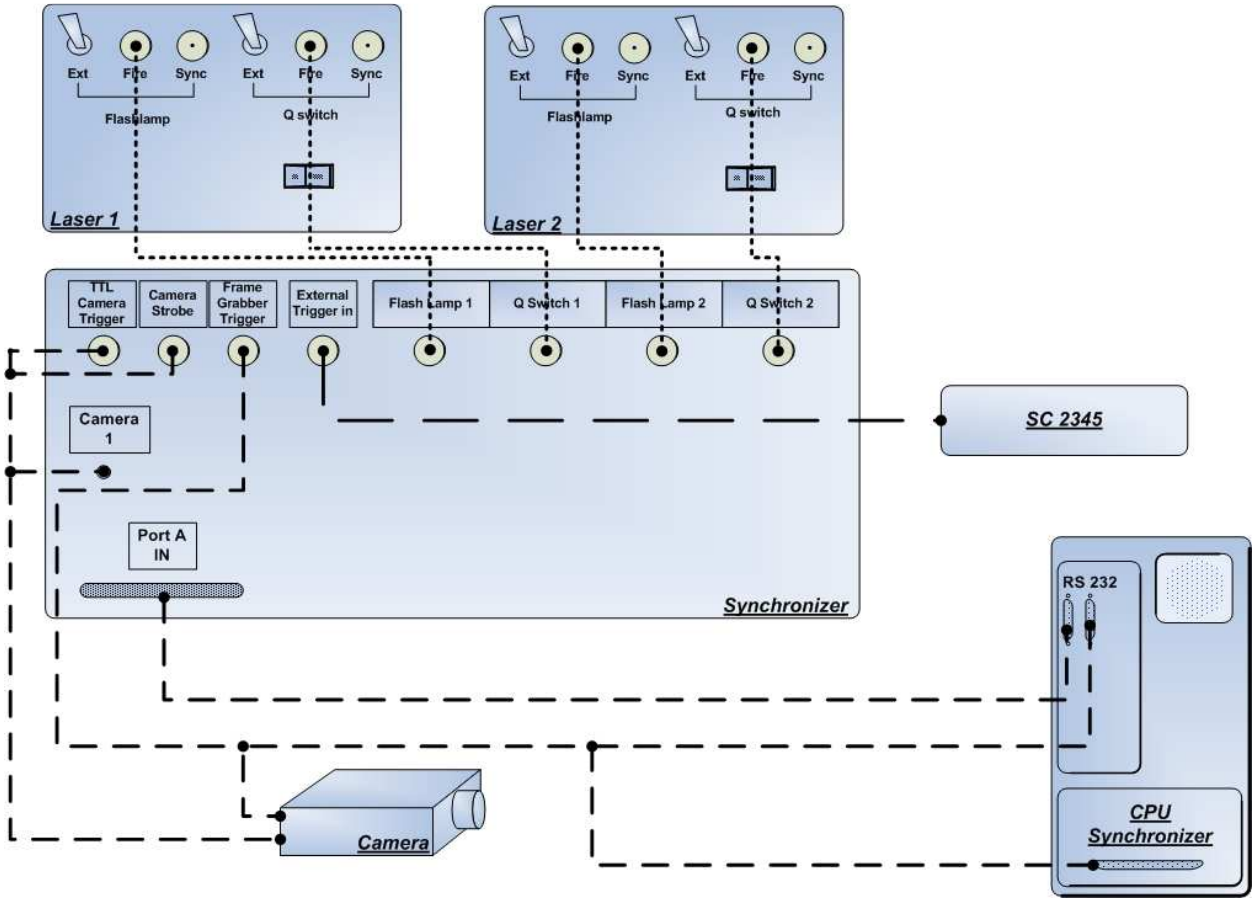

Figure 3-10: Visualization System detail.

3.4.2.5.4. Synchronizer

A synchronizer from TSI (Model 610034) is also part of the system and is principally used for phase locked visualizations, but also as an interface between the LASER, the camera, the valve control

computer and the visualizations computer. This device mainly controls the timing between LASER firing, Camera diaphragm opening and frame grabber acquisition.

3.4.2.5.5. Computer

The last part of the visualizations system is a computer equipped with a TSI Insight PIV version 1.5. software. This computer is equipped with a TSI frame grabber (Model 600067) for image acquisition from the camera, and is also used to control the synchronizer. The frame grabber has a limit acquisition rate of 28Hz. The Insight software is used to set the different parameters for the visualizations such as pulsed delays, camera delay, LASER intensity…

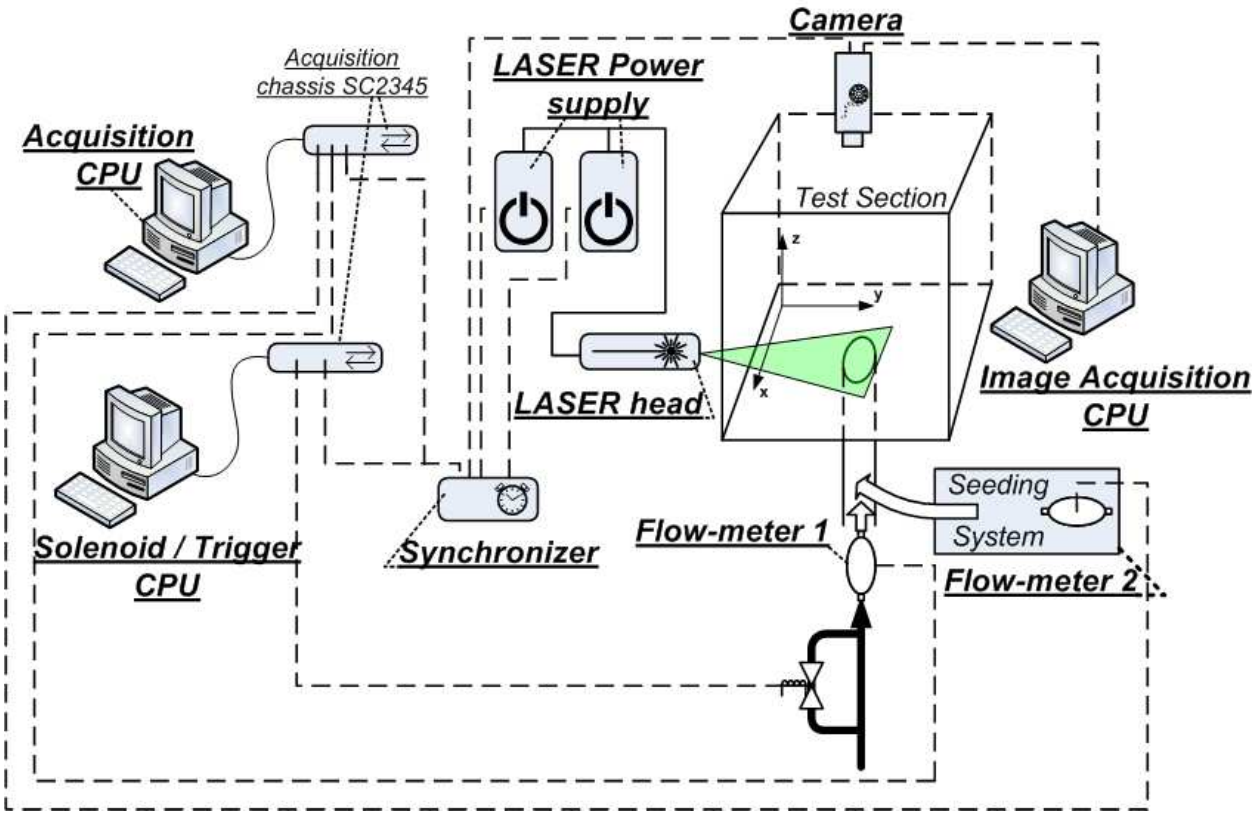

Figure 3-11: Setup in visualizations configuration (top-view).

3.4.2.6. Experiments

As explained earlier two different types of visualizations are made for this study and the only setup difference is the position of the camera and the LASER head that are inverted. For X-Y visualizations, the camera is mounted on the traverse and images are taken perpendicularly to the bottom

wall of the test section with the focus made at 1/8 Dj above the wall, while the LASER is mounted on a third X-axis beam and leveled at $Z=1/8D_j$ (Figure 3-11). For X-Z visualizations, the setup is inverted and the LASER head is mounted on the traverse system and the camera on the spare X-axis. Depending on the type of visualizations (steady state experiments or pulsed jet experiments) the software is operated differently. In the case of a steady state experiment, the timing master of the experiment is the synchronizer which determines the firing frequency, and triggers each LASER pulse and camera diaphragm opening. In the case of a forced experiment and in order to be synchronized with the solenoid valve opening and closing, the timing master is the solenoid valve control computer. At phase locked positions, the solenoid valve control computer sends a trigger signal to the synchronizer which launches the image acquisition sequence.

Chapter 4: Data Reduction

As explained in the previous chapter, a considerable amount of data is collected during the different phases of the study. From the calibration data to the experimental data, all the information needs to be treated. Most of the treatment is made using The MathWork software Matlab. This section explains briefly the data processing depending on the type of data collected and the outcome of this processing.

4.1. Constant Temperature Anemometry Measurements Processing

4.1.1. Calibration

The result of the calibration is a list of recorded voltages corresponding to effective velocities reached by the calibrator.

4.1.1.1. One Component Probe Calibration

This is the easiest case where only one polynomial fit is used. Using a homebrew interface, the calibration files and the 34 corresponding acquired voltages are loaded. A second interface (Matlab program) reads the data and executes the polynomial regression. The result of the calibration is a Microsoft Excel file with all the calibration information such as the calibration temperature, the polynomial coefficients from the regression, the gain and offset of the probe… A visual verification of the fitting is made to insure the validity of the polynomial regression (Figure 4-1).

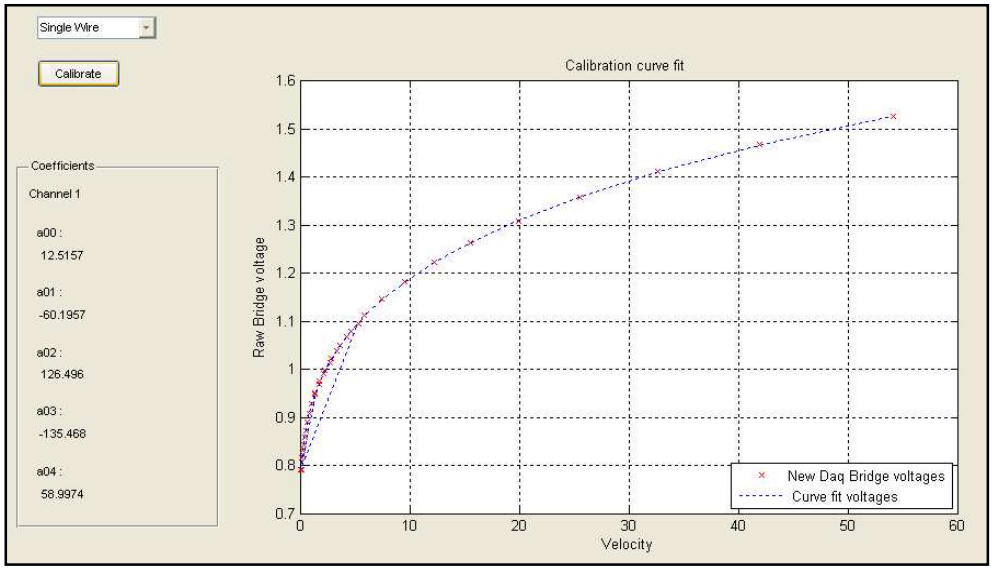

Figure 4-1: Matlab interface developed for single wire calibration purposes.

4.1.1.2. Two Components Probe Calibration

This calibration starts similarly with an acquisition of voltages as a function of calibrator airflow velocity. A second calibration is required for this type of probe in order to determine the sensibility of each sensor to flow incidence. A second series of acquisition is made of voltages corresponding to 11 measurements at a given velocity with changing angle, and this for 11 different values of the velocity. Two 4^{th} order polynomial fit are used (one for each sensor) and a visual verification of the fitting is made using another Matlab interface (Figure 4-2). The result of this calibration is a Microsoft Excel file containing the calibration information, the two series of coefficients from both polynomial regressions and a series of yaw angle coefficients.

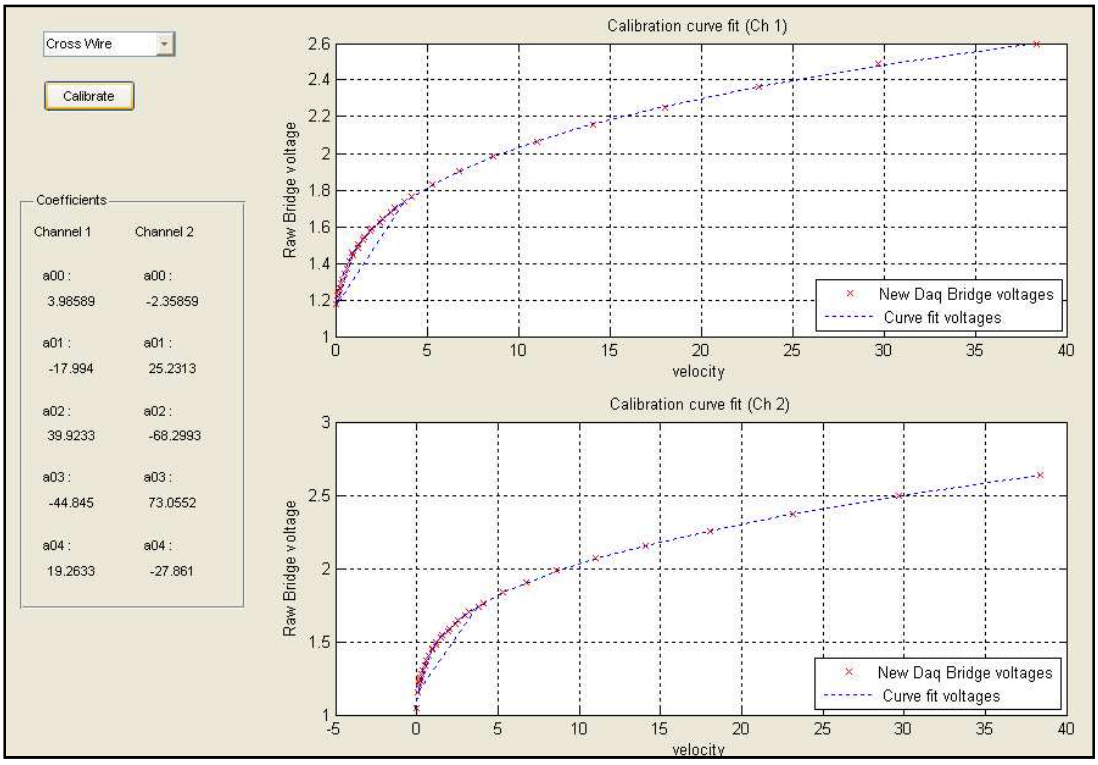

Figure 4-2: Matlab interface developed for cross-wire calibration purposes.

4.1.2. Experiments Data Reduction

Once the experiments done, the results are series of recorded voltages from the first hot-wire channel, the second hot-wire channel (if two components acquisition) and the thermocouple. Using the coefficients from the calibration, each voltage can be associated to a velocity magnitude. In addition, the

thermocouple voltages are transformed into actual flow temperatures and the temperature correction is applied. Once the actual flow velocitiy components are known, the following values are extracted:

- Flow properties (Mean velocity, Turbulence intensity, Standard deviation, root mean square, third (Skewness) and fourth (Kurtosis) moments)
- Fourier Power Spectrum
- Wavelet Spectrum Analysis Mapping (Using algorithm from Torrence et al.)

The wavelet spectral analysis is used as a complement to the Fourier spectrum analysis for its ability to detect intermittent frequency events and its ability to obtain frequency information as a function of time which is very useful in intermittent and pulsed conditions. Figure 4-3 presents the advantages of wavelet analysis over Fourier spectrum analysis in pulsed conditions. While the acoustic frequency of the system is confused with the harmonics of the pulsing frequency in the Fourier analysis (Figure 4-3 b), red circle), the 45Hz signature is perfectly identifiable on the wavelet analysis mappings (Figure 4-3 a), red arrow).

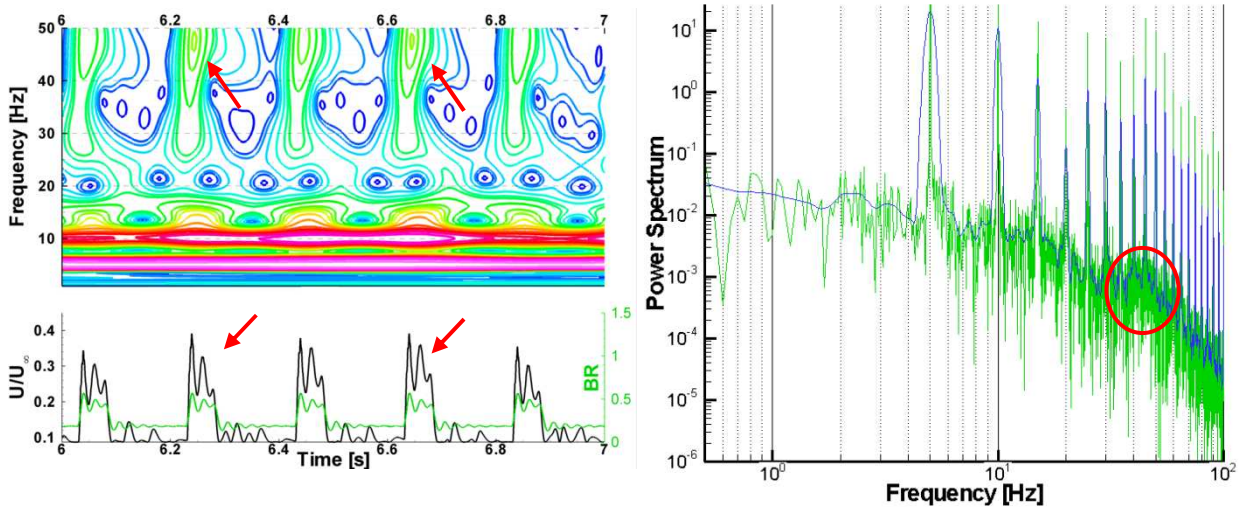

a) b)

Figure 4-3: Comparison between a) wavelet analysis and b) Fourier spectrum analysis in pulsed conditions.

Figure 4-4 presents a comparison between wavelet analysis and Fourier spectrum analysis for a record exhibiting intermittency in the velocity signal (probe located slightly offset of the region of interest). Even though a signature is visible on the Fourier spectrum, it is unclear whether or not this

signature is relevant (Figure 4-4 b), red circle). The wavelet analysis however shows clearly that the oscillatory behavior is not well-defined, except at one point, where the frequency is clearly analyzed (Figure 4-4 a), red arrows)

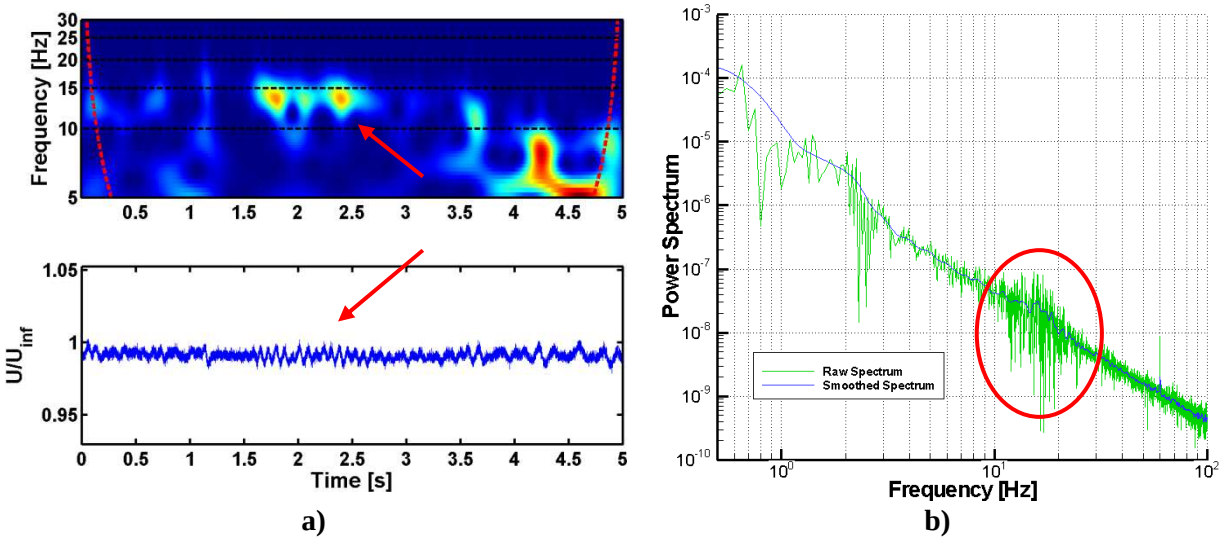

Figure 4-4: Comparison between a) wavelet analysis and b) Fourier spectrum analysis in intermittent conditions.

4.2. Flow-Meter Measurements Processing

The flow-meter measurements serve two principal purposes which are to first have an instantaneous reading of the blowing ratio for setup and verification during experiments and also to have a time-resolved record of the blowing ratio during the tests.

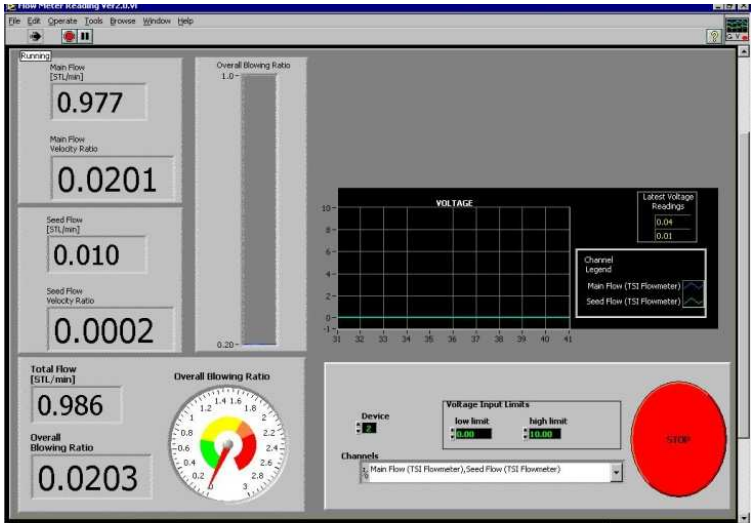

Figure 4-5: Flow-meters instantaneous reading virtual instrument.

4.2.1. Instantaneous Blowing Ratio Reading

This reading is made on the acquisition computer using a National Instrument Labview Virtual Instrument giving (Figure 4-5) readings of the jet flow-meter, the seeding flow-meter and the total of the two as the overall blowing ratio. A later version of the virtual instrument integrates a low-pass filter on the values of the blowing ratio for easier setup.

4.2.2. Experiments Data Reduction

The same algorithm used for instantaneous readings is applied to recorded flow-meter signal to obtain the actual blowing ratio values during the experiment using a Matlab interface program. Additional information is extracted from these records depending on the nature of the experiment (steady state or forced flow experiment):

- Steady state: BR_m, standard deviation, Skewness and Kurtosis.
- Forced flow: BR_m, standard deviation, Skewness, Kurtosis, Phase Averaged signal, BR_l, BR_h, BR_{pp} and DC.

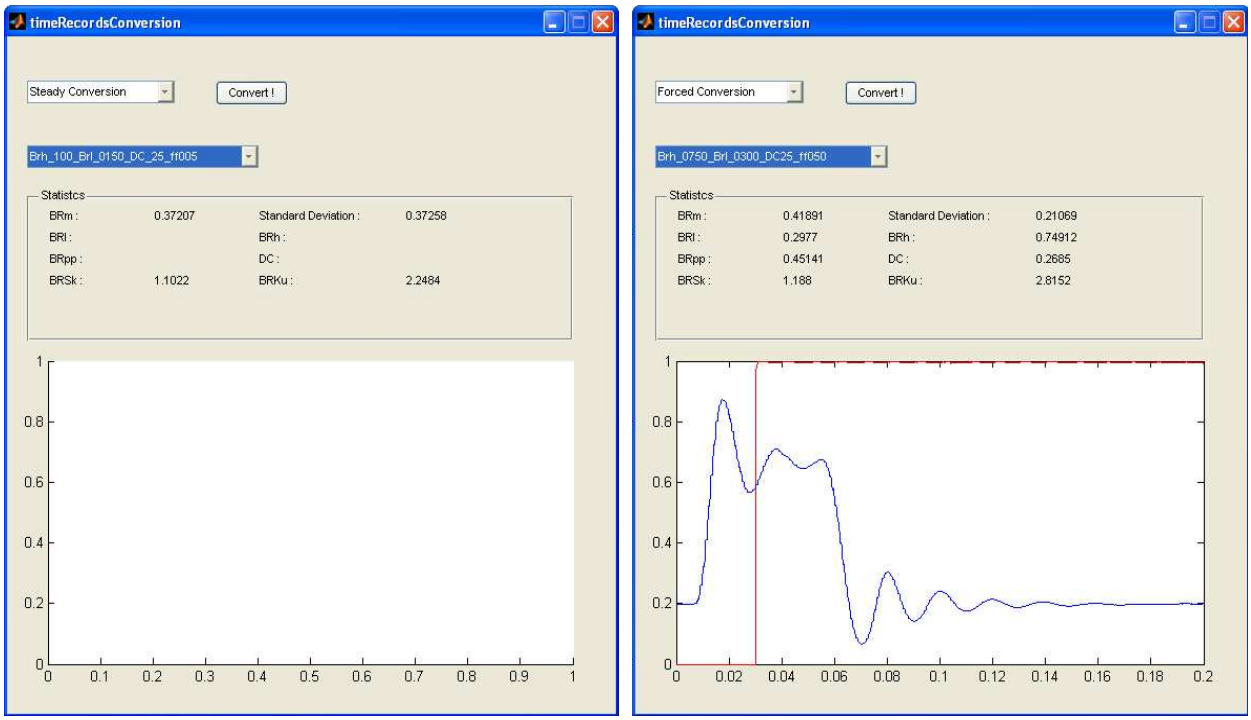

a) **b)**

Figure 4-6: Matlab interface developed for flow-meters time records conversion in a) Steady state experiments, b) Forced case experiments.

Some of the pulsed flow records were also analyzed with wavelet spectral analysis to resolve the flow frequencies in the jet feeding tube.

4.3. Image Processing

Images acquired with the visualization system are processed using Matlab. When imported into Matlab, each image is considered as a 1008x1016 matrix with coefficients going from 1 to 256 representing a grayscale value. This convenient format allows manipulations of the image itself for processing purposes such as extracting quantitative information and/or obtaining averaged visualizations.

4.3.1. Averaging

For steady state cases, 3 series of 32 images are taken for each blowing ratio. This number of 96 visualizations assures statistically accurate results. Each image is then imported into Matlab and converted into a 1008x1016 matrix. The averaging process consists in taking the mean value of each element over the 96 matrices and storing it in another matrix called the averaged matrix. This matrix is then transformed back into a grayscale image similar to a time averaged image of the flow.

4.3.2. Phase Averaging

Phase averaging is used for pulsed flow experiments. The visualizations protocol for pulsed flow experiments is different from the steady state flow experiments and from one frequency to another:

- For f_f = 0.5 and 1Hz, 10 images are taken at 10 equally spaced phase locations within the cycle. For instance at a forcing frequency of f_f = 1Hz, 10 images are taken at the initial time (t_0) of 10 consecutive cycles, then 10 images are taken at the moment t_0+1/10 of 10 consecutive cycles, then 10 images at the moment t_0+2/10 of 10 consecutive cycles…
- For f_f = 5 and 10Hz, 10 images are taken at 50 equally spaced phase location within the cycle. For instance at a forcing frequency of f_f = 5Hz, 10 images are taken at the initial time (t_0) of 10 consecutive cycles, then 10 images are taken at the moment t_0+0.2/50 of 10 consecutive cycles, then 10 images at the moment t_0+0.2*2/50 of 10 consecutive cycles…

Phase averaging consists in computing the average (as explained in section 4.3.1) for each set of 10 images taken at given phase location. The result is 10 or 50 phase averaged images depending on the

forcing frequency. Finally, a global average of all the obtained images (100 for f_f = 0.5 and 1Hz, 500 for f_f= 5 and 10Hz) is made to obtain an overall representation of the flow over a complete cycle.

4.3.3. Quantification

Even though the visualizations were intended for qualitative analysis and understanding of the flow, quantitative data was also extracted from the images obtained during the experiments on both X-Y and X-Z visualizations. The main source for visualizations quantification is the averaged image for steady state cases and the overall averaged image for pulsed flow cases. However, the overall averaging is not exactly the same as described in the previous section for forcing frequencies of 5 and 10Hz. Indeed to prevent any statistical bias by adding more pictures to the average at f_f = 5 and 10Hz than to the average at f_f= 1 0.5 and 1Hz, a re-sampling is made and only 100 pictures (10 pictures at 10 equally spaced phase locations) are taken in consideration for the overall averaged matrix $[I_{i,j}]$ used in quantifications. Finally, a calibration image is acquired at the beginning of each experiment to determine the position of the jet exit, the jet centerline, and the scaling information (Figure 4-7).

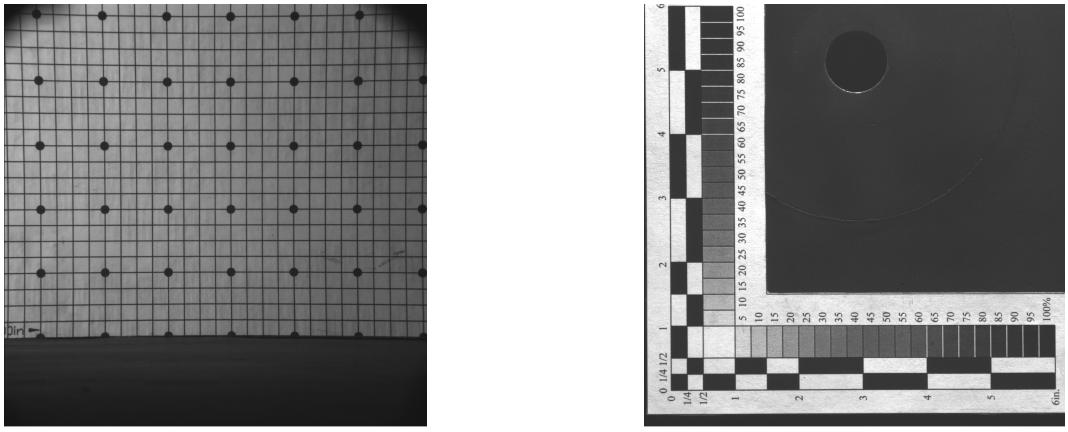

a) **b)**

Figure 4-7: Calibration targets used in visualizations experiments for a) Side-view visualizations, b) Top-view visualizations.

One of the main concerns in visualizations quantifications is the consistency and the ability to compare the quantity extracted between all cases. However, during visualizations the seeding flow-rate is maintained constant, and the tracer density tends to decrease as the overall blowing ratio increases, resulting in a decreased illumination of the camera sensor because of the dilution of the tracer. A

normalization factor needs to be applied to the overall averaged images in order to limit the influence of the decreasing light intensity on the quantification. Moreover, where no seeding and no particles are transported, the intensity should be the same on all averaged images and is set equal to zero.

4.3.3.1. X-Z Visualizations Quantification : Jet Penetration

For X-Z visualizations, the chosen normalization factor is the averaged intensity over a small patch taken above the jet exit $\langle I_{i,j} \rangle_{patch}$. The normalized matrix $\left[I_{i,j}^N\right]$ is then computed on the averaged matrix with Equation 4-1:

$$I_{i,j}^N = \frac{I_{i,j} - min_{i,j}(I_{i,j})}{\langle I_{i,j} \rangle_{patch} - min_{i,j}(I_{i,j})}$$

Equation 4-1: Intensity normalization equation for side-view visualizations.

The quantification on the side views (X-Z plane) consists in the detection of the jet upper limit as an estimation of the jet penetration. Even if the usual jet penetration is computed using the jet core line, the fact that the jet is attached to the bottom wall during most of the experiments, and because of the existence of a recirculation region behind the jet, makes its detection very complicated and inaccurate. The upper limit detection is made using the contour at $\left[I_{i,j}^N\right] = 0.1$ (10% of the normalization patch intensity).

4.3.3.2. X-Y Visualizations Quantification: Jet Coverage

The chosen normalization factor for this type of visualization is the averaged intensity over the jet exit area $\langle I_{i,j} \rangle_{exit}$. The normalized matrix $\left[I_{i,j}^N\right]$ is computed using the following formula:

$$I_{i,j}^N = \frac{I_{i,j} - min_{i,j}(I_{i,j})}{\langle I_{i,j} \rangle_{exit} - min_{i,j}(I_{i,j})}$$

Equation 4-2: Intensity normalization equation for top-view visualizations.

The coverage of the jet is estimated using the surface covered by the $\left[I_{i,j}^N\right]$=0.5 contour (50% of the jet exit intensity) from which is subtracted the jet area. Finally, the computed area is normalized by the jet area to give a number called the coverage coefficient C_c.

The equation used to obtain the normalized intensity matrix is very close to the one used to compute the adiabatic effectiveness η in film cooling experiments. Indeed, the adiabatic effectiveness is locally computed during adiabatic experiments with Equation 4-3.

$$\eta_{x,y} = \frac{T_{wall_{x,y}} - T_{cross-flow}}{T_{coolant} - T_{cross-flow}}$$

Equation 4-3: Adiabatic efficiency definition

If the tracer density at a particular point $d^t_{x,y}$ was used as a passive scalar and assuming the luminosity received by a pixel of the camera sensor is directly related to the tracer density at the corresponding point in space, each image would be a measurement of the passive scalar. In addition if an analogy is made between temperature and tracer density, we would have:

$$T_{wall_{x,y}} \leftrightarrows d^t_{x,y} \leftrightarrows I_{i,j}$$

$$T_{cross-flow} \leftrightarrows min\left(d^t_{x,y}\right) \leftrightarrows min_{i,j}\left(I_{i,j}\right)$$

$$T_{coolant} \leftrightarrows \langle d^t_{x,y} \rangle_{exit} \leftrightarrows \langle I_{i,j} \rangle_{exit}$$

$$q(@wall) = 0 \leftrightarrows \dot{m}_{tracer}(@wall) = 0$$

Equation 4-4: Equivalence between temperature of the wall in adiabatic experiments and tracer intensity.

However, several limitations remain such as:

- The tracer accumulates in some areas (recirculation regions…) allowing values of tracer density above the averaged tracer density at the exit. This is not the case with the temperature since no region of the wall has a lower temperature than the coolant temperature. The result is normalized intensity coefficients above 1 in some areas.
- Even though the Prandtl number of the experiment is of order one (Pr), the typical Schmidt number (Sc) for Titanium Dioxide particles in laminar flow is of the order of 100 to 1000. This means that the momentum diffusivity is higher than the TiO_2 diffusivity and what is visible does not reflect exactly flow properties. Similarly, the heat transfer analogy is made in a conservative manner since the Lewis number (Le) is of order 100 to 1000, reflecting the higher thermal

diffusivity compared to the tracer mass diffusivity. In these conditions, coverage coefficient, span-wise average normalized intensity and estimated jet penetration are under-estimated when compared to the actual values. Even though these considerations make impossible any quantitative comparison with actual values, it is expected that the trends obtained using these quantities should be similar.

Chapter 5: Results and Discussion

5.1. System Characterization

The system characterization was made during the early part of the project. A brief description of the system characterization is given in this paragraph. A complete description can be found in P.E Boulladoux MSc Thesis (2006) and J. Oertling MSc Thesis (2006). Most of the data, graphs and tables from this paragraph are extracted from the two documents previously cited and marked this way †.

5.1.1. Wind Tunnel Characterization

In order to provide accurate inlet and boundary conditions, the wind tunnel properties were documented using hot-wire anemometry and spectral analysis.

The wind tunnel velocity is set using a controller and a remote control which input corresponds to the fan rotation frequency in Hertz (Hz). To obtain a calibration, a hot-wire survey of the wind tunnel free stream velocity was realized for several values of the controller frequency. Because of the scaling of the experiment, the desired cross-flow velocity is chosen constant and equal to 1.6m.s^{-1} and is found to correspond to 3Hz on the controller, according to velocity calibration (Figure 5-1). In addition, this calibration reveals that the relationship between controller frequency and wind tunnel velocity is linear with a slope of about 0.52, and that the wind tunnel is operated in the low part of its range of operation going from 0 to 30m.s^{-1}.

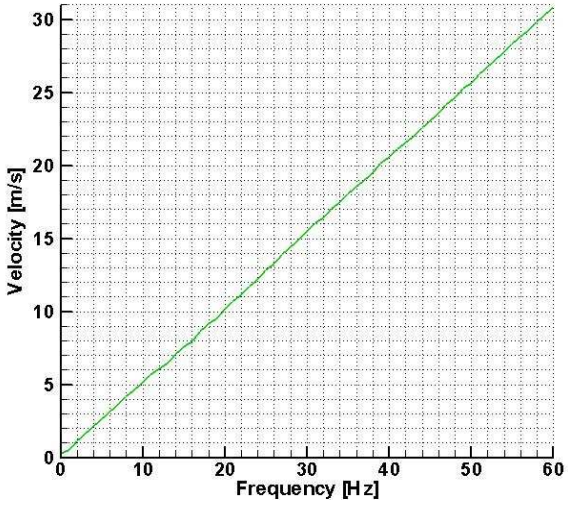

Figure 5-1: Wind tunnel velocity calibration as a function of the controller frequency†.

Using several measurements in the stream-wise direction along the test section (and jet) centerline, the uniformity of the flow was verified by computing the mean velocity and turbulence intensity at operating conditions (U_∞ = 1.6m.s^{-1}). The measured velocity values were consistent with the nominal wind tunnel velocity and the turbulence intensity was found to be inferior to 0.25%.

Records of the free stream velocity were also analyzed using Fourier spectrum analysis to determine the frequencies proper to the cross-flow (Figure 5-2).

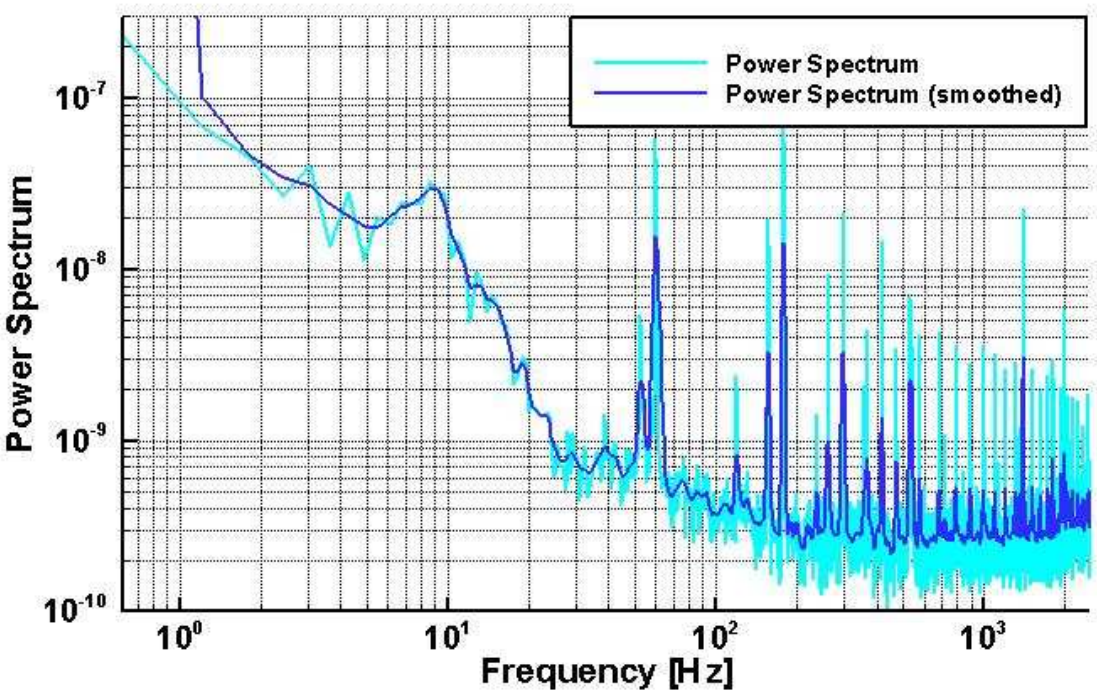

Figure 5-2: Free stream power spectrum at X/D$_j$=0 for U=1.6m.s^{-1}†.

The frequencies observed on the spectrum analysis (3, 9, 13, 19, 23, 28, 38, 53, 74, 160 Hz…) are related to the fan properties and electrical properties and all have low energy levels. Indeed, the fan has 9 vanes on the stator, 12 blades on the rotor and runs at a frequency of 3Hz. Consequently, the expected frequencies are 3, 9 & 12Hz, their harmonics (18, 24…) and their combinations (3*9=27, 3*12=36). Finally, most of the energy is concentrated at frequencies lower than 10Hz.

5.1.1.1. Boundary Layer

The boundary layer is an important factor for jet in cross-flow configurations, especially when the jet is mounted flush with the test section. An exploratory survey (for determination of statistically

accurate sampling conditions) and several boundary layer profiles measurements were performed in order to completely characterize this region of the cross-flow.

The power spectrums of hot-wire measurements at the jet exit ($X/D_j=0$, $Y/D_j=0$) and for different heights above the bottom wall of the test section, exhibit comparable frequencies than the one found in the free stream (9, 13, 24-27, 70Hz…) with again a strong influence of the fan characteristic frequencies and most of the energy concentrated at low frequencies (Figure 5-3).

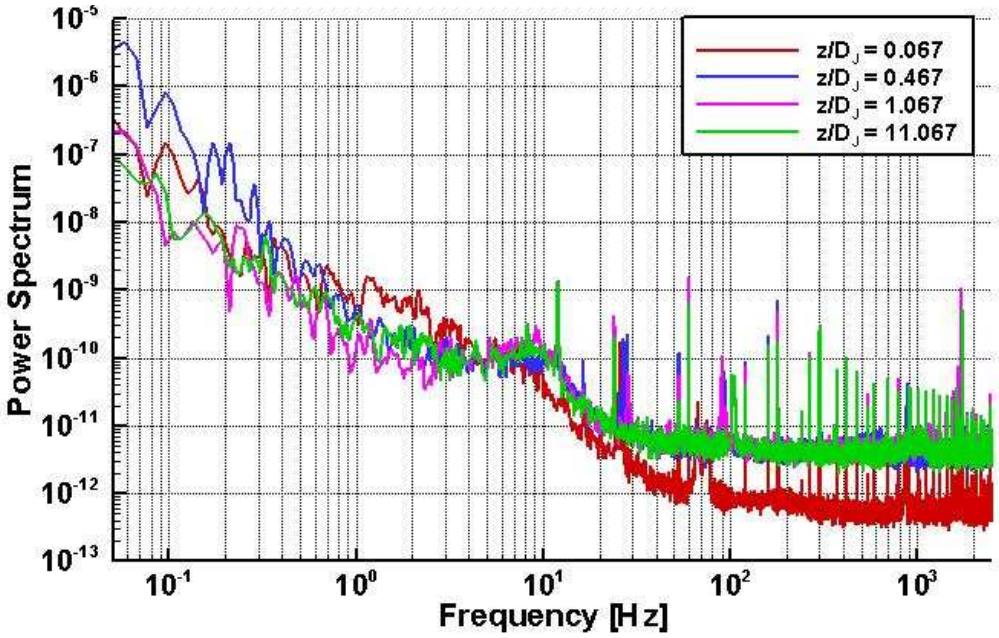

Figure 5-3: Power spectrum of the boundary layer with a free stream velocity U_∞ = 1.6m.s^{-1} and at four different heights of (Z/D_j=0.067, 0467, 1.067, 11.067)[†].

A series of five boundary layer profiles were measured in the neighborhood of the jet and show good agreement with the Blasius solution of a flow over a flat plate. The results of these measurements are summarized in Table 5-1 and Figure 5-4.

Table 5-1: Boundary layer characteristics[†].

	Y/D_J =-4.00	**Y/D_J = 0.00**	**Y/D_J =+4.00**
X/D_J = -4.75		U_∞ = 1.60 m/s TI = 0.65 % δ = 1.8 cm δ^* = 0.440 cm θ = 0.199 cm H = 2.21	

Table 5-1 cont.

X/D_J = 0.00	U_∞ = 1.58 m/s TI = 0.44 % δ = 1.34 cm δ^* = 0.451 cm θ = 0.189 cm H = 2.38	U_∞ = 1.59 m/s TI = 0.64 % δ = 1.49 cm δ^* = 0.462 cm θ = 0.187 cm H = 2.46	U_∞ = 1.57 m/s TI = 0.85 % δ = 1.86 cm δ^* = 0.485 cm θ = 0.216 cm H = 2.25
X/D_J = 4.75		U_∞ = 1.60 m/s TI = 0.46 % δ = 1.59 cm δ^* = 0.471 cm θ = 0.207 cm H = 2.27	

The boundary layer profiles are corresponding to laminar profiles, which is in agreement with the value of the Reynolds number Re_x based on the cross-flow mean velocity and distance from the test section inlet to the jet exit which is of the order of 80,000.

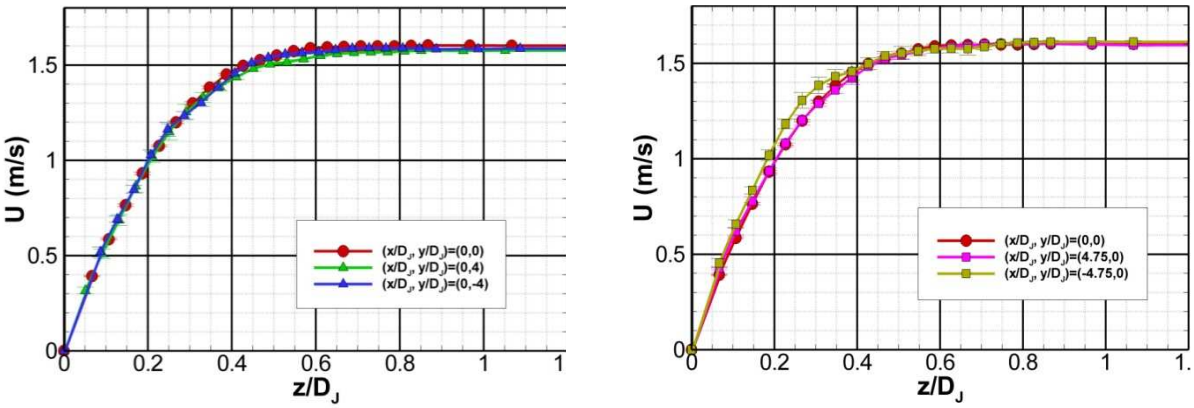

a) **b)**

Figure 5-4: Boundary layer profiles at a) X/D_j = 0, b) Y/D_j = 0†.

Even though the complete characterization of the wind tunnel was performed earlier, an additional survey of the main parameters was conducted in order to verify the consistency of the conditions. The cross-flow free stream velocity was measured using an L shaped single sensor probe and was found to be 1.6m.s^{-1} at a set controller frequency of 3Hz. The boundary layer profiles on the jet centerline, at X/D_j=-4.75 and X/D_j=0 were reacquired and are presented in Table 5-2 and Figure 5-5. The results of our verification are satisfying when comparing the shape of the profiles and the values of the different metrics representative of the boundary layer with the previous measurements.

Table 5-2: Verification of boundary layer characteristics - Metrics at X/D_j = -4.75 and X/D_j = 0.

	Y/D_j = 0.0
X/D_j = -4.75	U_∞ = 1.61 m.s^{-1} δ = 1.60 cm δ^* = 0.439 cm θ = 0.195 cm H = 2.25
X/D_j = 0.0	U_∞ = 1.60 m.s^{-1} δ = 1.60 cm δ^* = 0.472 cm θ = 0.202 cm H = 2.34

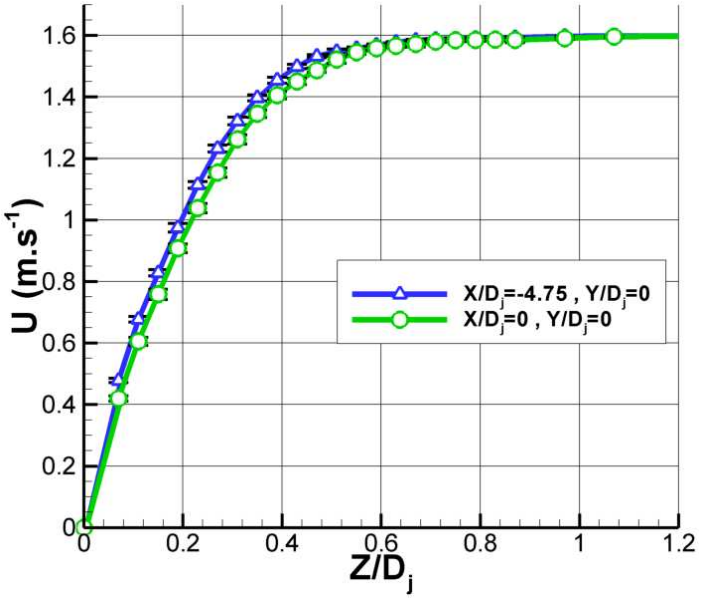

Figure 5-5: Verification of boundary layer characteristics – Velocity profiles at X/D_j = -4.75 and X/D_j = 0.

5.1.2. Jet Characterization

5.1.2.1. Measurements without Cross-Flow

Measurements of the vertical component (along the Z-axis) of the jet velocity were realized at the jet exit using a hot-wire probe with a single sensor, and analyzed using Fourier spectrum analysis (Figure 5-6). These measurements were made without cross-flow and without flow-meter which was not yet available at that time.

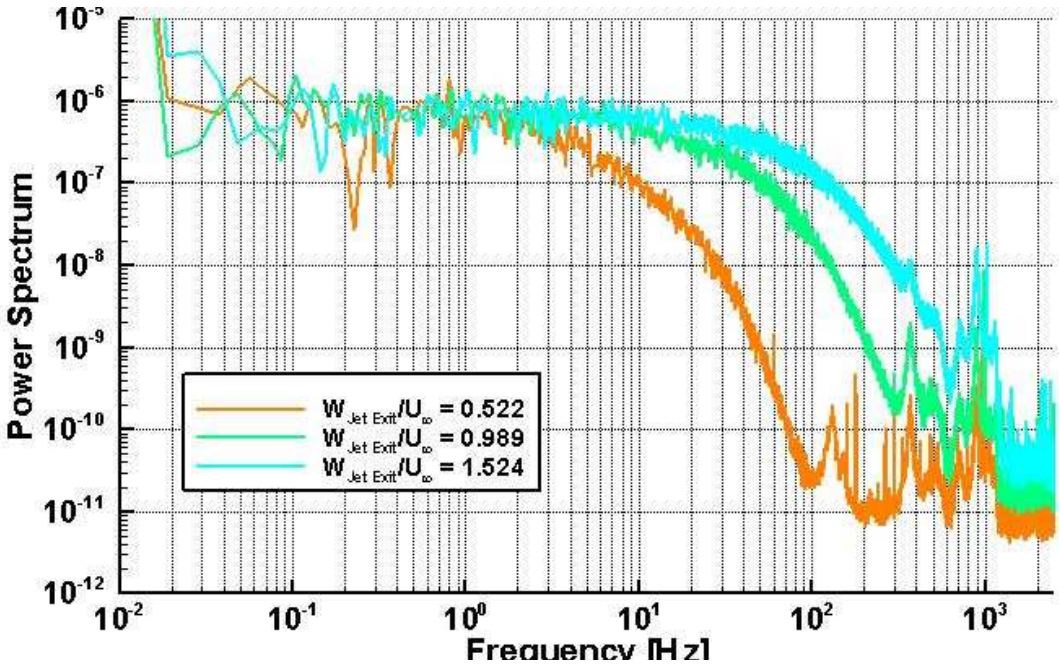

Figure 5-6 : Power spectrum from hot-wire measurements performed at the jet exit for different values of $W_j^{\dagger}$.

These spectrums, even though not related to any blowing ratios, cover a wide range of jet velocities and assure that the jet frequency signature is located in the high frequencies with peaks present at constant values (350, 700, 900Hz), suggesting no possible interaction with the chosen forcing frequencies of 0.5, 1, 5 and 10Hz.

Jet exit vertical velocity profiles (Figure 5-7) were also recorded using the same hot-wire probe for several values of W_j trying to match the jet exit velocity obtained in the previous record.

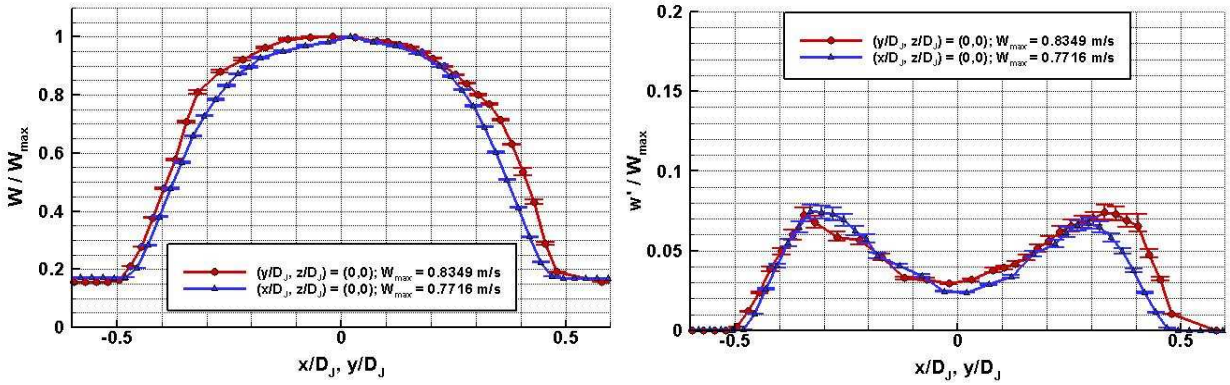

Figure 5-7: Mean velocity and RMS velocity profiles at $W_{max}/U_\infty \approx 0.5$ (a, b); $W_{max}/U_\infty \approx 1.0$ (c,d); $W_{max}/U_\infty \approx 1.5$ (e,f) without cross flow scaled with $W_{max}^{\dagger}$. (Figure 5-7 cont.)

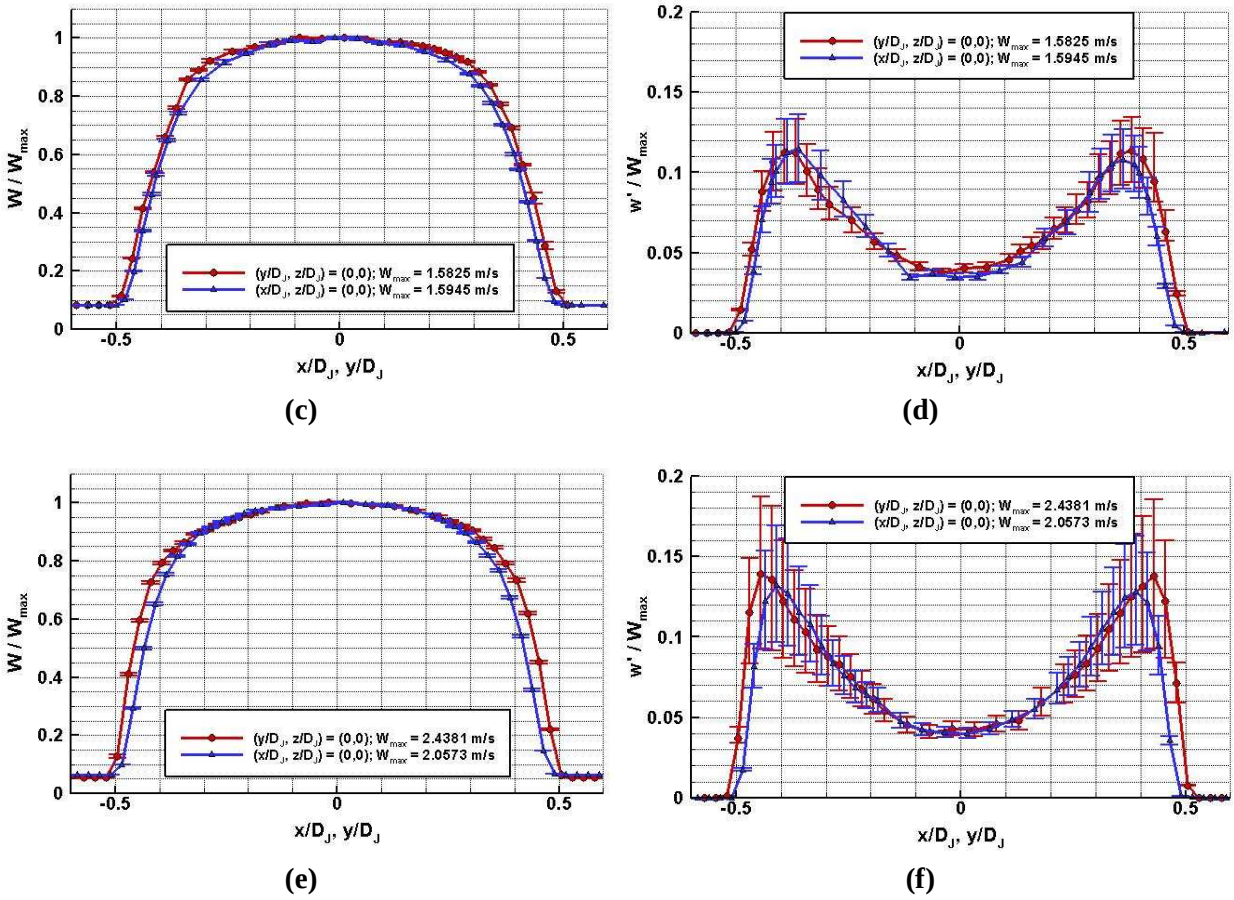

These profiles show that as the jet velocity (and blowing ratio) increases, the jet gets stronger (thinner shear layers), going from a parabolic-like profile toward a top hat-like profile. In addition, as W_{max} increases, the RMS velocity, higher in the shear layer, also increases and so does the turbulence in this area. The symmetry of the profile is satisfying, even though a slight asymmetry is noticeable on the low velocity measurements probably due to residual flow in the test section triggered by convection effects.

5.1.2.2. Measurements with Cross-Flow

Measurements with cross-flow were performed at the nominal wind tunnel velocity of 1.6m.s^{-1}. However, like previous jet characterization measurements, the flow-meters were not available at that time, and no corresponding blowing ratio can be given. Even so, these measurements show the strong influence of the cross-flow on the jet exit velocity profiles which appear strongly skewed (Figure 5-8). One may also notice the small but non zero stream-wise velocity at the jet exit (u_j) and negative values

upstream and downstream of the jet exit. Finally, the jet blowing ratio (in this case measured via the maximum vertical velocity) appears to have only a negligible effect on the stream wise velocity at the jet exit.

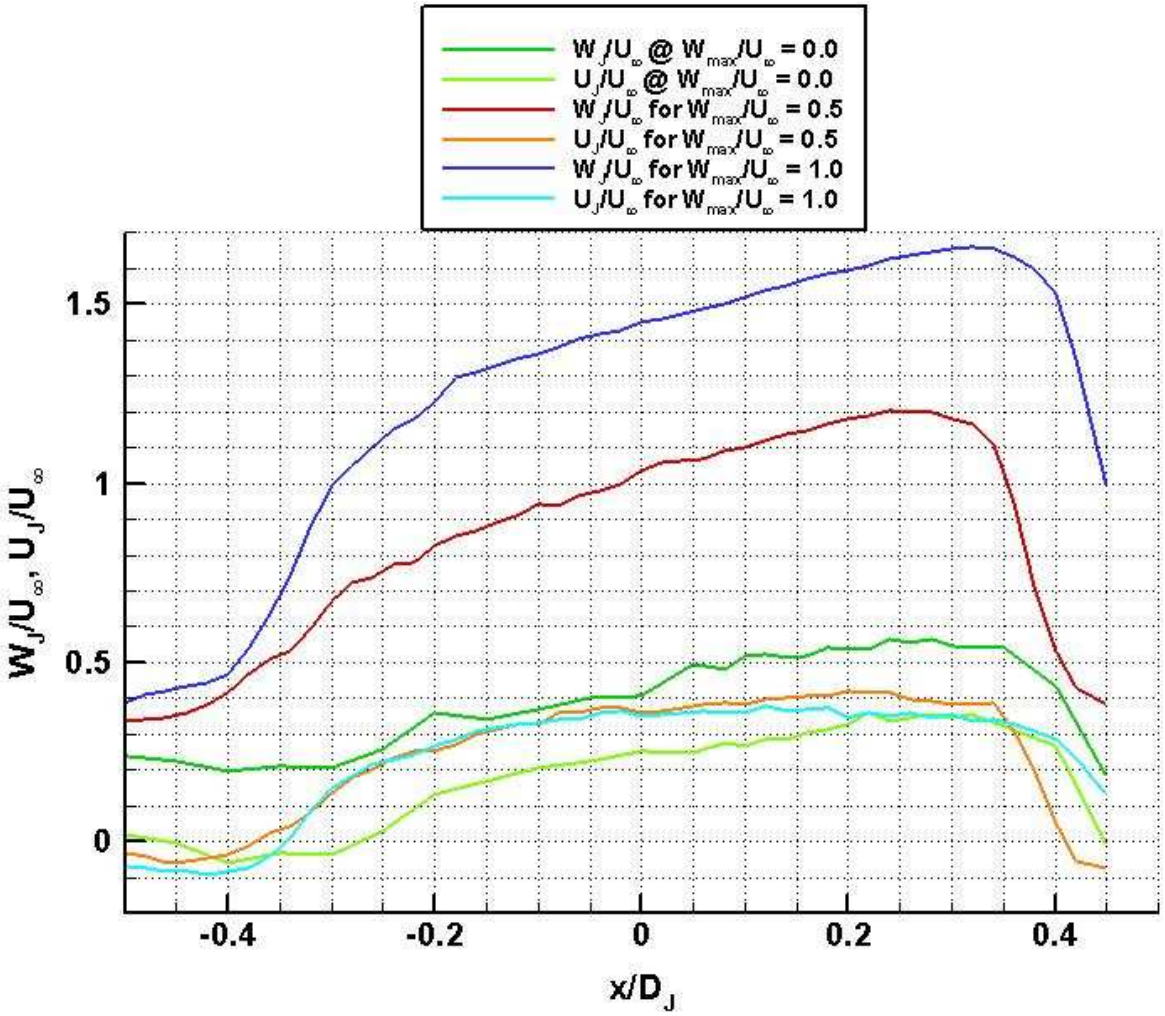

Figure 5-8: Vertical (w_j) and stream-wise (u_j) velocity profiles at the jet exit for different values of W_{max} with cross-flow at U_∞=1.6m.s^{-1}†.

The RMS value and the third and fourth moments are computed for the two non zero jet velocity measurements (Figure 5-9 a), b), c)). They show that the highest turbulence levels are located in the upstream shear layer (upstream lip of the jet) and at the downstream shear layer (downstream lip of the jet). According to the skewness and Kurtosis values, the areas of negative stream wise velocity observed in the previous velocity profiles measurement are most likely due to recirculation regions located outside of the jet.

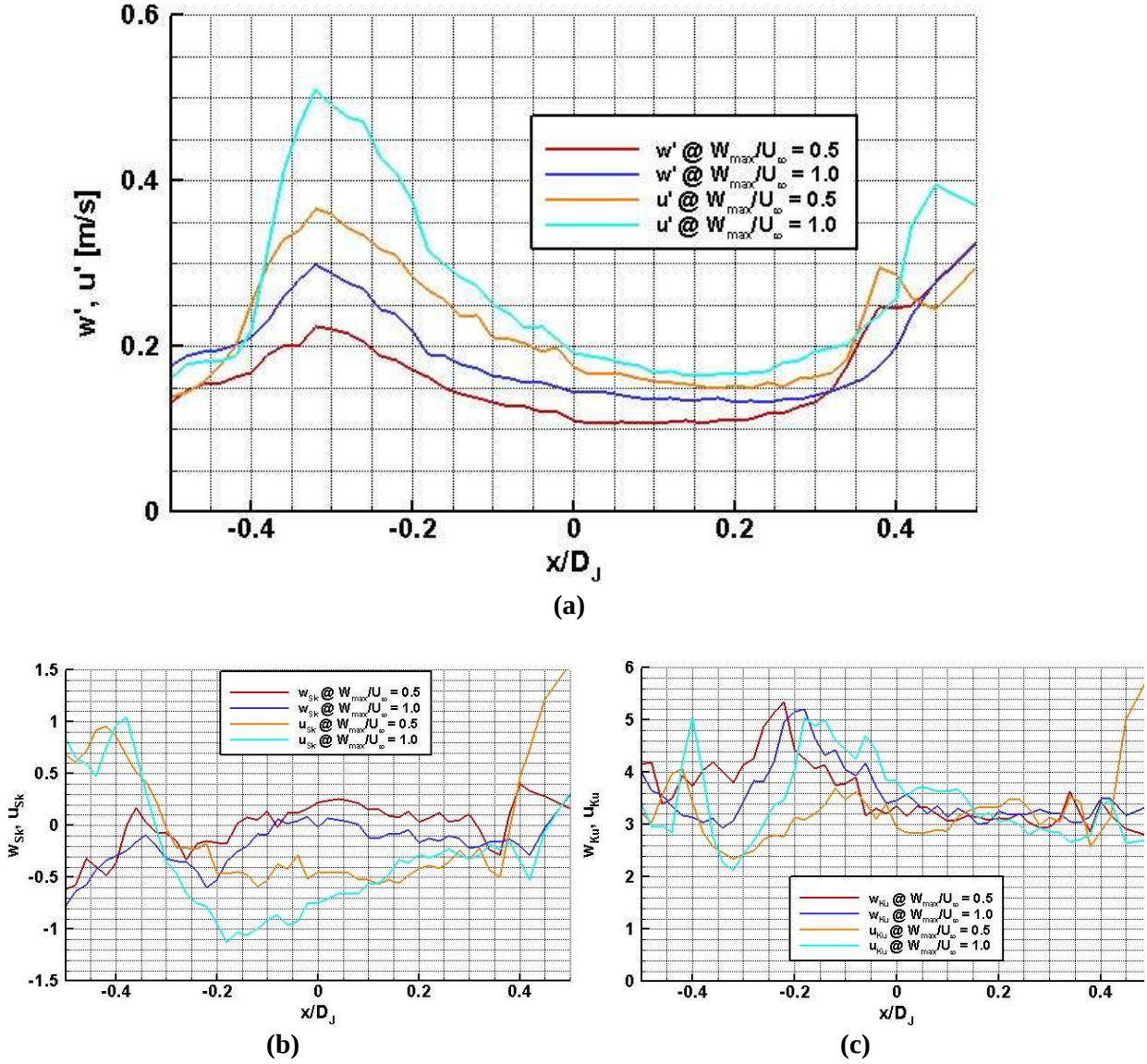

Figure 5-9: RMS velocities (a), Skewness (b) and Kurtosis (c) of the unforced JICF†.

5.2. Steady State Results

During all the experiments the wind tunnel was operated at the same velocity of 1.6m.s^{-1}, corresponding, according to the previous calibration to a controller frequency of 3Hz. All X-Z instantaneous visualizations (or side-view) presented in this part are extracted from P.E Boulladoux MSc Thesis (2006) and J. Oertling MSc Thesis (2006) and work. Steady state blowing ratios studied in this thesis cover most of the blowing ratios encountered later in the forced flow experiments, with a range from BR=0.150 to BR=0.600. These values correspond to a range of Reynolds number, based on the jet

mean velocity and the jet diameter, from Re_j=400 to Re_j=1600, staying in the laminar region, well below the transitional region.

5.2.1. Visualizations and Constant Temperature Anemometry

5.2.1.1. Protocols and Actual Conditions

5.2.1.1.1. Visualizations

As explained in Chapter 4, the visualizations acquisition followed an established protocol. Three sets of 32 images were acquired for each studied blowing ratio. The LASER sheet is fired at a frequency close from 30Hz which is at the limit of the system capability but barely enough to resolve structures evolution over time especially at higher blowing ratios. A time record of the different metrics (principally the flow-meters readings) is made at the beginning of each test with a sampling frequency of 10 kHz for 600,000 points (corresponding to 1min.). The intensity of the LASER is adjusted (using the optical attenuator) at the beginning of a test session over the complete range of blowing ratios in order to obtain enough light, but no saturation, from the lowest blowing ratio to the highest without having to readjust during a test because of dilution of the tracer. This precaution is taken in order to not introduce any bias on image quantification by adjusting the light source intensity between two tests.

The actual conditions during the tests are summarized in Table 5-3.

Table 5-3: Blowing ratio actual values during a) X-Z visualizations, b) X-Y visualizations.

Nominal BR	BR_{exp}	Std(BR_{exp})
0.150	0.145	1.00E-03
0.188	0.189	1.00E-03
0.250	0.251	1.40E-03
0.300	0.303	3.20E-03
0.365	0.365	3.10E-03
0.465	0.464	3.50E-03
0.600	0.600	4.10E-03

a)

Nominal BR	BR_{exp}	Std(BR_{exp})
0.150	0.149	1.47E-03
0.188	0.187	1.37E-03
0.250	0.250	1.58E-03
0.300	0.299	2.72E-03
0.365	0.365	3.28E-03
0.465	0.464	3.72E-03
0.600	0.599	4.26E-03

b)

These values show good agreement with the nominal values and support the validity of the results presented below.

5.2.1.1.2. Hot-wire Measurements

The hot wire measurements were realized using the hot-wire system, the traverse system and the acquisition system described in Chapter 3. Sampling conditions were different regarding of the type of measurements. The profiles were realized with the same protocol as boundary layer profiles consisting in:

- Exploratory survey at high sampling frequency using a large number of points (>1,000,000).
- Determination of the time scale integral and the number of points for statistical accuracy based on the previous sample.
- Actual profile measurement using the data previously computed.

The flow conditions are summarized in Table 5-4.

Table 5-4: Flow conditions for velocity profiles.

Nominal BR	BR_{exp}	$Std(BR_{exp})$
0.150	0.148	0.81E-03
0.188	0.186	0.95E-03
0.250	0.247	2.46E-03
0.465	0.465	3.9E-03

Localized velocity measurements were taken at several points on the jet centerline with a sampling frequency of 5000Hz and a low pass filter of 2000Hz for 100,000 points (20 sec). These points were chosen according to side-view visualizations in order to record characteristic frequencies of the typical structures observed on these images. Three measurements were made at and above the jet exit for $X/D_j = 0$ and $Z/D_j = 0$, 0.25 and 0.5, and five at a downstream location of $X/D_j = 3.5$ for $Z/D_j = 0.75$, 1.0, 1.25, 1.5 and 2.0 in order to catch the limit of the detached structures. The measurements at the jet exit ($X/D_j = 0$, $Z/D_j = 0$) are made with a vertical single sensor probe, while the other acquisitions are performed using a horizontal single sensor probe (L-shaped) oriented along the Y-axis. As explained earlier, single sensor probes cannot completely resolve the flow field at a given point since they record only one component of the velocity. However, data acquired in the frequency domain using these probes is still relevant and characterizes the flow structures or instabilities at this particular location. The actual experiments conditions of the hot-wire measurements are summarized in Table 5-5.

Table 5-5: Flow and jet conditions during localized hot-wire measurements.

BR	Location	BR_{exp}	$Std(BR_{exp})$	BR_{Ku}	U_{mean}/U_{∞}	U_{rms}	U_{Sk}	U_{Ku}	TI (%)
0.150	X/D_j=0, Z/D_j=0	0.150	7.60E-04	3.79	0.288	0.056	-1.365	4.792	19.54
	X/D_j=3.5, Z/D_j=0.75	0.149	8.68E-04	2.22	0.835	0.255	-1.367	3.294	30.55
0.188	X/D_j=0, Z/D_j=0	0.188	8.08E-04	4.08	0.275	0.016	-0.517	4.371	5.85
	X/D_j=3.5, Z/D_j=0.75	0.187	8.48E-04	3.16	0.903	0.155	-2.011	7.244	17.19
0.250	X/Dj=0, Z/Dj=0	0.250	1.90E-03	3.99	0.412	0.030	1.063	4.612	7.37
	X/Dj=0, Z/Dj=0.25	0.250	2.50E-03	3.45	0.394	0.082	0.029	4.817	20.89
	X/Dj=3.5, Z/Dj=1.25	0.250	2.50E-03	3.47	0.925	0.134	-1.847	7.665	14.43
0.300	X/Dj=0, Z/Dj=0	0.299	2.63E-03	3.58	0.517	0.043	0.161	3.133	8.26
	X/Dj=0, Z/Dj=0.25	0.300	3.09E-03	3.29	0.452	0.120	0.366	2.801	26.64
	X/Dj=3.5, Z/Dj=1.50	0.297	3.12E-03	3.32	0.991	0.039	0.458	4.750	3.91
0.365	X/D_j=0, Z/D_j=0	0.366	3.27E-03	3.04	0.670	0.060	-0.415	2.731	9.01
	X/D_j=0, Z/D_j=0.25	0.365	3.43E-03	3.20	0.554	0.151	0.537	3.055	27.37
	X/D_j=3.5, Z/D_j=1.50	0.365	3.39E-03	3.23	0.984	0.076	-2.490	15.921	7.75
0.465	X/D_j=0, Z/D_j=0	0.466	3.60E-03	3.12	0.834	0.071	-0.354	2.730	8.55
	X/D_j=0, Z/D_j=0.25	0.465	3.70E-03	2.97	0.810	0.176	-0.130	3.168	21.72
	X/D_j=3.5, Z/D_j=1.50	0.465	3.70E-03	3.10	0.842	0.214	-0.779	2.885	25.42
0.600	X/D_j=0, Z/D_j=0	0.600	4.42E-03	3.08	1.108	0.168	-0.620	3.962	15.17
	X/D_j=0, Z/D_j=0.50	0.600	4.61E-03	3.09	0.467	0.202	0.584	2.868	43.26
	X/D_j=3.5, Z/D_j=2.0	0.599	4.29E-03	3.17	1.053	0.059	-0.595	3.647	5.63

5.2.1.2. Results

Two separate regimes characterized by two different types of instabilities can be identified by analyzing the side-view (X-Z plane) and top-view (X-Y plane) visualizations. The first regime is associated with the low blowing ratios (in our case BR=0.150 and BR=0.188) and characterized by shear layer type of instability downstream of the jet exit (Figure 5-10 a) 1 and Figure 5-12 a) 1, dashed arrows). In this regime the jet is highly bent by the cross flow with a momentum deficit immediately downstream of the jet, near the wall. A well-defined and stable horse-shoe vortex located just above the jet exit at approximately Z/D_j=0.125 on the windward side is clearly visible (Figure 5-10 a) 1 & b) 1' and Figure 5-12 a) 1, 4 & b) 1', solid arrows). As the blowing ratio increases from BR=0.150 to BR=0.188, the horse-shoe vortex is pushed upstream from X/D_j=-0.4 to X/D_j=-0.45. A second horse-shoe vortex of smaller radius and randomly seeded by the tracer particles can be located upstream of the first one at X/D_j=-0.7 for BR=0.188 (Figure 5-12 a) 4, dotted arrow). The fact that the horse-shoe vortex is made

visible by the transport of tracer particles shows that jet fluid is carried by this structure and supports the potential importance of such structure for film cooling applications. The shear layer instability starts developing around X/D_j=2 and the jet breaks up approximately at X/D_j=4. On the top visualizations, the shear-layer instability is visible around X/D_j=3 as two lumps symmetrical with respect to the jet centerline, with apparently opposite vertical vorticity (Figure 5-10 b) 1' and Figure 5-12 b) 2', dashed arrow). Along the centerline, a dark line not seeded by the tracer appears on most of the top-view visualizations, especially at BR=0.150, and could be the trace of the counter rotating vortex pair (CRVP) (Figure 5-10 b) 1', d) & e) and Figure 5-12 b) 2', black arrow).

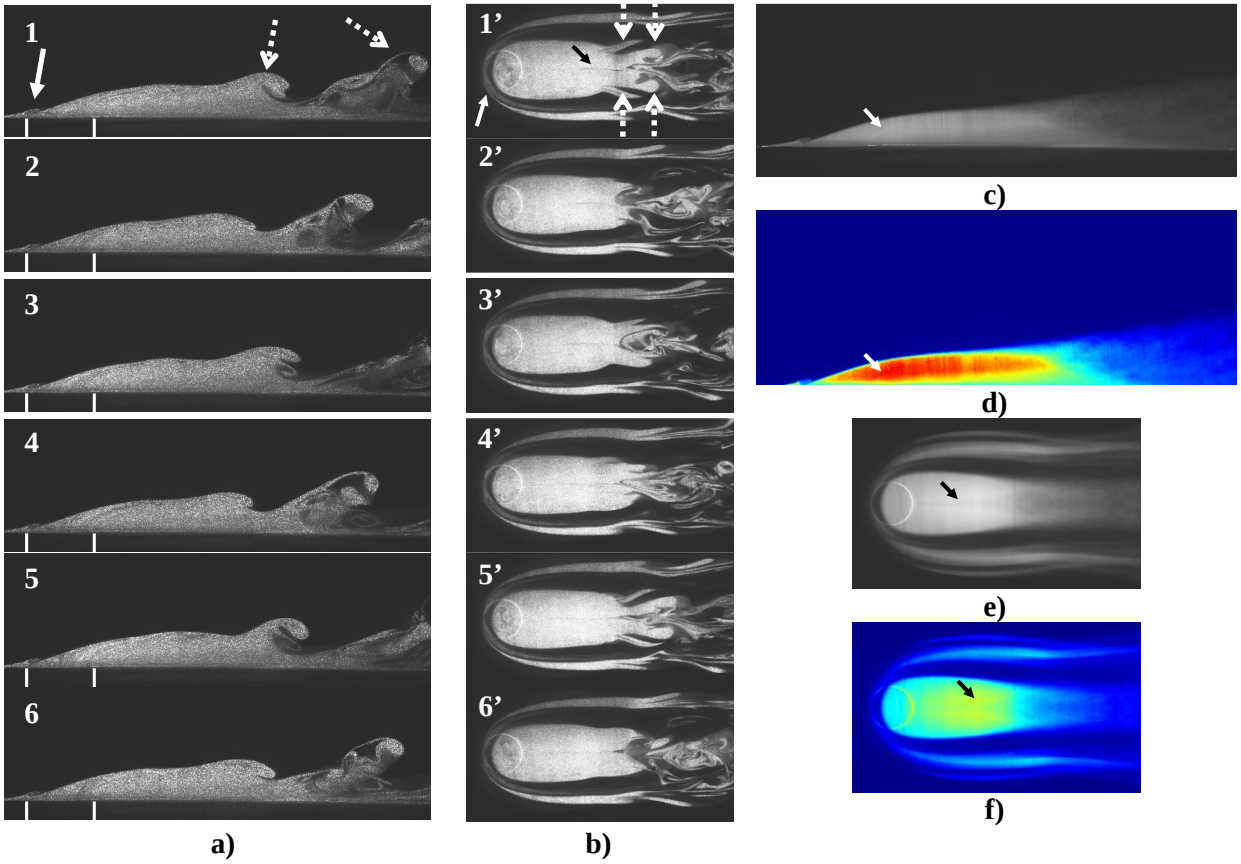

Figure 5-10: Steady State Visualizations at BR=0.150. a) (1-6) X-Z visualizations. b) (1'-6') X-Y visualizations. c) Averaged X-Z image. d) Colorized Normalized Averaged X-Z image. e) Averaged X-Y image. d) Colorized Normalized Averaged X-Y image.

At these blowing ratios, the jet is attached to the wall thus the cross-flow/jet interface and the jet footprint at the wall are stable. In addition, a recirculation region is visible behind the jet on time averaged

images mostly on the side-view visualizations for BR=0.150, and both on the side-view and the top-view visualizations for BR=0.188, suggesting a increased strength as the blowing ratio increases (Figure 5-10 c) & d) and Figure 5-12 c) through e), solid arrow).

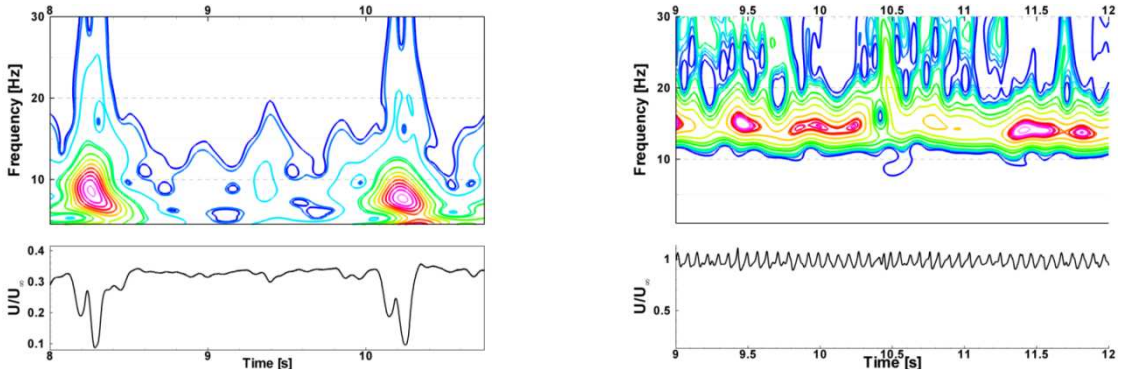

Figure 5-11: Wavelet Analysis for hot-wire measurements at BR=0.150 for a) X/D_j=0,Z/D_j=0, b) X/D_j=3.5, Z/D_j=0.75

The hot-wire measurements at the jet exit, analyzed using wavelet spectral analysis, show intermittent frequencies of the order of 6 to 8Hz for BR=0.150 (Figure 5-11 a)) and 8 to 10Hz for BR=0.188 (Figure 5-13 a)). The measurements above the jet exit did not reveal any particular frequency and are not shown here. However, at the downstream location of X/D_j=3.5 and Z/D_j=0.75, the hot-wire records show well-defined oscillations in the velocity measurements which, given the probe location, can clearly be related with the shear layer type of instability observed on the side-view and top-view visualizations. The wavelet spectral analysis (Figure 5-11 b) and Figure 5-13 b)) gives an estimation of the characteristic frequency associated with the shear layer type of instability which is of the order of 13.5 to 16Hz for BR=0.150 and 15 to 18Hz for BR=0.188. Interestingly, the frequency found at the jet exit appears to be a sub-harmonic of the frequency found at the downstream location characteristic of the shear layer instability and would suggest a relationship between one and the other. However, the shear layer instability being a convective-type of instability would unlikely be sensed at the jet exit which is located upstream of the rollups formation. An interaction between the shear layer instability and the recirculation region could be the source of the signature at the jet exit location since the recirculation region instability is an absolute-type of instability and radiates in every directions.

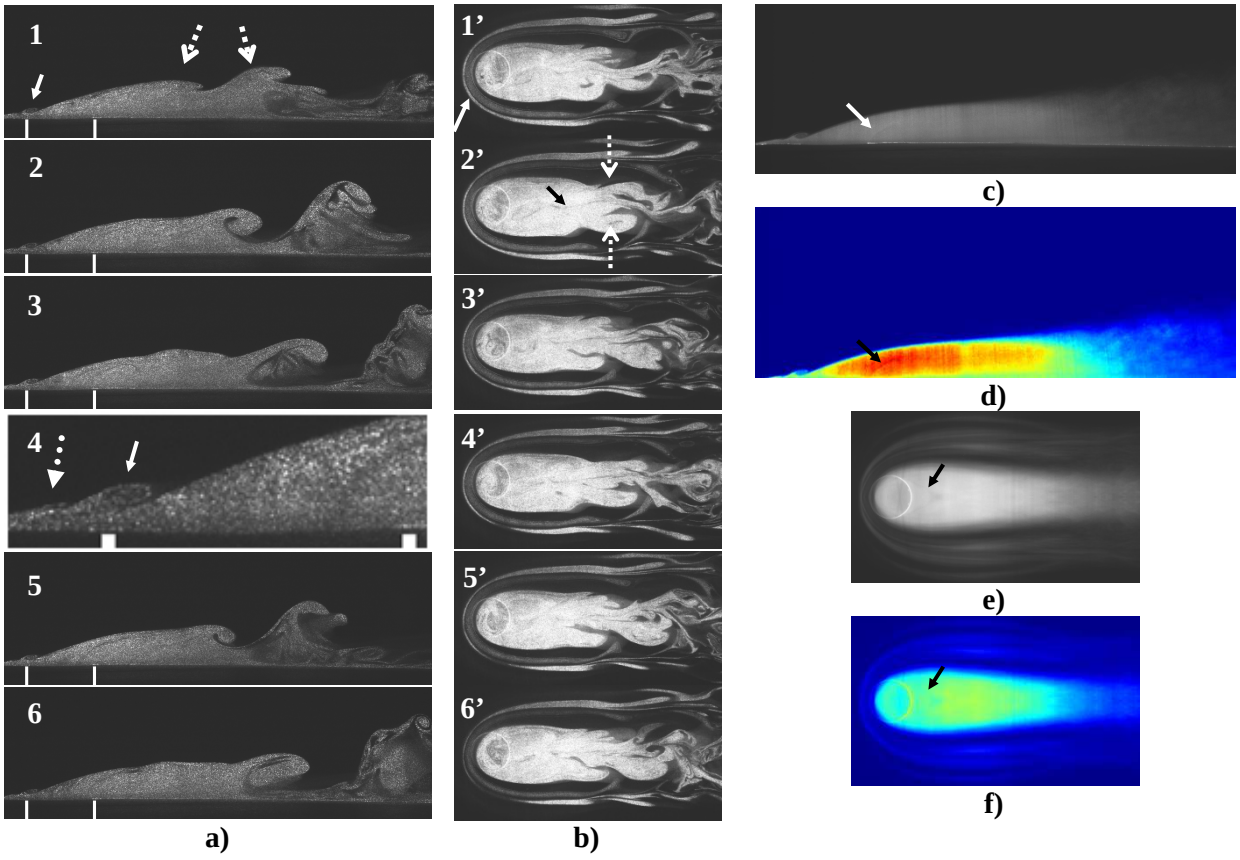

Figure 5-12: Steady State Visualizations at BR=0.188. a) (1-6) X-Z visualizations. b) (1'-6') X-Y visualizations. c) Averaged X-Z image. d) Colorized Normalized Averaged X-Z image. e) Averaged X-Y image. d) Colorized Normalized Averaged X-Y image.

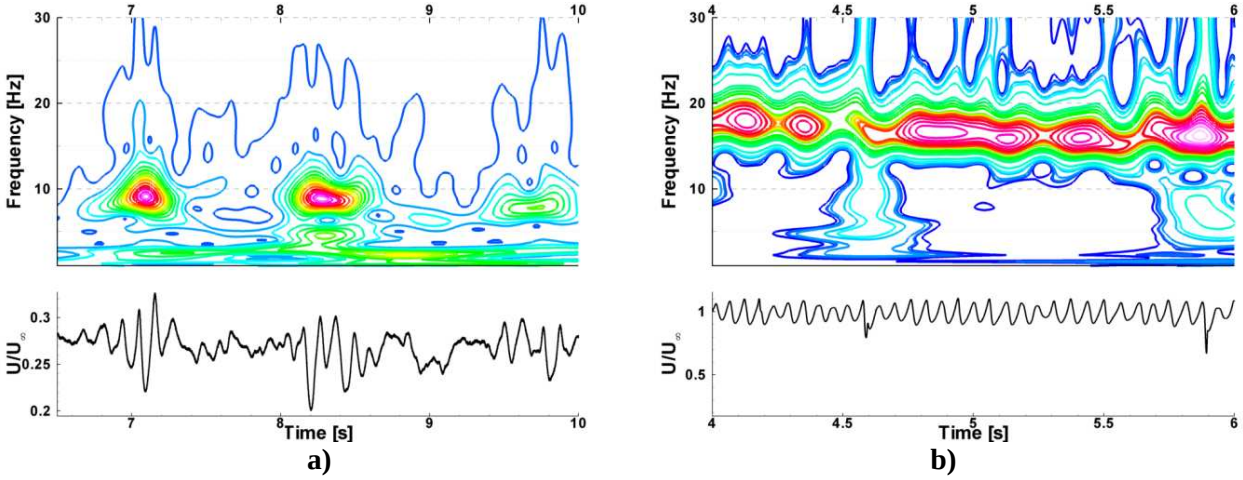

Figure 5-13: Wavelet Analysis for hot-wire measurements at BR=0.188 for a) X/Dj=0,Z/Dj=0, b) X/Dj=3.5, Z/Dj=0.75

A series of stream wise velocity profiles at X/D_j=3.5 for Z/D_j=0 to 3 for BR=0.150 and BR=0.188 was acquired using the automated traverse and sampling conditions statistically determined from exploratory measurements. The results show a clear inflectional profile characteristic of convective shear layer type of instability (Figure 5-14 a)) and the corresponding RMS velocity profiles show higher turbulence in the shear layer which is expected since this is the location where the instability is developing (Figure 5-14 b)).

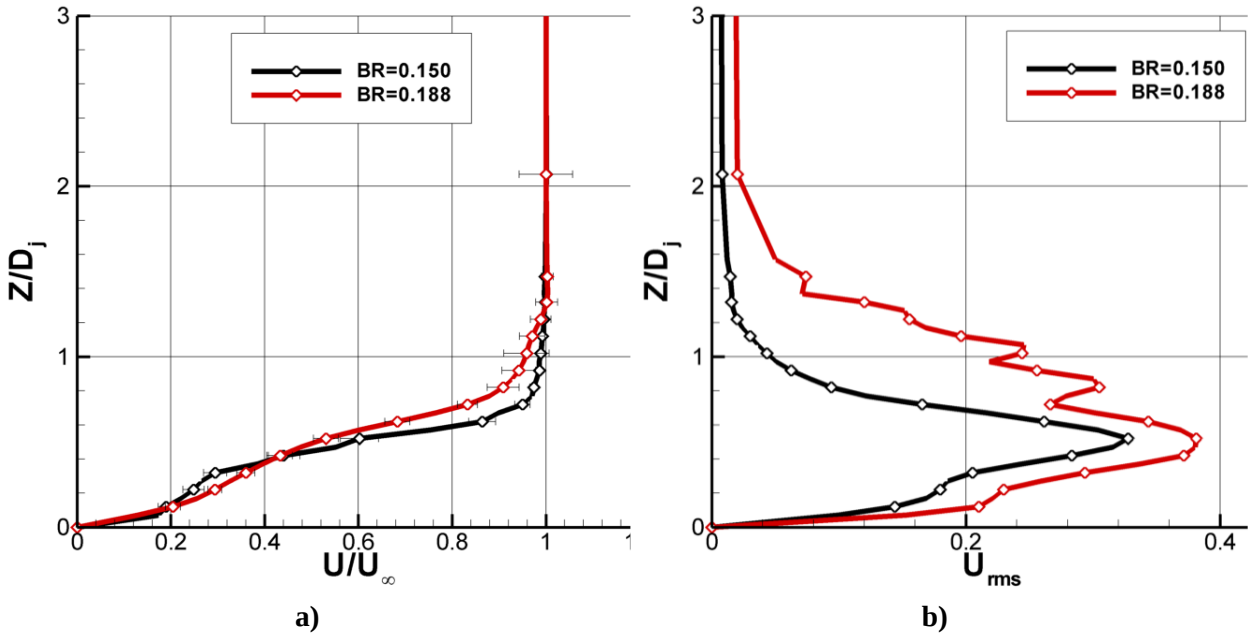

Figure 5-14: Stream wise a) Velocity profile, b) Rms velocity profile, at X/Dj=3.5, for BR=0.150 and BR=0.188.

At the highest blowing ratio of BR=0.600, the second regime is characterized by ring-like vortices forming at the exit of the jet similarly to the jet column mode instability of jet issuing in a quiescent environment (Figure 5-15 a) 1 and b) 3' dashed arrow). As the ring-like vortices penetrate into the cross-flow, the upstream part of the structure which is exposed to the free stream velocity is convected faster than the downstream part resulting in a tilting of the ring plane in a clockwise direction (Figure 5-15 a) 5, dashed line representing the plane of the ring). At this blowing ratio the jet is completely detached from the wall (Figure 5-15c) & d)) and the ring-like vortices are periodically shed. On both top-view and side-view visualizations, wake-like vortices are visible under the jet after shedding of a ring-like

vortex (Figure 5-15 a) 5 & 7 and b) 6', solid arrows). The horse-shoe vortex is no longer continuously visible on the side-view visualizations but happens to be intermittently seeded by the tracer (Figure 5-15 a) 8, solid arrow) when a ring-like vortex is forming. Similar observation can be made on the top-view visualizations where the horse-shoe vortex is sometimes seeded at the windward side like in Figure 5-15 b) 8' (solid arrow), and sometimes not like in Figure 5-15 b) 5'. This intermittent seeding explains the general discontinuous appearance of the structure and its weak signature on the averaged and colorized images (Figure 5-15 e) & f)) but is not a statement of the absence of the structure. The general footprint of the jet at the bottom wall appears to be composed of two lumps formed on each side of the jet exit, symmetric with respect of the jet centerline, swept back by the cross-flow with apparently opposite vertical vorticity (Figure 5-15 b) 5', dotted arrow). This observation is supported by the averaged images also exhibiting such forms (Figure 5-15 e) & f), dotted arrow). The lack of complementary observations, with a different plane of visualization for instance, prevents us from fully understanding the three dimensional geometry of these "counter rotating" symmetrical structures.

The hot-wire measurements at the jet exit, above the jet exit and at the downstream location show a continuous oscillation in the velocity signal (Figure 5-16 a), b), c)). According to the visualizations, these signatures are mostly due to the passage of ring-like vortices, and the frequencies observed using the wavelet analysis should be characteristic of these structures shedding frequency. According to the wavelet analysis, the fundamental frequency of these signatures is around 25Hz but can vary from 20Hz to 30Hz. In opposition to the low blowing ratios cases (BR=0.150 & BR=0.188), the fundamental frequency observed at the jet exit is of the same order as the one observed downstream which reinforces the initial supposition of the ring-like vortices being the source of the signature. Finally, the value of the shedding frequency explains why on several series of visualizations the structures appear to be fixed in time (Figure 5-15 a) 4, 5, 6, 7) or even going in the opposite direction as the one expected (Figure 5-15 a) 2, 3, 4), since the visualizations sampling frequency (30Hz) is close to the ring-like vortices shedding frequency.

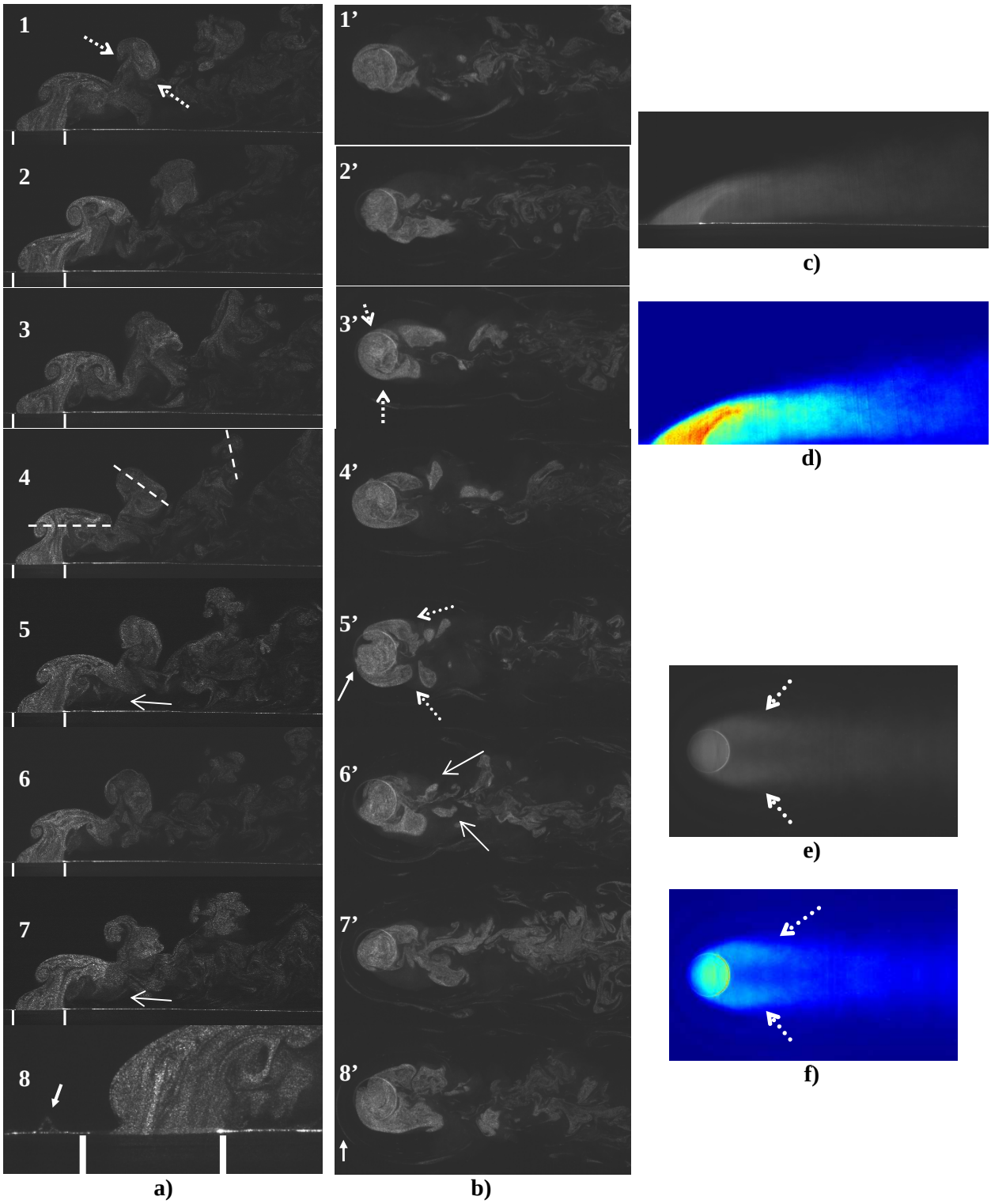

Figure 5-15: Steady State Visualizations at BR=0.600. a) (1-8) X-Z visualizations. b) (1'-8') X-Y visualizations. c) Averaged X-Z image. d) Colorized Normalized Averaged X-Z image. e) Averaged X-Y image. d) Colorized Normalized Averaged X-Y image.

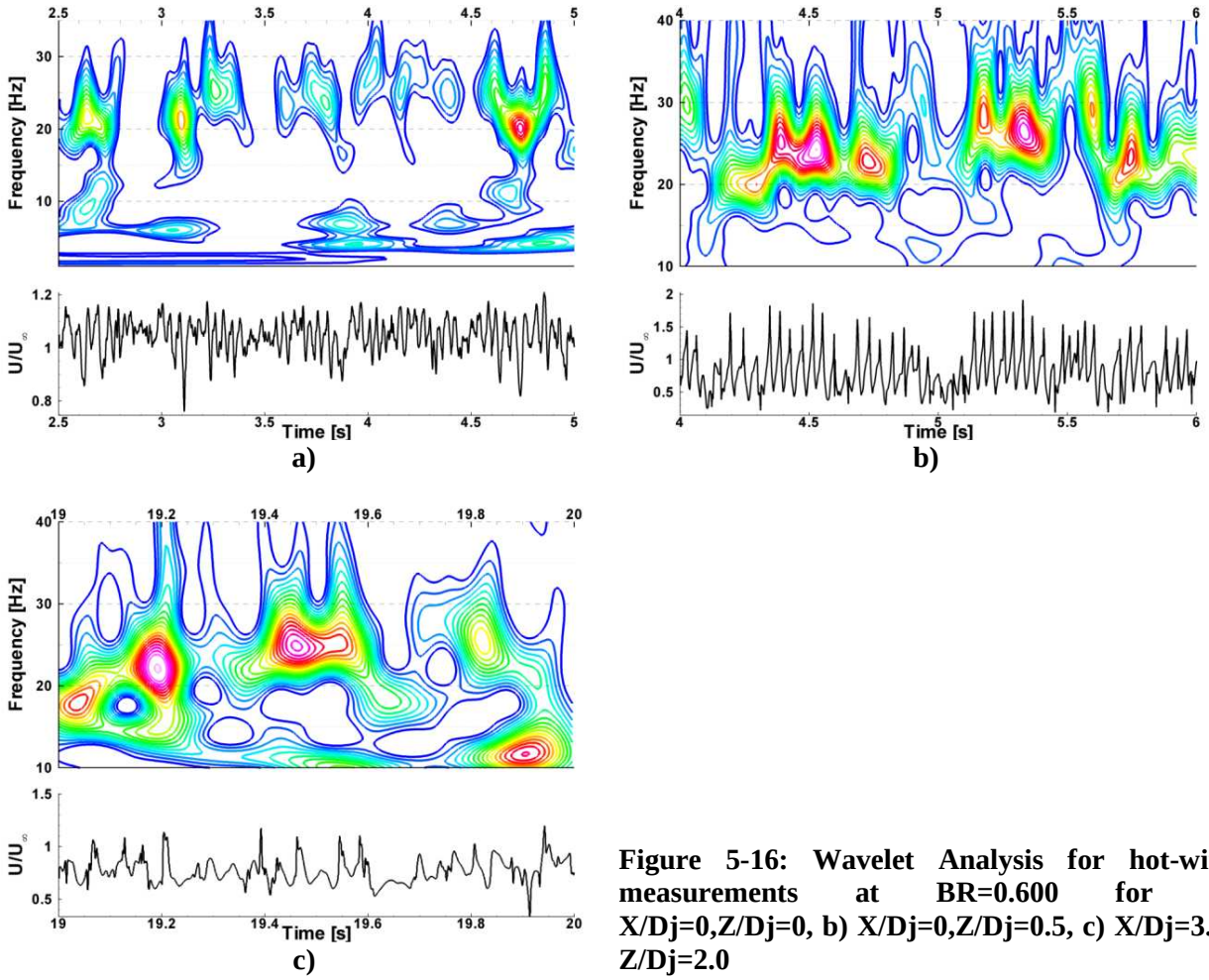

Figure 5-16: Wavelet Analysis for hot-wire measurements at BR=0.600 for a) X/Dj=0,Z/Dj=0, b) X/Dj=0,Z/Dj=0.5, c) X/Dj=3.5, Z/Dj=2.0

The cases with blowing ratios between BR=0.188 and BR=0.600, constitute several transition phases which combine the main characteristics of the two previously described regimes. One interesting feature from BR=0.150 to BR=0.600 is the evolution of the jet from an attached state at the wall with a separation region to a completely detached position. Consequently, the transition phases are characterized by destabilization, interaction with the principal structures previously observed (shear layer instabilities, ring-like vortices, horse-shoe vortex…) and eventually shedding of the separation region.

The first transition case studied was at a blowing ratio of BR=0.250. At the particular blowing ratio, the shear layer instability mode is still dominant but the structures generated indicate a possible interaction with the separation region. This transition phase is characterized by an erratic alternation of a stable separation region with shear layer instability (Figure 5-17 a) 1 & 8, dotted arrow for the recirculation region, dashed arrow for the shear layer instability), similar to first regime, and shedding of

vorticity directly from the separation region distinguished on the side-views by larger clockwise rotating structures (Figure 5-17 a) 5, 6, 7 & 8, blue arrow).

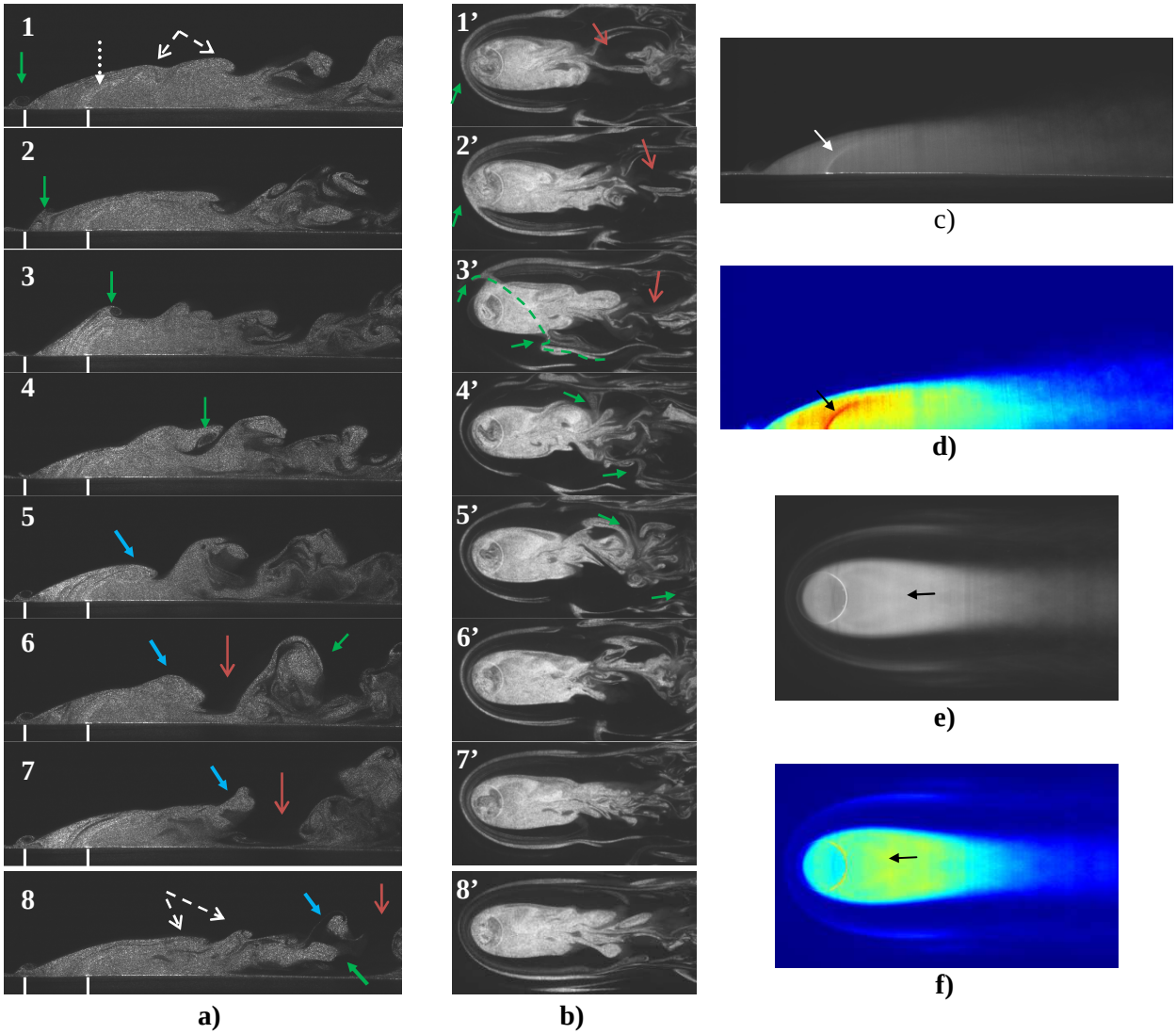

Figure 5-17: Steady State Visualizations at BR=0.250. a) (1-8) X-Z visualizations. b) (1'-8') X-Y visualizations. c) Averaged X-Z image. d) Colorized Normalized Averaged X-Z image. e) Averaged X-Y image. d) Colorized Normalized Averaged X-Y image.

When the recirculation region becomes unstable, the cross-flow is allowed to penetrate the jet and eventually creates an early break up in the jet coverage (Figure 5-17 a) 5, 6, 7, 8 and b) 1', 2', 3', red arrow). Occurrences of horse-shoe vortex transport on top of the jet upper interface are frequently observed (Figure 5-17 a) 1, 2, 3, 4 and b)1', 2', 3', 4', 5', green solid arrows and dashed lines) adding clockwise vorticity to the shear-layer instability structures resulting in an increase of their size (Figure

5-17 a) 6, green arrow) and most of the time, triggering the separation region vorticity shedding (Figure 5-17 a) 5, blue arrow). The downstream shear layer and recirculation region are clearly visible on the phase averaged and the colorized images (Figure 5-17 c), d), e) & f), solid arrow). On the same images, the horse-shoe vortex appears less defined when compared to similar images in the previous cases at BR=0.150 and BR=0.188, which is in agreement with the observed instability of this structure.

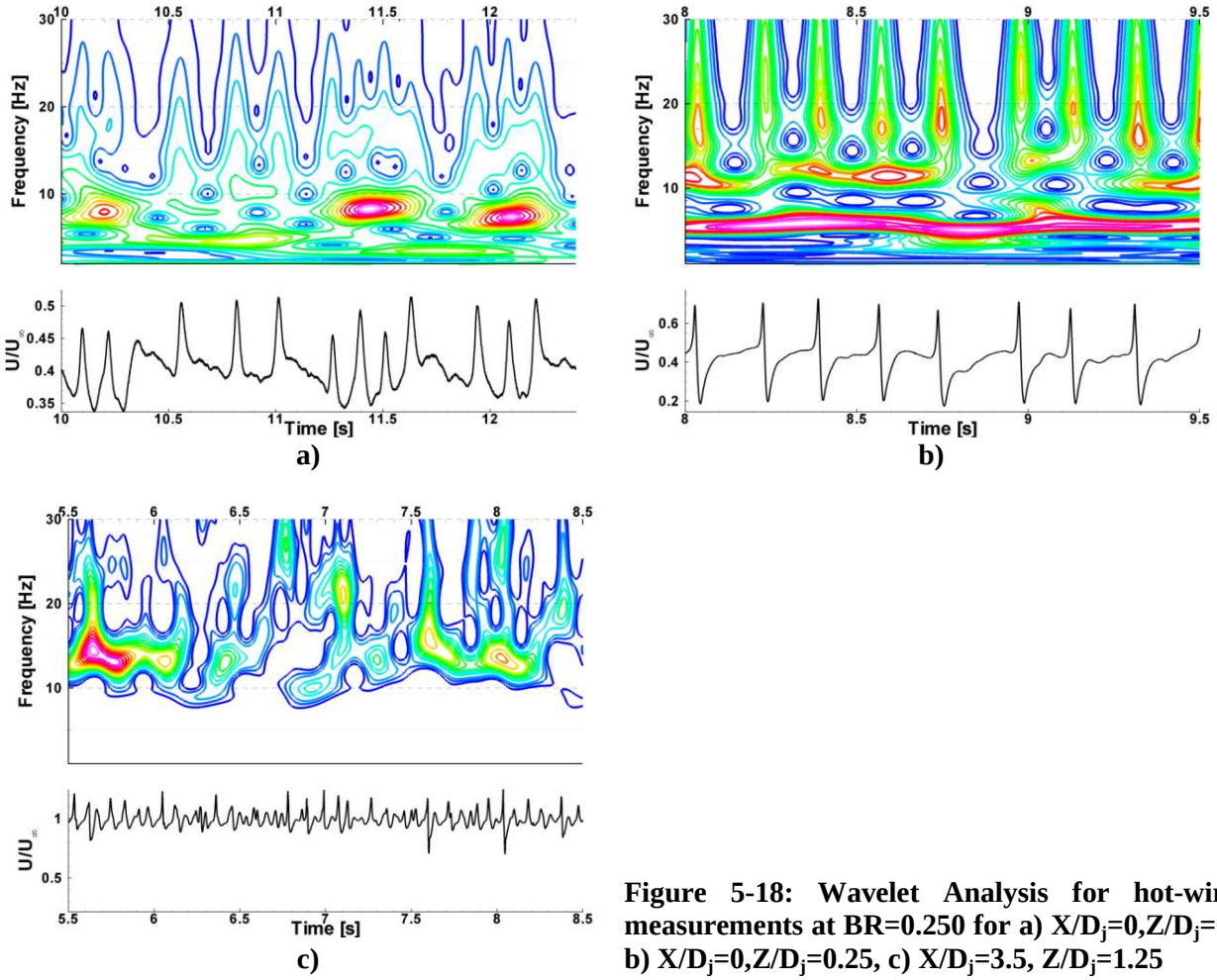

Figure 5-18: Wavelet Analysis for hot-wire measurements at BR=0.250 for a) $X/D_j=0, Z/D_j=0$, b) $X/D_j=0, Z/D_j=0.25$, c) $X/D_j=3.5$, $Z/D_j=1.25$

The velocity records obtained at the jet exit exhibit intermittent oscillations with a fundamental frequency around 8Hz which can drop to 4.5Hz (Figure 5-18 a)). From the visualizations, no apparent structure can be associated with this signature, and it is probable that the recirculation region instability is the source of these oscillations. The measurements performed above the jet exit, in the jet upper shear layer, show a clearly periodic signal with a fundamental signature of the order of 6Hz but also identified first and second harmonics of 12 and 18Hz (Figure 5-18 b)). However, these harmonics are probably a

result of the wavelet analysis as a response to the signal periodic discontinuity given that no apparent other signature is visible on the velocity record. According to the visualizations, these oscillations in the flow velocity have two possible sources. One of them is the horse-shoe vortex transport, since the probe location is directly on the path of the transported structure; the second one is the recirculation region instability shedding. Because the horse-shoe vortex transport is likely to trigger the recirculation region shedding, both events occur in fact at the same frequency. The last CTA measurement is performed at the downstream location for Z/D_j=1.25 and shows signs of oscillations at a fundamental frequency of 13.5Hz varying from 12 to 16Hz. The periodicity of the signal is not as well-defined as for BR=0.150 and BR=0.188 at the same location probably because of the intermittency of the shear layer type of instability.

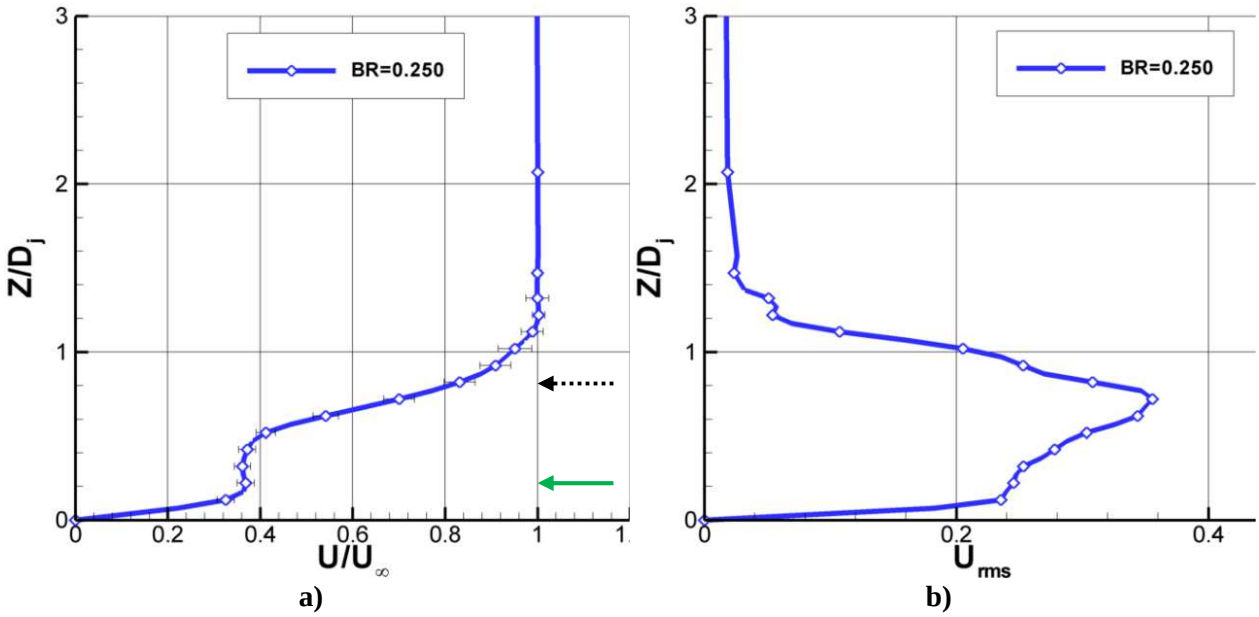

Figure 5-19: Stream wise a) Velocity profile, b) Rms velocity profile, at X/Dj=3.5, for BR=0.250.

Similarly to BR=0.150 and BR=0.188, a stream wise velocity profile was recorded at the downstream location of X/D_j=3.5 for Z/D_j=0 to 3. These measurements show a double inflectional profile due to the upper shear layer (Figure 5-17 a), 1 and Figure 5-19 a), dashed arrows) and the recirculation region momentum shed when this structure becomes unstable (Figure 5-17 a) 8 and Figure 5-19 a) green solid arrows). The RMS velocity profile is similar to the previous two with a peak of turbulence in the region of the shear layer (Figure 5-19 b)).

The next steady state blowing ratio studied in the transition region is BR=0.300. For this case, the visualizations show another type of transition consisting in an alternation between attached jet with shear layer type of instability with horse-shoe vortex transport (Figure 5-20 a) 1, 2 & 3 and b) 1', 5', 6' & 7'), and periodic ring-like vortices/recirculation region shedding (Figure 5-20 a) 4 to 8), the former being similar to the previous case (BR=0.250), the latter to the higher blowing ratio case (BR=0.600).

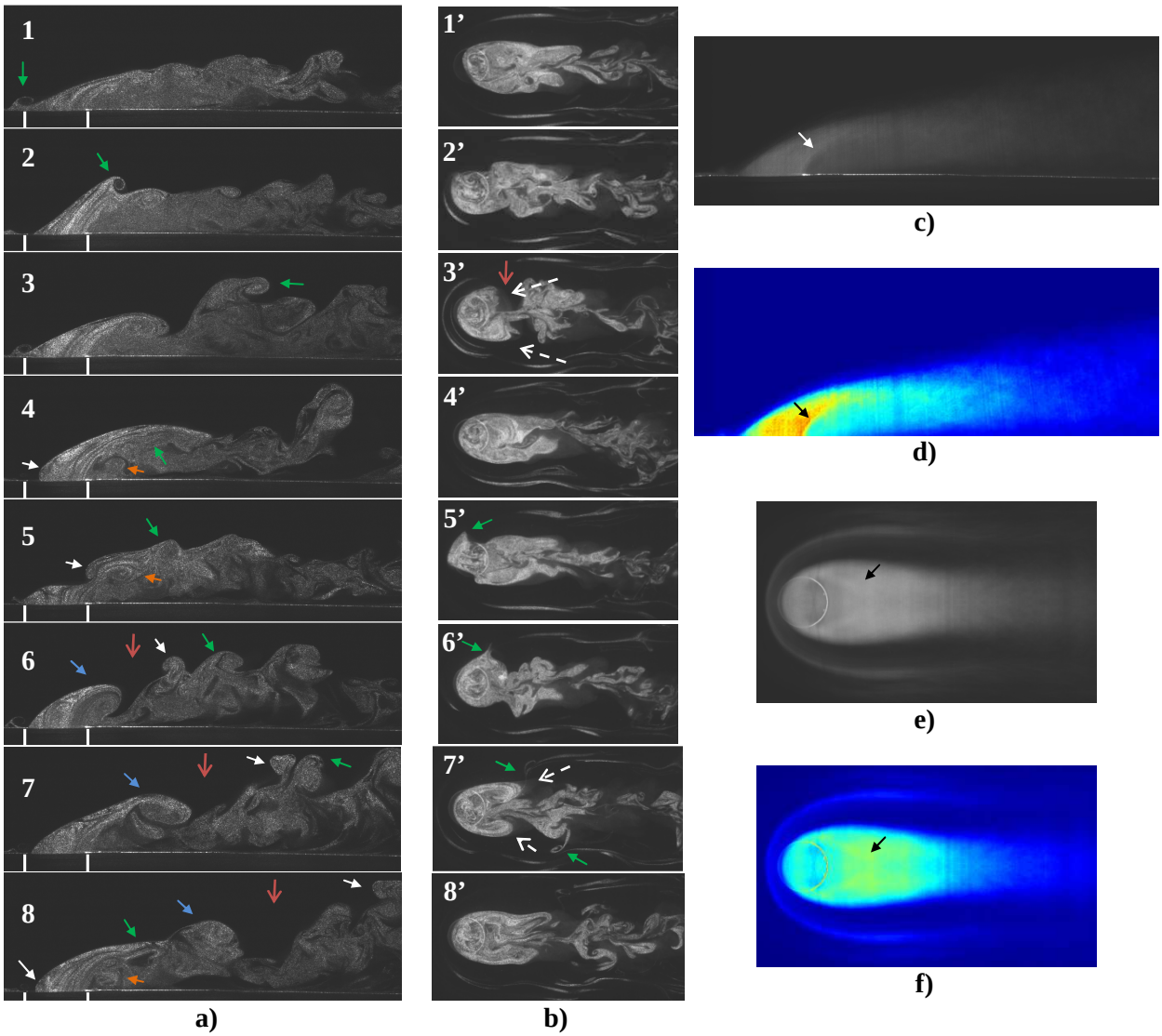

Figure 5-20: Steady State Visualizations at BR=0.300. a) (1-8) X-Z visualizations. b) (1'-8') X-Y visualizations. c) Averaged X-Z image. d) Colorized Normalized Averaged X-Z image. e) Averaged X-Y image. d) Colorized Normalized Averaged X-Y image.

The ring-like vortices have an unbalanced structure with smaller rollups upstream (Figure 5-20 a) 4, 5 & 8, solid arrow) forming inside the jet feeding tube, compared to the downstream part (Figure 5-20

a) 4, 5, 6 & 8, orange solid arrow) forming outside the jet and extracting vorticity from the recirculation region. The ring-like vortices are shed into the free stream allowing the cross-flow to flatten the jet upper interface above the jet exit (Figure 5-20 a) 5), penetrate the jet (Figure 5-20 a) 6), resulting in an early break up (Figure 5-20 a) 6, 7 & 8 and b) 3', red arrow) and triggering the detachment of the recirculation region vorticity (Figure 5-20 a) 6, 7 & 8, blue arrow). The horse-shoe vortex is not always visible and is periodically seeded during the cross-flow penetration where a part of the jet fluid is carried upstream (Figure 5-20 a) 5 & 8 b) 5' & 7'). This is supported by the intermittent visibility of the horse-shoe vortex at the windward side on the top-view visualizations (Figure 5-20 b) 2', 3' & 4'). The recirculation region vorticity shedding is followed by a redevelopment of the jet with lower shear layer instabilities (Figure 5-20 a) 4, 5, 6, 7 & 8, orange arrow) and formation of two lumps on each side of the jet exit, symmetrical with respect to the jet centerline, swept back by the cross-flow and of apparently opposite vorticity in the Z direction, very similar to the one observed in the BR=0.600 case (Figure 5-20 b) 3' & 7', dashed arrows). Visualizations also show occurrences of interactions between shear layer instability structures (green solid arrows) of positive y-vorticity with the next ring-like vortex upstream part (white solid arrows) of negative y-vorticity (Figure 5-20 a) 5, 6, 7 & 8). Horse-shoe vortex transport is observed on both side-view and top-view visualizations, but does not occur as often as in the case at BR=0.250 (Figure 5-20 a) 1 & 2 and b) 5', 6' & 7'green solid arrows). The averaged images clearly show the recirculation region (solid arrows) and already a trend to detach (Figure 5-20 c), d), e) & f)). On the top-view and side-view colorized averaged images, the trace of the horse-shoe vortex is weak and not well-defined which is in agreement with the instantaneous images where the structure is not always seeded by the tracer.

The jet exit velocity records exhibit intermittent oscillations at a fundamental frequency around 8Hz dropping to 4.5Hz occasionally (Figure 5-21 a)), comparable to the one observed at BR=0.250 and probably from the same source. The velocity measurements above the jet exit and inside the upper shear layer at Z/D_j=0.25 are slightly different than the previous one. Even though oscillations are clearly observable on the record at a fundamental frequency of 8Hz, a clear signature of a second harmonic (16Hz) and even a fourth (32Hz) is now visible. This signature could be explained by the coupled

shedding of structures in a periodic manner similarly to the cycle observed on Figure 5-21 a) 4 to 8, where the first peak in velocity could be due to the passage of the upstream rollup of the ring-like vortex (Figure 5-21 b), solid arrow) and the second to the shedding of vorticity from the recirculation region (Figure 5-21 b), dashed arrow). Finally, the record at the downstream location exhibits clear oscillations at a fundamental frequency of 16 Hz and is likely to be related to the coupled shedding.

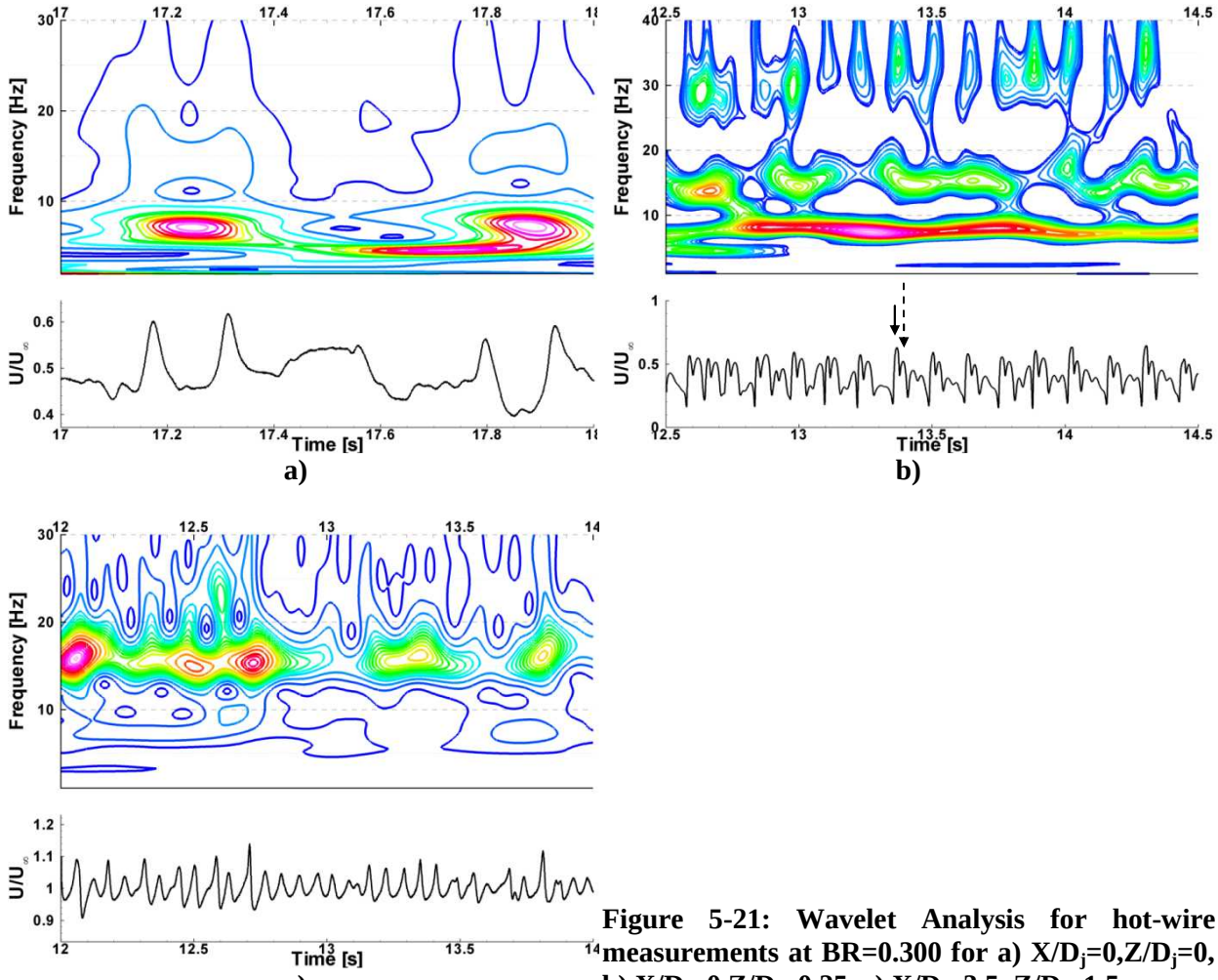

Figure 5-21: Wavelet Analysis for hot-wire measurements at BR=0.300 for a) X/D_j=0,Z/D_j=0, b) X/D_j=0,Z/D_j=0.25, c) X/D_j=3.5, Z/D_j=1.5

At BR=0.365 the structures are comparable to those observed at BR=0.300 with now only few occurrences of an attached jet and a predominance of ring-like vortices periodic shedding (Figure 5-21 a) 1 to 8), implying more break-ups and cross-flow brought to the wall (Figure 5-22a) 1 to 8 and b) 3' & 4', red arrows). The upstream part of the ring-like vortices is still formed inside the jet but appears to be closer from the jet exit (Figure 5-22 a) 1, 2, 4, 5 & 6, solid white arrow). On average, the jet breakup

appears to happen closer from the jet exit and the two symmetrical structures observed in the two previous cases and at BR=0.600 when the recirculation region is shedding are still present (Figure 5-22 b) 3', 4', 7' & 8', dashed arrows). These symmetrical structures are also noticeable on the top-view averaged and colorized normalized images revealing their preponderance in time (Figure 5-22 e) & f)).

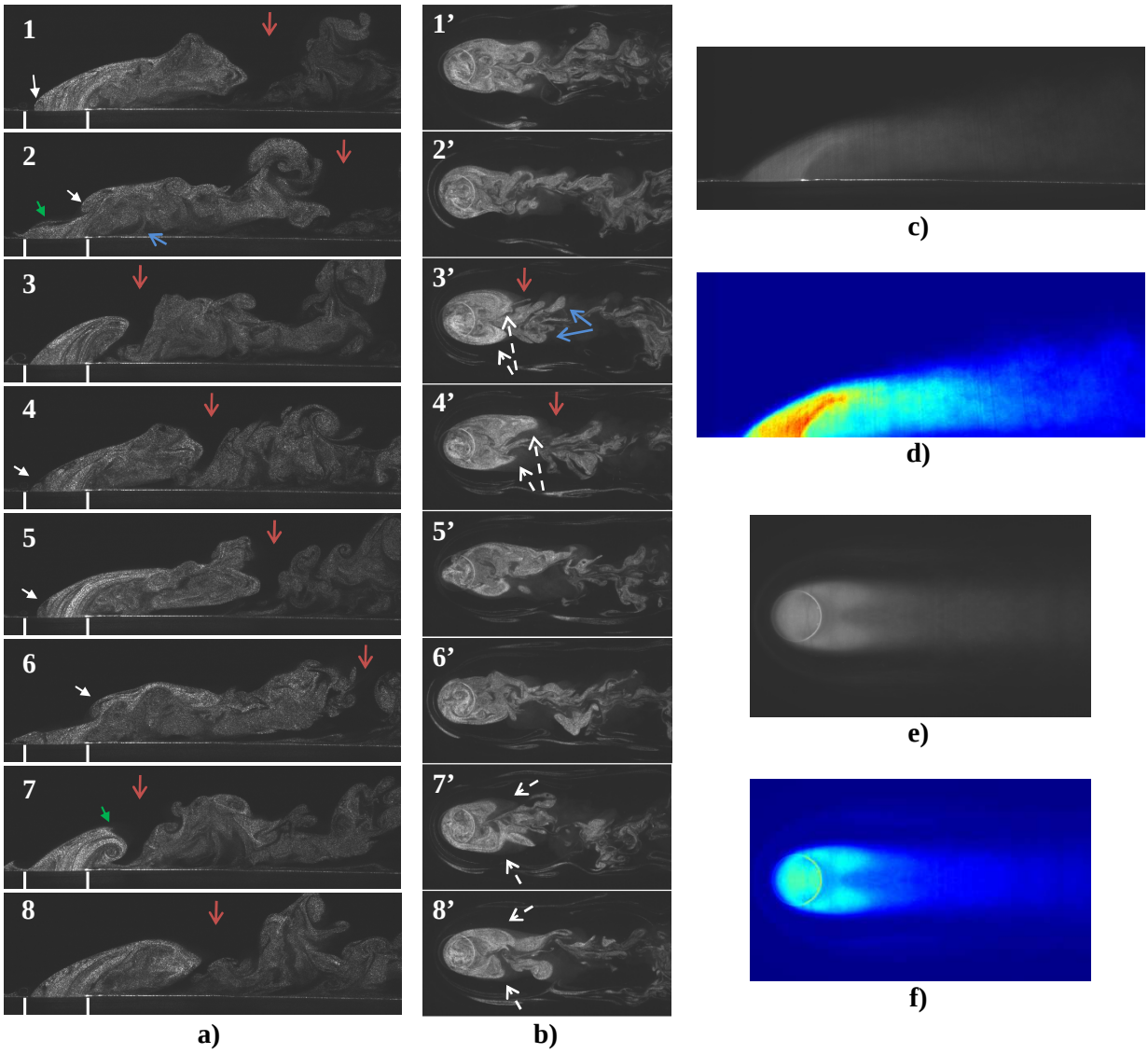

Figure 5-22: Steady State Visualizations at BR=0.365. a) (1-8) X-Z visualizations. b) (1'-8') X-Y visualizations. c) Averaged X-Z image. d) Colorized Normalized Averaged X-Z image. e) Averaged X-Y image. d) Colorized Normalized Averaged X-Y image.

Wake vortices are eventually visible but the formation of this kind of structures is secondary (Figure 5-22 a) 2 & b) 3', blue arrows). The horse-shoe vortex is only periodically seeded by the tracer

making it almost impossible to visualize, but some side-view visualizations suggest that when the jet top interface flattens at the shedding of a ring-like vortex, the horse-shoe vortex might ride on top of the interface (Figure 5-22 a) 2, & 7 and Figure 5-23, green arrow). The averaged side-view image is very similar to the previous case at BR=0.300 with a visible separation region downstream of the jet exit (Figure 5-22 c) & d)). The X-Y averaged image and colorized normalized averaged image show a net decrease in the footprint area of the jet at the wall (Figure 5-22 e) & f)).

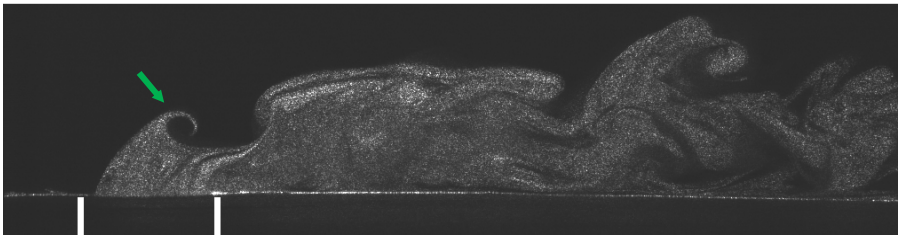

Figure 5-23: Example of a horse-shoe vortex riding the flattened interface of the jet after the ring-like vortex shedding.

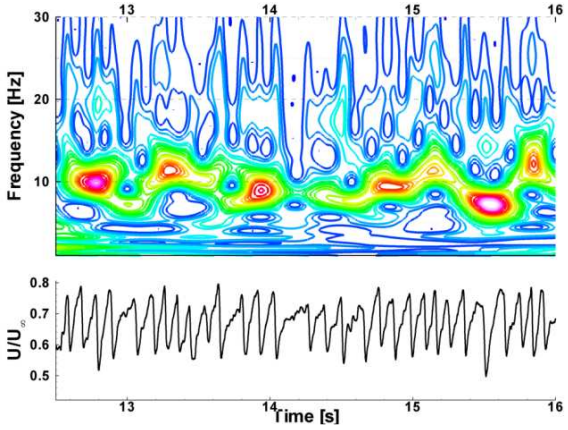

a)

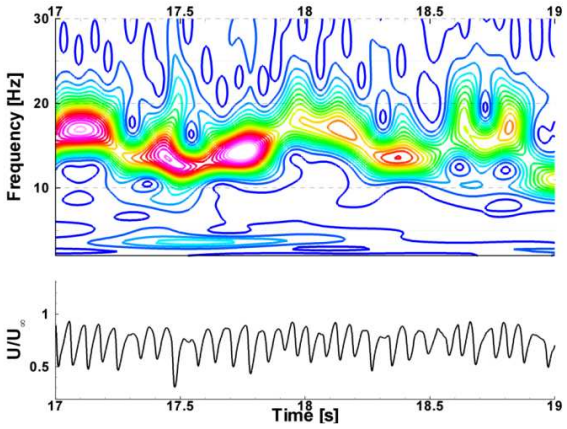

b)

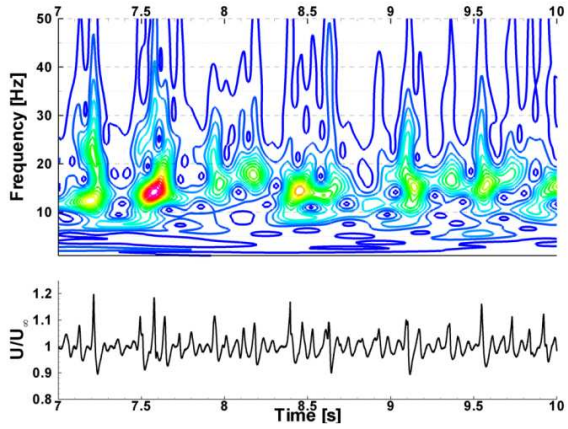

c)

Figure 5-24:Wavelet Analysis for hot-wire measurements at BR=0.365 for a) $X/D_j=0, Z/D_j=0$, b) $X/D_j=0, Z/D_j=0.25$, c) $X/D_j=3.5$, $Z/D_j=1.5$

Hot-wire measurements performed at the jet exit display oscillations with a fundamental frequency of 9 to 10Hz and a weak first harmonic around 18 to 20Hz can be spotted around t =13s and t=14s (Figure 5-24 a)). Above the jet exit, the velocity record is similar with oscillations at a frequency of the order of 15 to 18Hz probably coming from the ring-like vortex/recirculation region coupled shedding. The same range of frequencies is found on the CTA records at the downstream location for Z/D_j=1.5. The similarity in the signatures of these three velocity records suggests that their source is identical, probably convected from the jet exit to the downstream location, and supports the possibility of being characteristic to the structures shed such as the ring-like vortices or the recirculation region.

The last transition case (BR=0.465) has strong similarities with the previous case at BR=0.365 and the formation and shedding of ring-like vortices/recirculation region are now continuous. The ring-like vortices appear to have more balanced structure with bigger upstream rollups (Figure 5-25 a) 1, 3, 4, 5, 7 & 8, solid white arrow) that are forming almost outside of the jet (Figure 5-25 a) 4 & 7 and b) 2' & 6'). After shedding, the recirculation region appears to separate into two substructures one going upward in the free stream (Figure 5-25 a) 4, 5, 7 & 8, blue arrow), and the other part going toward the bottom wall (Figure 5-25 a) 4, 5, 7 & 8, red arrow). This separation was also observable in the previous case at BR=0.365 but the two substructures were hardly differentiable because of the lower jet penetration and the lack of space for the structures to really come apart (Figure 5-22 a) 2, 3, 4 & 8). Wake vortices (Figure 5-25 b) 2', blue arrows) and the two symmetrical structures developing after the recirculation region shedding (Figure 5-25 b) 2', 7' & 8', e) and f), dashed arrow) are visible on most of the top-view visualizations reminding of the higher blowing ratio case (BR=0.600). The averaged and colorized normalized averaged X-Z images exhibit an increased penetration of the jet and a more detached jet (Figure 5-25 c) & d)). Even though only periodically seeded and visible, the horse-shoe vortex appears to have stopped shedding and to occupy a stable location on the windward side of the jet exit.

The hot-wire measurements performed at the jet exit show clear oscillations in the velocity signature at a fundamental frequency of 18Hz (Figure 5-26 a)). In the upper shear layer, the stream wise velocity record is very similar to the previous one with identical frequencies around 18Hz (Figure 5-26

b)). Finally, the CTA record at the downstream location for Z/D_j=1.5, supposedly also in the in the upper shear layer, exhibits intermittent frequencies also around 18Hz with an unclear signature probably due to an inaccurate choice in the measurement location using the side-view visualizations (Figure 5-26 c)). These signatures are, according to the visualizations, characteristic of the ring-like vortices formation/shedding.

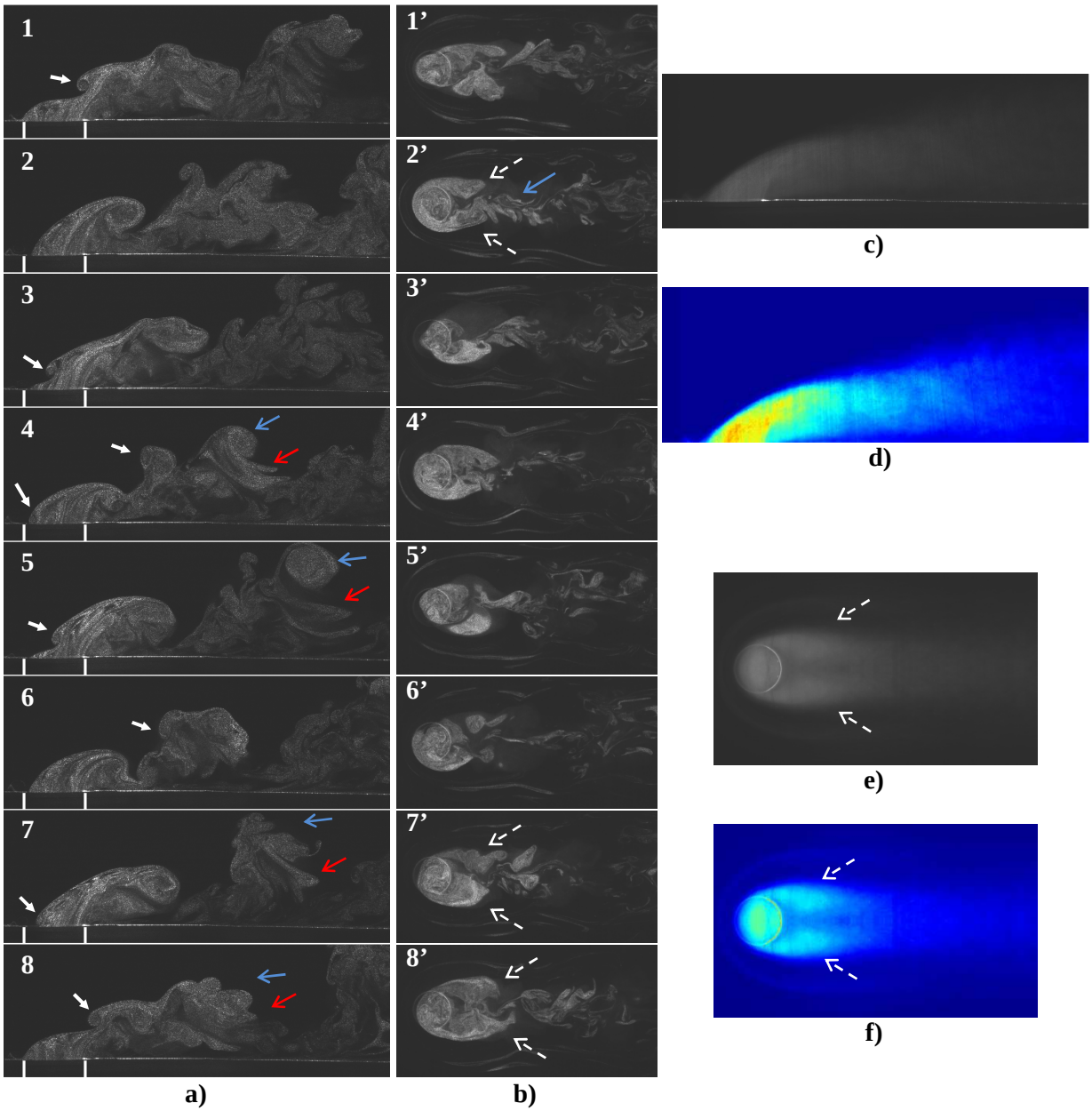

Figure 5-25: Steady State Visualizations at BR=0.465. a) (1-8) X-Z visualizations. b) (1'-8') X-Y visualizations. c) Averaged X-Z image. d) Colorized Normalized Averaged X-Z image. e) Averaged X-Y image. d) Colorized Normalized Averaged X-Y image.

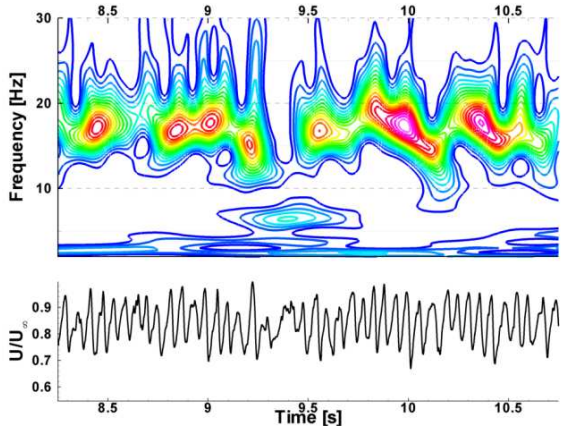

a)

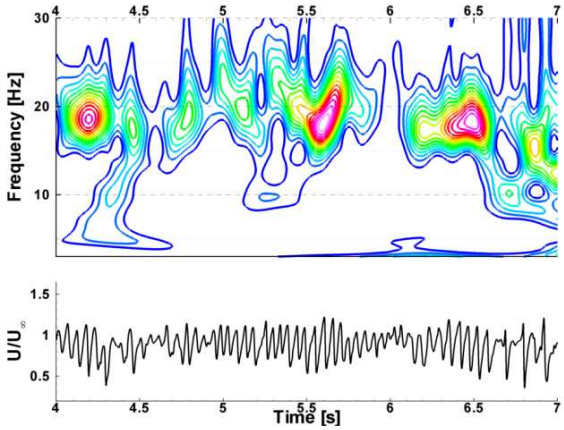

b)

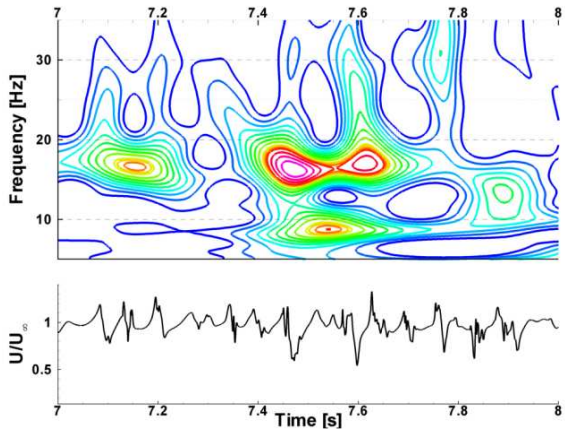

c)

Figure 5-26: Wavelet Analysis for hot-wire measurements at BR=0.465 for a) X/Dj=0,Z/Dj=0, b) X/Dj=0,Z/Dj=0.25, c) X/Dj=3.5, Z/Dj=1.5

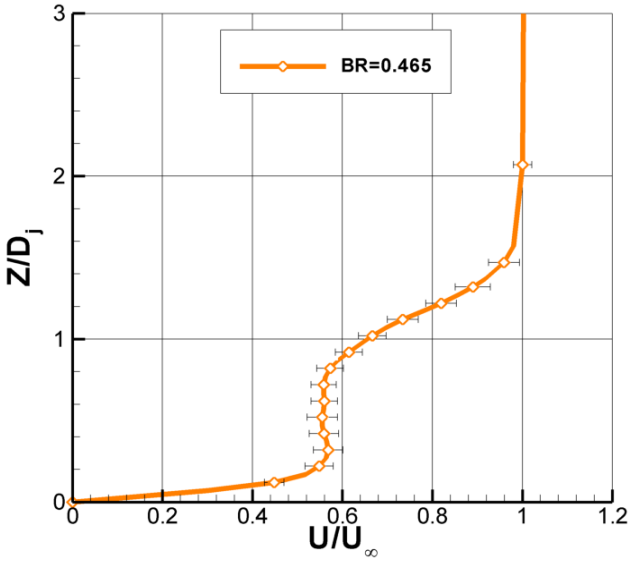

a)

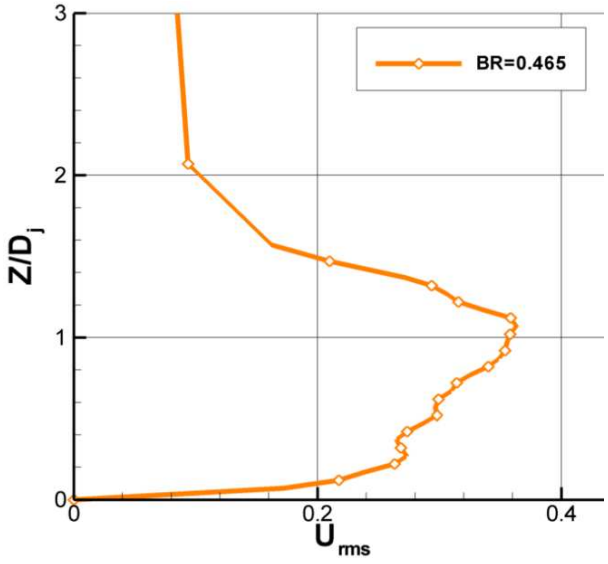

b)

Figure 5-27: Stream wise a) Velocity profile, b) RMS velocity profile, at X/Dj=3.5, for BR=0.465.

This case was one of the selected cases where a velocity profile was acquired (Figure 5-27). The profile is very comparable to the one measured at BR=0.250 with a double inflection but a higher shear layer region location. The corresponding RMS velocity profile shows without surprise higher turbulence in the shear layer region.

The ranges of fundamental frequencies found using wavelet analysis and the discrete fundamental frequencies found using the Fourier spectrum analysis are plotted as Strouhal numbers in Figure 5-23 a) & b) using two different types of scaling. The first Strouhal number St_∞ is computed based on the fundamental frequency, the jet diameter and the cross-flow velocity, while the second Strouhal number St_j is based on the fundamental frequency, the jet diameter and the jet mean velocity. The first scaling based on the cross-flow velocity appears to be accurate for blowing ratios below BR = 0.300, characterized by shear layer instabilities, while the Strouhal number based on the jet velocity appears to scale better the frequencies for blowing ratios above BR = 0.365 characterized by ring-like vortices formation. This was expected since shear-layer type of instabilities are usually scaled using the shear layer thickness which, according to the velocity profiles taken at $X/D_j = 3.5$, is of the order of the jet diameter, and the absolute velocity difference across the shear layer which for low blowing ratios is of the order of the cross-flow velocity.

Conversely, at higher blowing ratios, the jet generates structures similar to jet column mode structures of jet in free stream which are scaled with Strouhal numbers based on jet velocity and shear layer momentum thickness or jet diameter. An estimation of a characteristic St_∞ value for BR $\leq$ 0.300 is 0.236 +/- 0.02 downstream and 0.122+/-0.009 at the jet exit. Similarly, an estimation of a characteristic value of St_j for BR $\geq$ 0.365 is 0.643+/-0.06 (uncertainties with 95% confidence interval). One may notice the last value of estimated St_j relatively high for a jet entering in pseudo jet column mode which usually is between 0.25 for weak jets and 0.45 for strong jets. However, our computation of St_j is based on the jet mean velocity which is lower than the maximum velocity used in the jet column mode characterization. To obtain an estimate of this maximum velocity, we can use the hot-wire measurements made at the jet exit and compare its value to the mean value of the jet velocity computed from the flow-meter records.

The averaged jet mean velocity to hot-wire measured velocity ratio is 0.55 for BR ≥ 0.365 which would result in an approximated St_j based on the maximum velocity of 0.354, more acceptable for comparison.

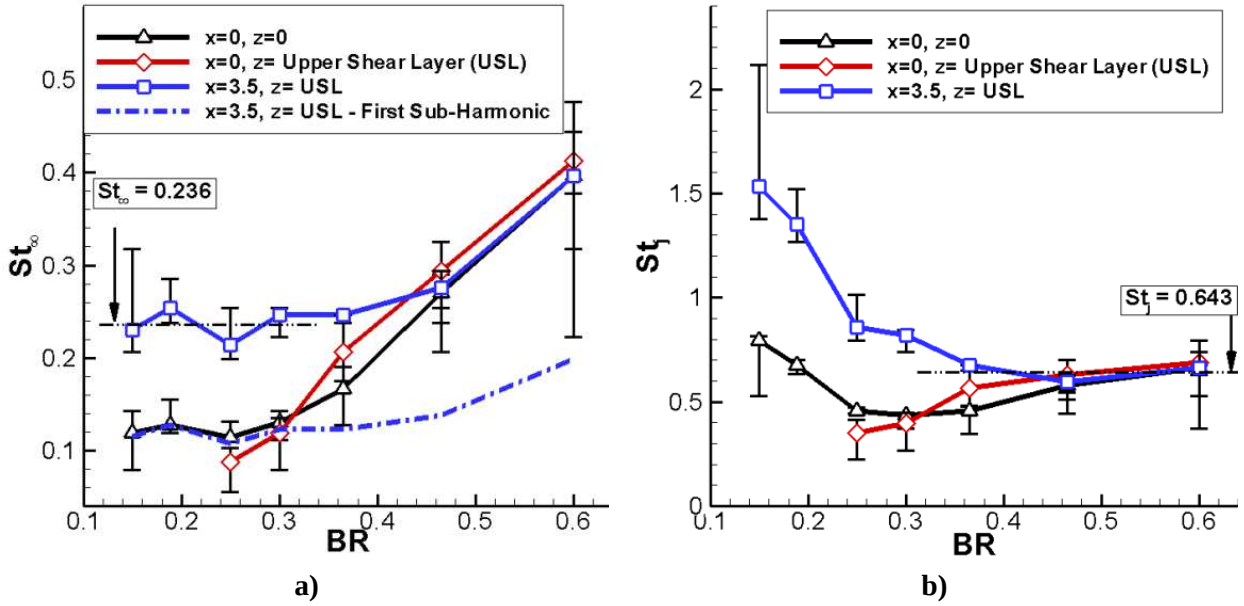

Figure 5-28: Fundamental frequencies from wavelet analysis scaled using: a) the Strouhal number based on the cross-flow velocity, b) the Strouhal number based on the jet mean velocity, plotted as a function of the blowing ratio.

As explained earlier, the lack of a third visualization plane prevents a complete explanation of the dynamics of the ring vortices and the symmetrical structures observed after the shedding of the recirculation region/ring-like vortices. First, the recirculation region vorticity shedding could be in fact a ring-like vortex with a large downstream rollup influenced by the recirculation region vorticity, and a very small upstream rollup, sometimes not visible when the structure is shed, but visible when the structure is formed (Figure 5-29).

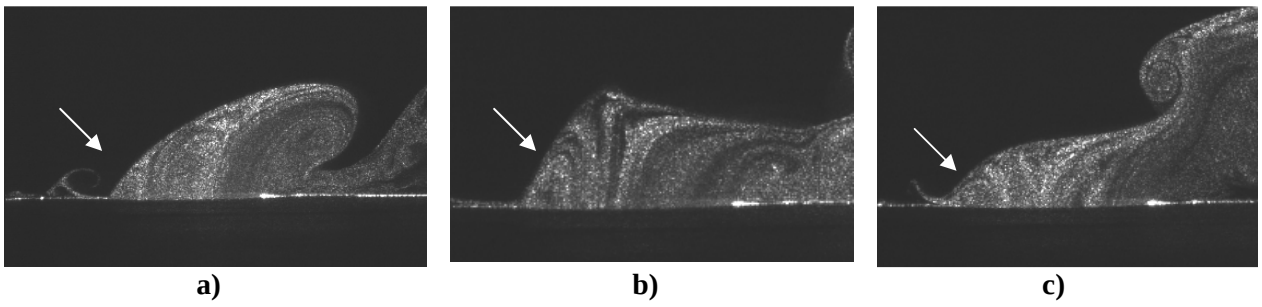

Figure 5-29: Recirculation region vorticity shedding at a) BR=0.300, b) BR=0.365, c) BR=0.465

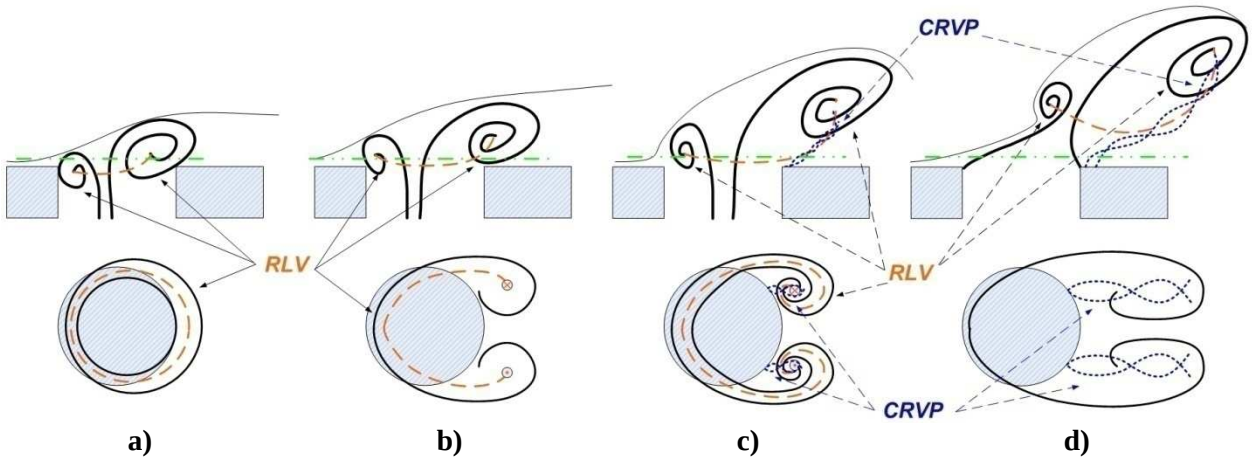

Figure 5-30: Possible dynamics of the ring-like vortices/recirculation region vorticity shedding.

In these conditions, an explanation to the formation of the symmetrical lumps visible on the top-view visualizations can be formulated. They could be the "side arms" of ring-like vortices, stretched by the convection of the downstream rollup, and folded behind the jet by the cross-flow (Figure 5-30 a), b), c) and Figure 5-31 1 to 4). Ultimately, the ring-like vortex is convected in the free stream, and the vertical vorticity generated by the folding of the side arms could be the origin of a redeveloping counter rotating vortex pair (Figure 5-30, c), d)). A schematic of the imagined evolution of the core of the ring-like vortex is presented in Figure 5-31:

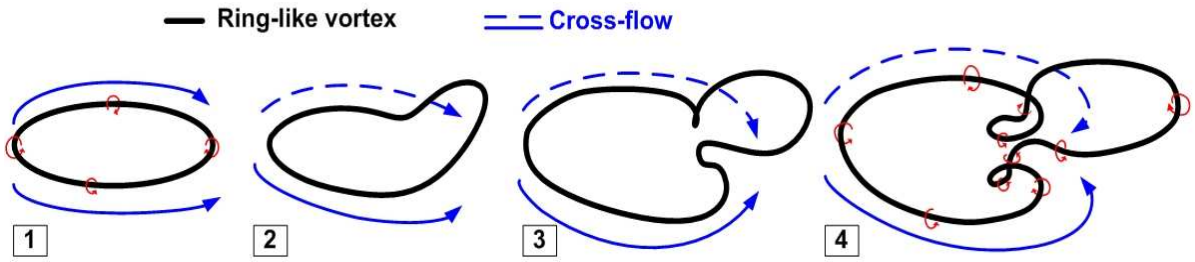

Figure 5-31: Imagined dynamics of the core of the ring-like vortex.

5.2.2. Image Quantification

5.2.2.1. X-Z Visualizations

Even though the side views gave precious qualitative information in term of the structures involved at different regimes of the jet, some quantitative data, mainly on the jet penetration have also been extracted. The jet trajectory was not computed using the jet core because of the difficulty introduced

by the attached character of the jet and the presence of the recirculation region. Instead, the penetration is extracted from time averaged X-Z visualizations, normalized using the intensity at the jet exit and is estimated detecting the 10% upper contour of the normalized image.

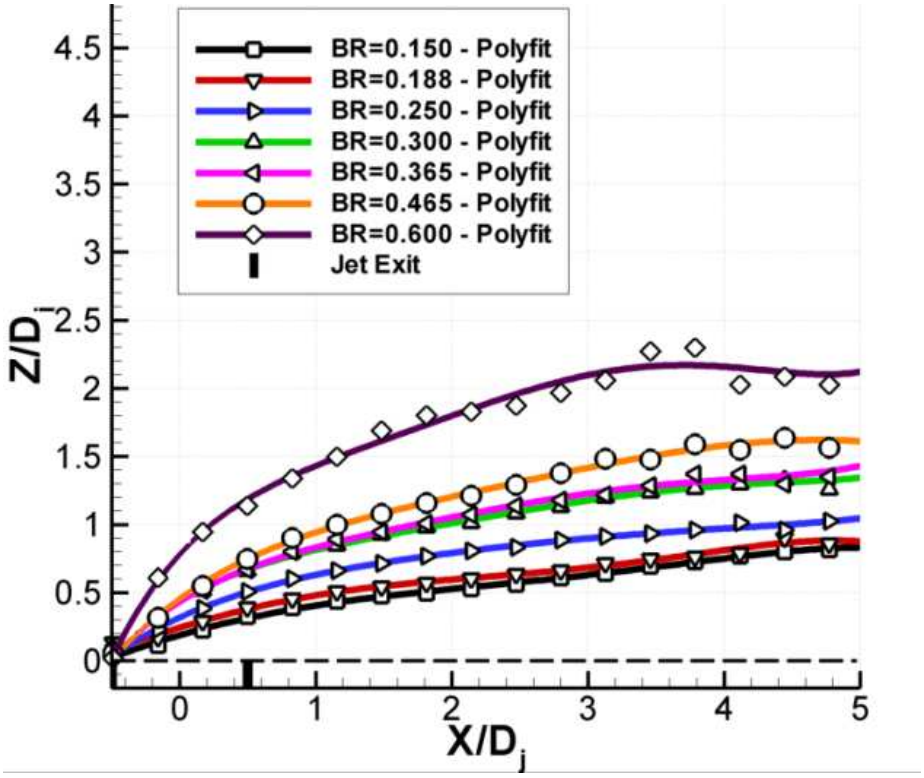

Figure 5-32: Jet penetration estimation for BR=0.150 to BR=0.600.

As expected, the top interface penetrates deeper in the jet as the blowing ratio increases. On Figure 5-32, two phases separated by a plateau are identified in terms of progression of the jet penetration. From BR=0.150 to BR=0.300 the penetration increases with a growing rate. Between BR=0.300 and BR=0.465 the top interface barely progresses as the blowing ratio increases. However, between BR=0.465 and BR=0.600 the penetration rate increases again.

Similarly, plots of the jet top interface location at given stream-wise positions show the same trends (Figure 5-33). At $X/D_j = 2$ the first phase shows an averaged penetration progression rate of 3.2 with respect of the blowing ratio, while the second phase shows a progression rate of 4.5 separated by a plateau with a penetration progression rate of only 1.2. The plateau observed between BR=0.300 and BR=0.465 corresponds to the transitional phases where ring-like vortices and instable separation region

coexist, showing that the interaction of these structures limits the growth rate of the jet penetration with respect to the blowing ratio.

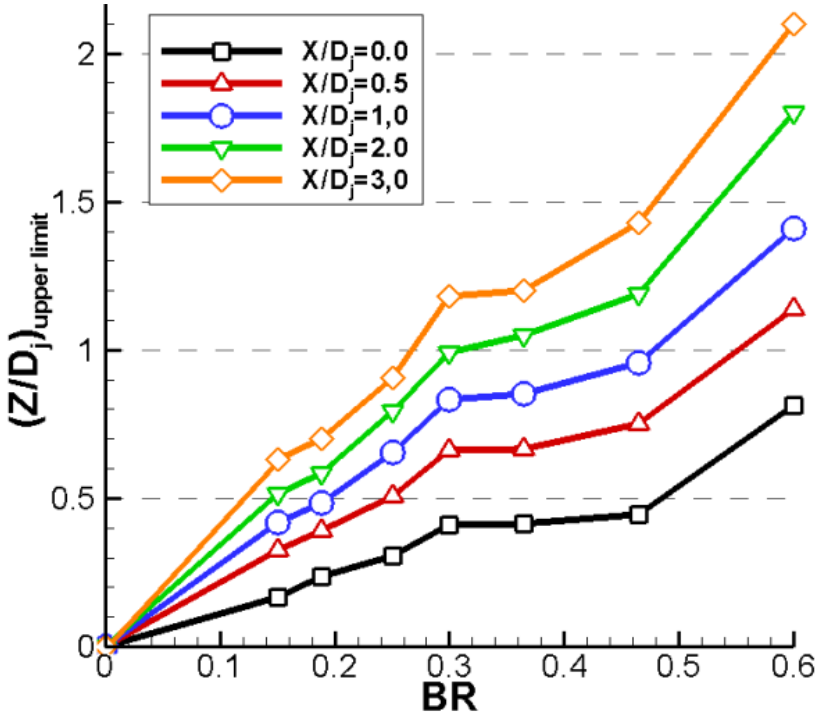

Figure 5-33: Jet upper limit extracted from the penetration at given streamwise locations for BR=0.150 to BR=0.600.

5.2.2.2. X-Y Visualizations

The visualizations from the top provide information on the jet spread, coverage and estimated efficiency at the wall. Quantitative information was extracted using a normalization process of the time averaged top visualizations. The coverage coefficient reflects the jet coverage at the wall, while the span-wise average gives a quantification of the estimated averaged efficiency trends. The jet coverage consistently decreases as the blowing ratio increases from a value of 8.45 at BR=0.150 to a value of 2.4 at BR=0.600 (Figure 5-34). The coverage trends also exhibit two different regimes. The first regime is characterized by a consistent drop in coverage from a value of 8.45 at BR=0.150 to a value of 5.86 at BR=0.300, representing a 35% loss in the covered area. The passage to the second regime (0.365<BR<0.600) is marked by a dramatic drop of more than 50% in the coverage coefficient value from 5.86 at BR=0.300 to 2.51 at BR=0.365 which is to be related to the previous observation from the top visualizations of a clear change in the jet footprint at the wall. The case BR=0.465 is somewhat singular

because of its 35 % increase in coverage compared to BR=0.300 which is not unexpected according to the side and top visualizations showing a decrease in cross-flow penetration between BR=0.365 and BR=0.465 while the recirculation region is shed. Finally from BR=0.465 to BR=0.600 the covered area decreases with a final value of the coverage coefficient equal to 2.4. Again this last phase is expected since the jet is completely detached from the wall at BR=0.600 and the coverage coefficient should asymptotically tend to zero as the blowing ratio tends to large values where the jet in cross-flow can be assimilated to a jet in quiescent environment.

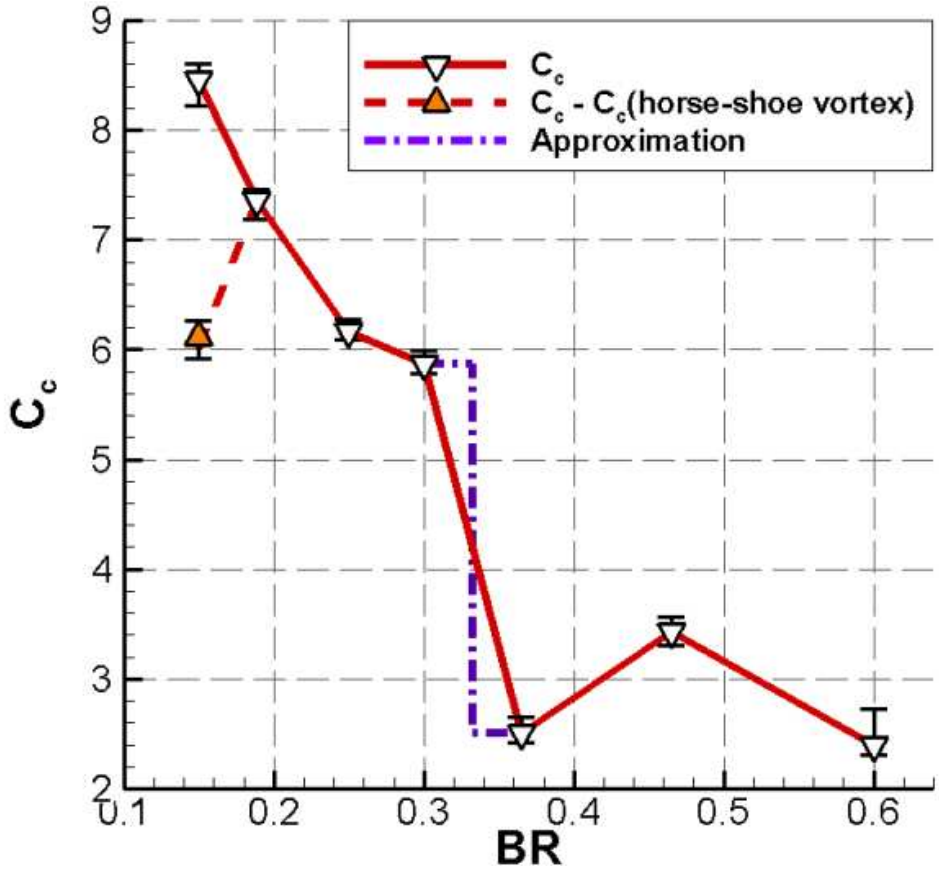

Figure 5-34: Coverage Coefficient (C_c) as a function of the blowing ratio (BR). Computation with and without horse-shoe vortex coverage.

The coverage coefficient was also computed excluding the horse-shoe vortex coverage at BR=0.150. The result exhibits a 40% difference in the coverage at this particular blowing ratio highlighting the potential increase in coverage brought by this structure. Considering only the coverage of the core of jet also reveals that BR=0.188 is an optimum in terms of coverage. Such an optimum is

expected since ultimately the coverage should consistently decrease as the blowing ratio drops, down to zero when the jet is completely shut down.

From the normalized intensity matrices, the iso-intensity contours were extracted and the 0.5 contours corresponding to the coverage coefficient computation were compiled in a single plot (Figure 5-35). The averaged stream wise location of the jet break up appears to follow the same trend as the jet core coverage with a maximum for BR=0.188 and a drastic drop between BR=0.300 and BR=0.365. An estimation of the jet breakup location will be given later.

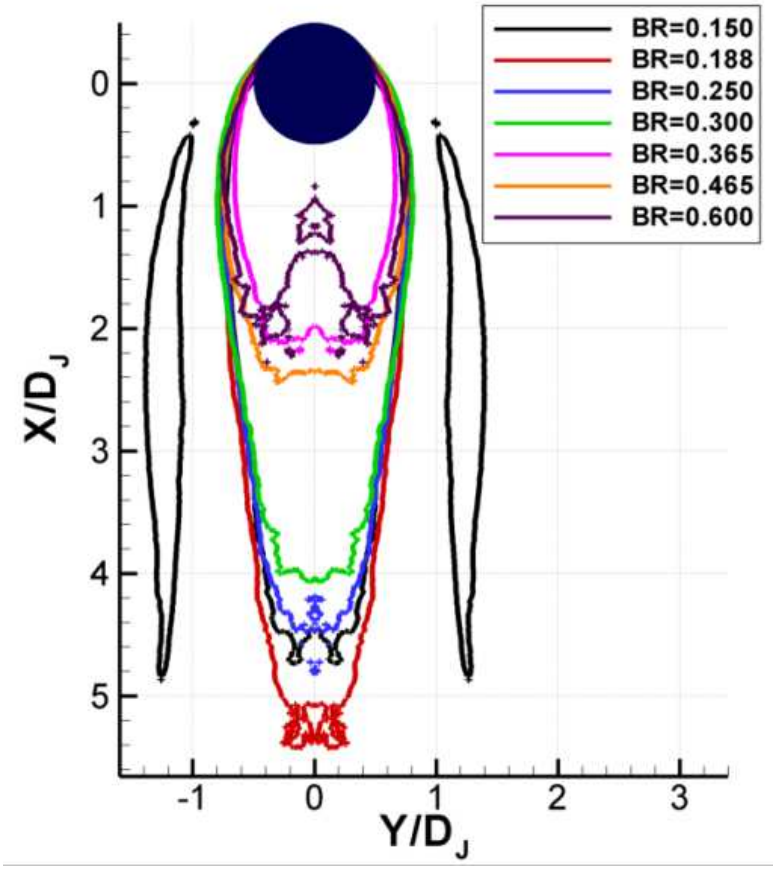

Figure 5-35: Jet footprint computed as the 0.5 contour of the Normalized Intensity matrix.

In Figure 5-36 the contour plots of the normalized intensity of the steady state cases show a decreasing influence of the horse-shoe vortex and an increasing spread as BR increases to a maximum of 1.8 jet diameters. The jet breakup location appears to be optimum at the case BR=0.188 at approximately X/D_j=5, but this result will be detailed and quantified later on with the jet centerline normalized intensity.

One may notice an area of normalized intensity above unity which is due to accumulation of tracer at the wall which decreases as BR increases.

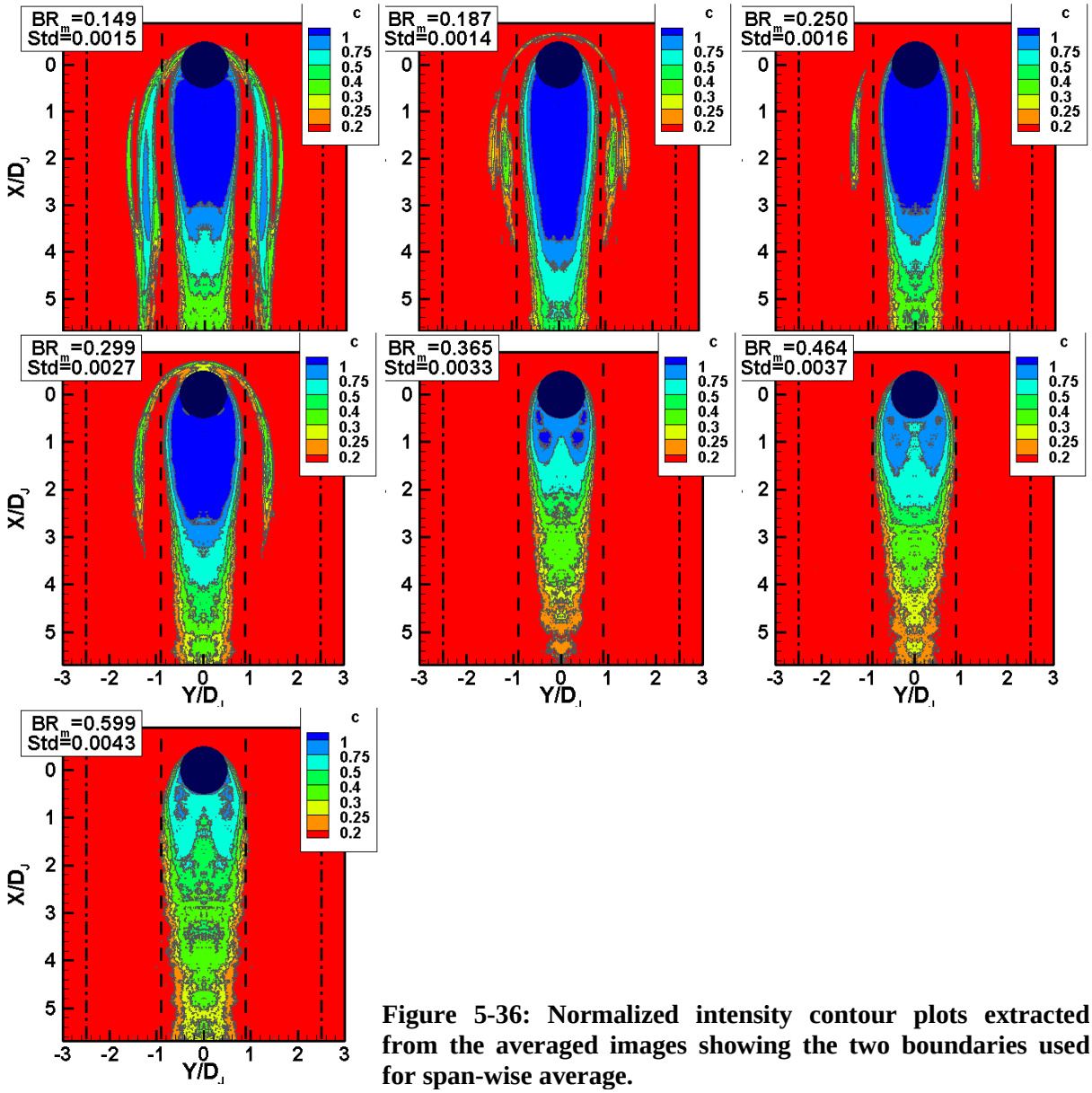

Figure 5-36: Normalized intensity contour plots extracted from the averaged images showing the two boundaries used for span-wise average.

The span-wise averaged normalized intensities were computed using two different integration boundaries of $Y/D_j = \pm 2.5$ and $Y/D_j = \pm 0.9$ (Figure 5-37 a) & b)). The first one was taken to be far enough from the jet centerline to be out of the jet influence, while the second one was chosen in order to exclude the horse-shoe vortex from the computation without excluding the jet core. The first computation shows that BR = 0.150 has the highest span-wise averaged intensity, and this result is probably highly influenced

by the horse-shoe vortex coverage. For higher blowing ratios, two groups can be identified. The first one for $0.188 \leq BR \leq 0.300$ shows as the blowing ratio increases, an increasing span-wise averaged intensity near the jet exit $X/D_j < 1.5$ and a conversely decreasing averaged intensity downstream for $X/D_j > 1.5$. The second group for $0.365 \leq BR \leq 0.600$ is characterized by an overall lower span-wise averaged normalized intensity compared to the first group with a maximum value around $X/D_j = 1$. The case BR = 0.465 is again singular with an overall higher span-wise averaged intensity compared to BR = 0.365. Another singularity can be found in the value of the span-wise averaged normalized intensity at BR=0.600 for $X/D_j>2.8$ which is above the other values of the second group. This can be explained by the presence of wake vortices visible on both side-view and top-view visualizations, entraining jet fluid and tracer particles beneath the jet even though it is detached.

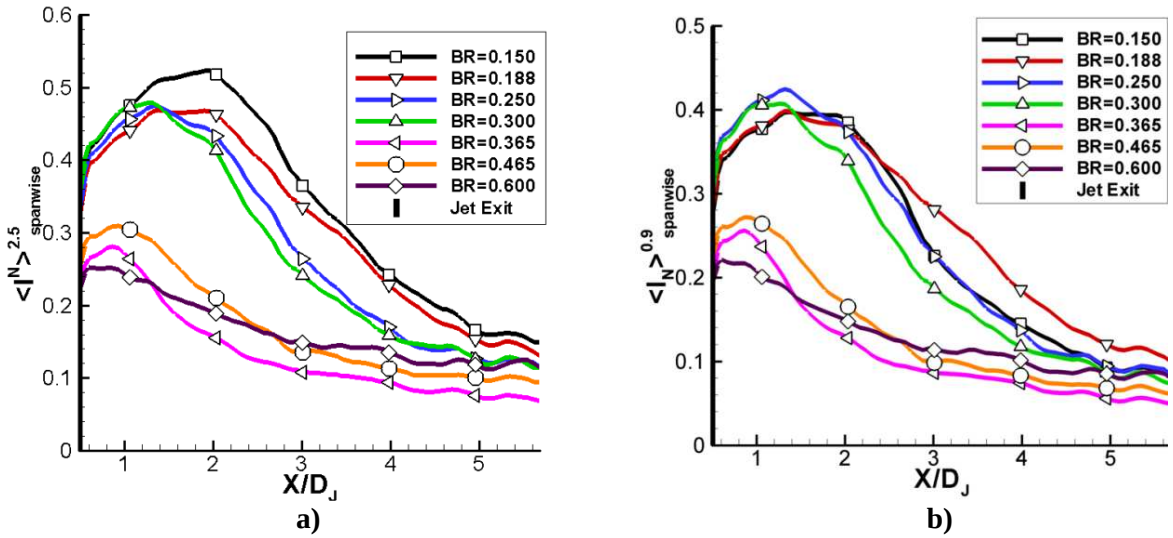

Figure 5-37: Span-wise averaged normalized intensity for a) $-2.5 < Y/D_j < 2.5$, b) $-0.9 < Y/D_j < 0.9$, as a function of X/D_j.

The general statement of a dramatic drop in span-wise averaged intensity for $BR \geq 0.365$ still applies for the second computation excluding the horse-shoe vortex. Even though the trends for blowing ratios above BR=0.365 are identical to the one of the first computation, revealing the limited influence of the horse-shoe vortex on the span-wise averaged intensity of the second group, the first group trends are modified when using the second computation. Indeed, considering only the jet core influence, the highest span-wise averaged intensity is no longer achieved at BR= 0.150 and no particular case exhibits an

overall maximum value. Instead, the maximum span-wise averaged intensity is reached at BR = 0.250 for $X/D_j < 2$ and at BR = 0.188 for $X/D_j > 2$ corresponding to the blowing ratio with the farthest jet break up location. These trends confirm the observations made on Figure 5-36 where the horse-shoe vortex trace disappears for BR ≥ 0.365.

The normalized intensity on the jet centerline is also extracted and shows trends comparable to the second computation (Figure 5-38 a)). However, a drop in the value of the normalized intensity right after the jet exit is noticeable and can be explained by the presence of the recirculation region. The value of the normalized intensity is generally high when compared to the span-wise averaged value. From the jet centerline normalized intensity the jet break up location was estimated by finding the stream wise location at which the value drops below 0.5 (Figure 5-38 b)). The trend is similar to the coverage coefficient excluding the horse-shoe vortex coverage and the values are consistent with the visualizations. The latest breakup is observed for BR = 0.188 at $X/D_j > 5$ and consistently decreases with the blowing ratio for higher values with a minimum breakup location at $X/D_j \approx 1$ for BR=0.600.

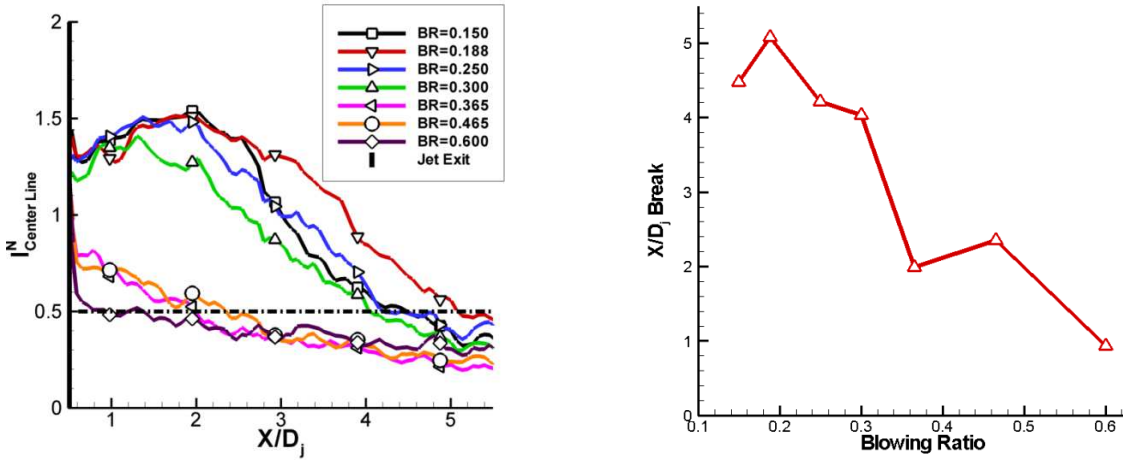

Figure 5-38: a) Normalized intensity on the jet centerline, b) Jet breakup location.

5.3. Pulsed Cases Results

A series of ten cases were observed using the pulsing system previously described in Chapter 3. Each case allows three parameters among the BR_m, BR_l, BR_h, BR_{pp} and DC to be fixed. Each one of these 10 cases was then observed at four different forcing frequencies of f_f=0.5, 1.0, 5.0, and 10.0Hz

corresponding to cross-flow based Strouhal numbers of St_∞=8.10^{-3}, $1.6.10^{-3}$, 8.10^{-2} and 0.16. These tests were divided into two groups, the first one at a mean blowing ratio over a cycle (BR_m) of 0.250, the second one at BR_m=0.350, which are in terms of steady state cases respectively before and after the dramatic drop in coverage coefficient. Measurements similar to the one made in steady state were performed, including side and top visualizations and CTA measurements.

5.3.1. Visualizations and Constant Temperature Anemometry

As explained earlier, a series of ten cases, forced at four different forcing frequencies were studied resulting into an ensemble of 40 different sets. The characteristics of these cases were chosen in order to be able to study the influence of one parameter when two others are fixed and are presented in Table 5-6.

Table 5-6: Characteristics of the ten cases studied during the pulsed jet survey.

	Case #	BR_l	BR_h	BR_{pp}	DC (%)
BRm=0.250	**1**	0.188	0.313	0.125	50
	2	0.175	0.325	0.150	50
	3	0.188	0.438	0.250	25
	4	0.125	0.375	0.250	50
	5	0.075	0.325	0.250	70
BRm=0.350	**6**	0.188	0.513	0.325	50
	7	0.275	0.425	0.150	50
	8	0.288	0.538	0.250	25
	9	0.225	0.475	0.250	50
	10	0.175	0.425	0.250	70

5.3.1.1. Protocols and Actual Conditions

5.3.1.1.1. Visualizations

Similarly to steady state visualizations a protocol was followed to acquire images in pulsed jet conditions. The visualizations were made at phase locked positions in the cycle to have a clear understanding of the evolution of the structures in time. The time master in forced tests is the computer generating the square wave signal sent to the solenoid. At fixed phase position within a cycle, the solenoid valve control computer sends a signal to the synchronizer which triggers the image acquisition sequence by sending signals to the LASER, the camera and the frame grabber.

Table 5-7: Jet actual conditions during forced jet visualizations at BR_m=0.250.

			Top-view Visualizations					Side-view Visualizations				
			BR_m	BR_l	BR_h	BR_{pp}	DC	BR_m	BR_l	BR_h	BR_{pp}	DC
Nominal BR_m=0.250	Case # 1	**Nominal**	**0.250**	**0.188**	**0.313**	**0.125**	**0.50**					
		f_f=0.5	0.252	0.188	0.312	0.124	0.52					
		f_f=1.0	0.254	0.188	0.314	0.125	0.53					
		f_f=5.0	0.261	0.201	0.314	0.114	0.53					
		f_f=10.0	0.270	0.218	0.316	0.098	0.53					
	Case # 2	**Nominal**	**0.250**	**0.175**	**0.325**	**0.150**	**0.50**					
		f_f=0.5	0.252	0.175	0.323	0.149	0.52					
		f_f=1.0	0.255	0.177	0.326	0.148	0.53					
		f_f=5.0	0.259	0.187	0.325	0.138	0.53					
		f_f=10.0	0.269	0.201	0.329	0.128	0.53					
	Case # 3	**Nominal**	**0.250**	**0.188**	**0.438**	**0.250**	**0.25**	**0.250**	**0.188**	**0.438**	**0.250**	**0.25**
		f_f=0.5	0.256	0.187	0.448	0.261	0.27	0.255	0.188	0.444	0.256	0.26
		f_f=1.0	0.258	0.185	0.447	0.262	0.28	0.254	0.185	0.429	0.244	0.28
		f_f=5.0	0.254	0.184	0.434	0.251	0.28	0.251	0.187	0.421	0.234	0.28
		f_f=10.0	0.257	0.185	0.417	0.232	0.31	0.252	0.188	0.401	0.213	0.30
	Case # 4	**Nominal**	**0.250**	**0.125**	**0.375**	**0.250**	**0.50**	**0.250**	**0.125**	**0.375**	**0.250**	**0.50**
		f_f=0.5	0.257	0.122	0.384	0.262	0.51	0.252	0.123	0.374	0.252	0.52
		f_f=1.0	0.258	0.123	0.381	0.258	0.52	0.252	0.122	0.372	0.249	0.52
		f_f=5.0	0.255	0.127	0.378	0.251	0.51	0.244	0.127	0.362	0.236	0.50
		f_f=10.0	0.260	0.132	0.373	0.241	0.53	0.248	0.137	0.359	0.221	0.50
	Case # 5	**Nominal**	**0.250**	**0.075**	**0.325**	**0.250**	**0.70**	**0.250**	**0.075**	**0.325**	**0.250**	**0.70**
		f_f=0.5	0.254	0.074	0.327	0.253	0.71	0.256	0.088	0.325	0.238	0.71
		f_f=1.0	0.258	0.076	0.329	0.253	0.72	0.259	0.091	0.325	0.234	0.72
		f_f=5.0	0.257	0.091	0.328	0.237	0.70	0.255	0.114	0.320	0.206	0.69
		f_f=10.0	0.274	0.121	0.328	0.206	0.74	0.271	0.147	0.321	0.174	0.71

The number of phase locked images varies with respect to the forcing frequency. For f_f = 0.5 and 1.0Hz, ten, equally spaced phase positions are used for visualizations acquisition. A series of ten images in a row, corresponding to the same phase position is taken over ten consecutive cycles. Then, the next phase position is selected and a new series of ten images is acquired. At forcing frequencies of f_f = 5.0 and 10.0Hz, fifty equally spaced phase positions are chosen to acquire images. Again, for each phase position a series of ten images taken over ten consecutive cycles is acquired. As the forcing frequency increases,

the time resolution of the images within a cycle increases because of the shortening of the cycle period. Visualizations were acquired on both X-Z and X-Y plane resulting in a total of 24,000 images.

Table 5-8: Jet actual conditions during forced jet visualizations at BR_m=0.350.

			Top-view Visualizations					Side-view Visualizations				
			BR_m	**BR_l**	**BR_h**	**BR_{pp}**	**DC**	**BR_m**	**BR_l**	**BR_h**	**BR_{pp}**	**DC**
Nominal BR_m=0.350	**Case # 6**	**Nominal**	**0.350**	**0.188**	**0.513**	**0.325**	**0.50**	**0.350**	**0.188**	**0.513**	**0.325**	**0.50**
		f_f=0.5	0.355	0.188	0.514	0.326	0.51	0.355	0.183	0.520	0.337	0.51
		f_f=1.0	0.357	0.187	0.512	0.326	0.52	0.358	0.183	0.520	0.337	0.52
		f_f=5.0	0.354	0.191	0.510	0.318	0.51	0.351	0.185	0.518	0.333	0.50
		f_f=10.0	0.359	0.201	0.505	0.304	0.52	0.350	0.193	0.512	0.318	0.49
	Case # 7	**Nominal**	**0.350**	**0.275**	**0.425**	**0.150**	**0.50**	**0.350**	**0.275**	**0.425**	**0.150**	**0.50**
		f_f=0.5	0.354	0.277	0.427	0.150	0.51	0.351	0.271	0.428	0.157	0.51
		f_f=1.0	0.357	0.279	0.427	0.148	0.53	0.352	0.270	0.427	0.157	0.52
		f_f=5.0	0.361	0.289	0.426	0.137	0.53	0.352	0.277	0.422	0.146	0.52
		f_f=10.0	0.369	0.303	0.424	0.122	0.54	0.359	0.289	0.421	0.132	0.53
	Case # 8	**Nominal**	**0.350**	**0.288**	**0.538**	**0.250**	**0.25**	**0.350**	**0.288**	**0.538**	**0.250**	**0.25**
		f_f=0.5	0.351	0.286	0.532	0.246	0.27	0.356	0.287	0.552	0.265	0.26
		f_f=1.0	0.355	0.287	0.527	0.240	0.28	0.359	0.286	0.544	0.257	0.28
		f_f=5.0	0.358	0.289	0.533	0.245	0.29	0.357	0.285	0.544	0.259	0.28
		f_f=10.0	0.366	0.294	0.513	0.219	0.33	0.357	0.286	0.522	0.237	0.30
	Case # 9	**Nominal**	**0.350**	**0.225**	**0.475**	**0.250**	**0.50**	**0.350**	**0.225**	**0.475**	**0.250**	**0.50**
		f_f=0.5	0.355	0.227	0.476	0.249	0.51	0.355	0.222	0.482	0.260	0.51
		f_f=1.0	0.353	0.223	0.471	0.248	0.53	0.357	0.222	0.482	0.260	0.52
		f_f=5.0	0.353	0.229	0.468	0.239	0.52	0.353	0.224	0.479	0.255	0.51
		f_f=10.0	0.362	0.243	0.468	0.226	0.53	0.352	0.231	0.474	0.243	0.50
	Case # 10	**Nominal**	**0.350**	**0.175**	**0.425**	**0.250**	**0.70**	**0.350**	**0.175**	**0.425**	**0.250**	**0.70**
		f_f=0.5	0.358	0.177	0.431	0.254	0.71	0.354	0.175	0.428	0.253	0.71
		f_f=1.0	0.357	0.179	0.425	0.246	0.72	0.356	0.175	0.428	0.253	0.72
		f_f=5.0	0.356	0.199	0.424	0.225	0.70	0.351	0.187	0.426	0.240	0.69
		f_f=10.0	0.376	0.242	0.426	0.184	0.73	0.365	0.209	0.425	0.216	0.72

The jet flow-rate is recorded at the beginning of each test with a sampling frequency of 10,000Hz and 600,000 points, and the actual jet characteristics can be computed to verify the validity of the results (Table 5-7 and Table 5-8). The computation is made on a phase averaged time record of the blowing ratio based on the valve signal. The processing determines the actual BR_m and DC by detecting the parts of the signal above BR_m and below. The actual values of BR_h and BR_l are computed by taking the averaged

value of the signal in the detected high part and the detected low part. Generally, the highest forcing frequency tests show actual values slightly different from the nominal. This is explained by the relatively slow response time of the system which is not allowing the flow to settle at higher forcing frequency.

All the instantaneous side-views visualizations presented in this part of the thesis are extracted from P.E Boulladoux MSc Thesis (2006) and J. Oertling MSc Thesis (2006) and work. The actual values observed in the tests are satisfying and confirm the validity of the results presented in this section.

5.3.1.1.2. Hot-wire Measurements

All the raw data from hot-wire measurements in pulsed cases were acquired previously by P.E Boulladoux and J. Oertling. The hot-wire measurements were acquired with the exact same protocol as the one used for steady state measurements. The sampling frequency is maintained at 5,000Hz with a low-pass filter of 2000Hz, and the length of the records is 100,000 samples. Only three positions in the test section were investigated: (X/D_j=0, Z/D_j=0), (X/D_j=0, Z/D_j=0.5), and (X/D_j=3.5, Z/D_j=1.25). Indeed, given the number of studied cases it was unpractical to adapt the hot-wire measurement locations to each case and blowing ratio.

5.3.1.2. Results

The understanding of the dynamics of the jet implies the comprehension of the actuation and the response of the jet to forcing. The flow-meter records of cases 3, 4, 5, 8, 9 and 10 were analyzed using wavelet analysis to resolve the flow frequencies in the jet feeding tube during pulsing. However, in order to fully understand the decomposition obtained by wavelet analysis, a series of pre-analyses of ideal square waves was performed with characteristics identical to the one used in the experiments (frequency and duty cycle). The discontinuities of the square signal are locally detected by the wavelet analysis because of its ability to analyze a signal in time in opposition to the Fourier spectrum analysis. This discontinuity is visible on the wavelet analysis mappings as a localized vertical line of higher coefficients across the frequency domain. The decomposition of the square wave using wavelet analysis displays the fundamental frequency of the signal and different harmonics depending on the duty cycle. Harmonics

visible in the perfect square wave decomposition using the wavelet analysis, and the one found using classic Fourier decomposition are summarized in **Table 5-9**.

Table 5-9: Harmonics found in both type of analysis for a given frequency x.

	DC=0.25		DC=0.50		DC=0.70	
Harmonics found in both type of analysis for a given frequency **x**	Wavelet Analysis	Fourier Analysis	Wavelet Analysis	Fourier Analysis	Wavelet Analysis	Fourier Analysis
	2**x**	2**x**			2**x**	2**x**
	3**x**	3**x**	3**x**	3**x**		3**x**
						4**x**
		5**x**	5**x**	5**x**	5**x**	5**x**
	6**x**	6**x**				6**x**
		7**x**	7**x**	7**x**		7**x**
					8**x**	8**x**
		9**x**	9**x**	9**x**		9**x**
	10**x**	10**x**				10**x**

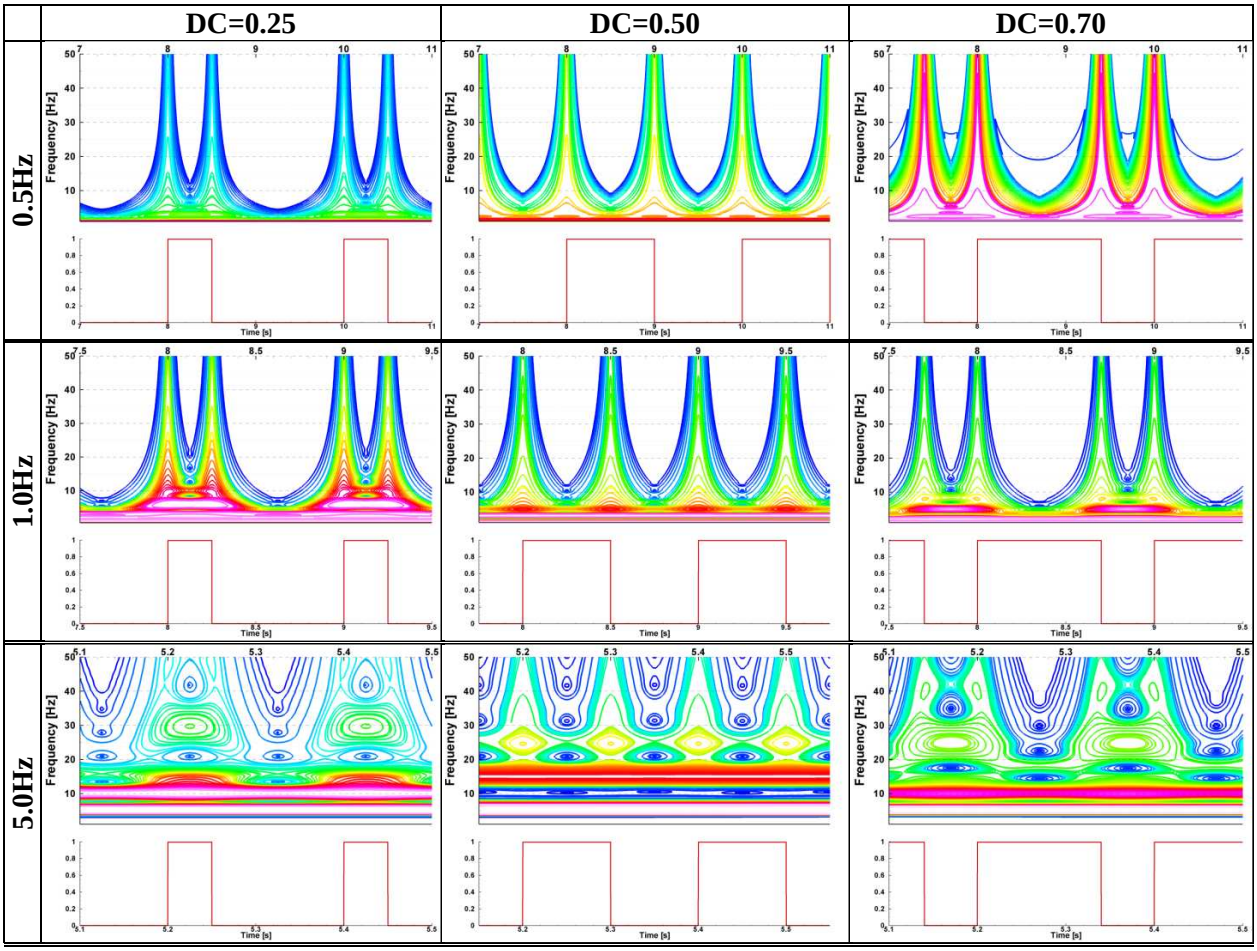

Figure 5-39: Ideal square waves decomposed in the frequency domain using wavelet analysis. (Figure 5-39 cont.)

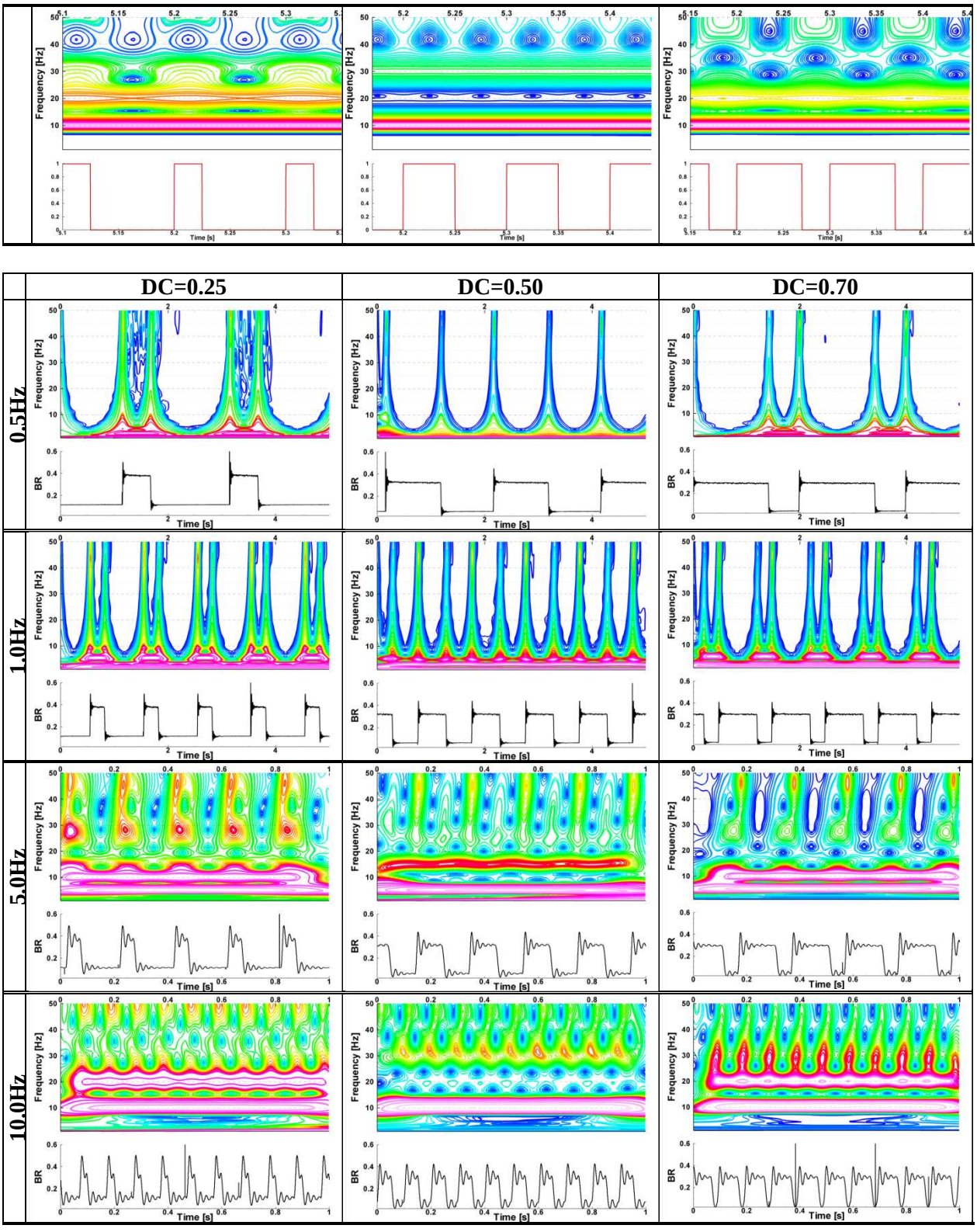

Figure 5-40: Flow-meter records decomposed in the frequency domain using wavelet analysis.

The wavelet analysis of the time resolved flow-meter records (Figure 5-40) gives results very comparable to the decomposition of the corresponding ideal square wave. The principal difference is the presence of a 45Hz component after the drop and rise in blowing ratio, due to the system properties. This frequency corresponds to Helmholtz volumetric mode which is present in any pulsed film cooling system fed by a cavity or a plenum. On the blowing ratio records, the integrity of the square signal appears well conserved at the lower frequencies of f_f =0.5 and 1Hz, and relatively good at higher frequencies, even though the flow-rate records of the latter set of frequencies are strongly dominated by oscillations due to the Helmholtz volumetric mode.

The increase in blowing ratio at the opening of the solenoid valve is accompanied by an overshoot due to the accumulation of pressure upstream of the closed solenoid valve during the low part of the cycle. This overshoot is of the order of 20% to 30% of the BR_h value, depending on the BR_{pp} value as reported in Figure 5-41. The oscillations in blowing ratio caused by the acoustics fade generally within a period of 100ms +/- 10ms depending on the value of BR_h and regardless of the forcing frequency. Considering this fading time of approximately 100ms explains the predominance of the acoustic oscillations on the flow-meter records over the cycles at f_f=5 and 10Hz which periods are respectively 200ms and 100ms.

The visualizations show that all the studied cases involve complex structures which cannot be completely resolved with only two visualization planes. However, these cases present common features and the general behavior of the jet can be studied as a function of the main forcing parameters (BR_m, BR_l, BR_h, BR_{pp}, DC and f_f).

The first general observation is the apparent difference in jet behavior between forced cases at f_f = 0.5 and 1.0Hz and forced cases at f_f = 5.0 and 10Hz. In the group of lower frequencies, the jet behaves in the low part and the high part of the cycle similarly to the corresponding steady state cases (respectively $BR=BR_l$ and $BR=BR_h$), exhibiting comparable structures after the transient part introduced by the overshoot or the eventual ingestion. Figure 5-42 and Figure 5-43 present visualizations from case 3 (see Table 5-6) at respectively low frequencies of f_f=0.5 and 1Hz. The side-views show clearly in Figure 5-42

on frame a) 1, 6, 7, 8, 9 and 10 and in Figure 5-43 a) 1, 7, 8, 9 and 10 that the flow is dominated by shear layer instability, similarly to the steady state case BR=BR_l=0.188. In the same way, the high part of the cycle (Figure 5-42 & Figure 5-43 a) 2, 3 and 4) displays ring-like vortices comparable to the one observed in the steady state case at BR=0.365 and 0.465

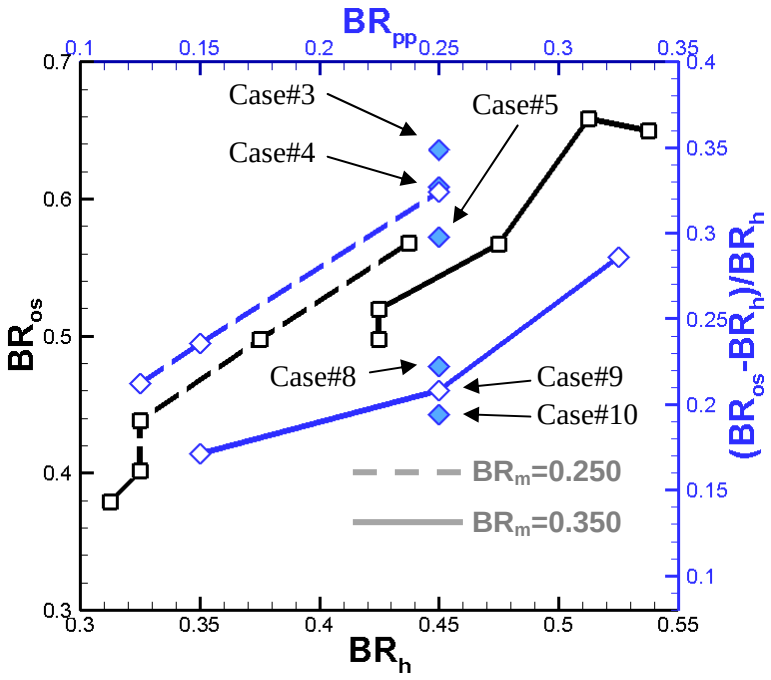

Figure 5-41: Value of the overshoot (BR_{os}) as a function of BR_h and relative value of BR_{os} with respect to BR_h as a function of BR_{pp}.

However, in the group of higher frequencies (f_f=5 and 10Hz), the predominant phenomenon is the transient part characterized by an initial burst of jet fluid, or starting vortex. The structure of the starting vortex is very similar to a ring-like vortex, with a strong imbalance between the upstream and the downstream rollups sizes (Figure 5-44 a) 10 to 40 and Figure 5-45 a) 18 to 49, white arrows). The initial shape of the starting vortex appears to be a ring (visible in Figure 5-44 b) 10' Figure 5-45 b) 18') but evolves with time as it is convected downstream by the cross flow, and up in the free-stream by the jet. The upstream rollup tends to stay close to the windward lip of the jet with a relatively small size, probably influenced by the region of opposite vorticity located upstream of the jet which is feeding the horse-shoe vortex. Meanwhile, the lee-side rollup grows and is pushed up in the free stream, fed by the eventual recirculation region that has developed during the low part of the cycle.

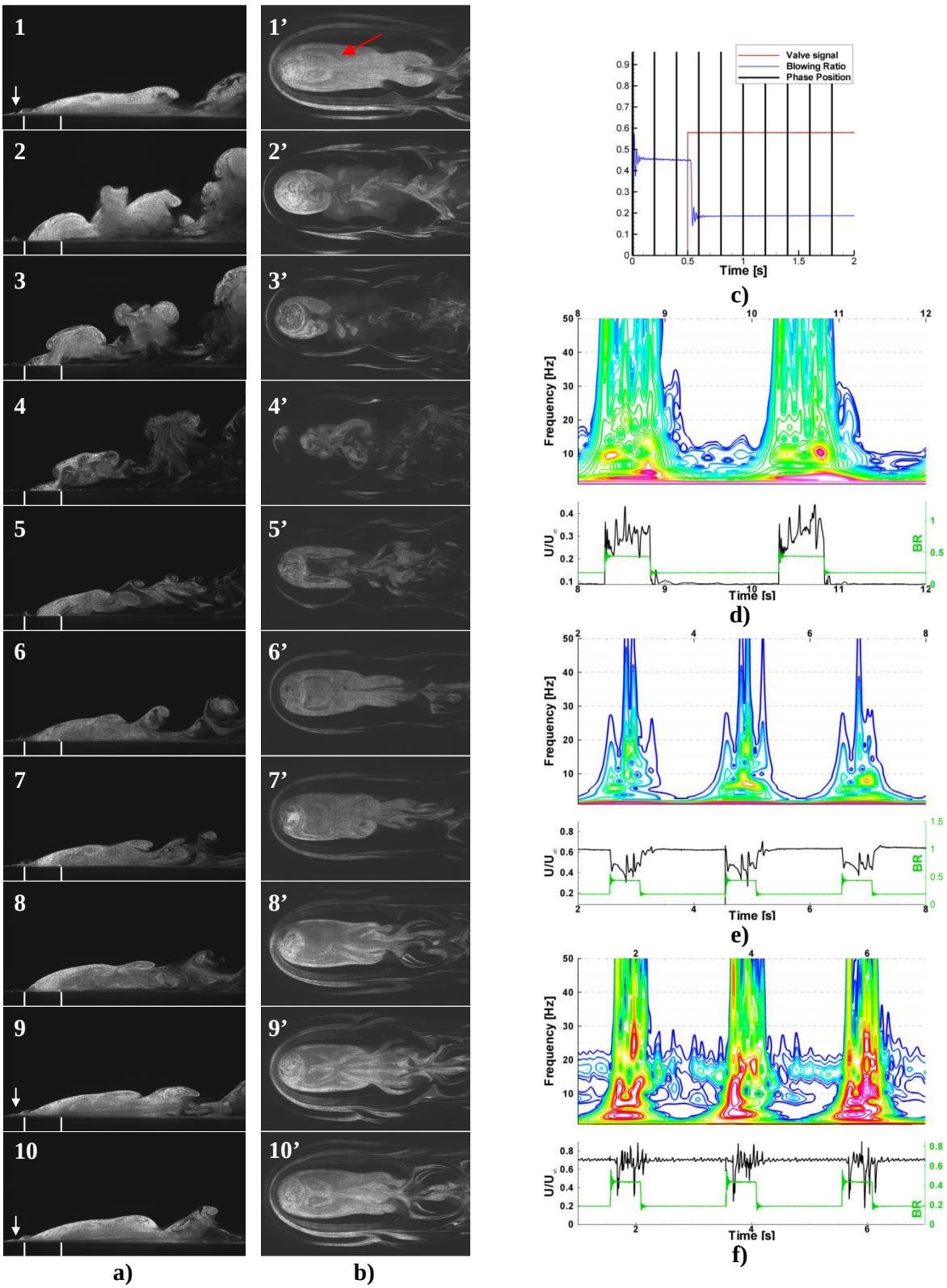

Figure 5-42: Pulsed cases Visualizations at BR_m=0.250, BR_{pp}=0.250, DC=0.25, f_f=0.5Hz - a) (1-10) X-Z visualizations. b) (1'-10') X-Y visualizations. c) Phase averaged flow-meter record. d)-f) Wavelet analysis of the hot-wire records at d) X/D_j=0, Z/D_j=0, e) X/D_j=0, Z/D_j=0.5, f) X/D_j=3.5, Z/D_j=1.25 - Case#3.

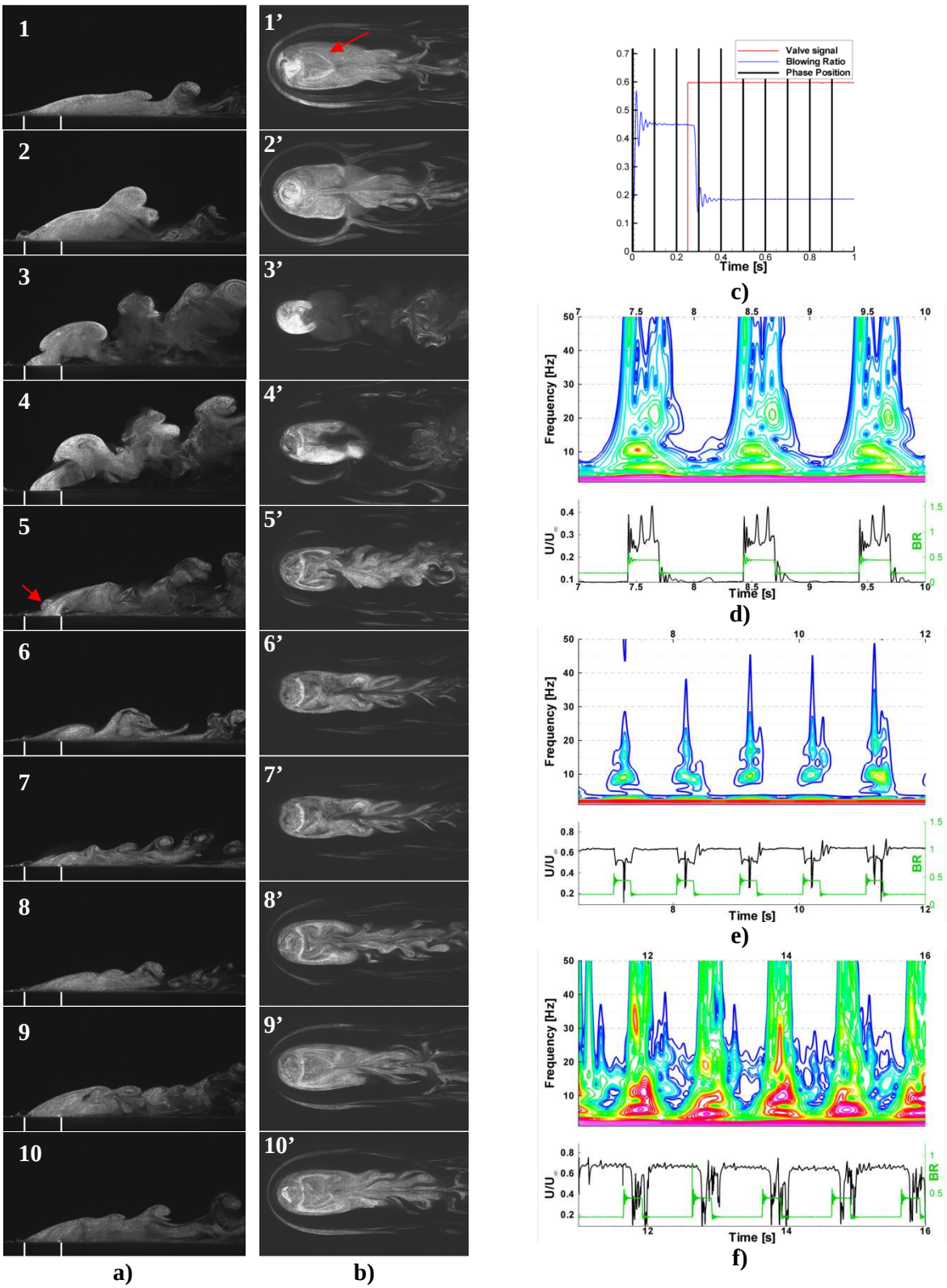

Figure 5-43: Pulsed cases Visualizations at BR_m=0.250, BR_{pp}=0.250, DC=0.25, f_f=1.0Hz - a) (1-10) X-Z visualizations. b) (1'-10') X-Y visualizations. c) Phase averaged flow-meter record. d)-f) Wavelet analysis of the hot-wire records at d) X/D_j=0, Z/D_j=0, e) X/D_j=0, Z/D_j=0.5, f) X/D_j=3.5, Z/D_j=1.25 - Case#3.

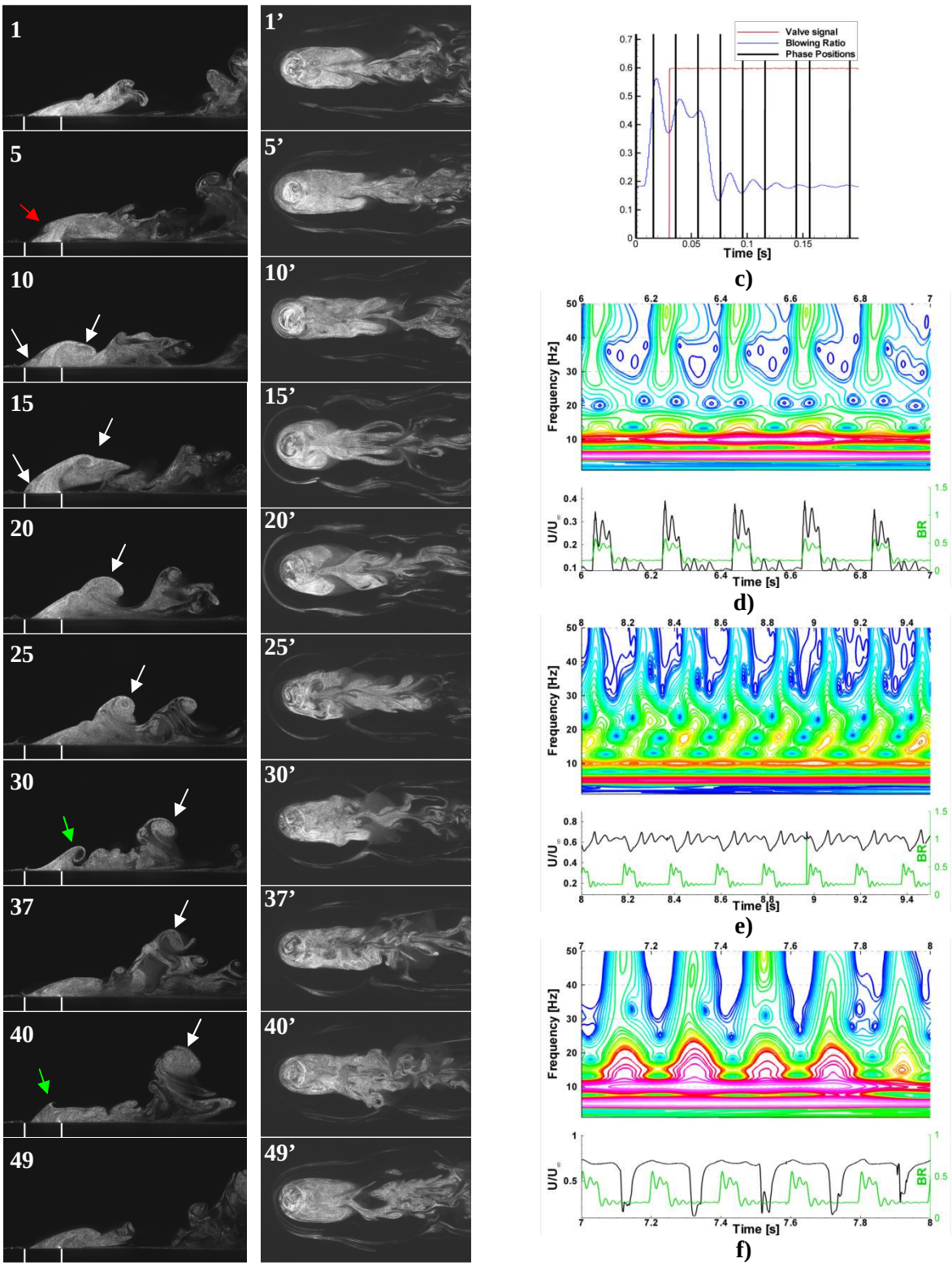

Figure 5-44: Pulsed cases Visualizations at BR_m=0.250, BR_{pp}=0.250, DC=0.25, f_f=5Hz - a) (1-49) X-Z visualizations. b) (1'-49') X-Y visualizations. c) Phase averaged flow-meter record. d)-f) Wavelet analysis of the hot-wire records at d) X/D_j=0, Z/D_j=0, e) X/D_j=0, Z/D_j=0.5, f) X/D_j=3.5, Z/D_j=1.25 - Case#3.

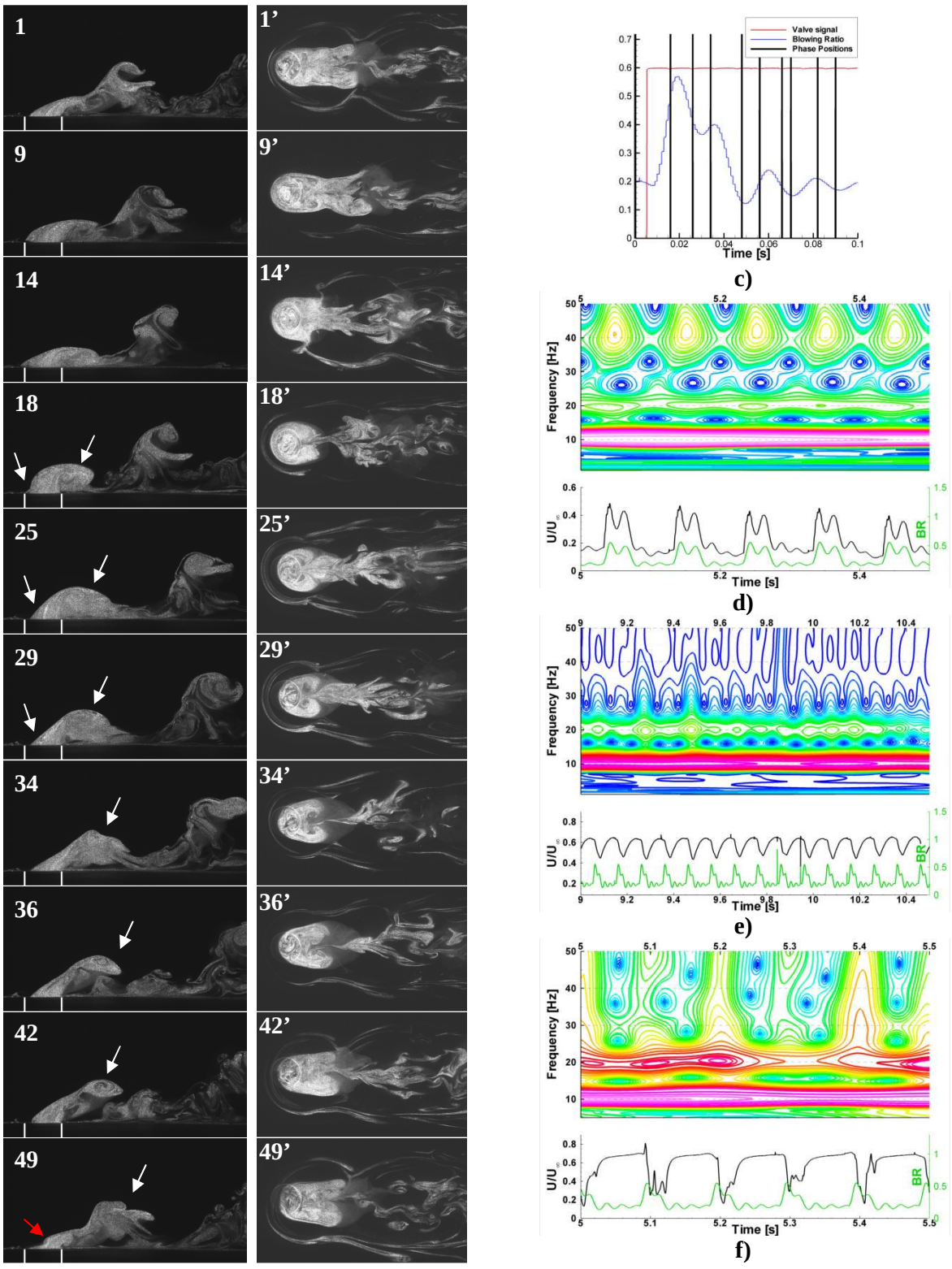

Figure 5-45: Pulsed cases Visualizations at BR_m=0.250, BR_{pp}=0.250, DC=0.25, f_f=10Hz - a) (1-49) X-Z visualizations. b) (1'-49') X-Y visualizations. c) Phase averaged flow-meter record. d)-f) Wavelet analysis of the hot-wire records at d) X/D_j=0, Z/D_j=0, e) X/D_j=0, Z/D_j=0.5, f) X/D_j=3.5, Z/D_j=1.25 – Case#3.

After the shedding of the downstream part of the starting vortex, a pair of swept-back lumps appears on each side of the jet and folded behind the jet exit in a manner very comparable to the symmetrical structures observed on the steady state cases after the shedding of ring-like vortices and/or the recirculation region vorticity (Figure 5-44 b) 15' to 25' and Figure 5-45 b) 25' to 49'). It appears that the dynamics of the starting vortex follow closely the imagined behavior of the ring-like vortices presented in Figure 5-30 and Figure 5-31.

The ring like vortices formation in the high part of the cycle is inhibited in most of the cases at forcing frequencies of f_f = 5 and 10Hz (Figure 5-44, Figure 5-45, Appendice). On the visualizations of tests performed at BR_l of the order of 0.188, BR_{pp} above 0.150 and DC below 70% (Case 2, 3 and 6), we can see that pulsing at 5 and 10Hz, sometimes at 1Hz, can trigger intermittent formation of ring-like vortices in the low part of the cycle, while the corresponding steady state cases show no RLVs and are dominated by shear layer instability (Figure 5-44 a) 5 and Figure 5-45 a) 49). This intermittent formation may be related to the oscillations in the flow-rate provoked by the acoustic frequency which could, during the low part of the cycle, fluctuate around the critical blowing ratio at which ring-like vortices start to form. It can also be associated to the great instability of the horse-shoe vortex in forced jet conditions. Indeed, especially at forcing frequencies of 5 and 10Hz, the horse-shoe vortex is highly unstable and sheds during the low part of cycles with BR_l lower than the critical value of 0.250 where shedding was observed in steady state. This transport of structure on the jet upper interface could trigger ring-like vortices formation by locally perturbing the flow, in the same way it was observed in steady state at BR=0.250.

A last possibility could be the ingestion of cross-flow at the jet upstream lip which could locally decrease the jet exit area and artificially increase the blowing ratio (blockage effect). On the other hand, the forced cases with BR_l between 0.225 and 0.300 (cases 7, 8 and 9) display continuous horse-shoe vortex transport during the low part of the cycle which is in total agreement with the steady state visualizations. The horse-shoe vortex transport can also be observed in the high part of the cycle of most of the sets even though all the cases studied have high blowing ratios above 0.300, which is the upper

value for HSV shedding in steady state. In the top-view visualizations series, a clear interaction between the horse-shoe vortex and the starting vortex and/or ring-like vortices can be observed. Because the horse-shoe vortex is not always seeded, it is impossible to track the path of this structure on all the side views, but not on the top-views. Indeed, in steady state, a disruption or a folding or a contraction of the horse-shoe vortex structure is visible nearly any time ring-like vortices or recirculation region are shed, suggesting an influence of these two structures on the horse-shoe vortex. The pulsed cases visualizations exhibit similar clues of influence, and even clues of interaction between the horse-shoe vortex and the starting vortex and/or ring-like vortices suggesting that the transport of this structure occurs more often than what can be seen on the side-views and maybe anytime a ring-like vortex and/or a starting vortex is formed and shed (Figure 5-42 b) 4', 5', Figure 5-43 b) 2', 4' Figure 5-44 b) 15', 25', 30', 40', Figure 5-45 b) 1', 14', 25', 34', 42', 49'). The "main" horseshoe vortex is visible in most of the cases and at every forcing frequency. An additional horse-shoe vortex located upstream of the "main" one with the same vorticity sign is visible in most of the cases at BR_m=0.250, but not at BR_m=0.350 (Figure 5-42 a) 1, 9 & 10, white arrow). At this last mean blowing ratio, the "main" structure also happens to receive less seed from the jet making it less visible, which would suggest that the second structure is present but not seeded by the tracer. The horse-shoe vortex appears to be entrained in the ring vortex dynamic. An interpretation of the horse-shoe vortex transport mechanism is given in Figure 5-46:

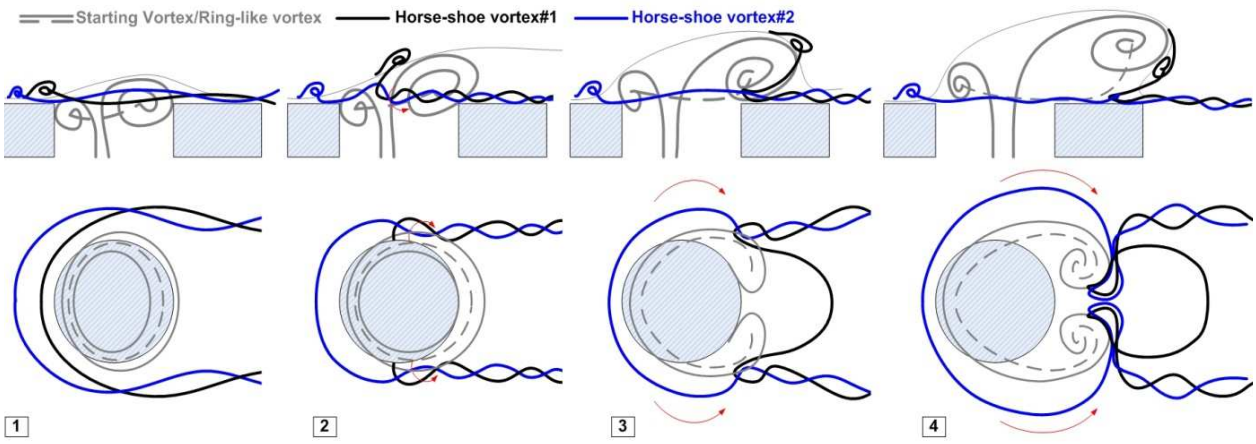

Figure 5-46: Potential mechanism of horse-shoe vortex transport associated with starting vortex/ring-like vortex

As mentioned earlier, one of the characteristics of pulsed jet in cross-flow is the ingestion of cross-flow at the windward lip of the jet exit when the blowing ratio drops from high to low (Figure 5-42 b) 4'). In our experiments, these ingestions were principally observed for BR_{pp} above 0.250. The time for the "quasi-steady" low flow to redevelop after ingestion mainly depends on the value of the BR_l which determines the strength and the velocity of the jet in the low part of the cycle, while the amount of time left in the cycle after the drop and before the next pulse is dictated by the forcing frequency and the duty cycle ($t\_low = (1 - DC)\ 1/ff$). In addition, since our experiments were carried at constant BR_m and BR_{pp}, the lowest BR_l values were achieved with duty cycle values of 70%, also corresponding to the shortest low part of the cycle. Thus at a given BR_m, as DC increases, the highest frequency at which the transient regime introduced by the ingestion is evacuated decreases. In addition, cases with an attached low flow exhibit bigger and more visible recirculation region (Figure 5-42 b) 1' and Figure 5-43 b) 1', red arrow) compared to the corresponding steady state. This can be explained by the influence of the high flow part of the cycle on the recirculation region, transferring more momentum to it.

At the jet exit, the vertical jet velocity record is very similar to the flow-meter time record, proving that the signal at the exit is indeed a square wave. The acoustic frequency is still observed, and the oscillations fading time is similar to the one of the flow-meter record. The hot-wire measurements support the different behavior between lower frequencies cases with cycle periods that are not of the order of the acoustics fading time, T_f>>100ms, (f_f=0.5 and 1Hz), and higher frequencies cases (f_f=5 and 10Hz) cycle period if of the order of the acoustic fading time. In the former group of frequencies, the signatures observed far from the transitions in the high and low part of the cycle are comparable to the one found in the corresponding steady state case and support the observations made on the visualizations of a quasi-steady state behavior (Figure 5-42 d) and Figure 5-43 d)). In the second group of cases, the vertical velocity records exhibit time records dominated by the acoustic frequency, the forcing frequency and its harmonics.

In the upper shear layer above the jet exit, the velocity records exhibit periodicity with a fundamental frequency equal to the forcing frequency. Here again two different types of velocity records

can be observed for low and high frequencies. At pulsing frequencies of 0.5 and 1 Hz the hot-wire measurements show in the low and high part of the cycle comparable signatures with similar frequencies to the one of the corresponding steady state cases (Figure 5-42 e) and Figure 5-43 e)). At pulsing frequencies of 5 and 10Hz, the constant temperature anemometry records also show oscillations at a fundamental frequency equal to f_f (Figure 5-44 e) and Figure 5-45 e)), and some of the cases also display another frequency may be characteristic of horse-shoe vortex shedding during the low part. These frequencies are summarized in Table 5-10.

Table 5-10: Wavelet analysis of upper shear layer velocity records and found frequencies.

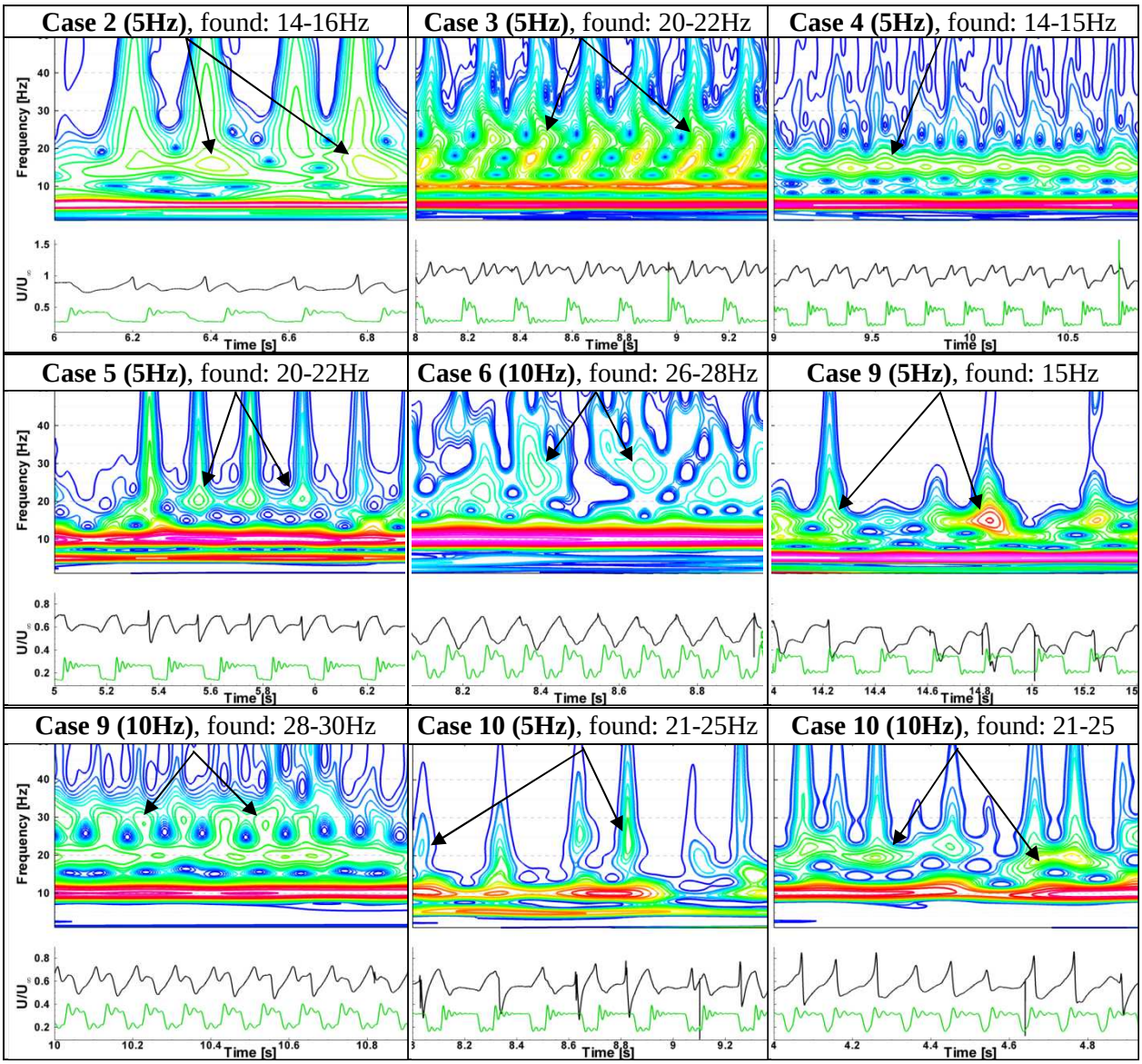

The downstream stream wise velocity records of cases at forcing frequencies of 0.5 and 1Hz reveal similar results to the jet exit signatures with frequencies corresponding to the steady state cases at $BR=BR_h$ and $BR=BR_l$. The signatures obtained for the second group of forcing frequencies (f_f= 5 and 10Hz) at the downstream location are again dominated by the forcing frequency and its harmonics. On records corresponding to cases with DC=25%, the characteristics of the signal are conserved downstream with a periodic signature at a frequency equal to f_f, and an effective duty cycle of approximately 25% (Figure 5-44 f) and Figure 5-45 f)).

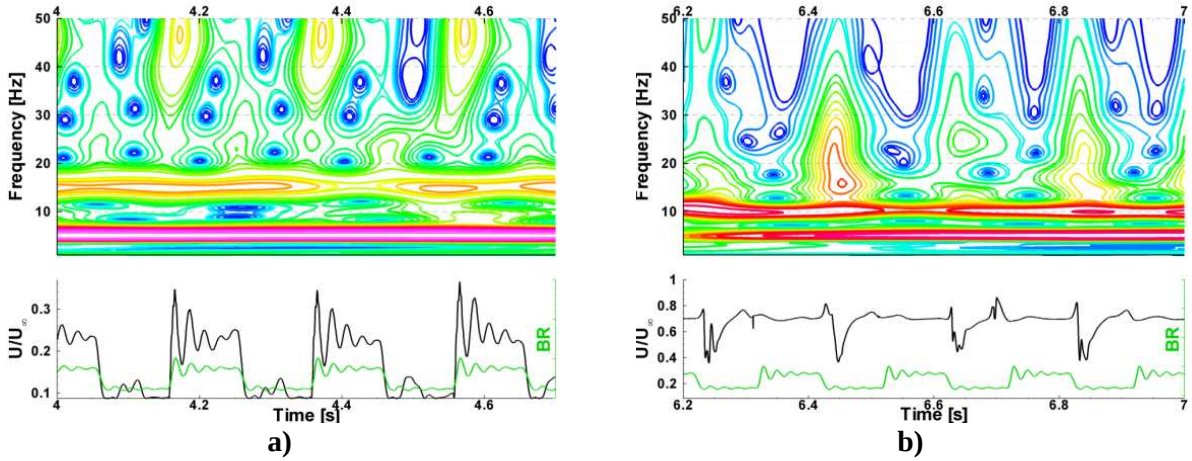

Figure 5-47: Velocity record at DC=50%, f_f=5.0Hz (Case#4) for a) X/D_j=0, Z/D_j=0, b) X/D_j=3.5, Z/D_j=1.25.

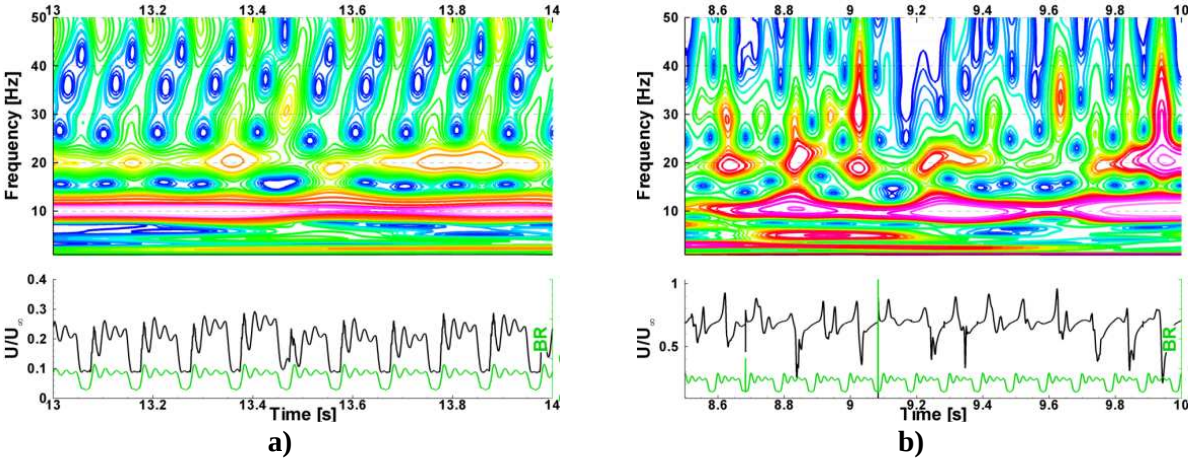

Figure 5-48: Velocity record at DC=70%, f_f=10Hz (Case#5) for a) X/D_j=0, Z/D_j=0, b) X/D_j=3.5, Z/D_j=1.25.

However, for DC=50% (Figure 5-47) and 70% (Figure 5-48) the effective duty cycle appears to be shorter than the one of the signal at the jet exit or on the flow-meter record. This is confirmed by the

harmonics observed on the wavelet analysis decomposition of the downstream signal which are different from the one found at the jet exit. According to the visualizations, this shift in a shorter duty cycle could be due to the fact that the only structure observed at these frequencies is the starting vortex which signature at the downstream location is mainly due to its shedding velocity, principally dictated by the cross-flow velocity and independent of the jet forcing duty cycle.

5.3.2. X-Z Visualizations

Figure 5-49 presents the penetration quantification using the 10% upper limit on the normalized phase averaged images. The results are consistent and all cases display an increased or equivalent (case#7 only) jet penetration at all forcing frequencies when compared to the corresponding steady state case at fixed mass-flow ($BR=BR_m$). The cases with high peak to peak blowing ratio and low duty cycle (case #3 and case#8) appear to provide increased penetration when compared to the cases at lower peak to peak (case#1, case#2 and case#7). This observation is somewhat expected since lower DC and higher BR_{pp} values at a fixed mean blowing ratio implies higher blowing ratio during the high part of the cycle. The forcing frequency has only a limited effect on the jet penetration.

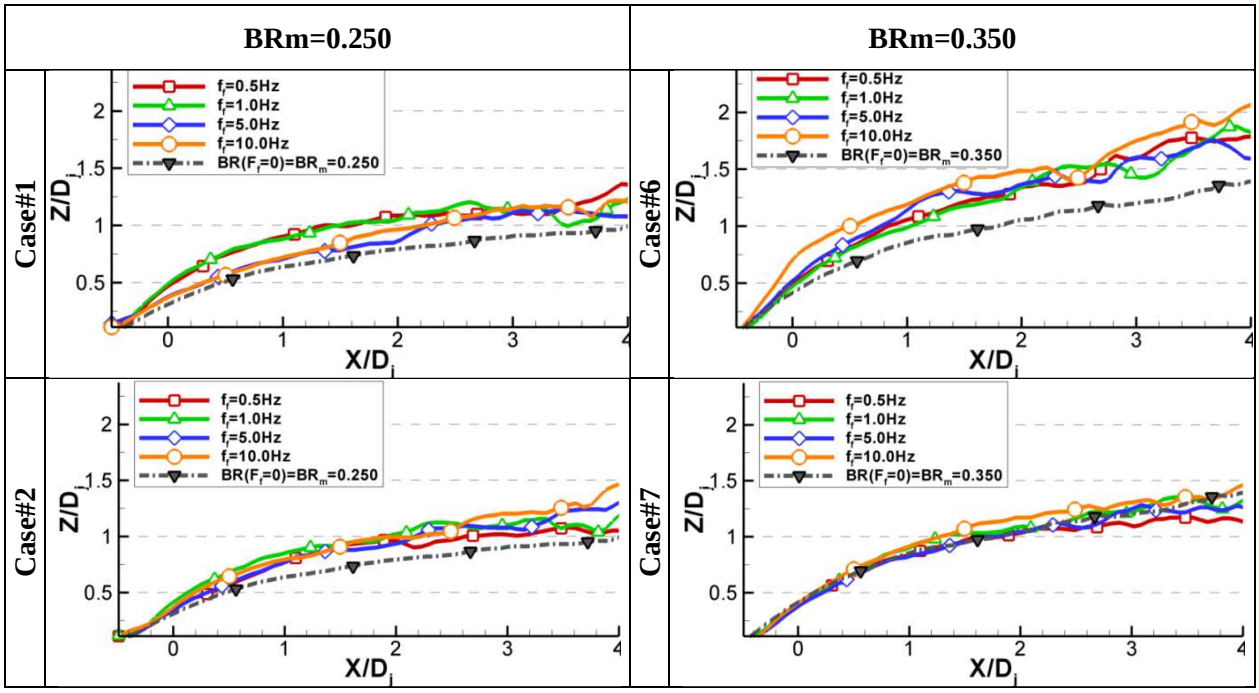

Figure 5-49: Jet penetration estimation for pulsed jet cases#1 to 10. (Figure 5-49 cont.)

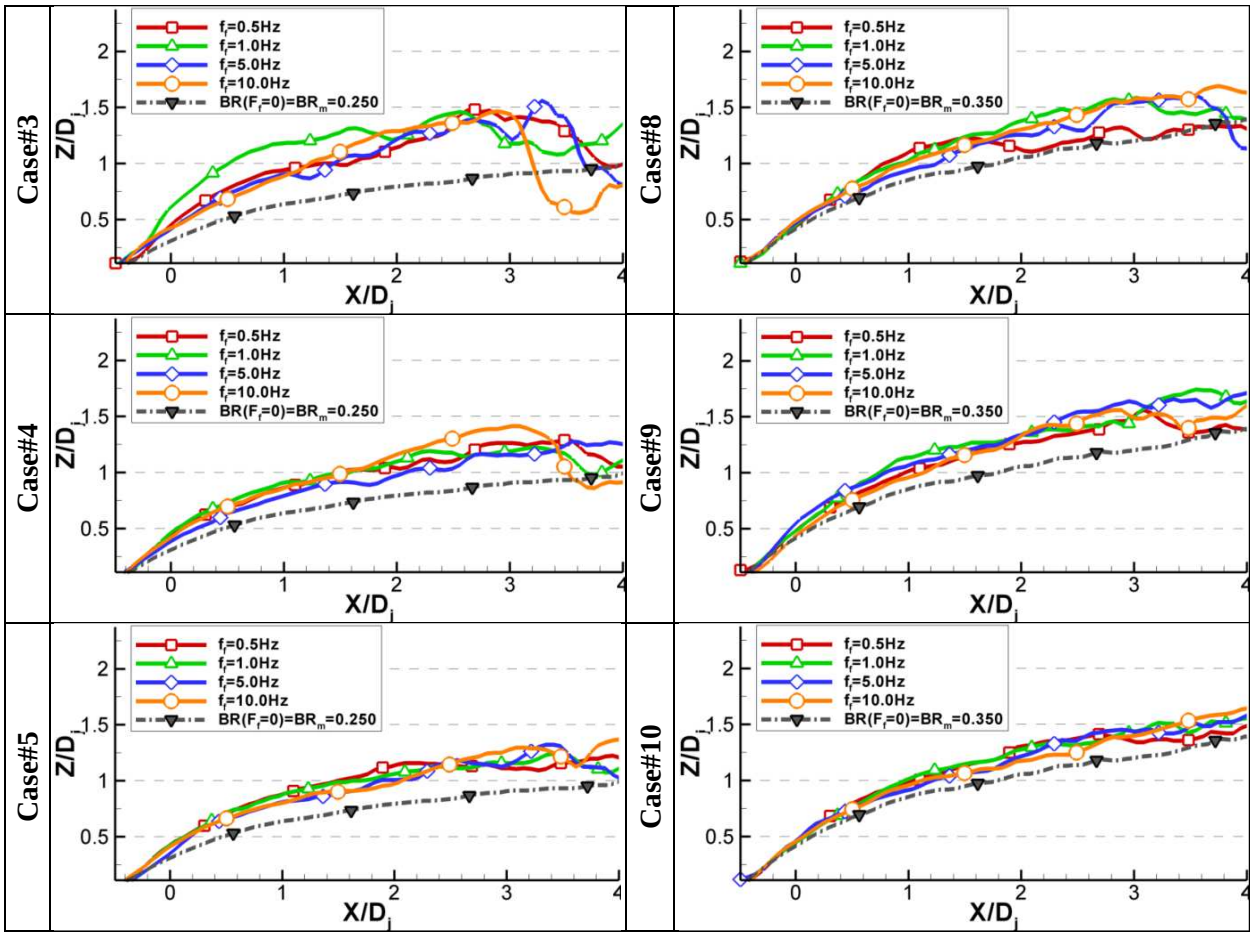

However, comparing cases with identical BR_h (case#2 vs. case#5 and case#7 vs. case#10) shows that the higher BR_{pp} cases have an increased jet penetration.

5.3.3. X-Y Visualizations

In the same way as the steady state cases, exploitation of the top-view visualizations gave information on the coverage coefficient, jet footprint and span-wise averaged normalized intensity.

Two steady state cases were used to quantify the influence of jet forcing in terms of coverage. The first coverage coefficient value used is the equivalent steady state case at fixed mass-flow ($BR=BR_m$), while the second one is the equivalent steady state case at fixed pressure supply ($BR=BR_h$). Only four cases at fixed BR_{pp} of 0.250 and DC of 25% and 50% for both BR_m=0.250 and BR_m=0.350, showed improvements or equivalent results when compared to the two reference steady state cases (Figure 5-50, Case#3, Case#4, Case#8 & Case#9).

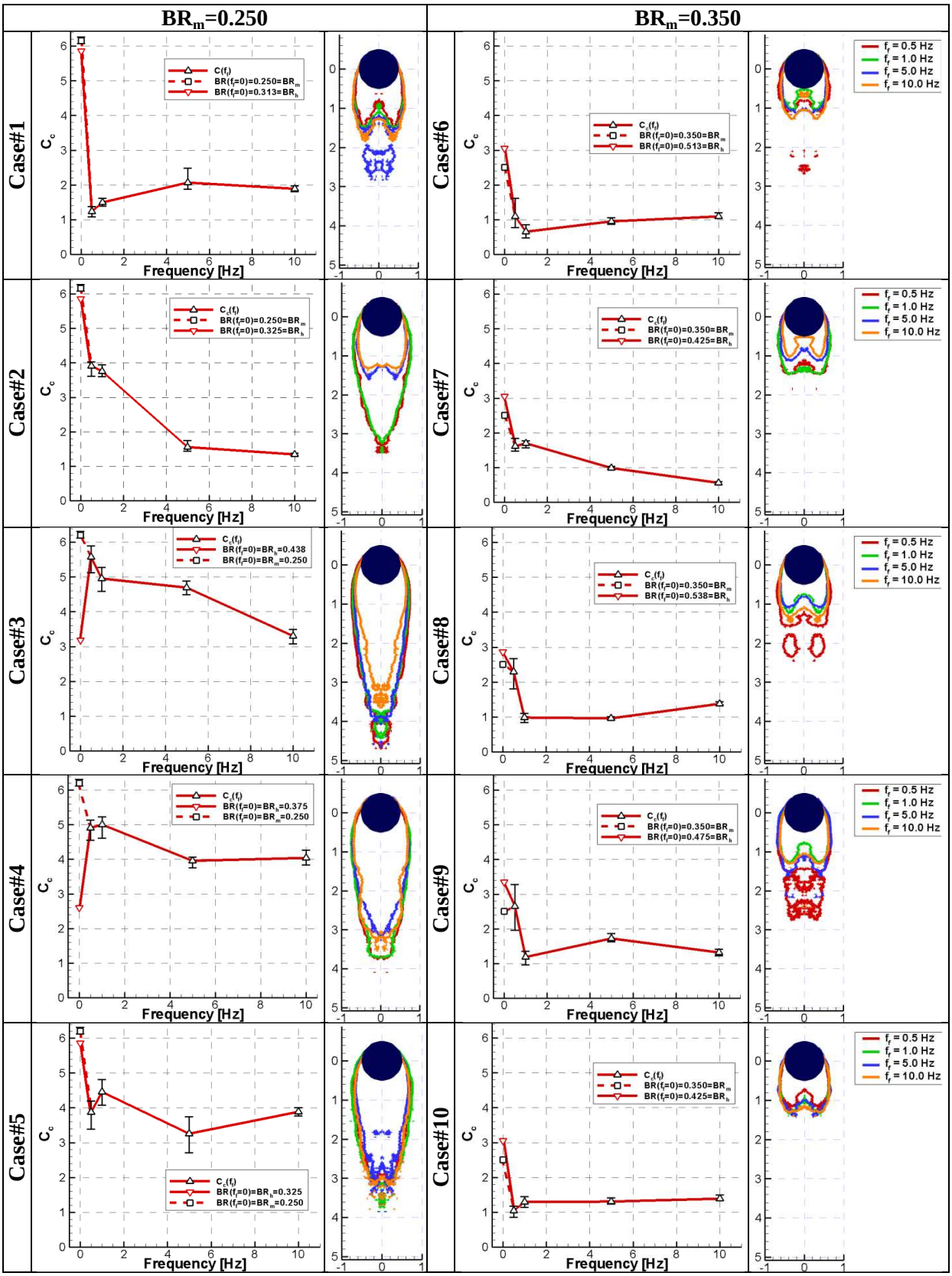

Figure 5-50: Coverage coefficient as a function of f_f and jet footprint for Case#1 to 10.

The two sets at BR_m=0.250 revealed no improvement when compared to the fixed mass-flow case, but an increase in coverage coefficient of 75% for DC=25% and 88% for DC=50% when compared to the fixed pressure case. The two sets at BR_m=0.350 show results matching the steady state case at fixed mass-flow and only a slight decrease in coverage coefficient when compared to the fixed pressure case.

In Figure 5-50, two different responses to the jet forcing frequency can be observed. The first type of response is a general decrease in coverage at high forcing frequency (f_f = 5 & 10Hz) for cases with a coverage coefficient at lower frequencies above unity (Cases#2, 3, 4, 5, 7, 8, & 9). The second type of response is a neutral response or slight improvement as the forcing frequency increases for cases with a coverage coefficient at low frequencies of the order of the unity (Cases#1, 6 & 10).The highest coverage was achieved at BR_m=0.250, BR_{pp}=0.250, DC=25% and a forcing frequency of 0.5Hz, with a coverage coefficient of 5.6. In comparison, the highest coverage coefficient in steady state was obtained at BR=0.150 with a value of approximately 8.5 if considering the horse-shoe vortex coverage, and at BR=0.188 with a value of 7.4 if discarding this structure.

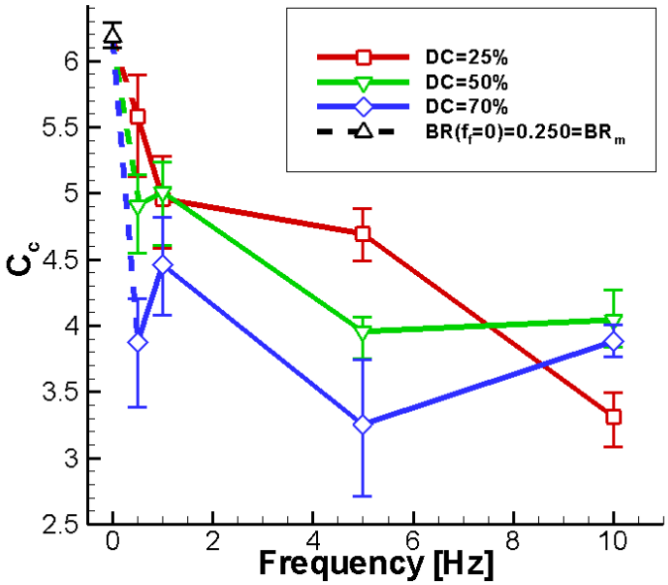

Figure 5-51: Coverage coefficient comparison at BR_m=0.250, BR_{pp}=0.250 for several duty cycles.

Figure 5-51 compares three cases at same the BR_m of 0.250 and same the BR_{pp} of 0.250, with varying duty cycle (Case#3, Case#4 & Case#5). The general trend is a decreasing coverage as the duty cycle increases for all frequencies except 10Hz, and the best coverage is generally achieved at DC=25%.

Two potential reasons to these trends can be found. First, all three cases have a BR_h above 0.300 which is critical in term of coverage in steady state. As the duty cycle increases, the amount of time the jet is in high position increases (low coverage). In addition, as the duty cycle increases, the blowing ratio in the low part decreases below 0.1875 which in steady state is a point of optimal coverage when discarding the horse-shoe vortex, highly unstable according to the visualizations and probably giving less coverage than at the corresponding steady state case. This plot also reveals that the influence of the duty cycle on the coverage coefficient is more significant at forcing frequencies of 0.5 and 5Hz where the coverage coefficient varies from one case to another of approximately 30%, while at forcing frequency of 1Hz and 10Hz, the coverage coefficient varies of respectively 10% and 17%. Finally, as the duty cycle increases, the frequency at which the optimum coverage is obtained for a given case goes from 0.5Hz at DC=25%, to 1Hz at DC=70% with an equivalent coverage at ff=0.5 and 1Hz for DC=50%.

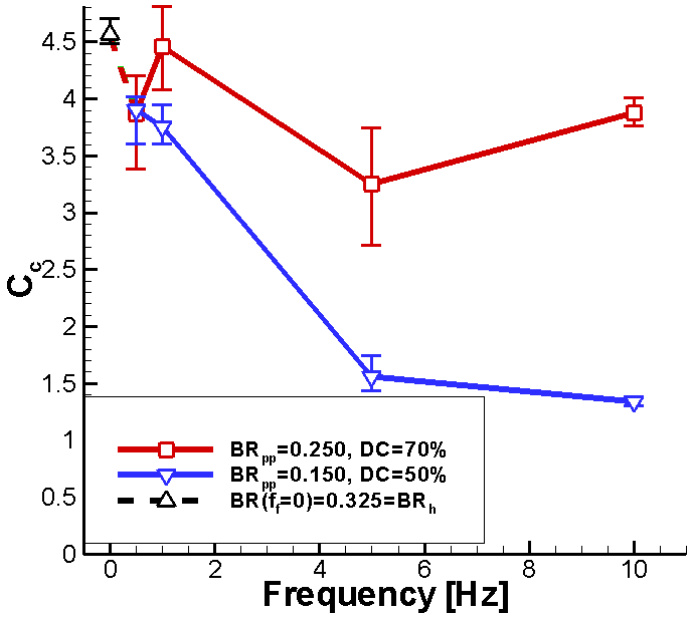

Figure 5-52: Coverage coefficient comparison at BR_m=0.250, BR_h=0.325 for several duty cycles and BR_{pp}.

Figure 5-52 compares two cases with identical BR_m and BR_h, respectively 0.250 and 0.325 and varying duty cycle / peak to peak blowing ratio (Case#2 & Case#5). It can be noticed that at forcing frequency of 0.5Hz both coverage coefficients are identical, but diverge as f_f increases with a systematic better coverage for the case with higher BR_{pp}. This result can be explained by the possiblity of a higher

overshoot in the DC=50% case pushing the high part of the cycle in an even more unfavorable position while the flow has time to settle at a more beneficial value in the DC=70% case. To support this explanation, the low frequencies results show comparable values because the transient part is negligible.

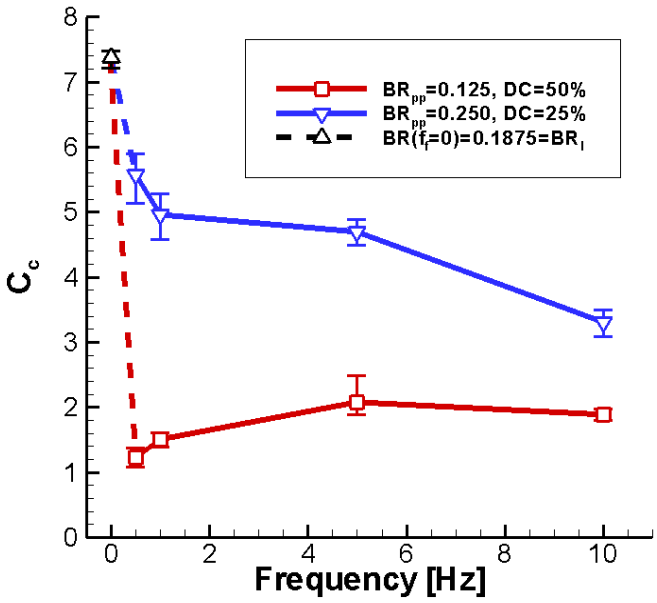

Figure 5-53: Coverage coefficient comparison at BR_m=0.250, BR_l=0.188 for several duty cycles and BR_{pp}.

Figure 5-53 displays a comparison of cases at equal BR_m and BR_l, respectively 0.250 and 0.1875, with a changing duty cycle (Case#1 & Case#3). At all forcing frequencies, the best coverage is obtained at DC=25%. Even though at DC=25% the BR_h is higher (0.438) than at DC=50% (0.313), they are both within or after the coverage drop area observed in steady state. In these conditions, the amount of time the jet is in unfavorable position (high part of the cycle), determined by the value of DC, plays a more important role than the actual value of the BR_h.

Figure 5-54 compares the influence of DC at a given BR_m of 0.350 and fixed BR_{pp} of 0.250 (Case#8 to 10). At this BR_m the overall coverage coefficients are lower than for the corresponding cases at BR_m=0.250. At given DC, the highest coverage coefficient is obtained at a forcing frequency of 0.5Hz for DC=25 and 50%, and at f_f=1Hz for DC=70%. For this last duty cycle value, the forcing frequency appears to have only a limited influence on the coverage coefficient which increases of only 30% with respect to the lowest coverage coefficient. Conversely, at DC=25% and DC=50%, the coverage

coefficient values varies with a large amplitude of respectively 135% and 125% with respect to the lowest coverage coefficient and a dramatic drop in coverage coefficient can be observed from f_f = 0.5 to f_f =1Hz. Similarly to the cases in Figure 5-51, the jet coverage appears more sensitive to changes in duty cycle at forcing frequencies of 0.5 and 5Hz with coverage coefficient variations of respectievely 125% and 79% with respect to the lowest value, while the fluctuation is only 30% at f_f =1Hz, and negligible at f_f =10Hz. Finally, the overall optimal coverage for these cases is achieved at DC=50%.

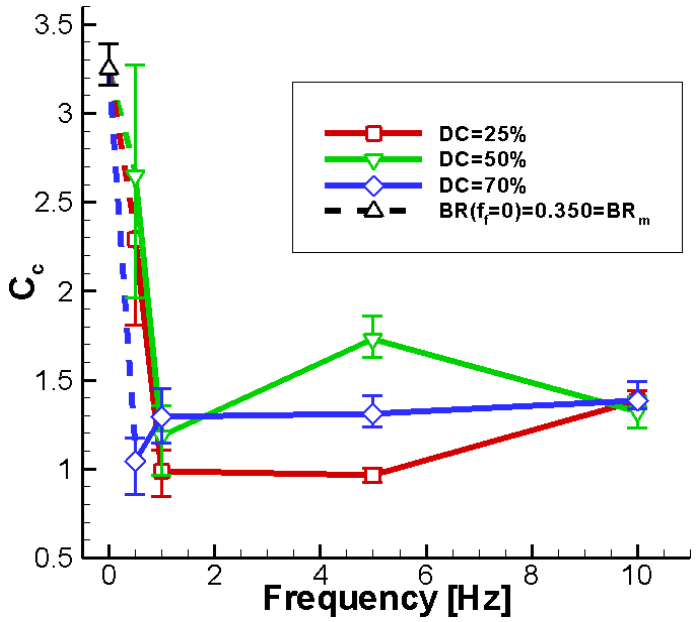

Figure 5-54: Coverage coefficient comparison at BR_m=0.350, BR_{pp}=0.250 for several duty cycles.

Figure 5-55 compares two cases with identical BR_m of 0.350 and identical BR_h of 0.425 (Case#7 & Case#9). The coverage coefficient is generally around unity, and none of these two cases displays an overall optimal coverage over the complete range of frequencies. The lower duty cycle of 50% offers the best coverage for $f_f \leq$ 1Hz, while for higher frequencies f_f = 5 and 10Hz, the cases with higer duty cycle shows higher coverage coefficients.

Figure 5-56 compares the coverage coefficient of two cases at BR_l=0.1875 and DC=50%, with changing BR_m (Case#1 & Case#6). This comparison reveals with no surprise that the highest coverage is achieved for the case with the lowest mean blowing ratio of 0.250. However, it may be noticed that the two cases have a similar coverage coefficient at f_f=0.5Hz and only diverge at higher frequencies,

suggesting that BR_h has a relatively low influence on the coverage coefficient at lower frequencies (at fixed DC).

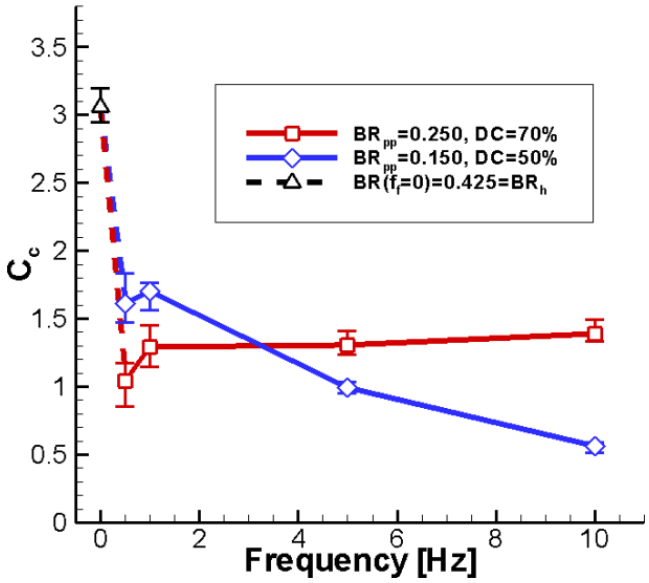

Figure 5-55: Coverage coefficient comparison at BR_m=0.350, BR_h=0.425 for several duty cycles and BR_{pp}.

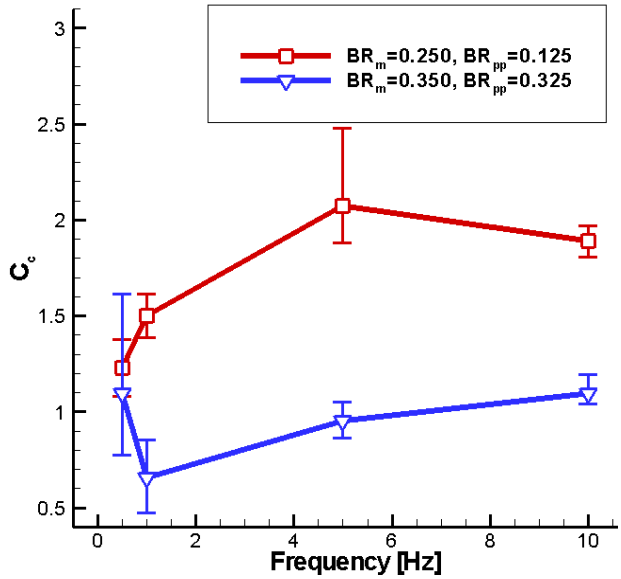

Figure 5-56: Coverage coefficient comparison at BR_l=0.188, DC=50% for several BR_m.

Figure 5-57 compares the coverage coefficients of cases at fixed BR_m of 0.250, fixed duty cycle of 50% for varying BR_{pp} (Case#1, Case#2 & Case#4). The overall best coverage is achieved at BR_{pp} = 0.250 at all frequencies. At f_f = 0.5 and 1Hz, the trend is monotonic and the coverage coefficient at a

given frequency consistently decreases with the BR_{pp} and the coverage coefficient values at fixed BR_{pp} barely vary from f_f = 0.5Hz to f_f = 1Hz. For frequencies higher than 1Hz, the coverage coefficient reaches a minimum at BR_{pp}=0.150 and is maximum at BR_{pp}=0.250. Again the variation in coverage coefficient for a given BR_{pp} is low between f_f = 5Hz and f_f = 10Hz.

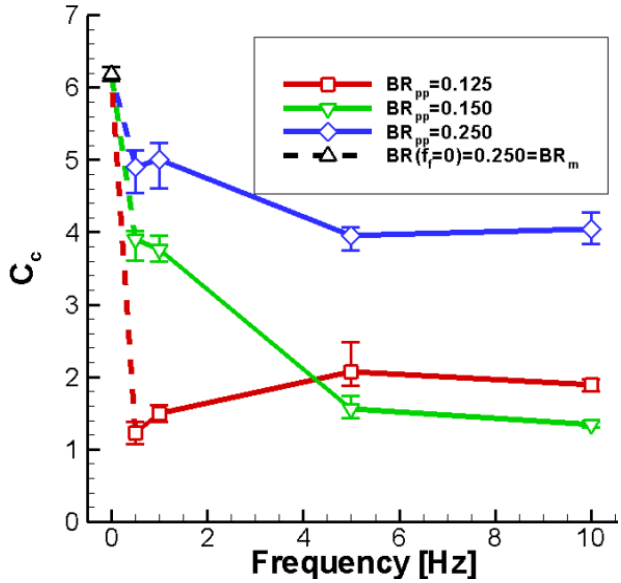

Figure 5-57: Coverage coefficient comparison at BR_m=0.250, DC=50% for several BR_{pp}.

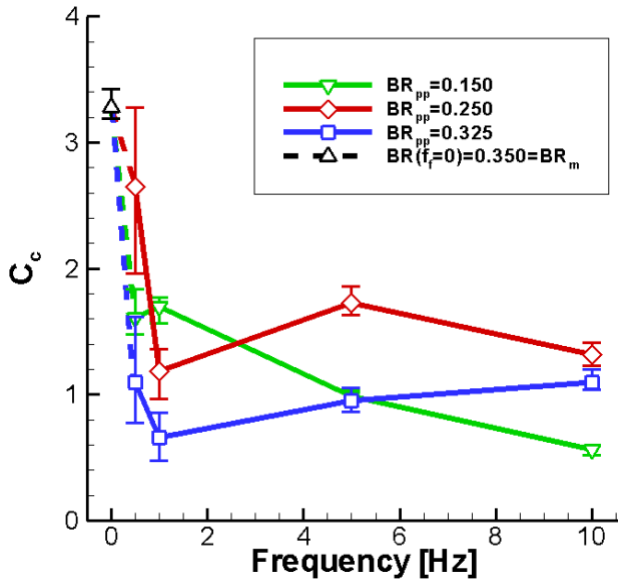

Figure 5-58: Coverage coefficient comparison at BR_m=0.350, DC=50% for several BR_{pp}.

Finally,Figure 5-58 compares the coverage coefficient of three cases at fixed BR_m of 0.350 and fixed duty cycle of 50% with changing BR_{pp} (Case#6, Case#7 & Case#9). In opposition to the previous

comparison in Figure 5-57, none of these cases achieves an overall best coverage over the whole cycle, even though the case BR_{pp}=0.25 achieves best coverage at ff=0.5, 5 and 10Hz.

Figure 5-59 presents span-wise averaged normalized intensity ($<I^N>_{spanwise}$) results. Both computations with $-2.5<Y/D_j<2.5$ and $-0.9<Y/D_j<0.9$ were carried in order to study the effect of the horseshoe vortex on the $<I^N>_{spanwise}$ quantity in pulsed jet experiments. Only some of the cases forced at f_f=0.5 exhibit a relatively low influence of the horse-shoe vortex on $<I^N>_{spanwise}$ (Case#2, Case#3, Case#6). This limited influence was somewhat expected since no trace of the horse-shoe vortex was observed on the footprint plots in Figure 5-50, and is in perfect agreement with the visualizations showing a highly unstable horse-shoe vortex. At BR_m=0.250, all the cases show a decreased $<I^N>_{spanwise}$ compared to the fixed mass-flow steady state case and only Case#2 shows an influence of the forcing frequency on $<I^N>_{span}$ with a clear decrease in value for f_f = 5 and 10Hz, which again was expected according to Figure 5-50. The $<I^N>_{spanwise}$ values of the pulsed cases and the corresponding steady state case at fixed mass-flow show good agreement far from the jet exit ($X/D_j>5$), supporting the validity of the comparison. At BR_m=0.350, the difference between the fixed mass-flow steady state case and the pulsed cases is reduced. For $X/D_j<2$, the steady state case shows higher values of $<I^N>_{spanwise}$, but for $X/D_j>2$ Cases#6, 8 and 9 achieve slightly higher values of $<I^N>_{spanwise}$. Similarly to BR_m=0.250, the values of the pulsed cases far from the jet exit ($X/D_j>4$) show good agreement with the one of the fixed mass flow steady state.

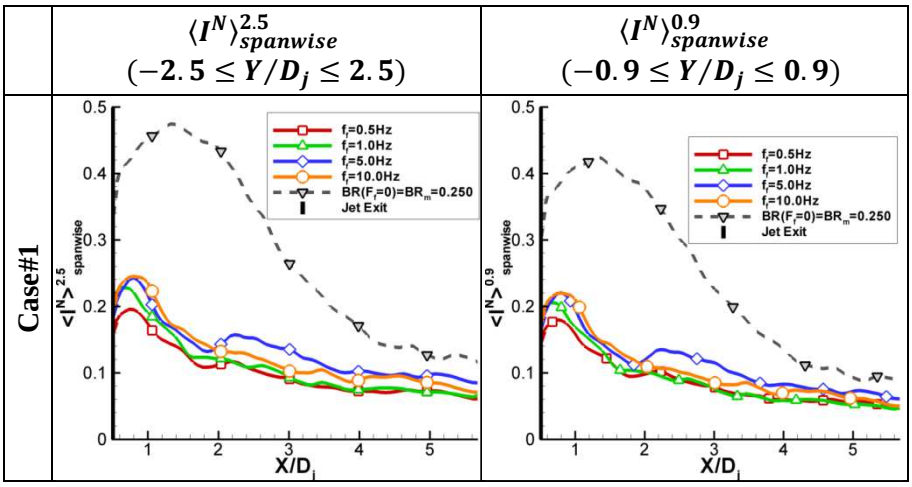

Figure 5-59: Span-wise averaged normalized intensity ($<I^N>_{spanwise}$) for $-2.5 \leq Y/D_j \leq 2.5$ and $-0.9 \leq Y/D_j \leq 0.9$. (Figure 5-59 cont.)

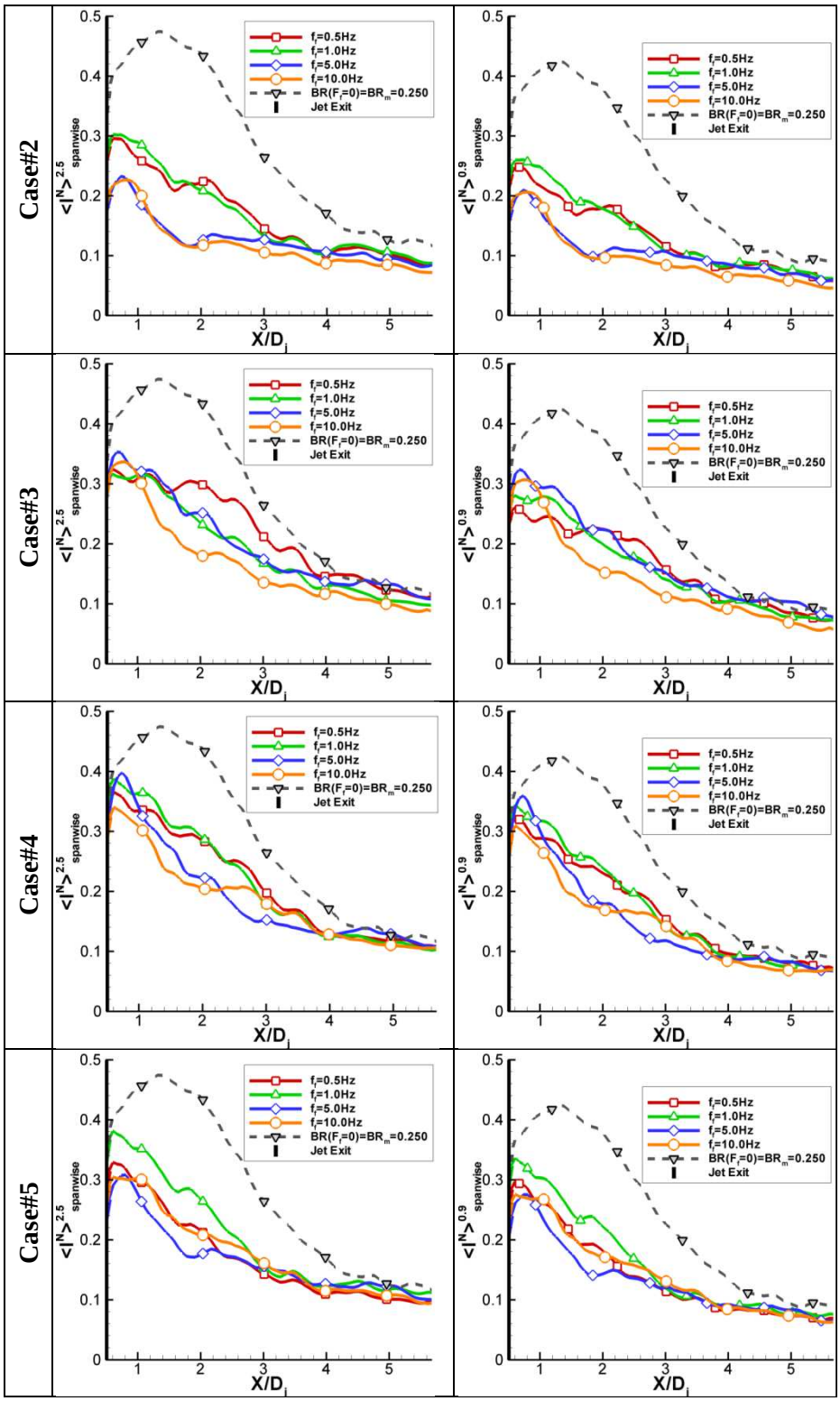

Figure 5-59 cont.

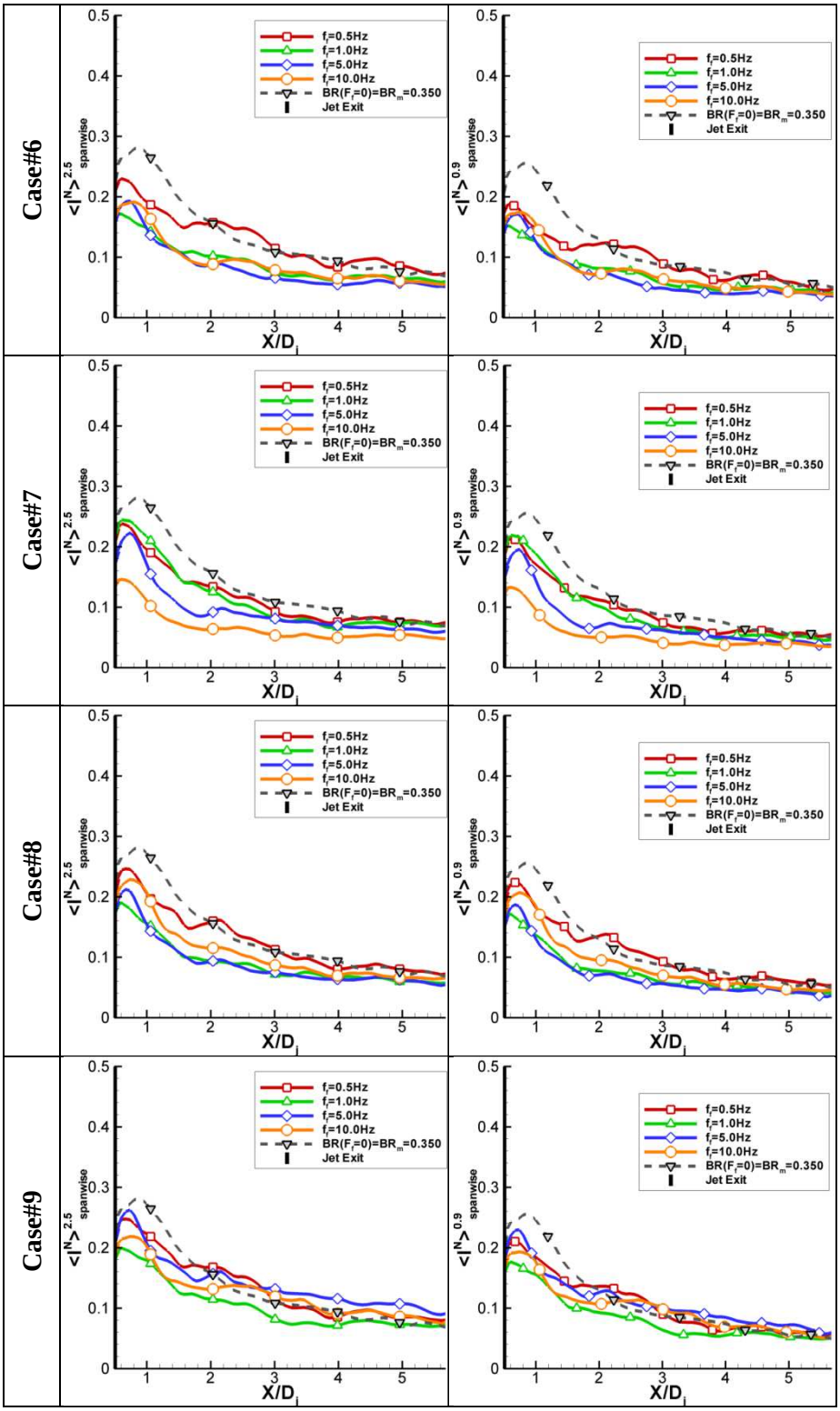

Figure 5-59 cont.

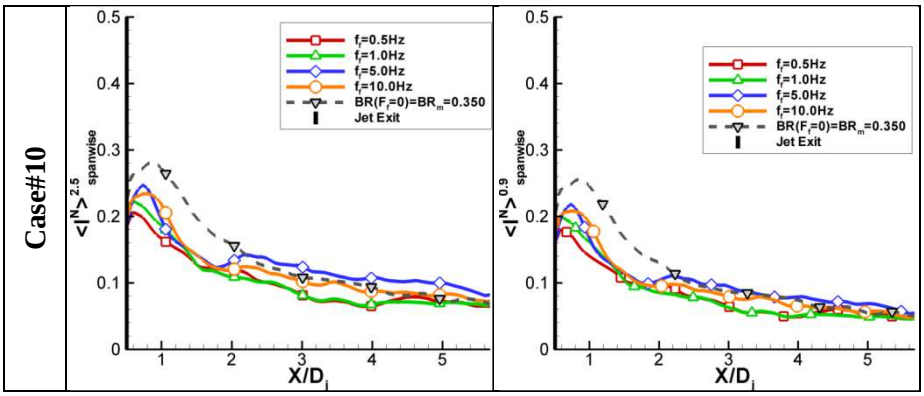
Case#10
0.5
0.4
0.3
0.2
0.1
0
1
2
3
4
5
X/D_j
<I^N>^2.5 spanwise
<I^N>^0.9 spanwise
f_j=0.5Hz
f_j=1.0Hz
f_j=5.0Hz
f_j=10.0Hz
BR(F_j=0)=BR_m=0.350
Jet Exit

Chapter 6: Conclusion

Using visualizations based on Mie scattering techniques and single component hot-wire measurements, we have studied the structures of a jet in cross-flow in steady and forced flow configurations, as well as theirs dynamics and characteristic frequencies.

The visualizations of the steady state revealed the existence of two distinct regimes. The first regime at low blowing ratios is characterized by an attached jet with dominating shear layer instabilities and a stable recirculation region located downstream of the jet exit. The second regime, visible at higher blowing ratios, is characterized by a completely detached jet with periodic ring-like vortices formation similar to jet column mode instabilities of a jet in quiescent environment. The intermediate cases exhibit mixing and interactions of the characteristic features from both regimes. The constant temperature anemometry measurements realized at several locations of all studied blowing ratios helped characterizing the periodicity of the structures formation and finding adapted scaling to the different regimes. As expected, the jet penetration increases with the blowing ratio with a plateau in penetration progression between BR=0.300 and BR=0.465, while the coverage coefficient and the estimated efficiency exhibit a dramatic decrease between BR=0.300 and BR=0.365.

The pulsed jet visualizations reveal the systematic formation of a starting vortex, comparable to a ring like-vortex, at the passage from low flow to high flow and we have been able to provide a plausible explanation of the dynamics of this structure. The horse-shoe vortex appears very unstable and sheds periodically, apparently interacting with the starting vortex. The visualizations and hot-wire measurement divide the forcing frequency domain in two different groups with, on one hand, quasi-steady state jet behavior at lower frequencies, and on the other hand, single structure shedding at higher frequencies. The jet penetration is consistently increased compared to the fixed mass-flow steady state and the jet coverage is consistently decreased in forced conditions with the exception of four cases with increased or matching performance compared to the corresponding fixed mass-flow and fixed pressure steady state case.

Overall, the forcing of the jet flow and the introduction of the starting vortex appear to be detrimental to the jet metrics in terms of film cooling purposes. In most of the cases, forcing at a given

blowing ratio appears to help the formation of structures generally visible at higher blowing ratios such as ring-like vortices, and to destabilize structures usually stable in corresponding steady state conditions such as the horse-shoe vortex. The result is an overall decreased coverage and an increased penetration and the only improvements observed are made over steady state cases with already low performances. The structures injected in the cross flow are systematically shed in the free stream and do not bring additional coverage. However, most of the actual film-cooling systems use injection holes at injection angles much lower than 90 deg (of the order of 35 deg). Dynamic structures formed in this type of system could benefit from stream wise momentum allowing them to stay close to the bottom wall and to bring extra coverage. The induction effect created by the mirror image of the starting vortex with respect to the wall could also play an important role as to keep this structure from penetrating in the free stream. The study of a single jet in cross-flow at comparable low blowing ratios with an injection angle of 35 deg. is part of the future work to be done, in addition to increased visualizations planes and velocity measurement methods such as PIV measurements in order to completely resolve the dynamics of the starting and horse-shoe vortex structures.

References

Bons (2001). "Turbine Separation Control Using Pulsed Vortex Generator Jets." Journal of Turbomachinery **123**.

Bons (2002). "The Fluid Dynamics of LPT Blade Separation Control Using Pulsed Jets." Journal of Turbomachinery **124**(January 2002): 77-85.

Boulladoux (2006). Pulsed Vertical Jet in Cross-flow at Mean Blowing Ratios of 0.35 and 0.45. Mechanical Engineering. Baton Rouge, Louisiana State University. **MSc**.

Coulthard (2007). "Effect of Pulsing on Film Cooling - Part I: Effectiveness and Flow-Field Temperature Results." Journal of Turbomachinery **129**: 232-246.

Coulthard (2007). "Effect of Pulsing on Film Cooling - Part II: Heat Transfer Results." Journal of Turbomachinery **129**: 247-257.

Ekkad (2001). "Recent Development in Turbine Blade Film Cooling." International Journal of Rotating Machinery **7**(1): 21-40.

Ekkad (2004). "A Transient Infrared Thermography Method for Simultaneous Film Cooling Effectiveness and Heat Transfer Coefficient Measurements From a Single Test." Journal of Turbomachinery **126**: 597-603.

Ekkad (2006). "Effect of Jet Pulsation and Duty Cycle on Film Cooling From a Single Jet on a Leading Edge Model." Journal of Turbomachinery **128**(July 2006): 564-571.

Fan (2006). On the Heat Transfer Enhancement Based on Micro-Scale Impinging Jets with Microstructure Heat Sink in Electronics Cooling.

Gharib (1998). "A universal time scale for vortex ring formation." Journal of fluid Mechanics **360**: 121-140.

Goldstein (1996). Fluid Mechanics Measurements, Taylor & Francis.

Gopalan (2004). "The structure of a jet in cross flow at low velocity ratios." Physics of Fluids **16**(6).

Johari (1999). "Penetration and Mixing of Fully Modulated Turbulent Jets in Crossflow." AIAA Journal **37**(3): 842-850.

Karagozian (2001). "On the formation of the counter-rotating vortex pair in transverse jets." Journal of fluid Mechanics **446**: 347-373.

Lele (2006). Large Eddy Simulation of Fil-Cooling above the Flat Surface with a Large Plenum and Short Exit Holes. Aerospace Sciences Meeting and Exhibit. Reno, NV.

Lienhard (1993). Mechanical Measurements.

Lim (2000). "On the developpement of large-scale structures of a jet normal to a cross flow." Physics of Fluids **13**(3): 770-775.

M'Closkey (2002). "The actively controlled jet in crossflow." Journal of fluid Mechanics **452**: 325-335.

Megerian (2007). "Transverse-jet shear-layer instabilities. Part 1. Experimental Studies." Journal of fluid Mechanics **593**: 93-129.

Narayanan (2003). "Dynamics and Control of an Isolated Jet in Crossflow." AIAA Journal **41**(12).

New (2003). "Elliptic jets in cross-flow." Journal of fluid Mechanics **494**: 119-140.

Nikitopoulos (2006). On Active Control of Film-Cooling Flows. ASME Turbo Expo: Power for Land, Sea and Air. Barcelona, Spain.

Oertling (2006). EFFECT OF BULK FLOW MODULATIONS ON A NORMAL JET IN CROSSFLOW AT A MEAN BLOWING RATIO OF 0.25. Mechanical Engineering. Baton Rouge, Louisiana State University. **MSc**.

Ou (2006). Shaped-hole film cooling with pulsed secondary flow. ASME Turbo Expo. Barcelona, Spain.

Said (2004). "Experimental and numerical analysis of pollutant dispersion from a chimney." Atmospheric Environment **39**: 1727-1738.

Torrence (1998). "A Practical Guide to Wavelet Analysis." Bulletin of the American Meteorological Society **79**(1): 61-78.

Appendix: Pulsed Cases Visualizations and CTA Measurements

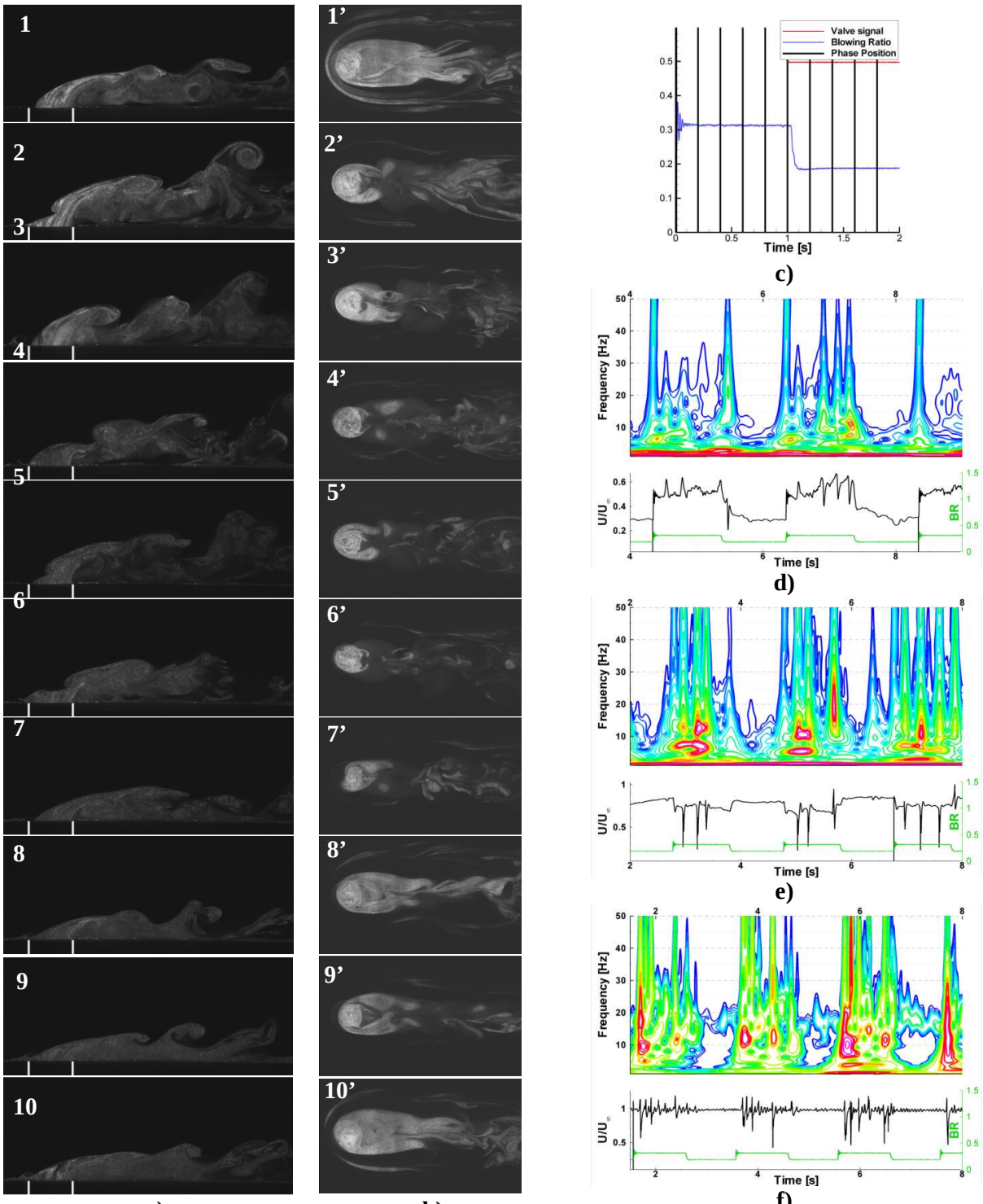

Figure A - 1: Pulsed cases Visualizations at BR_m=0.250, BR_l=0.1875, DC=0.50, f_f=0.5Hz - a) (1-10) X-Z visualizations. b) (1'-10') X-Y visualizations. c) Phase averaged flow-meter record. d)-f) Wavelet analysis of the hot-wire records at d) X/D_j=0, Z/D_j=0, e) X/D_j=0, Z/D_j=0.5, f) X/D_j=3.5, Z/D_j=1.25 – Case#1.

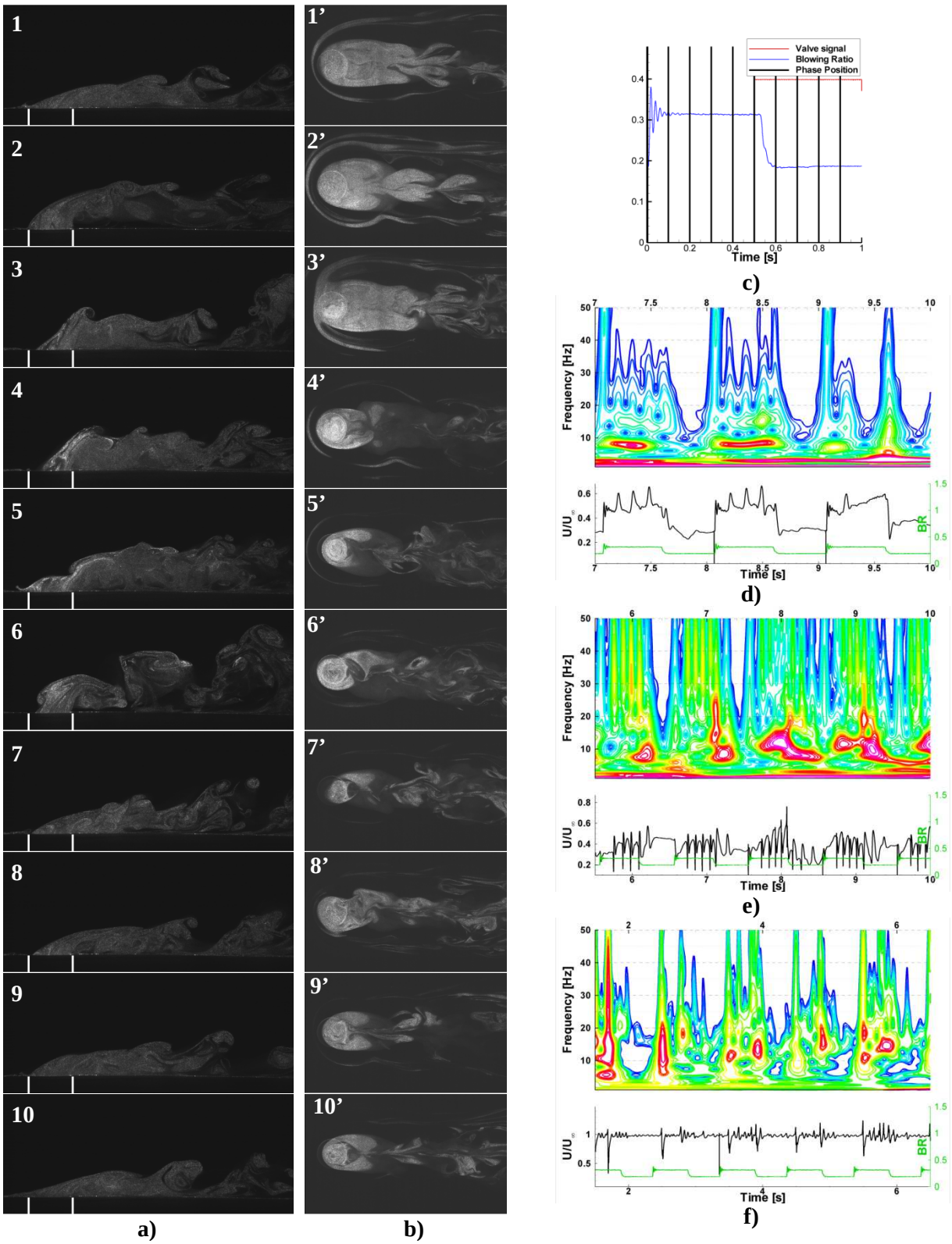

Figure A - 2: Pulsed cases Visualizations at BR_m=0.250, BR_l=0.1875, DC=0.50, f_f=1.0Hz - a) (1-10) X-Z visualizations. b) (1'-10') X-Y visualizations. c) Phase averaged flow-meter record. d)-f) Wavelet analysis of the hot-wire records at d) X/D_j=0, Z/D_j=0, e) X/D_j=0, Z/D_j=0.5, f) X/D_j=3.5, Z/D_j=1.25 – Case#1.

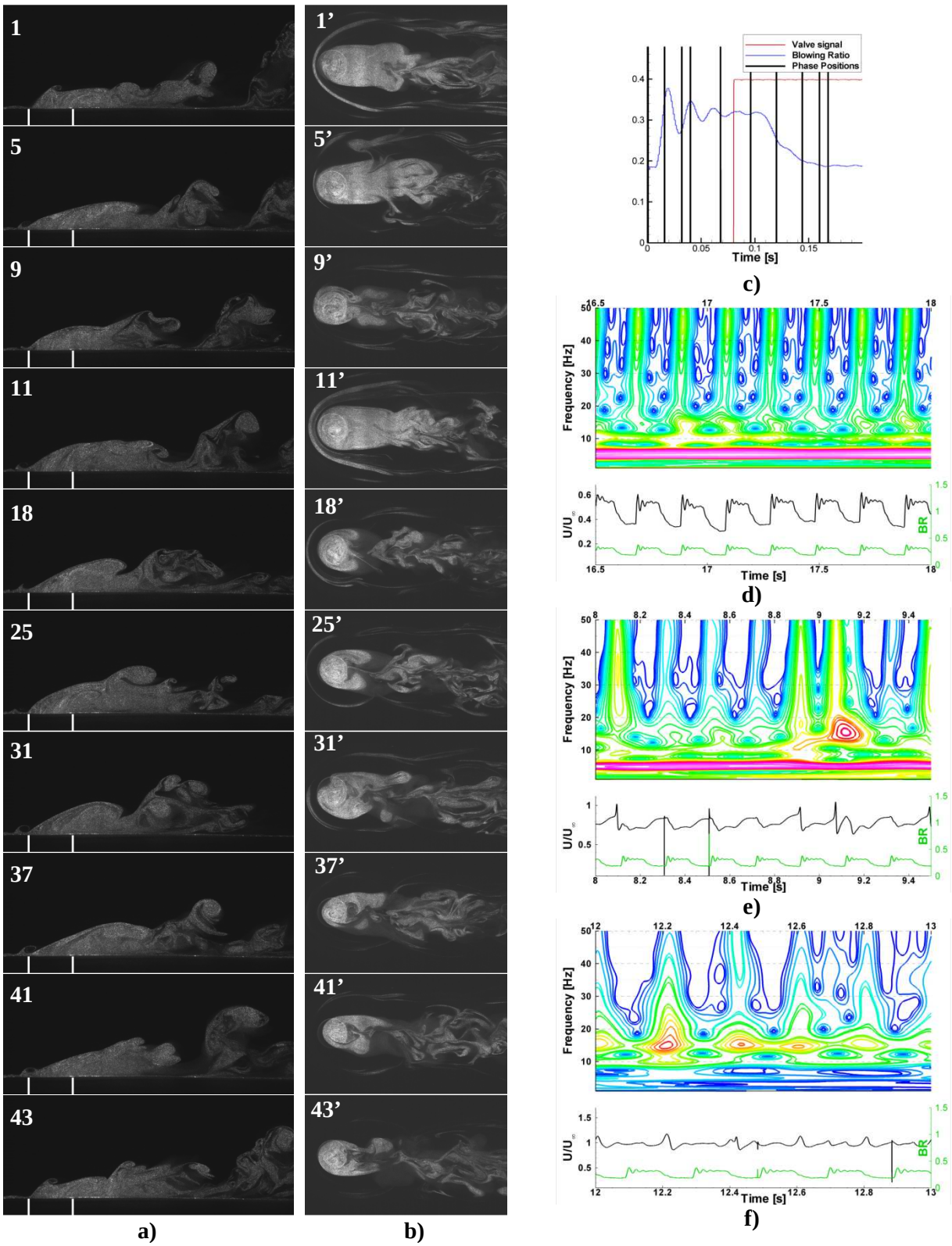

Figure A - 3: Pulsed cases Visualizations at BR_m=0.250, BR_l=0.1875, DC=0.50, f_f=5.0Hz - a) (1-43) X-Z visualizations. b) (1'-43') X-Y visualizations. c) Phase averaged flow-meter record. d)-f) Wavelet analysis of the hot-wire records at d) X/D_j=0, Z/D_j=0, e) X/D_j=0, Z/D_j=0.5, f) X/D_j=3.5, Z/D_j=1.25 – Case#1.

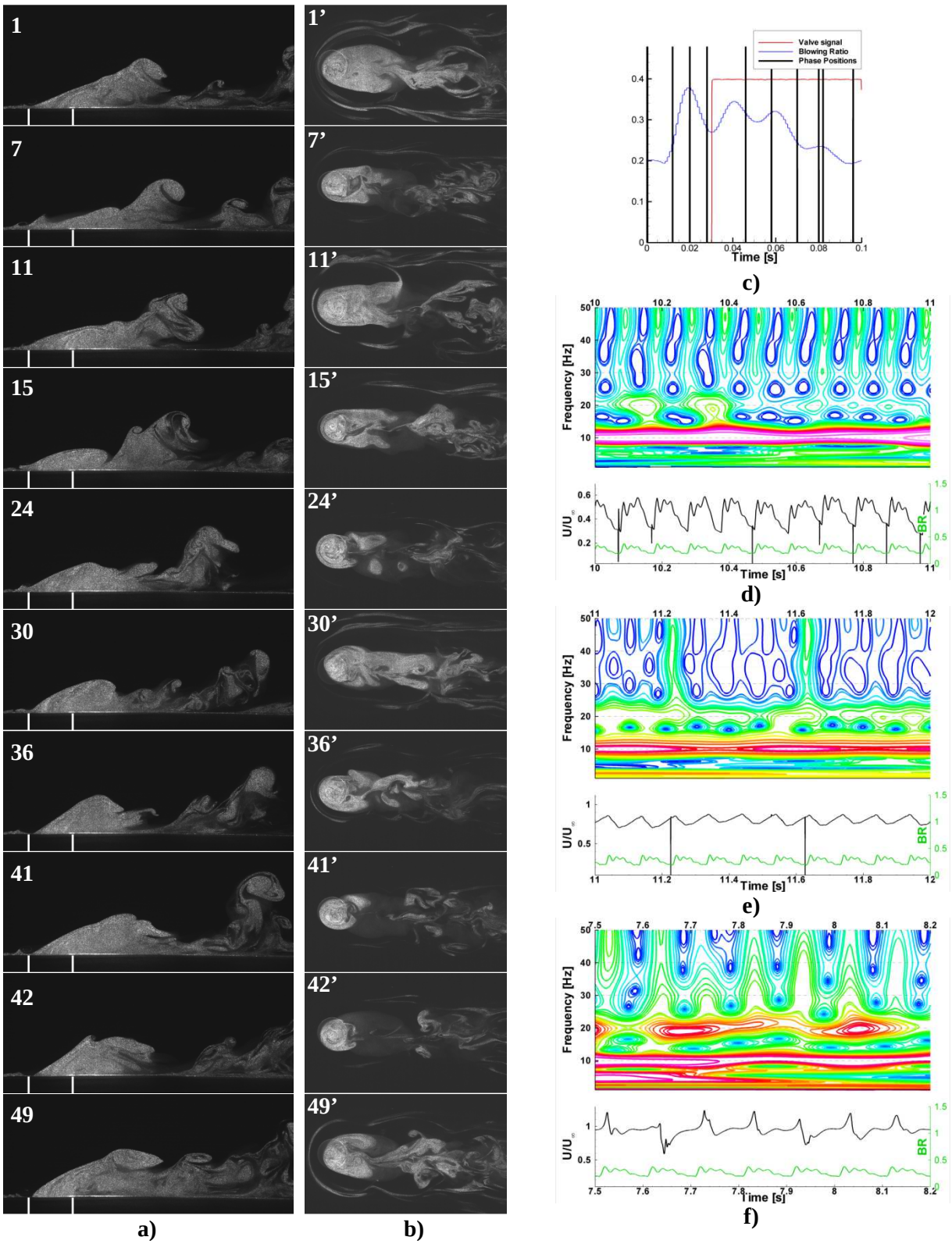

Figure A - 4: Pulsed cases Visualizations at BR_m=0.250, BR_l=0.1875, DC=0.50, f_f=10Hz - a) (1-49) X-Z visualizations. b) (1'-49') X-Y visualizations. c) Phase averaged flow-meter record. d)-f) Wavelet analysis of the hot-wire records at d) X/D_j=0, Z/D_j=0, e) X/D_j=0, Z/D_j=0.5, f) X/D_j=3.5, Z/D_j=1.25 – Case#1.

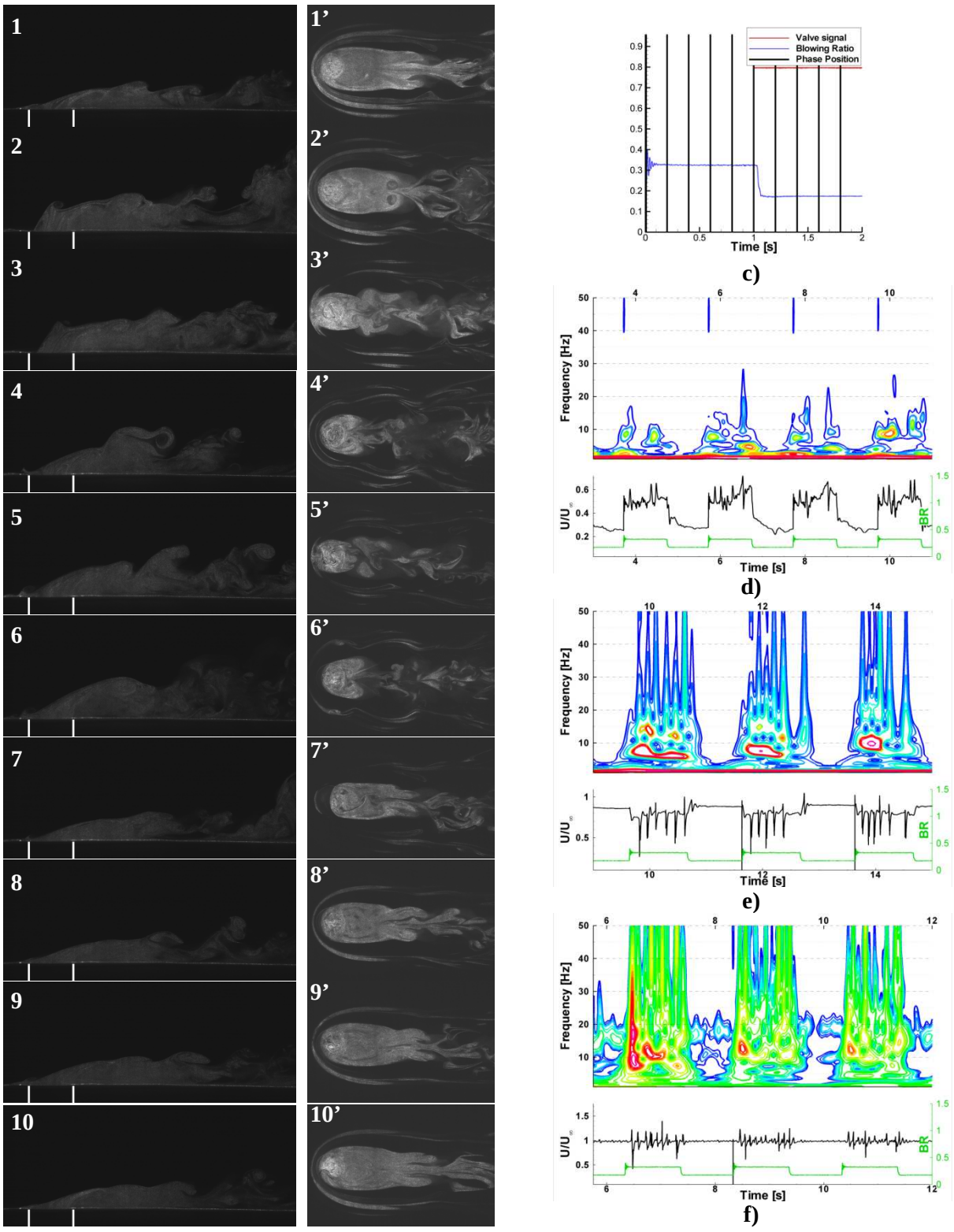

Figure A - 5: Pulsed cases Visualizations at BR_m=0.250, BR_{pp}=0.150, DC=0.50, f_f=0.5Hz - a) (1-10) X-Z visualizations. b) (1'-10') X-Y visualizations. c) Phase averaged flow-meter record. d)-f) Wavelet analysis of the hot-wire records at d) X/D_j=0, Z/D_j=0, e) X/D_j=0, Z/D_j=0.5, f) X/D_j=3.5, Z/D_j=1.25 – Case#2.

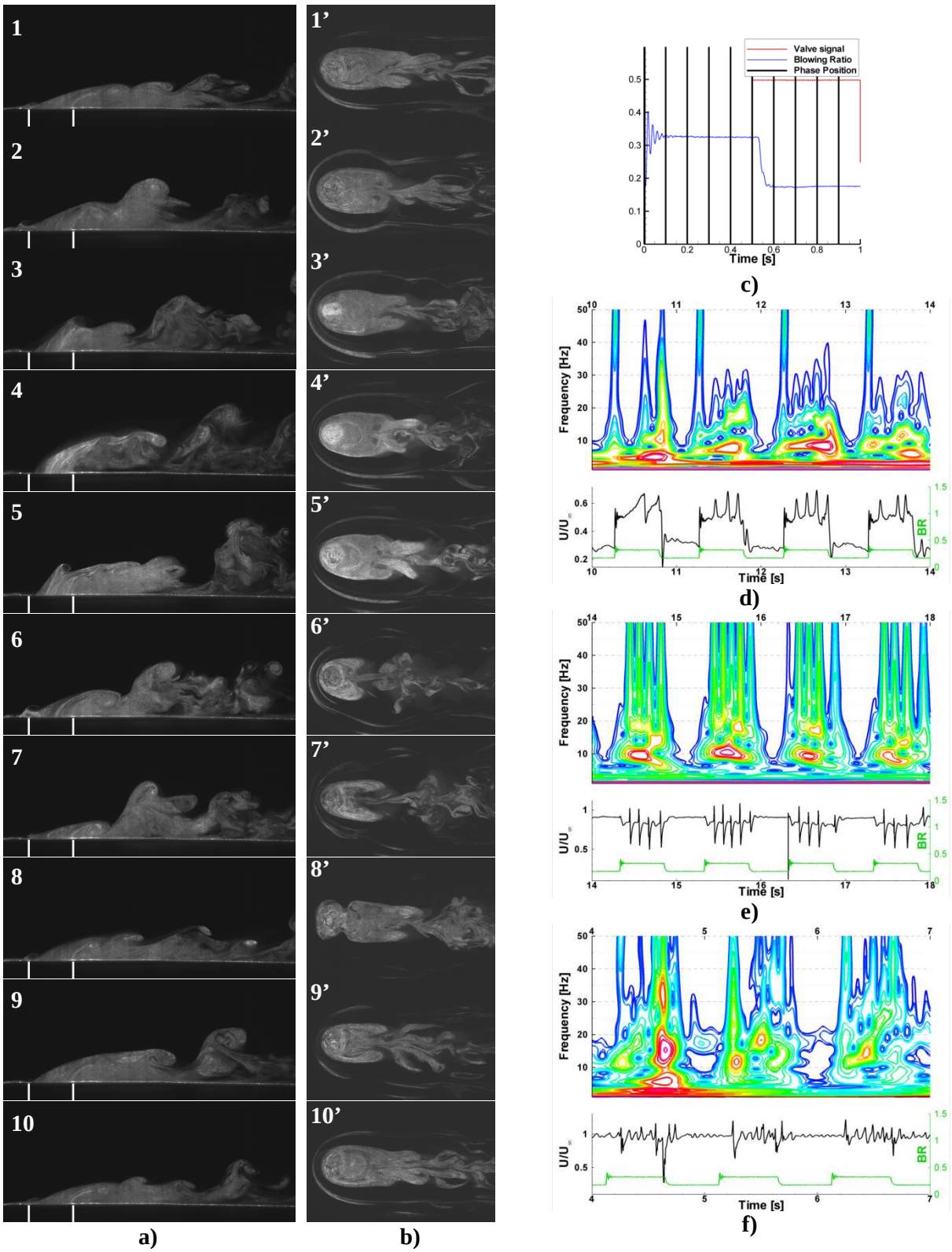

Figure A - 6: Pulsed cases Visualizations at BR_m=0.250, BR_{pp}=0.150, DC=0.50, f_f=1.0Hz - a) (1-10) X-Z visualizations. b) (1'-10') X-Y visualizations. c) Phase averaged flow-meter record. d)-f) Wavelet analysis of the hot-wire records at d) X/D_j=0, Z/D_j=0, e) X/D_j=0, Z/D_j=0.5, f) X/D_j=3.5, Z/D_j=1.25 – Case#2.

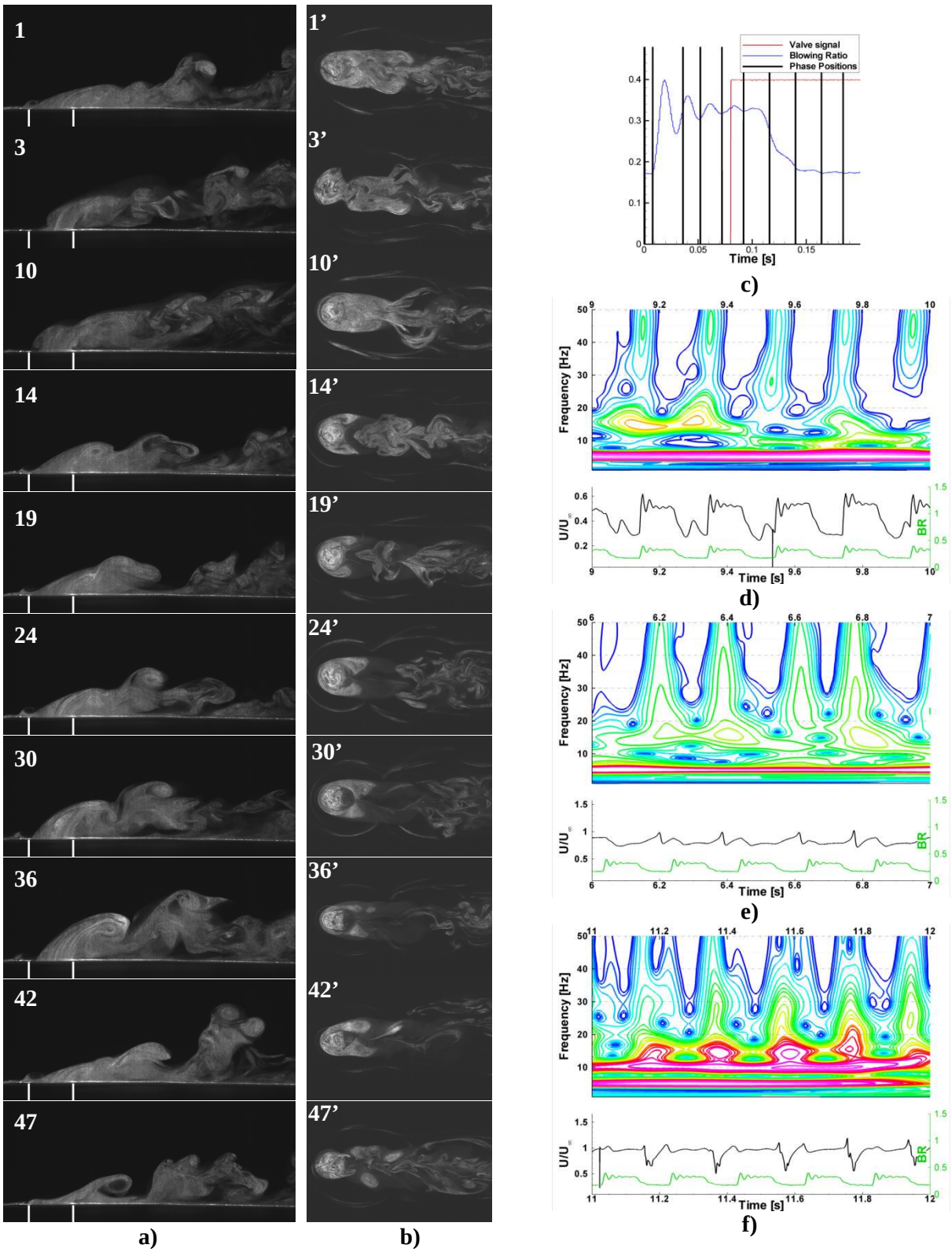

Figure A - 7: Pulsed cases Visualizations at BR_m=0.250, BR_{pp}=0.150, DC=0.50, f_f=5.0Hz - a) (1-47) X-Z visualizations. b) (1'-47') X-Y visualizations. c) Phase averaged flow-meter record. d)-f) Wavelet analysis of the hot-wire records at d) X/D_j=0, Z/D_j=0, e) X/D_j=0, Z/D_j=0.5, f) X/D_j=3.5, Z/D_j=1.25 – Case#2.

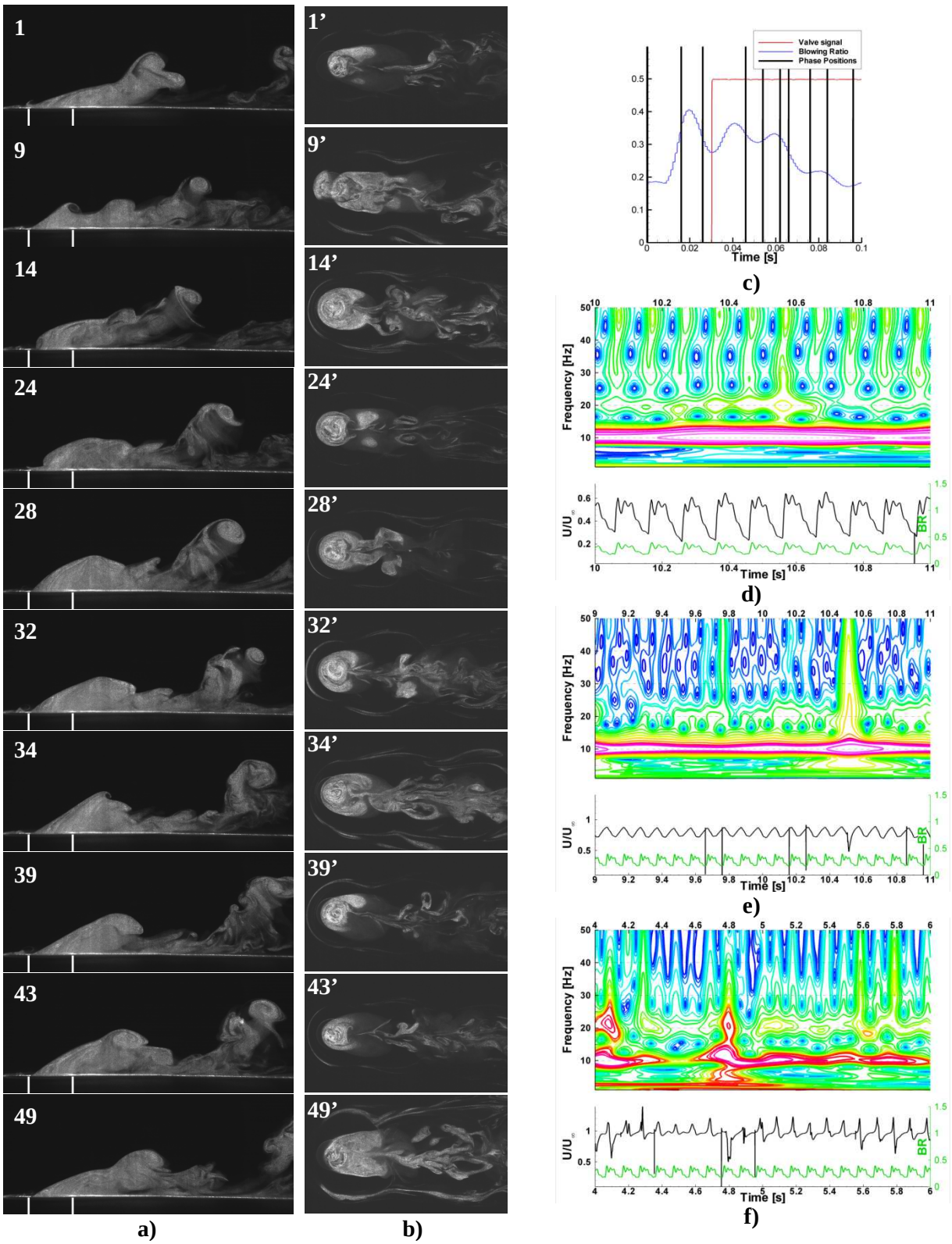

Figure A - 8: Pulsed cases Visualizations at BR_m=0.250, BR_{pp}=0.150, DC=0.50, f_f=10Hz - a) (1-49) X-Z visualizations. b) (1'-49') X-Y visualizations. c) Phase averaged flow-meter record. d)-f) Wavelet analysis of the hot-wire records at d) X/D_j=0, Z/D_j=0, e) X/D_j=0, Z/D_j=0.5, f) X/D_j=3.5, Z/D_j=1.25 – Case#2.

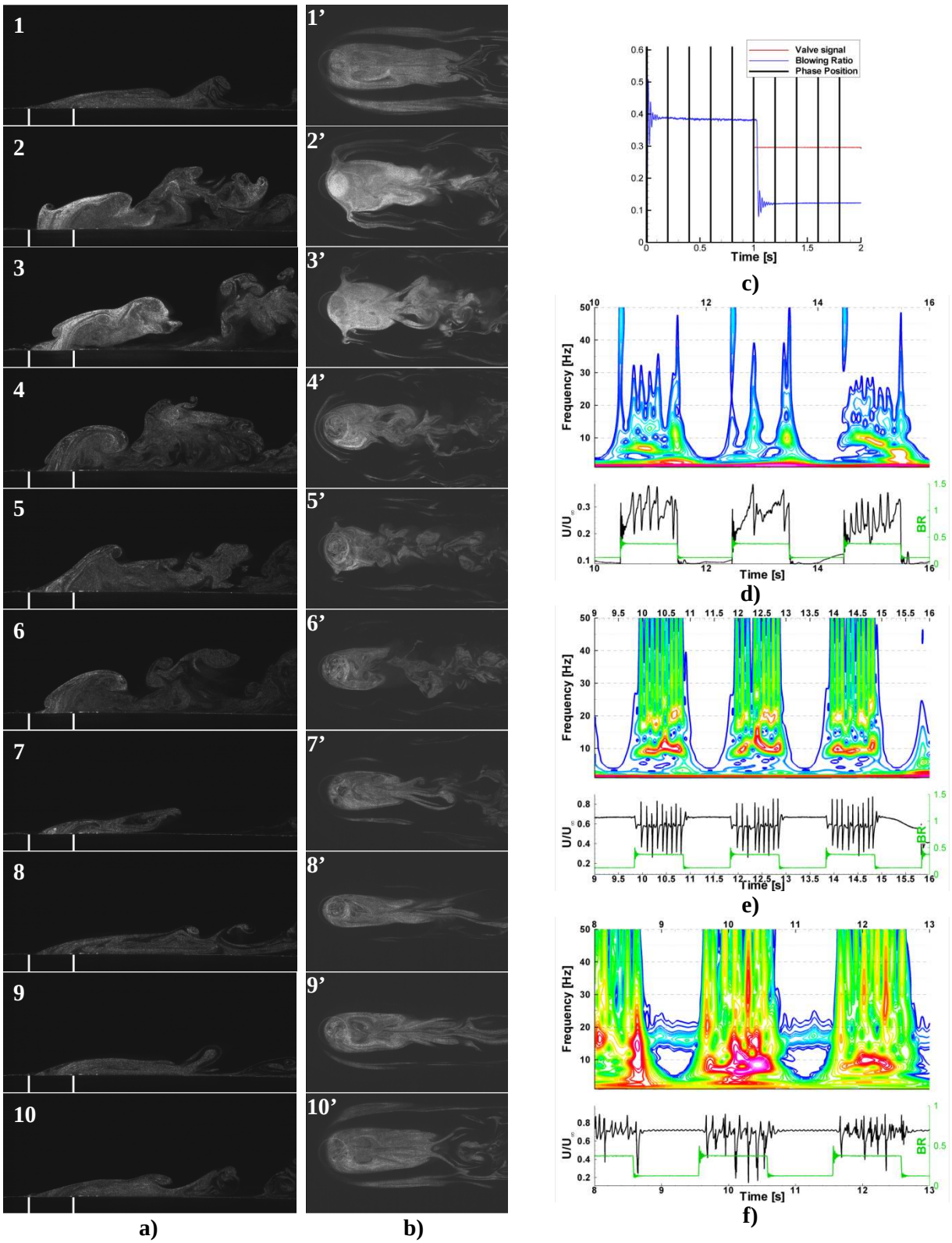

Figure A - 9: Pulsed cases Visualizations at BR_m=0.250, BR_{pp}=0.250, DC=0.50, f_f=0.5Hz - a) (1-10) X-Z visualizations. b) (1'-10') X-Y visualizations. c) Phase averaged flow-meter record. d)-f) Wavelet analysis of the hot-wire records at d) X/D_j=0, Z/D_j=0, e) X/D_j=0, Z/D_j=0.5, f) X/D_j=3.5, Z/D_j=1.25 – Case#4.

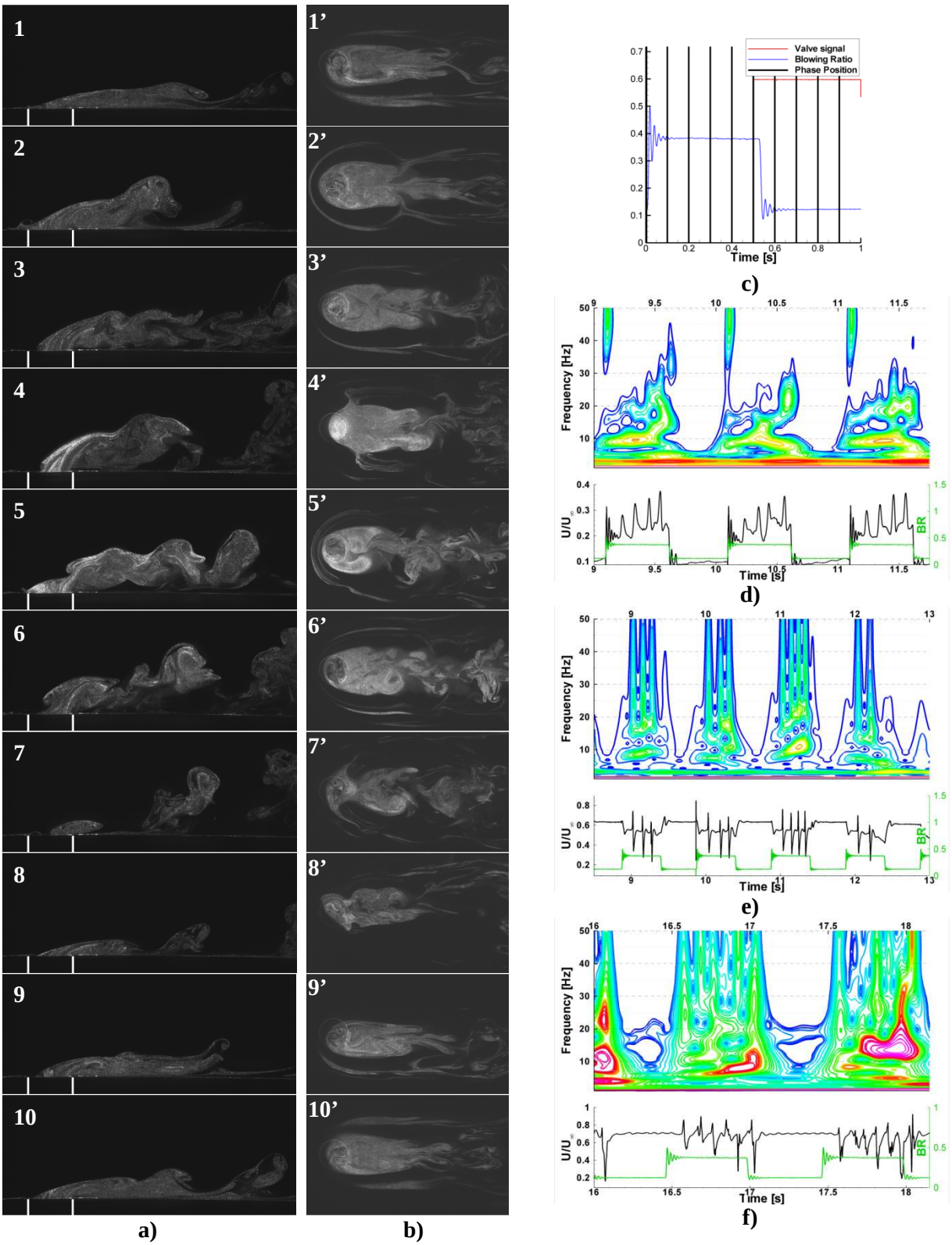

Figure A - 10: Pulsed cases Visualizations at BR_m=0.250, BR_{pp}=0.250, DC=0.50, f_f=1.0Hz - a) (1-10) X-Z visualizations. b) (1'-10') X-Y visualizations. c) Phase averaged flow-meter record. d)-f) Wavelet analysis of the hot-wire records at d) X/D_j=0, Z/D_j=0, e) X/D_j=0, Z/D_j=0.5, f) X/D_j=3.5, Z/D_j=1.25 – Case#4.

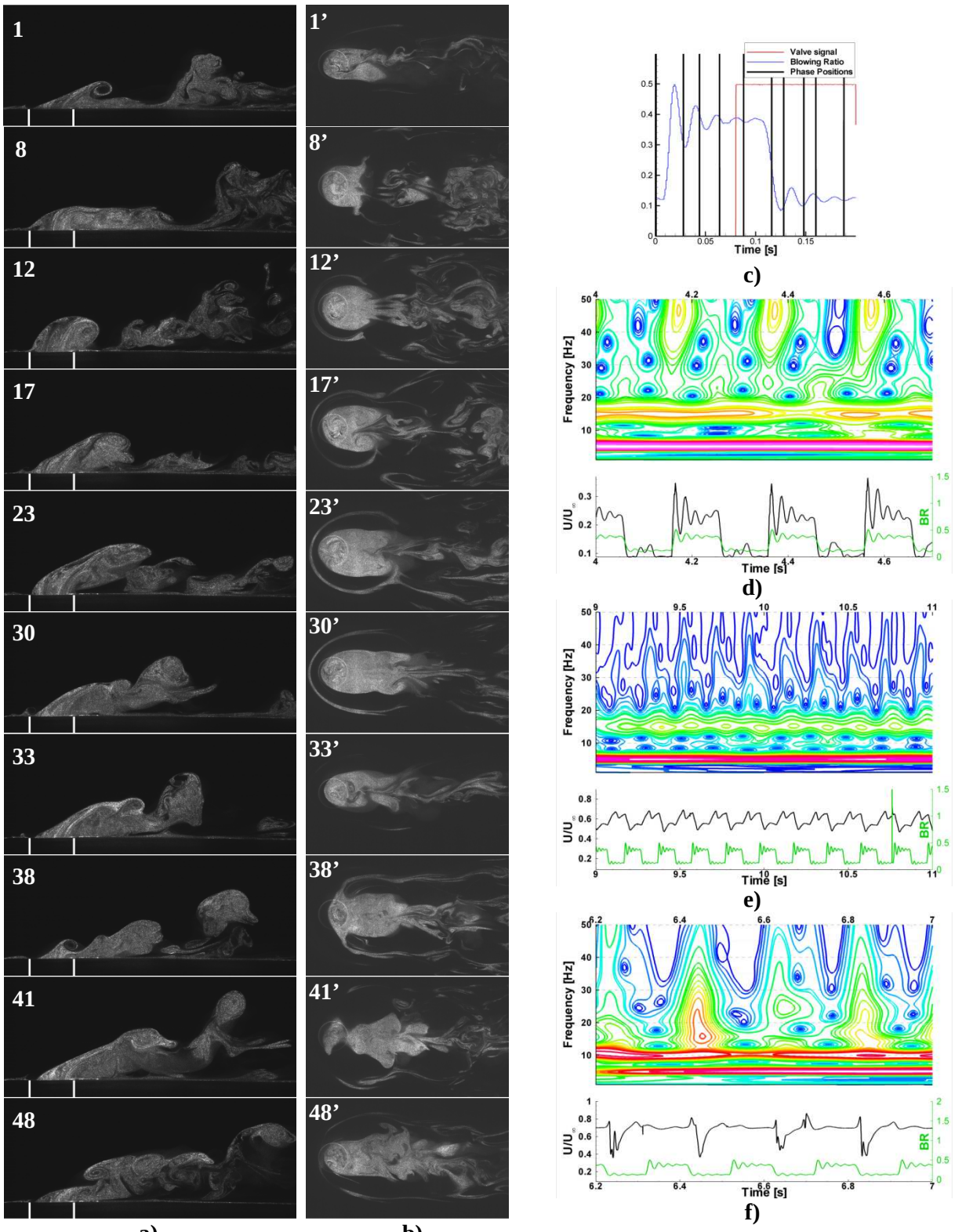

Figure A - 11: Pulsed cases Visualizations at BR_m=0.250, BR_{pp}=0.250, DC=0.50, f_f=5.0Hz - a) (1-48) X-Z visualizations. b) (1'-48') X-Y visualizations. c) Phase averaged flow-meter record. d)-f) Wavelet analysis of the hot-wire records at d) X/D_j=0, Z/D_j=0, e) X/D_j=0, Z/D_j=0.5, f) X/D_j=3.5, Z/D_j=1.25 – Case#4.

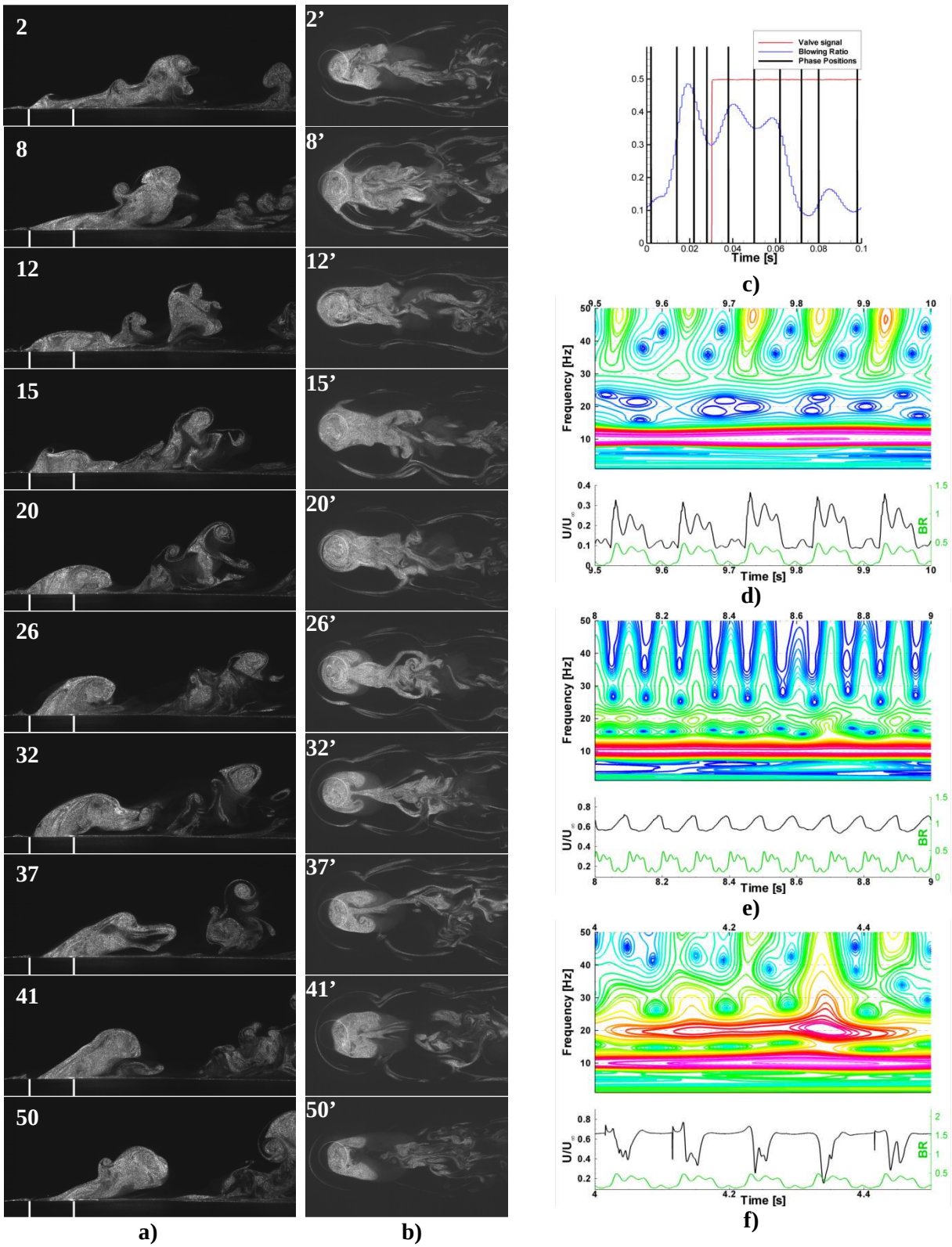

Figure A - 12: Pulsed cases Visualizations at BR_m=0.250, BR_{pp}=0.250, DC=0.50, f_f=10Hz - a) (2-50) X-Z visualizations. b) (2'-50') X-Y visualizations. c) Phase averaged flow-meter record. d)-f) Wavelet analysis of the hot-wire records at d) X/D_j=0, Z/D_j=0, e) X/D_j=0, Z/D_j=0.5, f) X/D_j=3.5, Z/D_j=1.25 – Case#4.

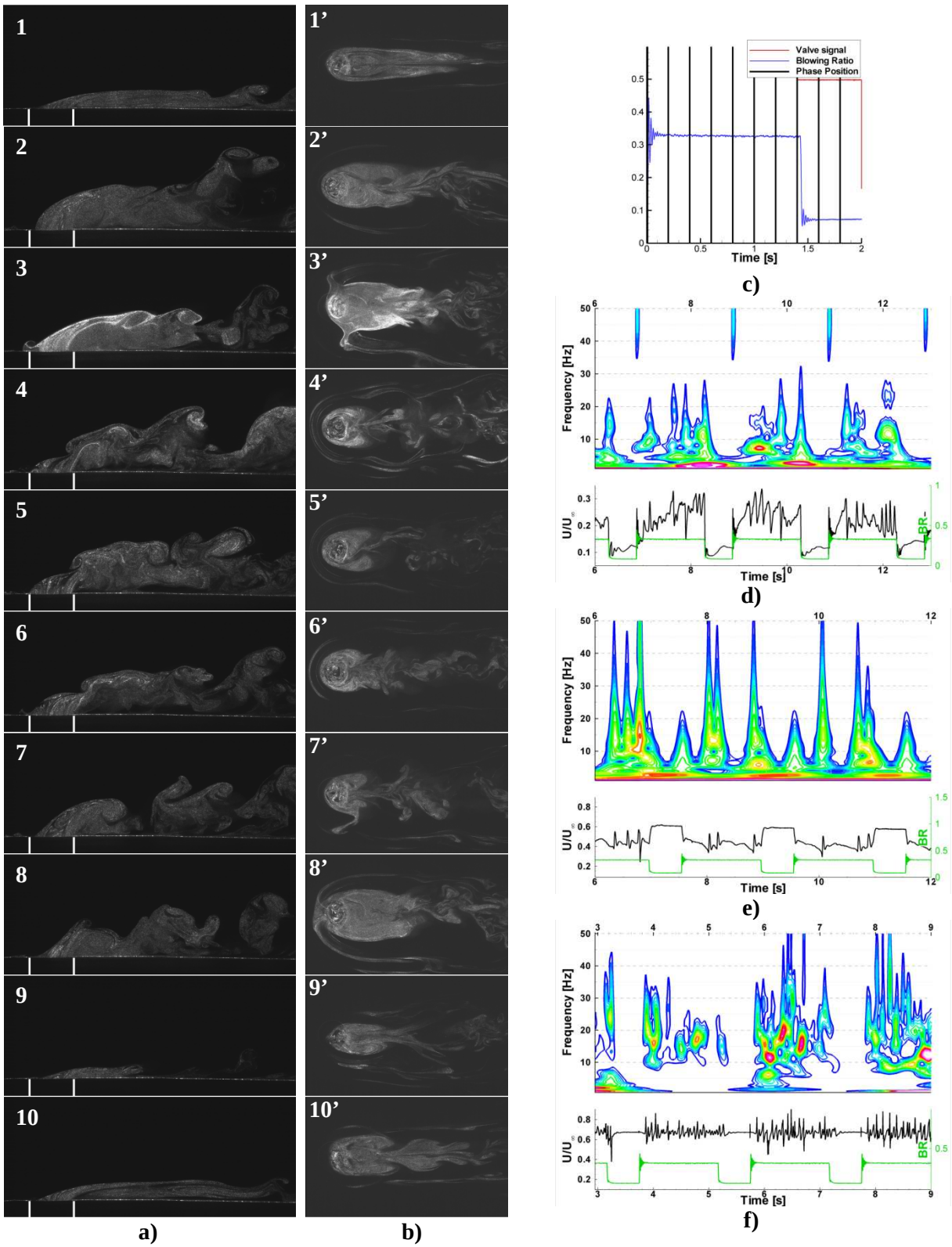

Figure A - 13: Pulsed cases Visualizations at BR_m=0.250, BR_{pp}=0.250, DC=0.70, f_f=0.5Hz - a) (1-10) X-Z visualizations. b) (1'-10') X-Y visualizations. c) Phase averaged flow-meter record. d)-f) Wavelet analysis of the hot-wire records at d) X/D_j=0, Z/D_j=0, e) X/D_j=0, Z/D_j=0.5, f) X/D_j=3.5, Z/D_j=1.25 – Case#5.

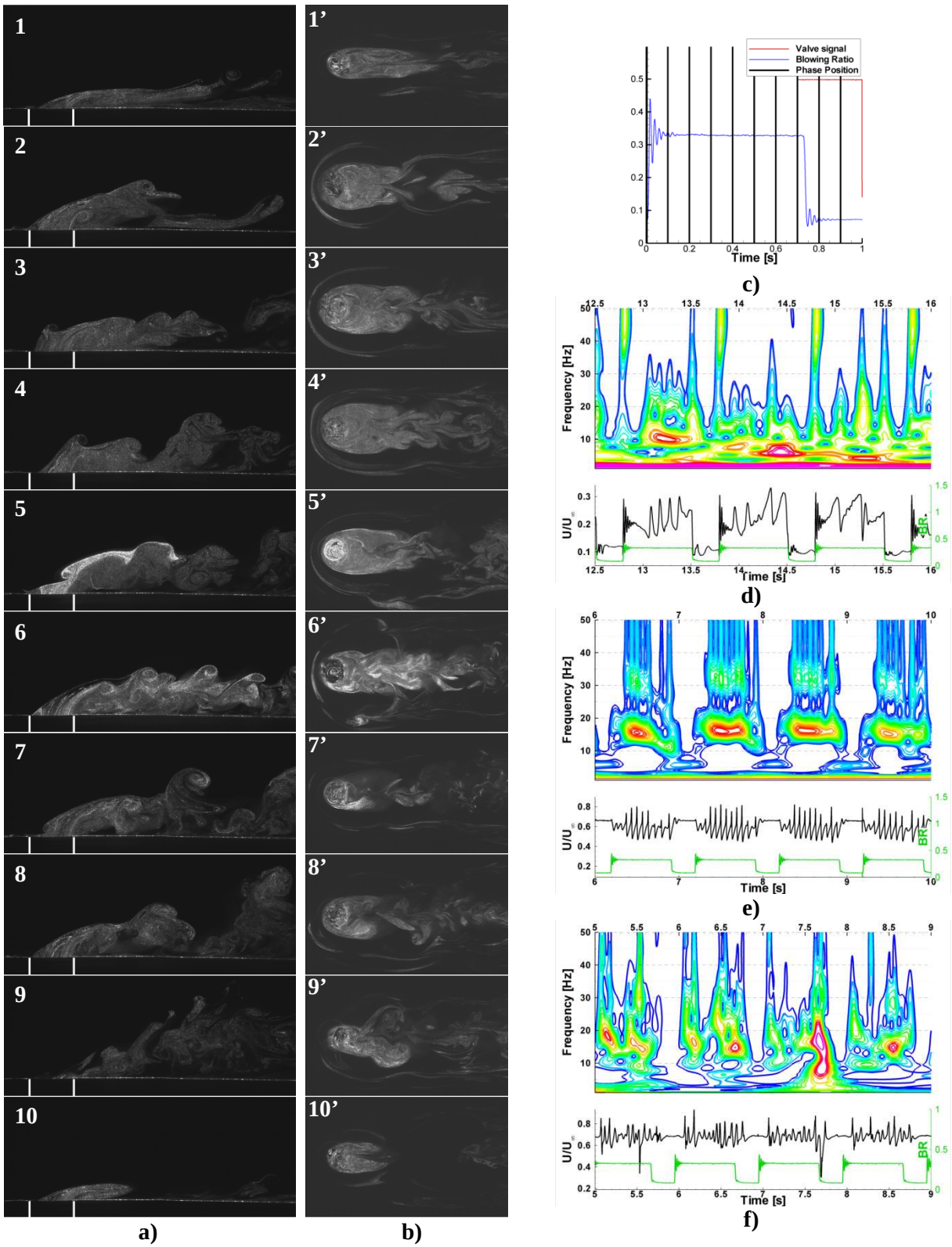

Figure A - 14: Pulsed cases Visualizations at BR_m=0.250, BR_{pp}=0.250, DC=0.70, f_f=1.0Hz - a) (1-10) X-Z visualizations. b) (1'-10') X-Y visualizations. c) Phase averaged flow-meter record. d)-f) Wavelet analysis of the hot-wire records at d) X/D_j=0, Z/D_j=0, e) X/D_j=0, Z/D_j=0.5, f) X/D_j=3.5, Z/D_j=1.25 – Case#5.

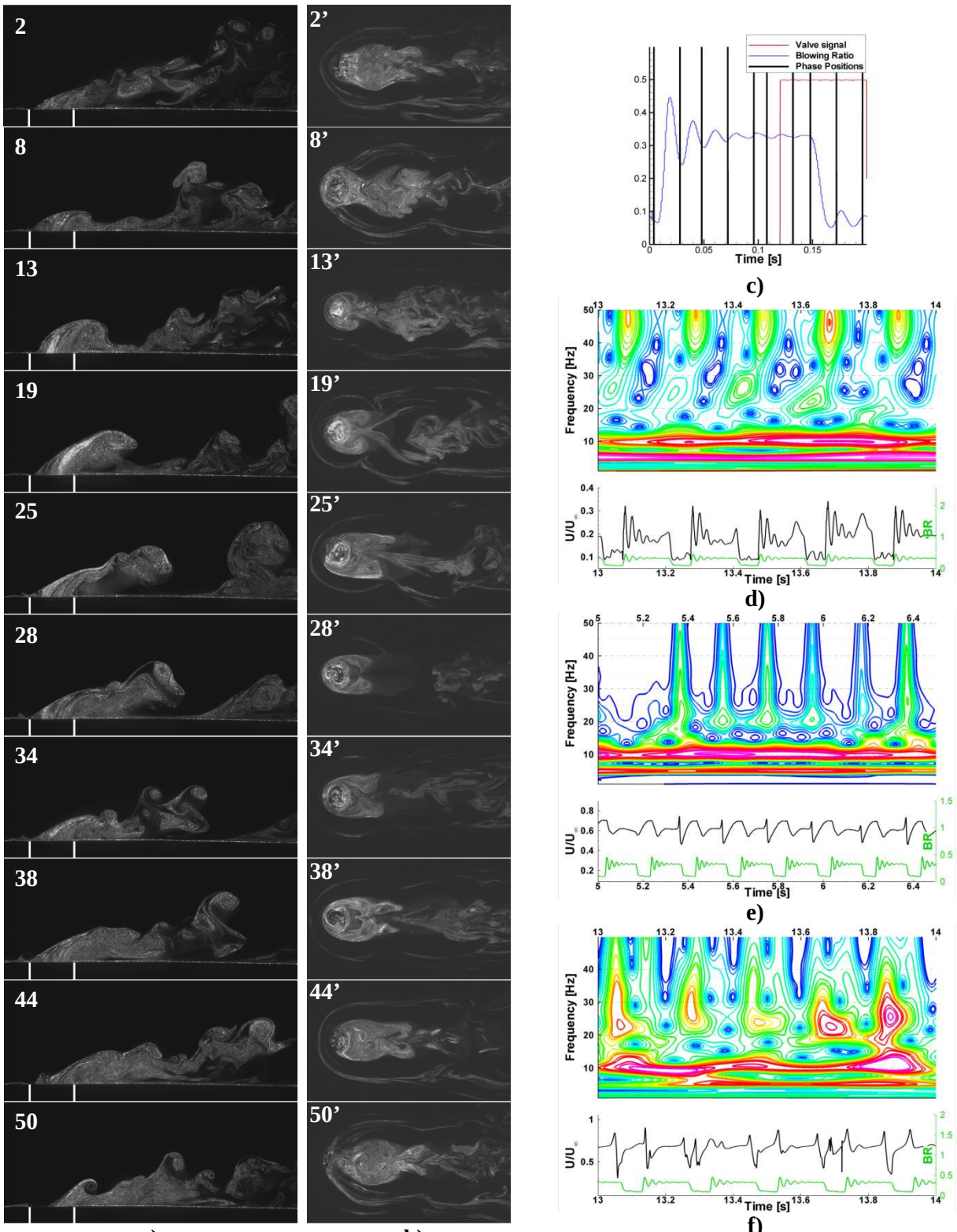

Figure A - 15: Pulsed cases Visualizations at BR_m=0.250, BR_{pp}=0.250, DC=0.70, f_f=5.0Hz - a) (2-50) X-Z visualizations. b) (2'-50') X-Y visualizations. c) Phase averaged flow-meter record. d)-f) Wavelet analysis of the hot-wire records at d) X/D_j=0, Z/D_j=0, e) X/D_j=0, Z/D_j=0.5, f) X/D_j=3.5, Z/D_j=1.25 – Case#5.

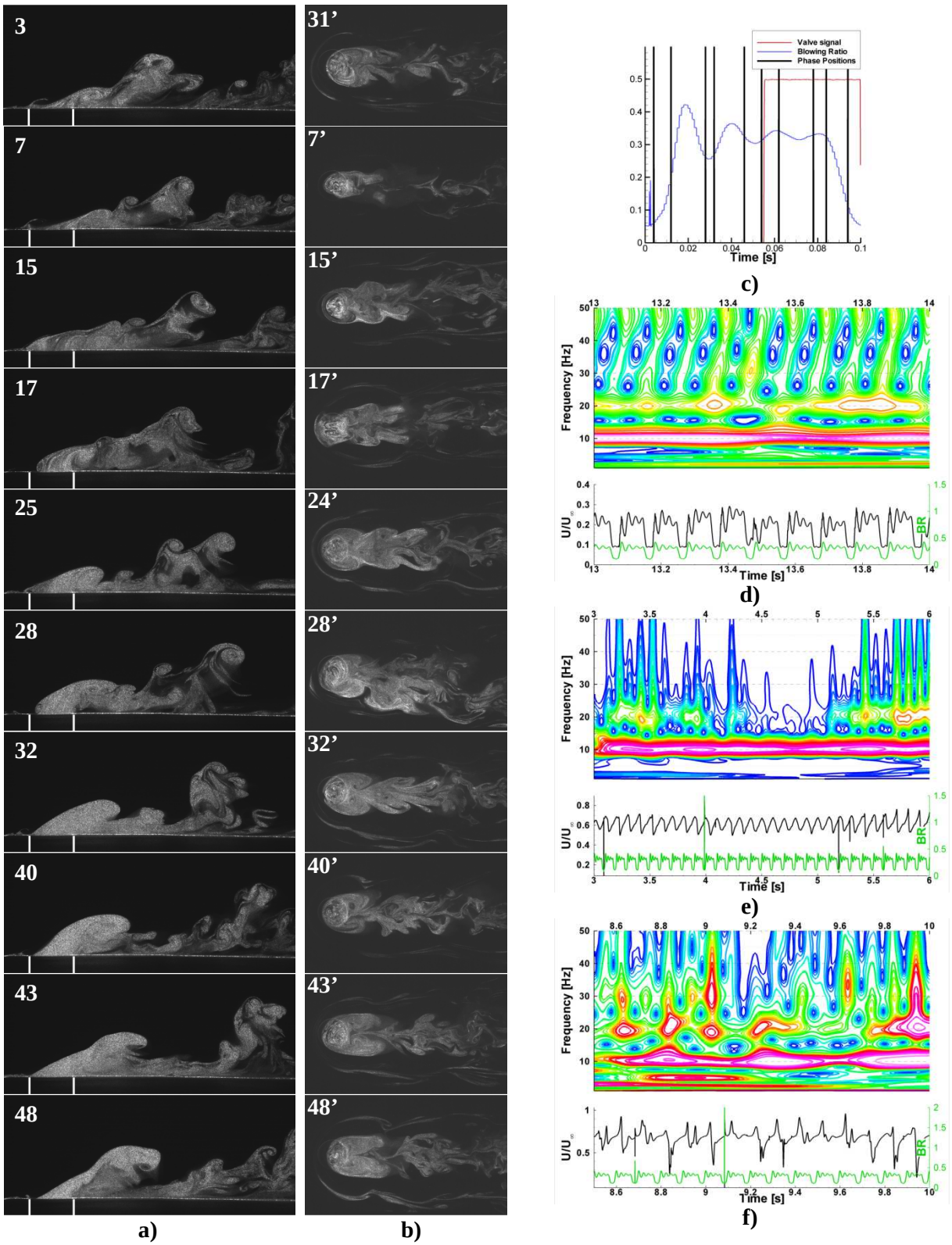

Figure A - 16: Pulsed cases Visualizations at BR_m=0.250, BR_{pp}=0.250, DC=0.70, f_f=10Hz - a) (3-48) X-Z visualizations. b) (3'-48') X-Y visualizations. c) Phase averaged flow-meter record. d)-f) Wavelet analysis of the hot-wire records at d) X/D_j=0, Z/D_j=0, e) X/D_j=0, Z/D_j=0.5, f) X/D_j=3.5, Z/D_j=1.25 – Case#5.

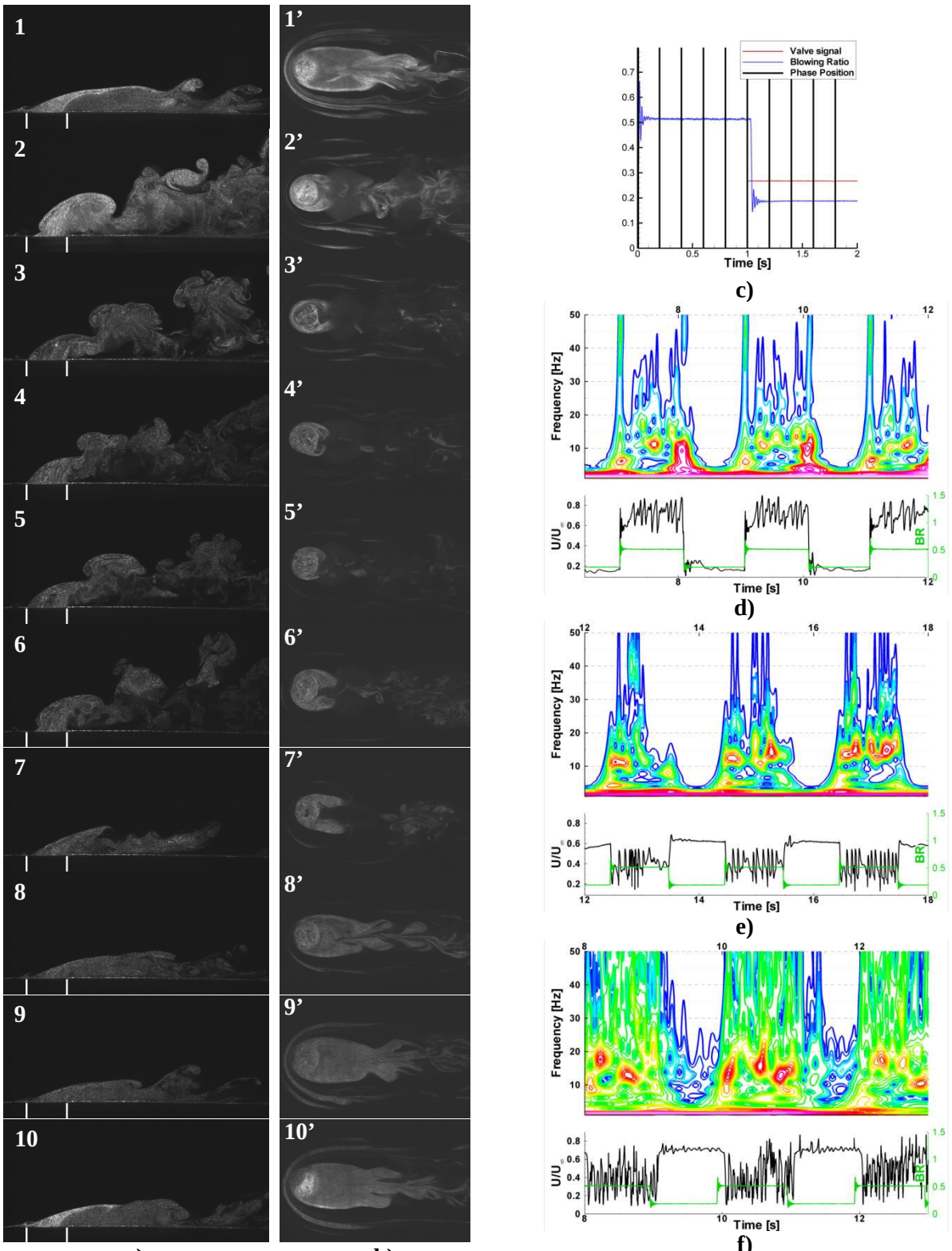

Figure A - 17: Pulsed cases Visualizations at BR_m=0.350, BR_l=0.1875, DC=0.50, f_f=0.5Hz - a) (1-10) X-Z visualizations. b) (1'-10') X-Y visualizations. c) Phase averaged flow-meter record. d)-f) Wavelet analysis of the hot-wire records at d) X/D_j=0, Z/D_j=0, e) X/D_j=0, Z/D_j=0.5, f) X/D_j=3.5, Z/D_j=1.25 – Case#6.

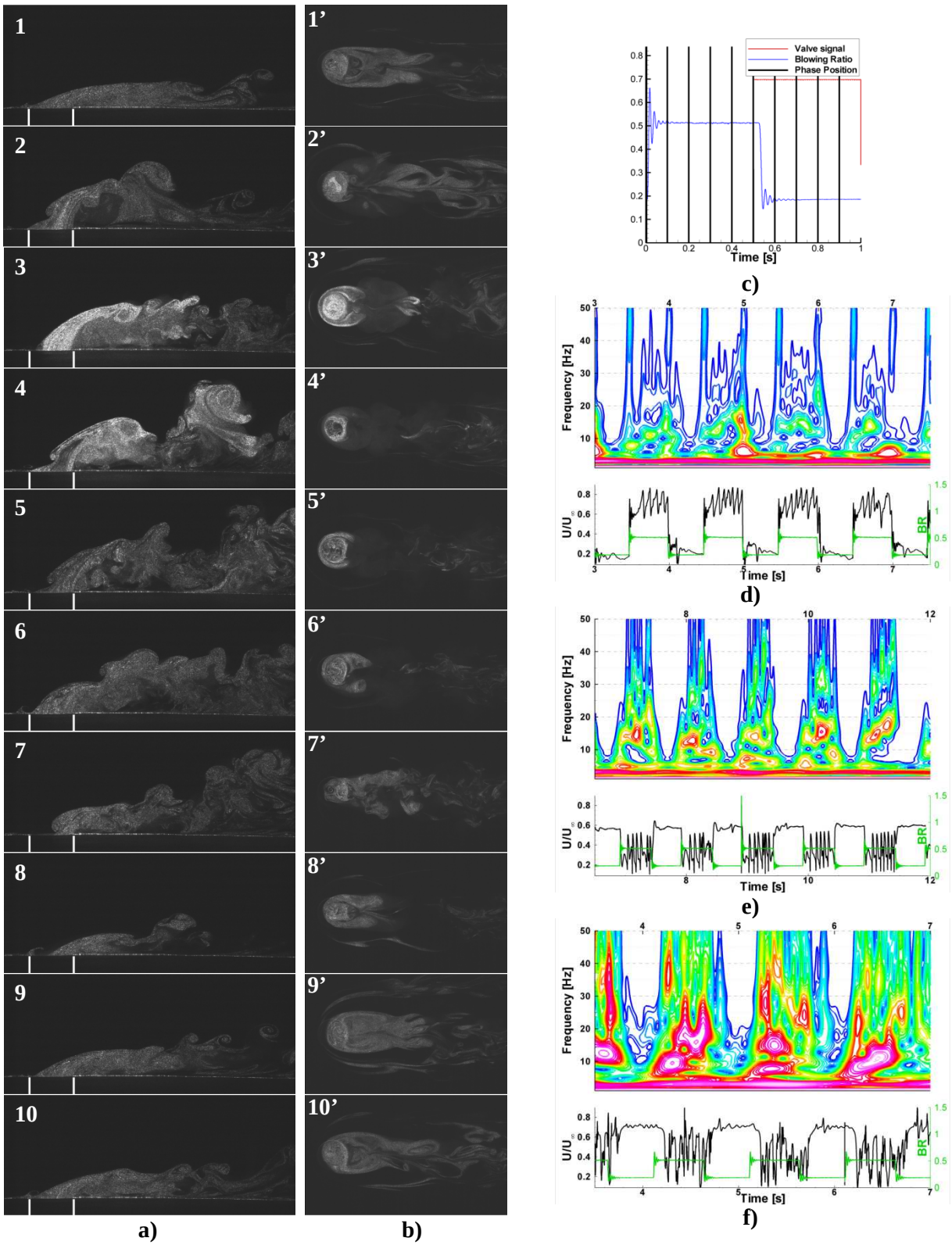

Figure A - 18: Pulsed cases Visualizations at BR_m=0.350, BR_l=0.1875, DC=0.50, f_f=1.0Hz - a) (1-10) X-Z visualizations. b) (1'-10') X-Y visualizations. c) Phase averaged flow-meter record. d)-f) Wavelet analysis of the hot-wire records at d) X/D_j=0, Z/D_j=0, e) X/D_j=0, Z/D_j=0.5, f) X/D_j=3.5, Z/D_j=1.25 – Case#6.

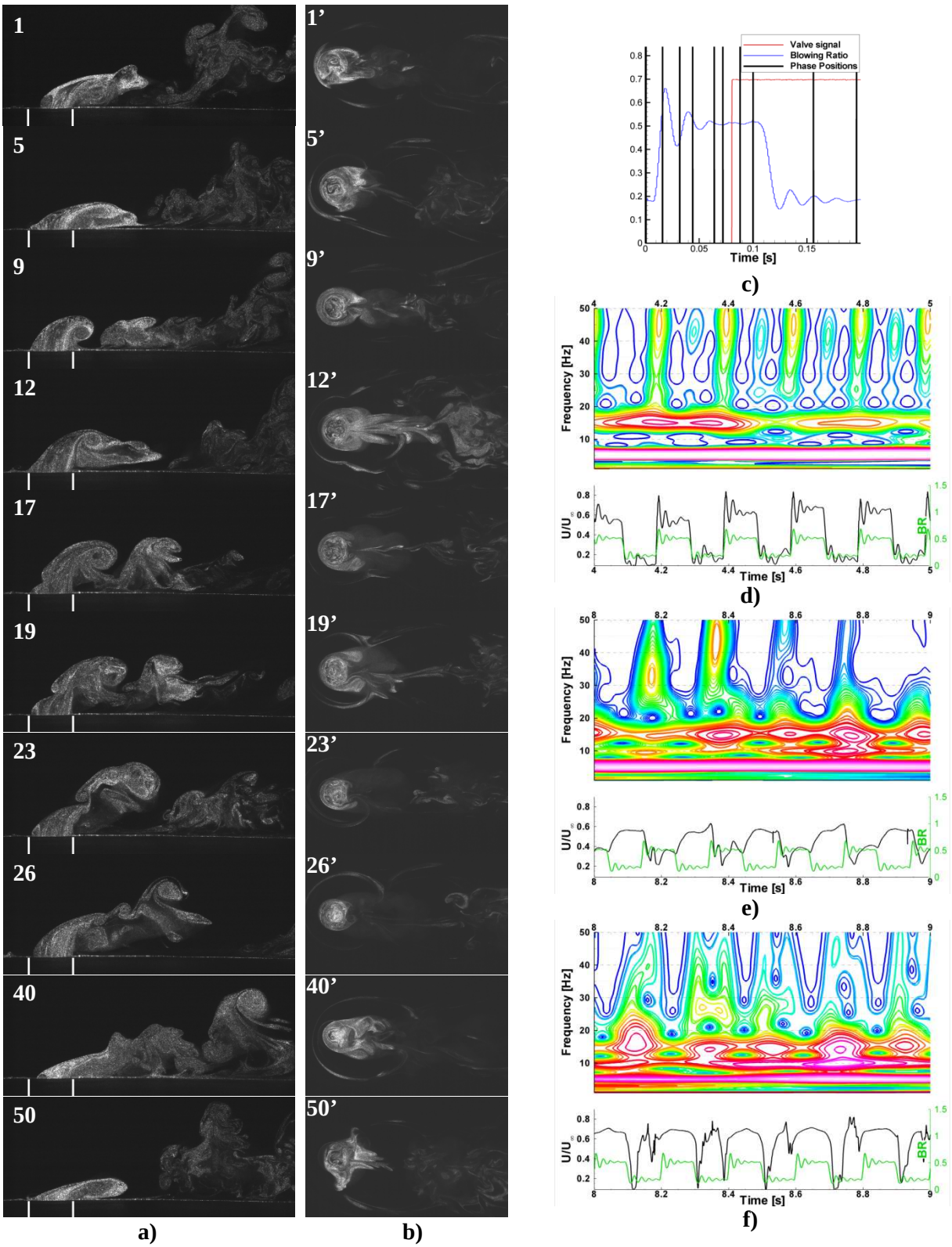

Figure A - 19: Pulsed cases Visualizations at BR_m=0.350, BR_l=0.1875, DC=0.50, f_f=5.0Hz - a) (1-50) X-Z visualizations. b) (1'-50') X-Y visualizations. c) Phase averaged flow-meter record. d)-f) Wavelet analysis of the hot-wire records at d) X/D_j=0, Z/D_j=0, e) X/D_j=0, Z/D_j=0.5, f) X/D_j=3.5, Z/D_j=1.25 – Case#6.

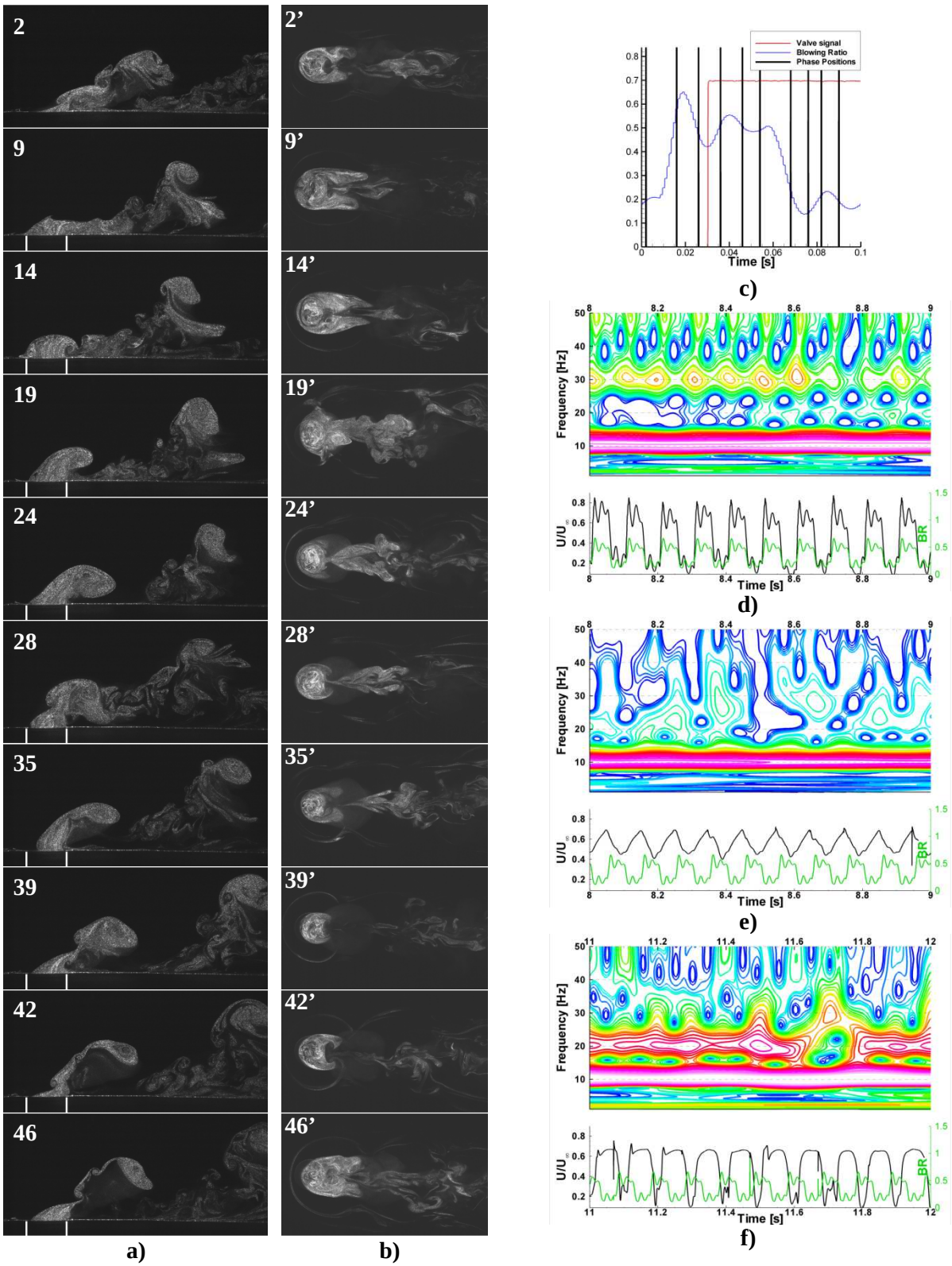

Figure A - 20: Pulsed cases Visualizations at BR_m=0.350, BR_l=0.1875, DC=0.50, f_f=10Hz - a) (2-46) X-Z visualizations. b) (2'-46') X-Y visualizations. c) Phase averaged flow-meter record. d)-f) Wavelet analysis of the hot-wire records at d) X/D_j=0, Z/D_j=0, e) X/D_j=0, Z/D_j=0.5, f) X/D_j=3.5, Z/D_j=1.25 – Case#6.

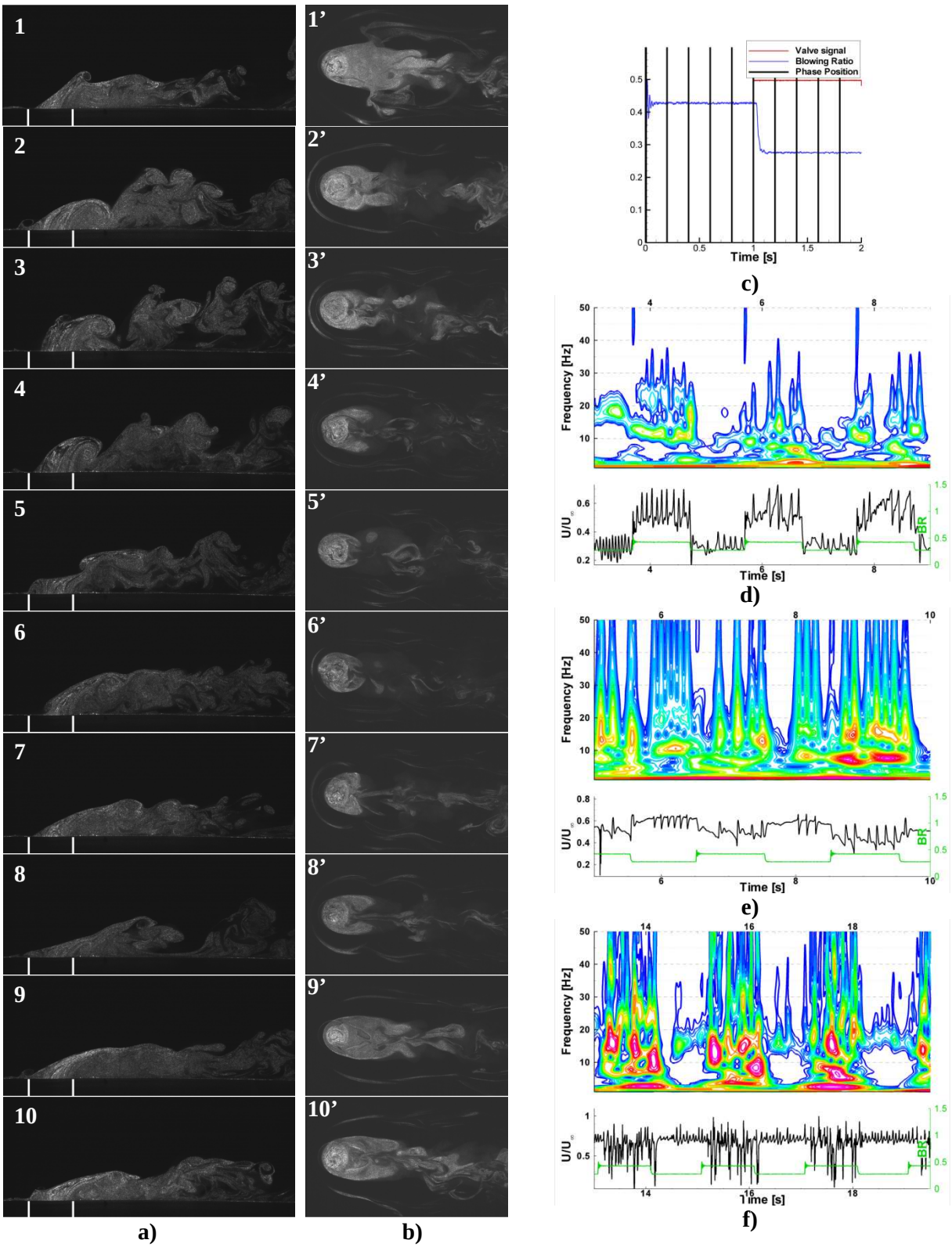

Figure A - 21: Pulsed cases Visualizations at BR_m=0.350, BR_{pp}=0.150, DC=0.50, f_f=0.5Hz - a) (1-10) X-Z visualizations. b) (1'-10') X-Y visualizations. c) Phase averaged flow-meter record. d)-f) Wavelet analysis of the hot-wire records at d) X/D_j=0, Z/D_j=0, e) X/D_j=0, Z/D_j=0.5, f) X/D_j=3.5, Z/D_j=1.25 – Case#7.

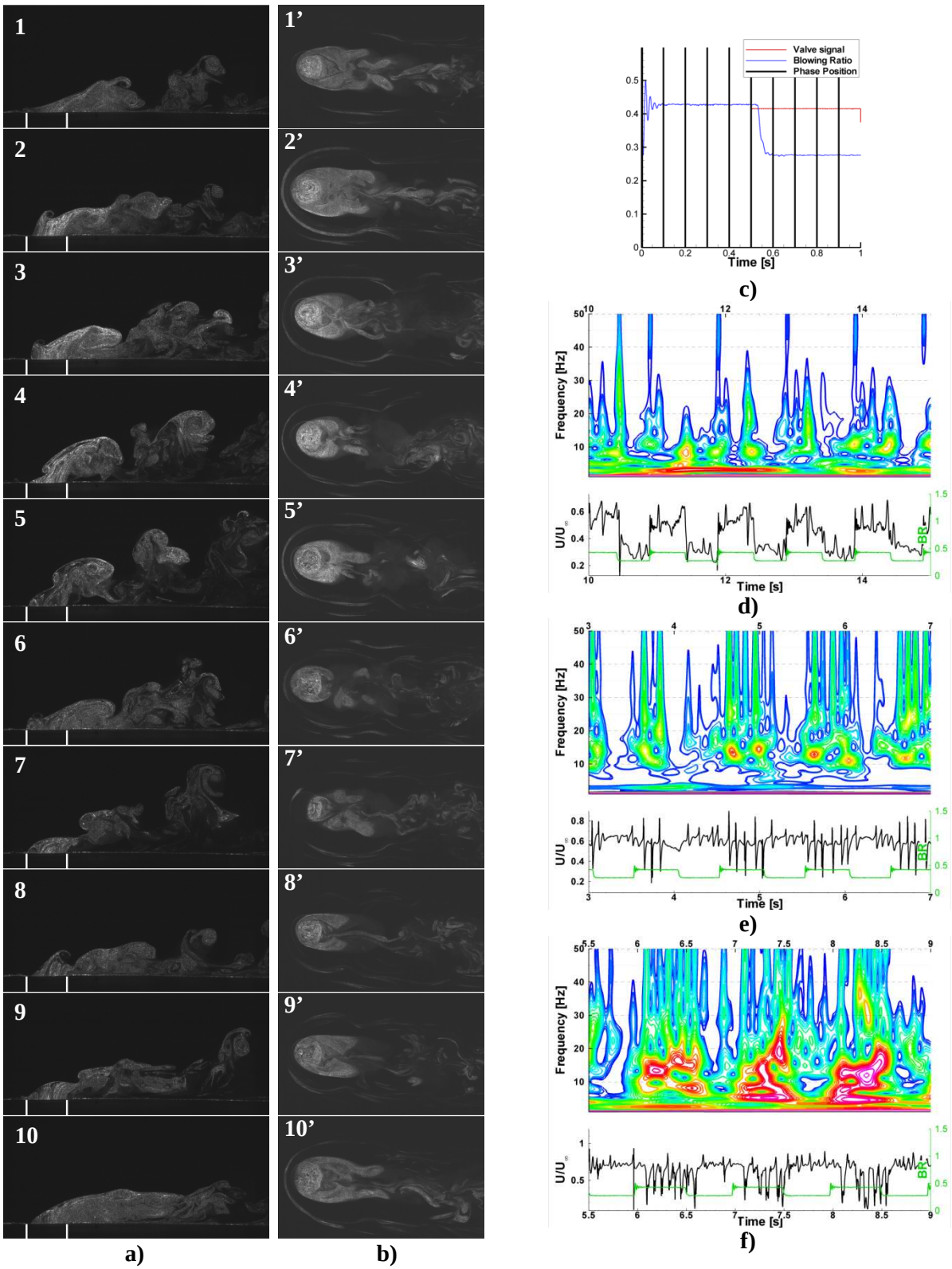

Figure A - 22: Pulsed cases Visualizations at BR_m=0.350, BR_{pp}=0.150, DC=0.50, f_f=1.0Hz - a) (1-10) X-Z visualizations. b) (1'-10') X-Y visualizations. c) Phase averaged flow-meter record. d)-f) Wavelet analysis of the hot-wire records at d) X/D_j=0, Z/D_j=0, e) X/D_j=0, Z/D_j=0.5, f) X/D_j=3.5, Z/D_j=1.25 – Case#7.

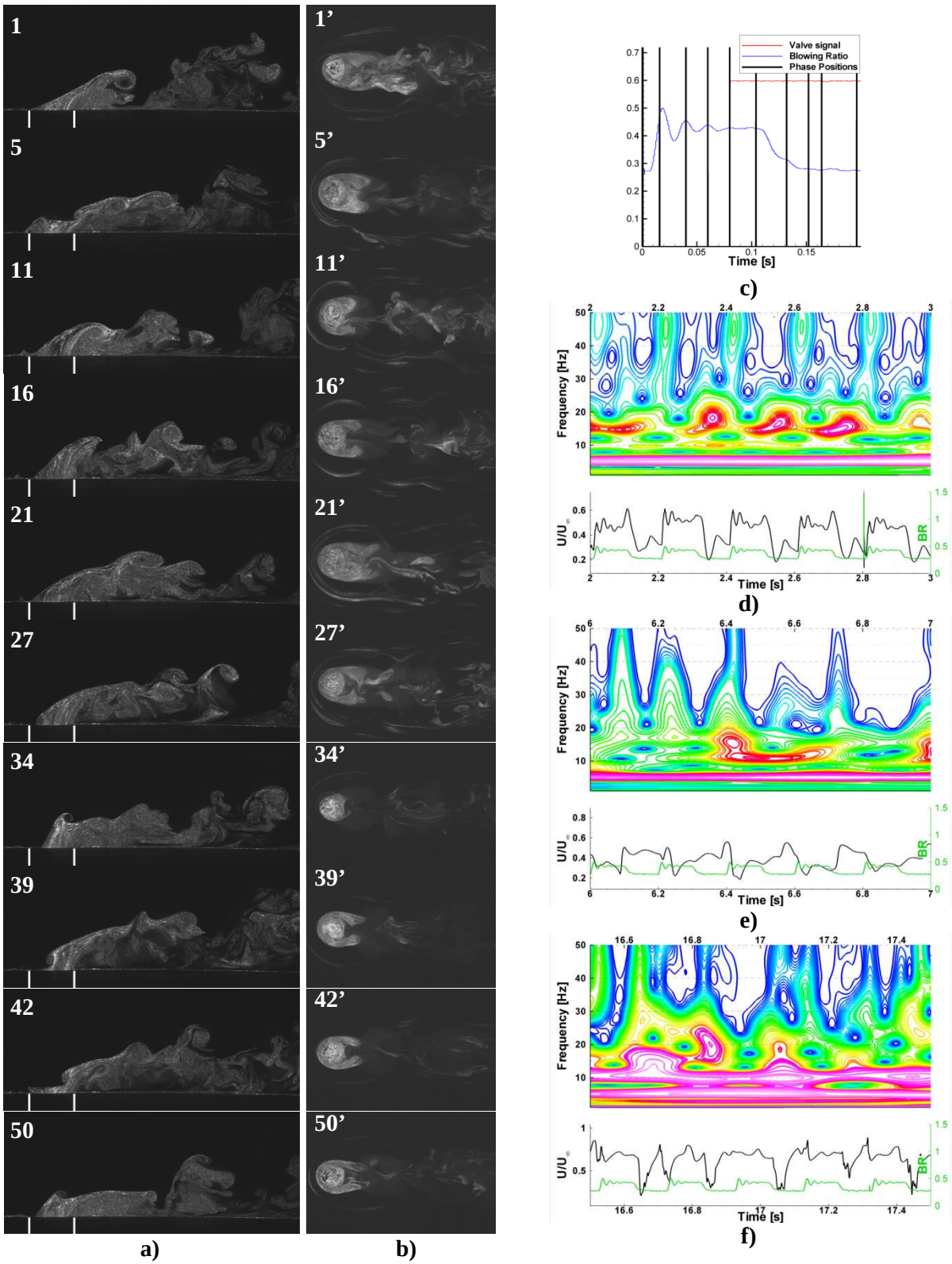

Figure A - 23: Pulsed cases Visualizations at BR_m=0.350, BR_{pp}=0.150, DC=0.50, f_f=5.0Hz - a) (1-50) X-Z visualizations. b) (1'-50') X-Y visualizations. c) Phase averaged flow-meter record. d)-f) Wavelet analysis of the hot-wire records at d) X/D_j=0, Z/D_j=0, e) X/D_j=0, Z/D_j=0.5, f) X/D_j=3.5, Z/D_i=1.25 – Case#7.

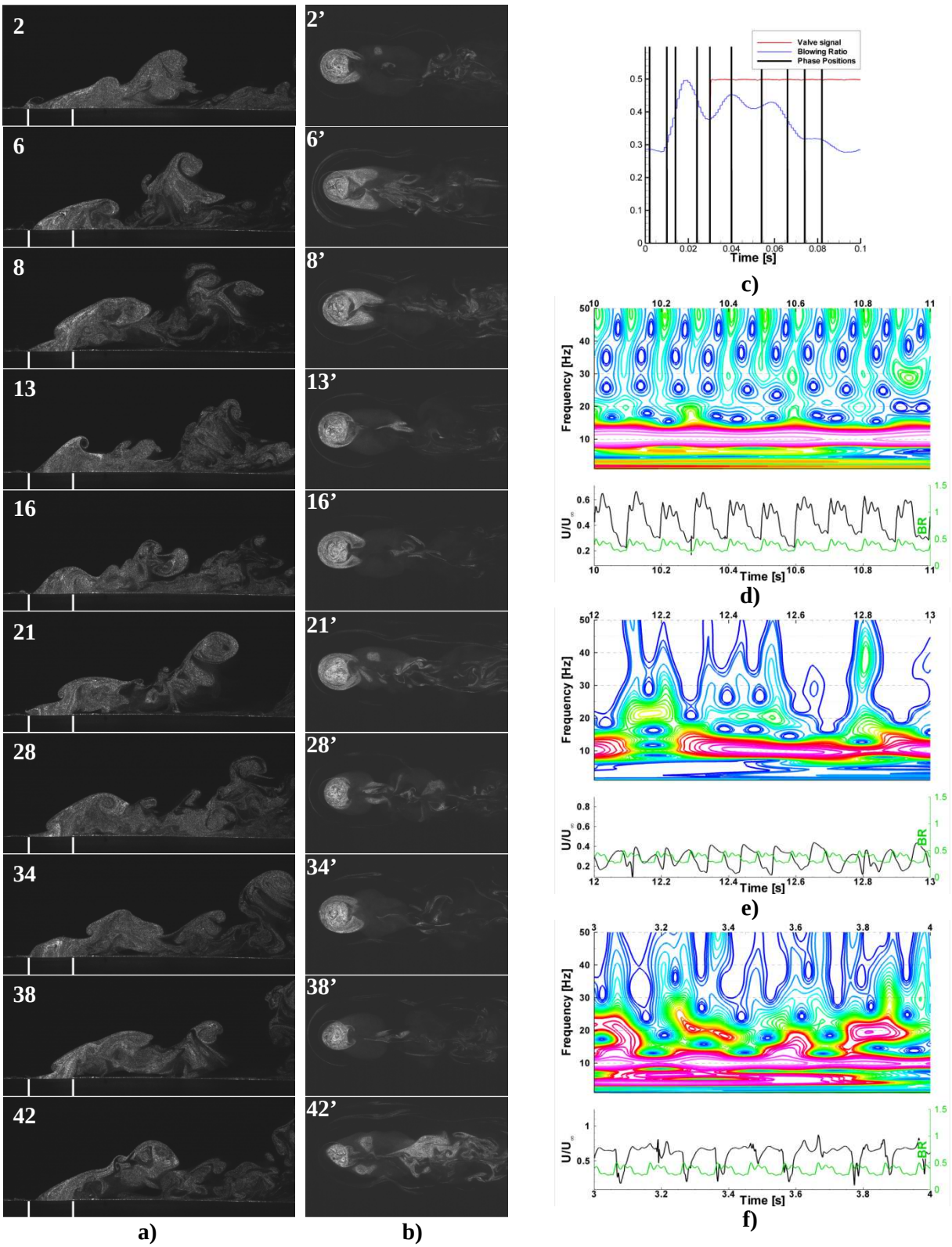

Figure A - 24: Pulsed cases Visualizations at BR_m=0.350, BR_{pp}=0.150, DC=0.50, f_f=0.5Hz - a) (2-42) X-Z visualizations. b) (2'-42') X-Y visualizations. c) Phase averaged flow-meter record. d)-f) Wavelet analysis of the hot-wire records at d) X/D_j=0, Z/D_j=0, e) X/D_j=0, Z/D_j=0.5, f) X/D_j=3.5, Z/D_j=1.25 – Case#7.

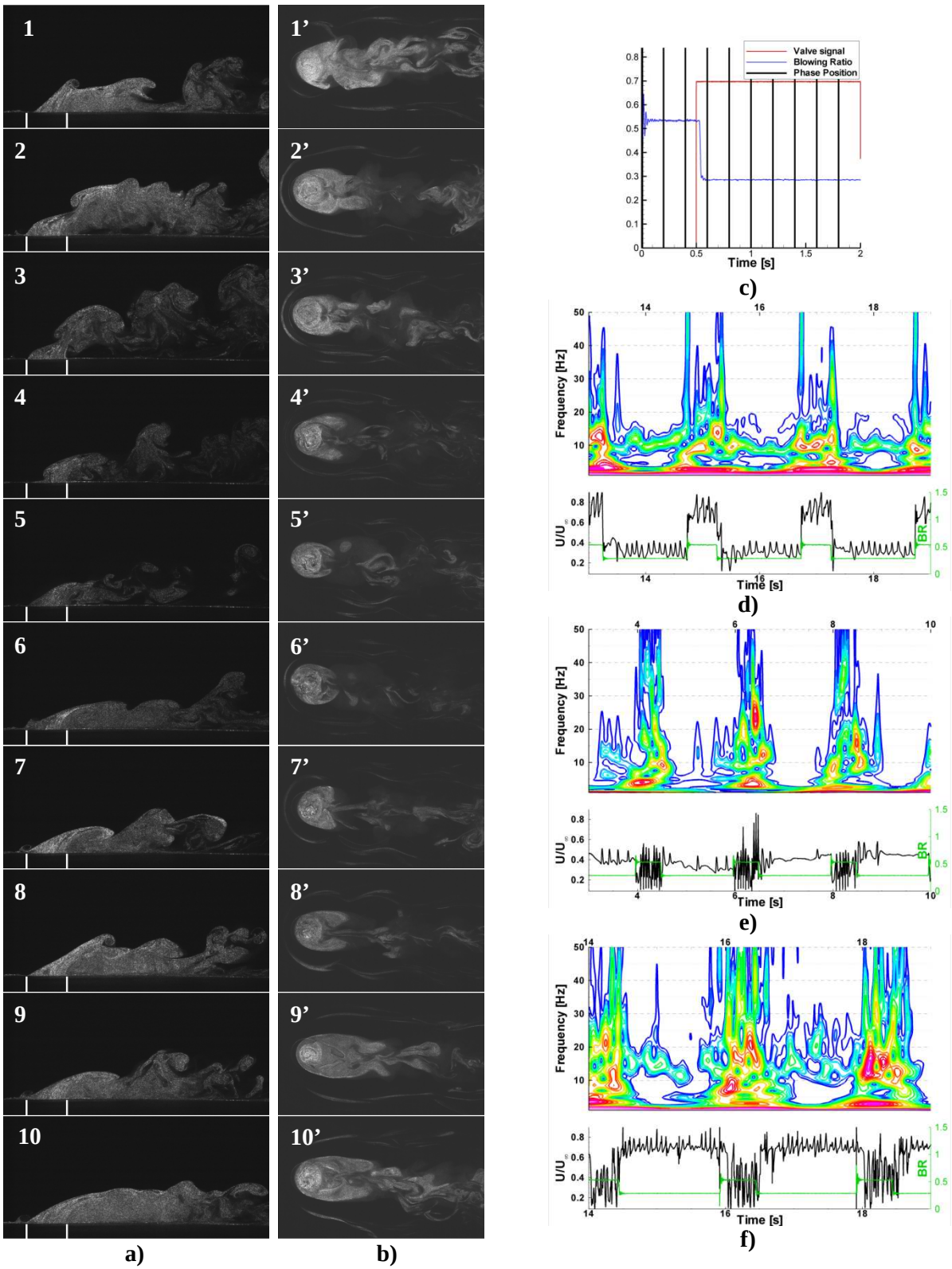

Figure A - 25: Pulsed cases Visualizations at BR_m=0.350, BR_{pp}=0.250, DC=0.25, f_f=0.5Hz - a) (1-10) X-Z visualizations. b) (1'-10') X-Y visualizations. c) Phase averaged flow-meter record. d)-f) Wavelet analysis of the hot-wire records at d) X/D_j=0, Z/D_j=0, e) X/D_j=0, Z/D_j=0.5, f) X/D_j=3.5, Z/D_j=1.25 – Case#8.

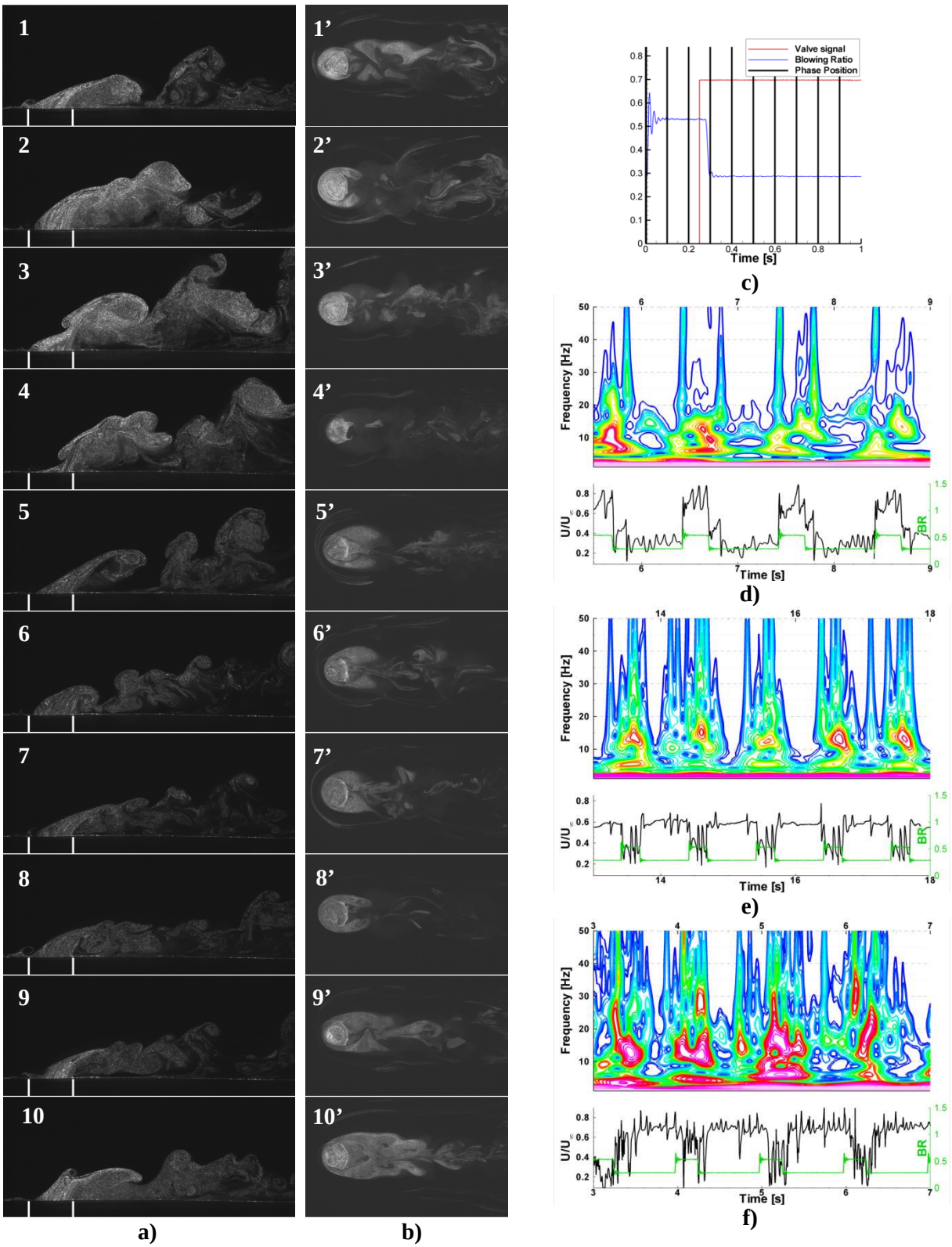

Figure A - 26: Pulsed cases Visualizations at BR_m=0.350, BR_{pp}=0.250, DC=0.25, f_f=1.0Hz - a) (1-10) X-Z visualizations. b) (1'-10') X-Y visualizations. c) Phase averaged flow-meter record. d)-f) Wavelet analysis of the hot-wire records at d) X/D_j=0, Z/D_j=0, e) X/D_j=0, Z/D_j=0.5, f) X/D_j=3.5, Z/D_j=1.25 – Case#8.

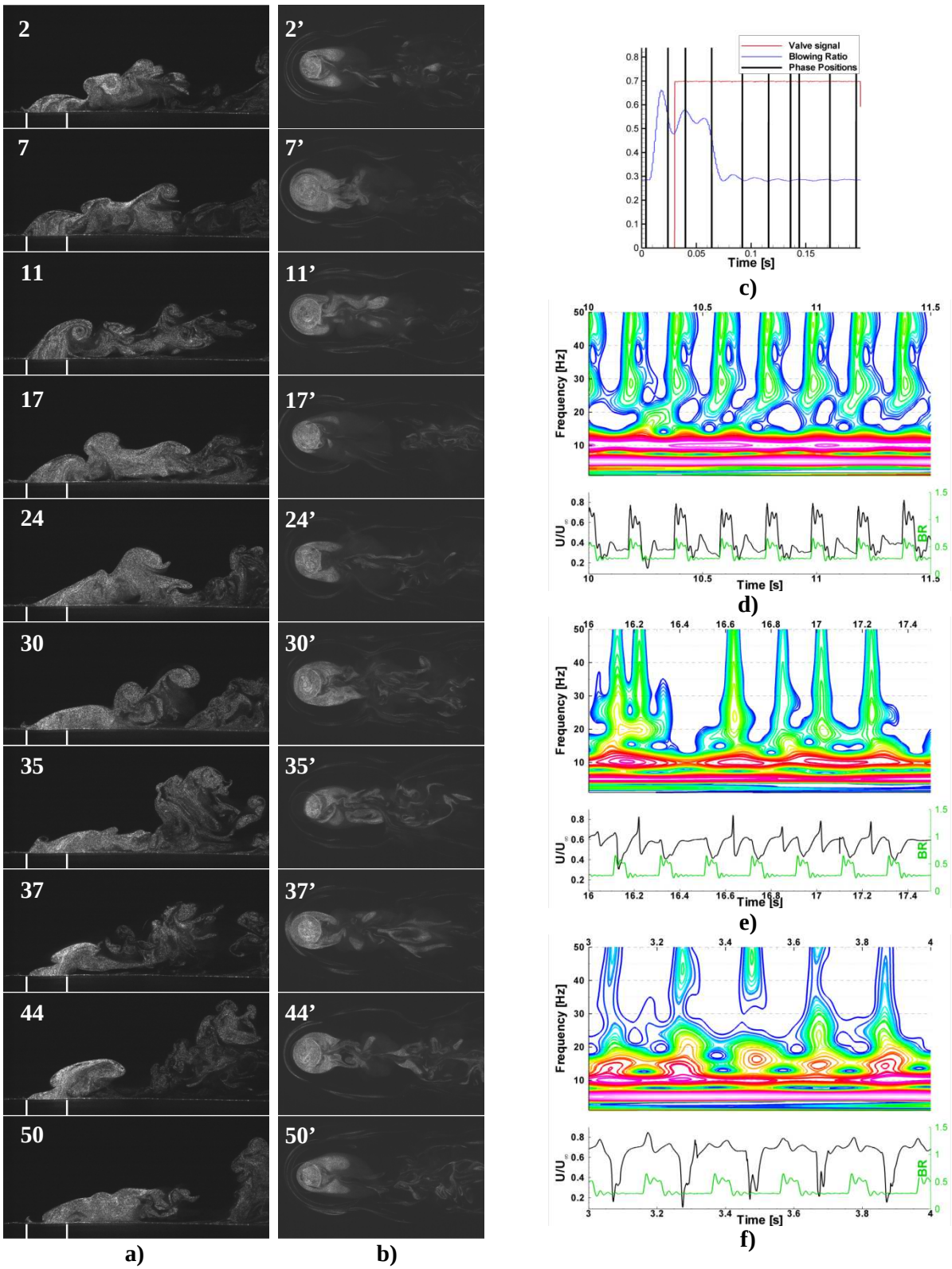

Figure A - 27: Pulsed cases Visualizations at BR_m=0.350, BR_{pp}=0.250, DC=0.25, f_f=5.0Hz - a) (2-50) X-Z visualizations. b) (2'-50') X-Y visualizations. c) Phase averaged flow-meter record. d)-f) Wavelet analysis of the hot-wire records at d) X/D_j=0, Z/D_j=0, e) X/D_j=0, Z/D_j=0.5, f) X/D_j=3.5, Z/D_j=1.25 – Case#8.

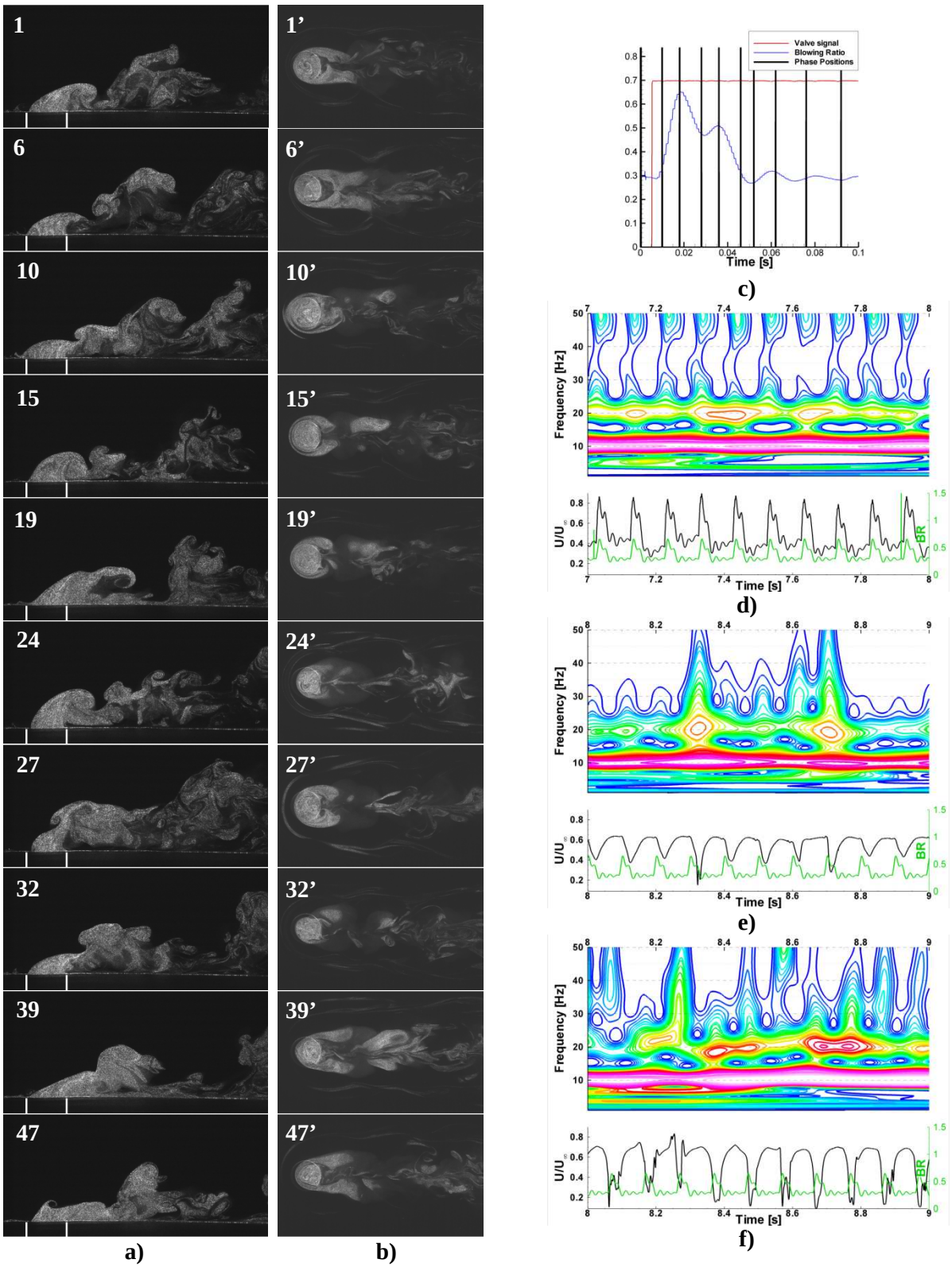

Figure A - 28: Pulsed cases Visualizations at BR_m=0.350, BR_{pp}=0.250, DC=0.25, f_f=10Hz - a) (1-47) X-Z visualizations. b) (1'-47') X-Y visualizations. c) Phase averaged flow-meter record. d)-f) Wavelet analysis of the hot-wire records at d) X/D_j=0, Z/D_j=0, e) X/D_j=0, Z/D_j=0.5, f) X/D_j=3.5, Z/D_j=1.25 – Case#8.

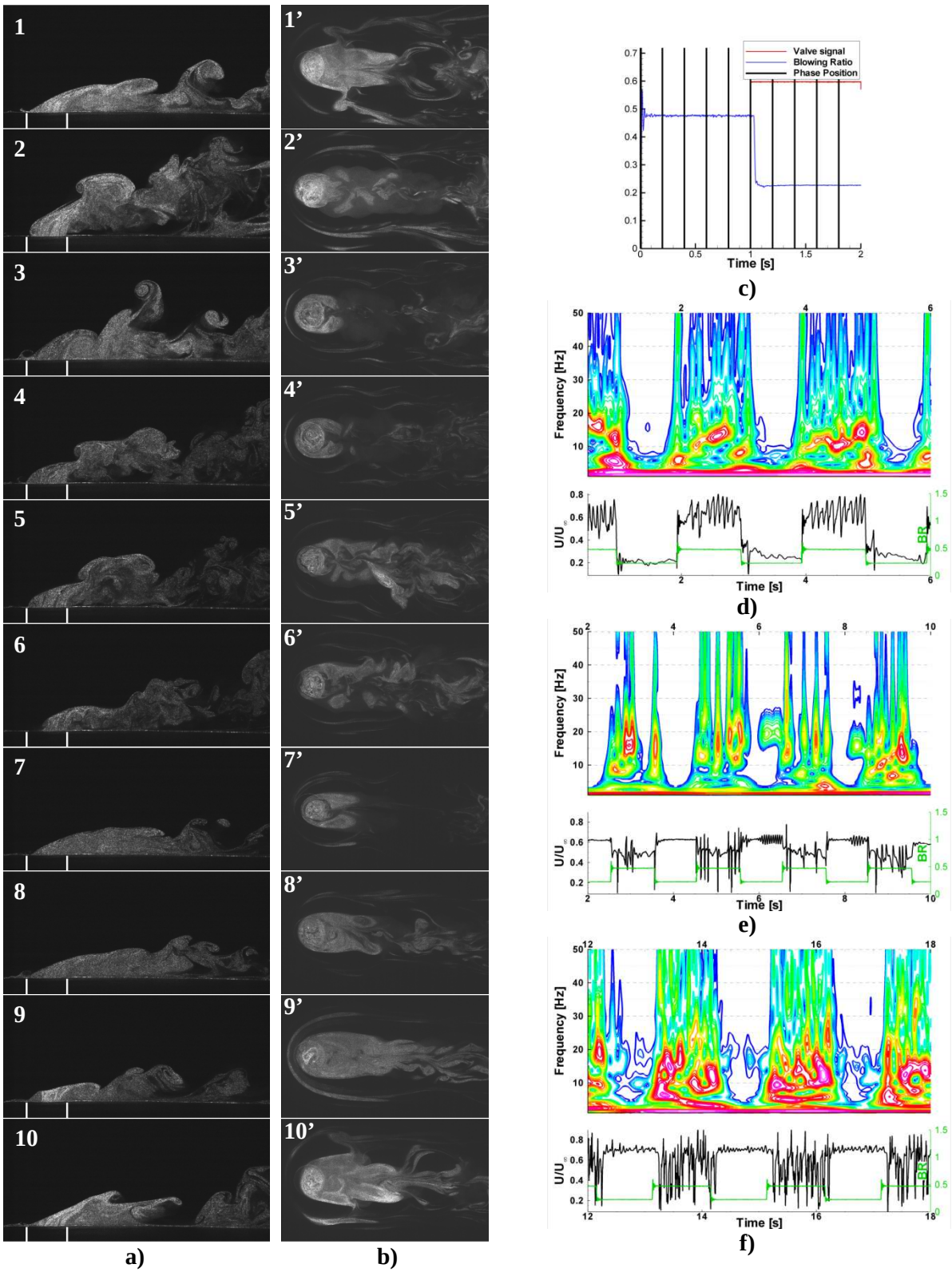

Figure A - 29: Pulsed cases Visualizations at BR_m=0.350, BR_{pp}=0.250, DC=0.50, f_f=0.5Hz - a) (1-10) X-Z visualizations. b) (1'-10') X-Y visualizations. c) Phase averaged flow-meter record. d)-f) Wavelet analysis of the hot-wire records at d) X/D_j=0, Z/D_j=0, e) X/D_j=0, Z/D_j=0.5, f) X/D_j=3.5, Z/D_j=1.25 – Case#9.

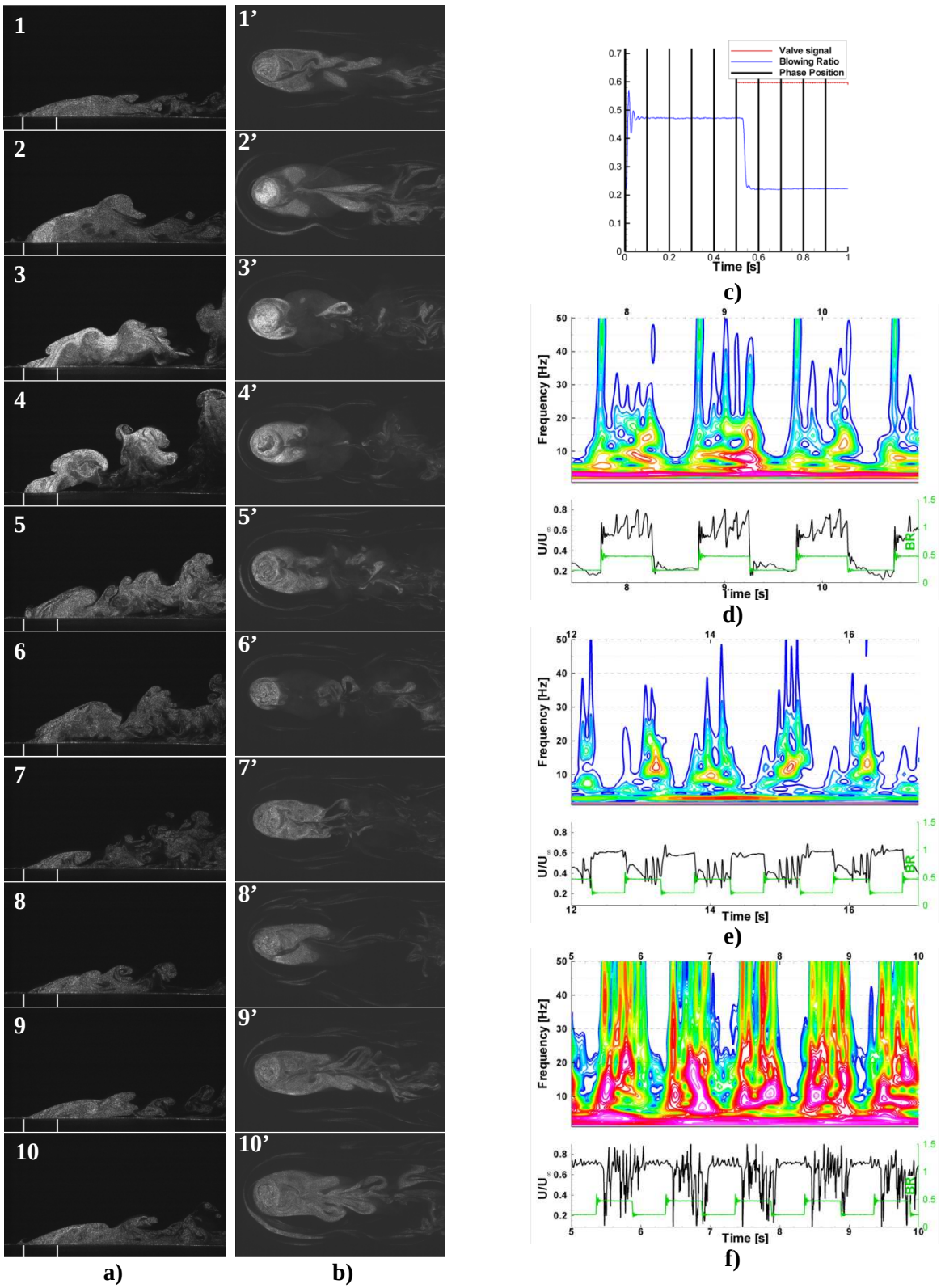

Figure A - 30: Pulsed cases Visualizations at BR_m=0.350, BR_{pp}=0.250, DC=0.50, f_f=1.0Hz - a) (1-10) X-Z visualizations. b) (1'-10') X-Y visualizations. c) Phase averaged flow-meter record. d)-f) Wavelet analysis of the hot-wire records at d) X/D_j=0, Z/D_j=0, e) X/D_j=0, Z/D_j=0.5, f) X/D_j=3.5, Z/D_j=1.25 – Case#9.

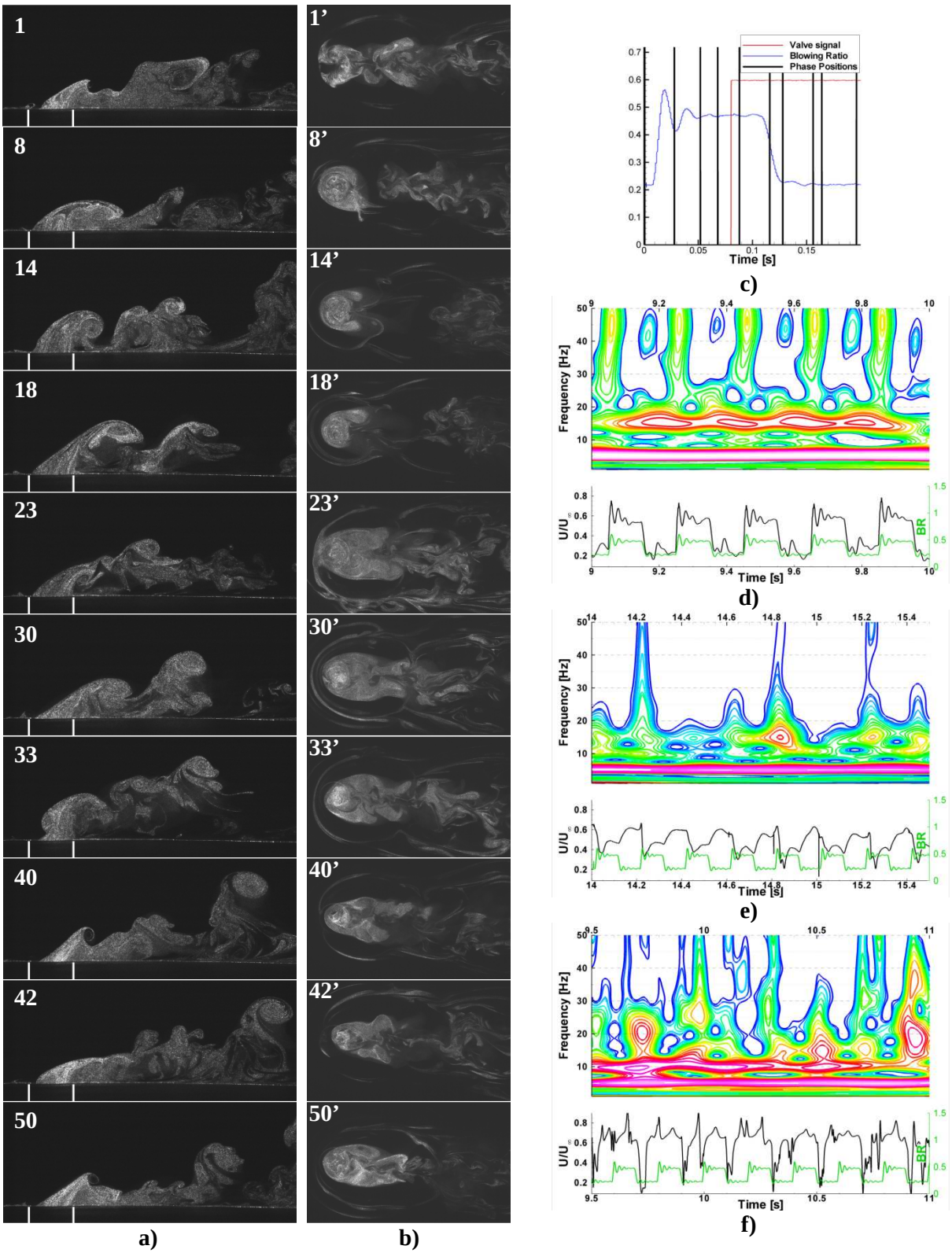

Figure A - 31: Pulsed cases Visualizations at BR_m=0.350, BR_{pp}=0.250, DC=0.50, f_f=5.0Hz - a) (1-50) X-Z visualizations. b) (1'-50') X-Y visualizations. c) Phase averaged flow-meter record. d)-f) Wavelet analysis of the hot-wire records at d) X/D_j=0, Z/D_j=0, e) X/D_j=0, Z/D_j=0.5, f) X/D_j=3.5, Z/D_j=1.25 – Case#9.

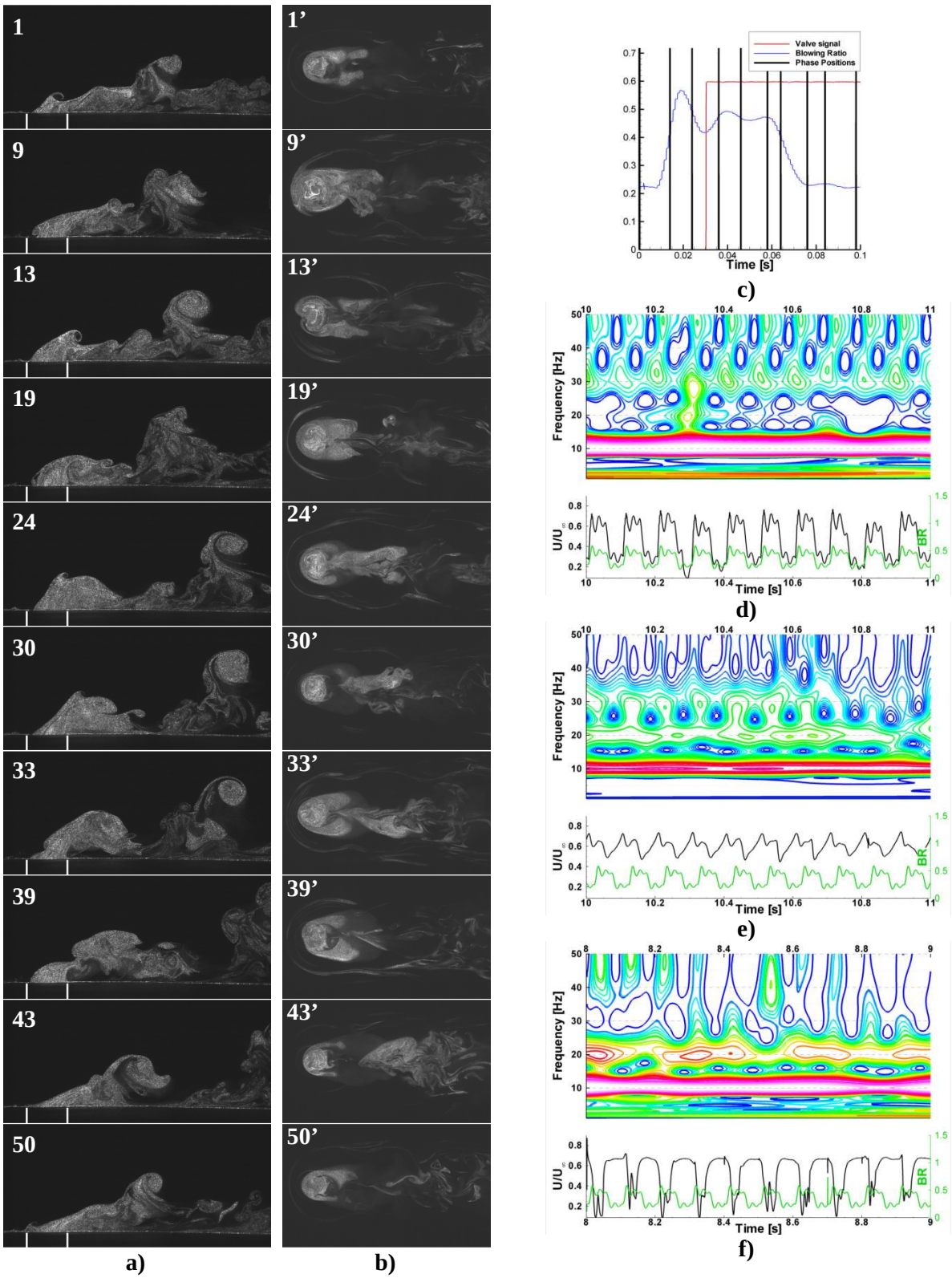

Figure A - 32: Pulsed cases Visualizations at BR_m=0.350, BR_{pp}=0.250, DC=0.50, f_f=10Hz - a) (1-50) X-Z visualizations. b) (1'-50') X-Y visualizations. c) Phase averaged flow-meter record. d)-f) Wavelet analysis of the hot-wire records at d) X/D_j=0, Z/D_j=0, e) X/D_j=0, Z/D_j=0.5, f) X/D_j=3.5, Z/D_j=1.25 – Case#9.

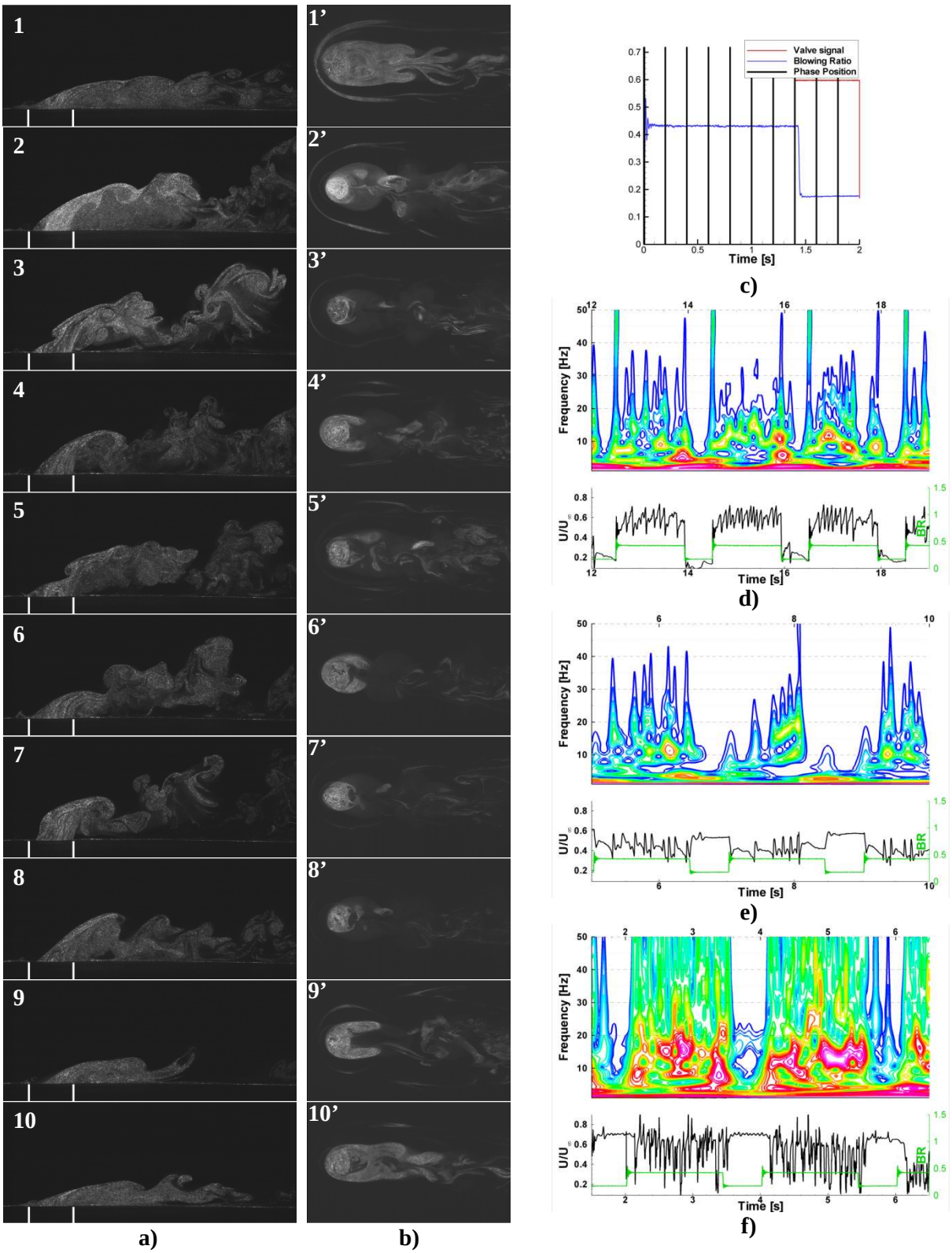

Figure A - 33: Pulsed cases Visualizations at BR_m=0.350, BR_{pp}=0.250, DC=0.70, f_f=0.5Hz - a) (1-10) X-Z visualizations. b) (1'-10') X-Y visualizations. c) Phase averaged flow-meter record. d)-f) Wavelet analysis of the hot-wire records at d) X/D_j=0, Z/D_j=0, e) X/D_j=0, Z/D_j=0.5, f) X/D_j=3.5, Z/D_j=1.25 – Case#10.

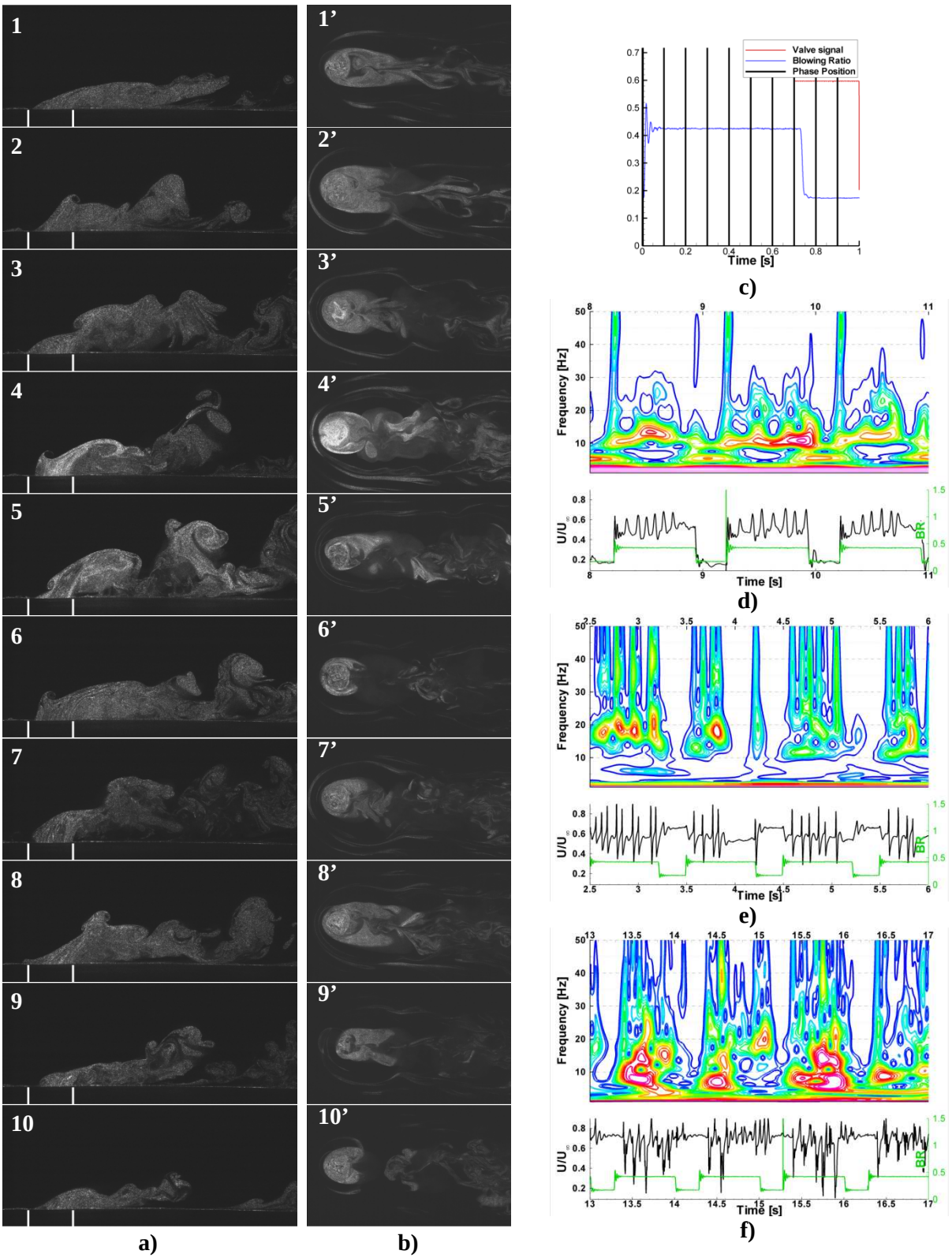

Figure A - 34: Pulsed cases Visualizations at BR_m=0.350, BR_{pp}=0.250, DC=0.70, f_f=1.0Hz - a) (1-10) X-Z visualizations. b) (1'-10') X-Y visualizations. c) Phase averaged flow-meter record. d)-f) Wavelet analysis of the hot-wire records at d) X/D_j=0, Z/D_j=0, e) X/D_j=0, Z/D_j=0.5, f) X/D_j=3.5, Z/D_j=1.25 – Case#10.

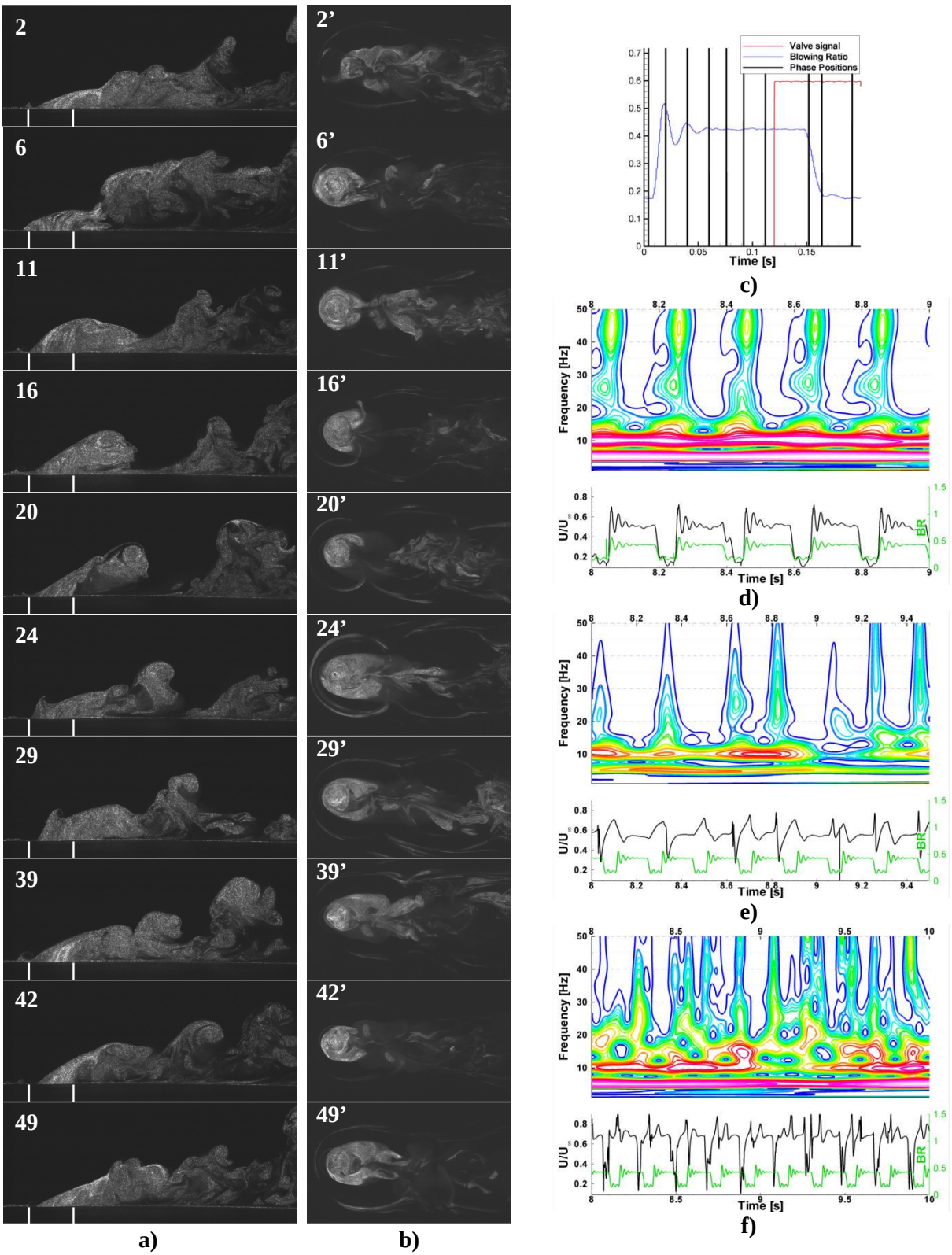

Figure A - 35: Pulsed cases Visualizations at BR_m=0.350, BR_{pp}=0.250, DC=0.70, f_f=5.0Hz - a) (2-49) X-Z visualizations. b) (2'-49') X-Y visualizations. c) Phase averaged flow-meter record. d)-f) Wavelet analysis of the hot-wire records at d) X/D_j=0, Z/D_j=0, e) X/D_j=0, Z/D_j=0.5, f) X/D_j=3.5, Z/D_j=1.25 – Case#10.

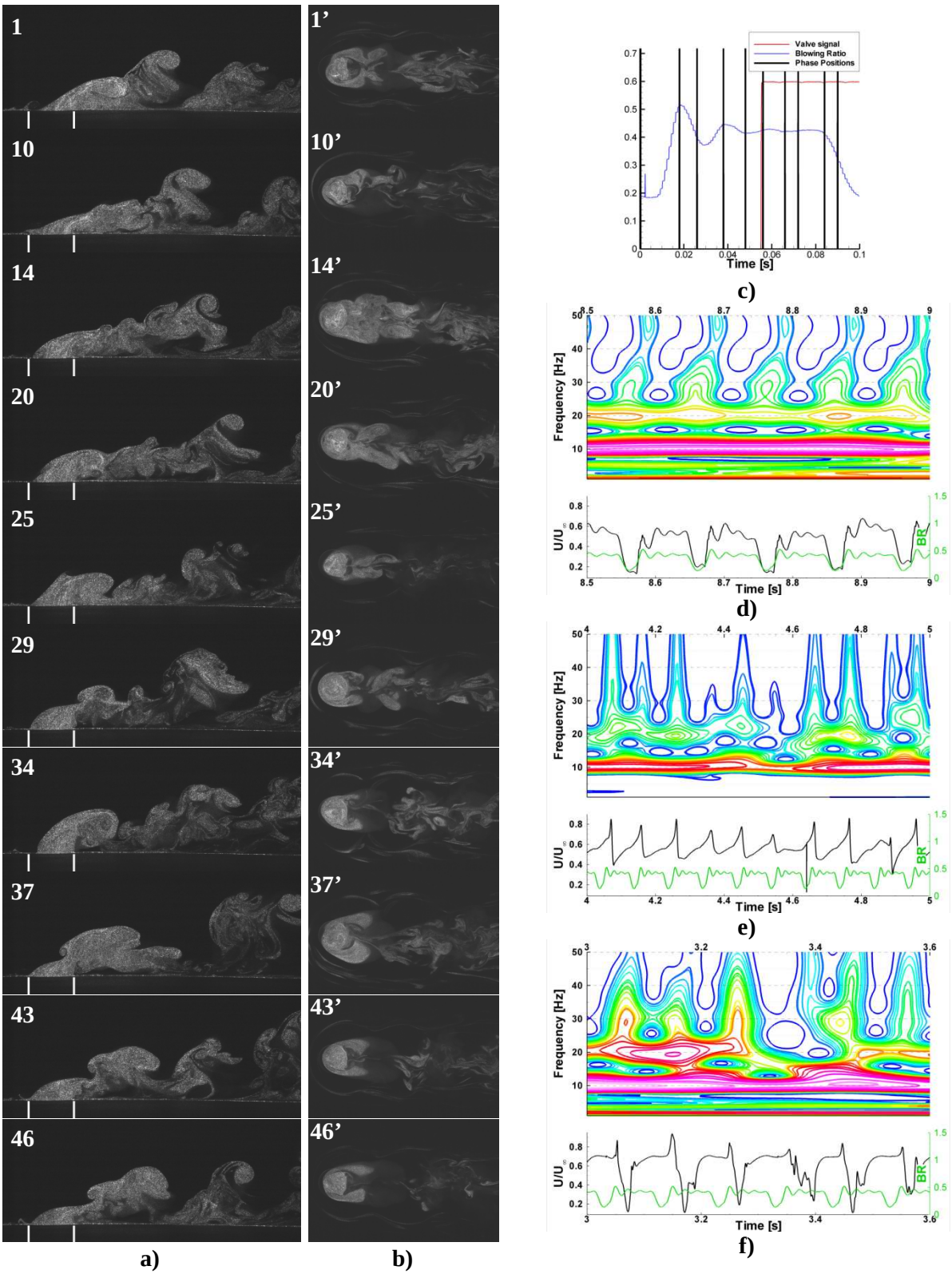

Figure A - 36: Pulsed cases Visualizations at BR_m=0.350, BR_{pp}=0.250, DC=0.70, f_f=10Hz - a) (1-10) X-Z visualizations. b) (1'-10') X-Y visualizations. c) Phase averaged flow-meter record. d)-f) Wavelet analysis of the hot-wire records at d) X/D_j=0, Z/D_j=0, e) X/D_j=0, Z/D_j=0.5, f) X/D_j=3.5, Z/D_j=1.25 – Case#10.

Vita

Guillaume Bidan was born in Cavaillon, France, in Provence, from the union of Sylvie and Philippe Bidan, in May 1985.

He obtained his Baccalauréat with Honors in June 2002 at the Lycée Ismael Dauphin in Cavaillon. He then joined the preparatory classes for engineering schools during two years at Lycée Paul Cézanne of Aix en Provence.

He entered the Ecole Nationale Supérieure d'Ingénieurs de Constructions Aéronautiques in September 2004 in Toulouse for two years. He was sent to Louisiana State University in August 2006 to complete a Master of Science in Mechanical Engineering under the supervision of Dr Dimitris E. Nikitopoulos in the Department of Mechanical Engineering. He submitted his research named Parametric Study of a Pulsed Vertical Jet in Cross-Flow to graduate in August 2008 and received the engineering diploma from his French school in September 2008.